UNIVERSITÀ
DEGLI STUDI
FIRENZE

DOTTORATO DI RICERCA IN
Scienza per la Conservazione dei Beni Culturali

CICLO XXVI

COORDINATORE Prof. Piero Baglioni

Development of innovative methodologies for non-invasive characterization of metal artefacts of archaeological, historical, and industrial interest, through neutron diffraction and neutron imaging techniques

Settore Scientifico Disciplinare FIS/07

Dottorando
Dott. Salvemini Filomena, Floriana

Tutore
Prof. Zoppi Marco

Co-Tutore
Prof. Grazzi Francesco

Coordinatore
Prof. Baglioni Piero

Anni 2011/2013

Alla mia famiglia

Abstract

Metal artefacts of archaeological and historical interest represent a large fraction of the rich cultural heritage which is conserved in national and private museums worldwide. As such, these objects, when properly studied, can reveal secrets of the past human history and we are only allowed to treat them using the most delicate care and avoiding, as much as possible, to accelerate the natural and unavoidable aging process. Moreover, as the technological knowledge evolves, we are not allowed to investigate these objects using invasive tools that might prevent further more involved techniques to operate properly on the same objects by future generations.

Until recently, the research activity in this field was mainly based on standard point-based analytical techniques like, for example, metallography. Traditional analysis, however, though extremely effective, is not always suitable for rare and unique objects of high scientific, cultural, and economic value. Lots of interesting metal items fall in this category: sculptures and artistic artefacts, archaeological finds, rare coins, and even meteorites. It has been shown that this technique, which is mainly based on a careful surface analysis following a cleaning and preparation process, can be effectively complemented by a well-recognized, non-invasive experimental approach, based on the use of thermal neutrons.

Thanks to their high penetration power, neutrons represent an ideal tool to probe the microscopic properties of bulk dense materials and can be used to characterize the microscopic structure (at the atomic level) of metal artefacts. As a matter of fact, neutron techniques are used to determine the qualitative and quantitative presence of different phases, as well as the presence and distribution of texture and residual strain at the atomic level. From this wealth of data it is possible to obtain information on the conservation status of the artefact, as well as on the smelting and smithing procedures, through identification of some peculiar signatures related to these processes. In fact, the study of forging techniques, and their time-evolution, represents one of the most interesting topics in the investigation of the manufacturing methods, which are considerably different among various cultures. To this aim, neutron diffraction can be used to quantitatively determine the relative amount of the various crystal phases composing the artefact, its conservation status, the presence of texture, measurements of residual strains, and the determination of the grain size of the phases in the sample.

In addition, neutron imaging techniques allows obtaining bulk detailed information on the micro-structural properties of the samples, through the tomographic reconstruction of the object's macroscopic cross section. However, this technique can be further improved, to achieve materials discrimination, by a proper selection of the neutron energy. In fact, monochromatic neutron beams give the possibility of modifying the image contrast for different phases taking advantage of the abrupt change of the attenuation coefficients in the proximity of the so-called Bragg cut-off.

In the present work, we have developed a comprehensive study of the metallurgy of museum metal artefacts of historical and archaeological interest aiming to investigate composition, assembly methods, and structural variations pertaining to different cultures and historical environments. The study has been developed in cooperation with several Museum Institutions (like, for example: Museo Stibbert – Firenze (IT) and The Wallace Collection - London (UK)) and some private collectors.

Beyond time-of-flight neutron diffraction, which represents the workhorse of the neutron techniques, white beam and energy selective radiography, tomography, and laminography have been successfully applied to determine the material composition and microscopic structures of the analysed samples. From these results, we could obtain information on the smithing techniques and the working process of the studied of ancient artefacts. For this investigation several experimental European facilities have been used, like the ICON, NEUTRA and POLDI beam-lines at the Paul Scherrer Institut (CH), the CONRAD II beam-line at the Helmholtz-Zentrum Berlin (DE), and the INES and ENGIN-X beam-lines at ISIS (UK).

Japanese sword (*katana*) blades pertaining to the Koto (987–1596) and the Shinto (1596–1781) periods in Japan have been characterized using neutron diffraction and neutron-imaging techniques (in this case both white beam and energy selective imaging have been used). However not only the blades were the object of the present investigation, but also the composite structures of the metal components at the handle's extremities of Japanese swords have been investigated: the hand-guard *tsuba*, the hilt collar *fuchi*, the pommel *kashira*, the small knife-handle fitting into the scabbard *kozuka*. In addition, we extended the study to the inner metal structure and manufacturing techniques of *kabuto* (helmets), which represent beautiful examples of past technology made in Japan in the 17th Century.

The present investigation, however, was not limited to the study of the Japanese historical objects but was extended to other cultural environments. Thus, we have done experiments on a set of five *kris*, the distinctive weapon of Malaysia and Indonesia, and on a *kanjar*, the Indian dagger. Morphological information and material distribution in the whole volume of these objects allowed us to identify the working procedures and, when possible, to define the authenticity of the investigated samples.

The study has been enriched by a methodological test, aiming to demonstrate the equivalence of the information content between the classical (invasive) technique of metallography and neutron diffraction and imaging techniques (non-invasive). An enlightening comparison could be obtained studying the cross sections of a Toledo-like sword, which has been studied thought neutron imaging. Fragments, taken at different height of two sacrificed samples, were investigated through energy selective images and the results have been compared to those obtained from standard metallography.

Once the neutron techniques were validated, on a qualitative and quantitative basis, a massive investigation was conducted on a large number (91) of *styli*, the small bar made of either iron, bronze or bone, used by the Romans for writing onto wax-coated surface of wooden flat tablets. All these samples, coming from the same archeological site of Julia Concordia - Venice (Italy), were carefully analyzed by neutron techniques and have disclosed peculiar morphological features related to the working techniques of ancient Romans.

Finally, it is worthwhile to note that, beyond the standard neutron diffraction and imaging experiments, a relevant number of samples (two selected Japanese swords and 11 Roman *styli*) that have been analyzed to obtain the residual strain mapping aiming to obtain information on the method and direction of working.

Contents

1 Introduction

An accurate knowledge of the composition (phase distribution) and the microstructure (size, shape, and orientation of grains) of materials represents the equivalent of the *Rosetta stone* in material science. Until recently, especially concerning metal objects, this task was mainly fulfilled basing on standard analytical techniques like, for example, metallography. Traditional analysis, however, though very accurate, is not always suitable for rare and unique objects of high scientific and economic value. Lots of interesting items related to cultural heritage fall in this category: sculptures and artistic artefacts, archaeological finds, rare coins, and even meteorites. It has been shown that this well established technique, which is mainly based on surface analysis, can be effectively complemented by an emerging non-invasive experimental approach based on thermal neutron analysis. In particular, neutron-imaging techniques, in combination with neutron diffraction, provide an attractive approach to determine the morphology, the qualitative and quantitative presence of different phases, as well as the presence and distribution of texture and residual strain. From this wealth of data it is possible to obtain information on the conservation status of the artefact, as well as the smelting and smithing procedures, through identification of some peculiar signatures related to these processes.

In order to characterize different examples of Cultural Heritage objects, disclosing different open questions about their origin or production method, this study, devoted to analyze the potential of the aforementioned neutron techniques, was developed in cooperation with several Research Groups and Museum Institutions.

In this thesis neutron diffraction and imaging techniques are applied for the development of methodological approaches aiming to a non-invasive characterization of metal artifacts of historical, archaeological and industrial interest pertaining to different periods and cultures.

Chapter 2 is dedicated to ancient metallurgy; briefly travelling through the development of human technology in time, space and culture. Here, the research questions that led to the present investigation are introduced. In Chapter 3, we briefly recall a number of introductory concepts concerning the study and technology of metals: alloys, working techniques, meaning of stress, strain and texture and so on. In Chapter 4, we introduce the neutron techniques with a particular attention to neutron imaging and diffraction used as diagnostic techniques for the characterization of metals. Finally, Chapter 5 reports a panoramic view of the various measurements and the results obtained for the different ancient and historical metal objects.

Chapter 2

Ancient metallurgy

2 Ancient metallurgy

Slowly moving from the Stone-age to a more advanced stage of mankind, our forefathers had several occasions to meet different kind of metals that gave, once the relative technology was developed, a sensible impulse to the human progress. Initially, of course, only those metals that were found as native ones (e.g. copper, silver, and gold) were used for the production of tools, weapons, and jewels. These metals were "easily" collected, and worked, to be used in the same areas where they could be found or to become precious objects of exchange. Some time, also meteoric iron was found, albeit in small and usually rapidly exhausted quantities. However, in this case, the technological skills necessary to transform this material into a useful tool were delayed until the copper technology reached its climax [Buchwald 2005].

Native copper was the first metal that was extensively used in Asia, Europe and North America [Coghlan 1975, Tylecote 1987, Wayman 1989]. It could be found in the lower part of the gossan, the secondary oxidized minerals which then covered many sulphidic copper deposits. The early metallurgy of native copper has been widely discussed by historians and metallurgists. Early evidences were found in southeastern Turkey around the end of the 9th millennium B.C. and the beginning of the 8th [Maddin *et al.* 1999]. It appears plausible that once early craftsmen had discovered the possibility to use charcoal fire to heat native copper in a clay crucible, up to the melting point (1083°C), it was not a long step to discover other means of pure copper production, starting from the attractive colorful oxycabonates, malachite and azurite. By this technique, a mixture of metal and slag[2.1] was formed in the furnace, and this was subsequently broken up and melted in crucible to purify the metal component [Buchwald 2005]. The subsequent discovery that adding a different metallic ore to the melt would improve the best technological features of pure copper [Wheeler and Maddin 1980], lead to the production of *arsenical bronze*. This was obtained from *co-smelting*[2.2] of ore minerals containing Cu and As. At a later stage, the exploitation of other metal ore mixtures, such as those containing tin, could lead to the formation of an alloy (a solid solution of two or more metals), such as bronze [Williams 2003].

Apparently the development in copper technology took place independently in many different places, as the early locations appear very widely spread. Evidences of these early attempts, dating back to the 6th millennium B.C., have been documented by archaeologists operating in Central Anatolia, in northern Mesopotamia, and in northwestern Iran. The first smelting activities, appearing in the Middle East, start from the 4th millennium B.C. [Flawn 1966, Hauptmann 1985, Hauptmann *et al.* 1992]. At any rate, it is customary to attribute the beginning of metallurgy to the early discovery of smelting and extracting copper from its ores [Buchwald 2005].

[2.1] A slag is defined as the by-product of smelting ore to purify metals. In nature, the ores of metals are found in impure states: an intimate association of metal (sulphide, oxide, native state), and an undesired embedding rock (*gangue*) known as *tout venant* [Yalçin and Pernicka 1999]. A slag generally consists in a mixture of metal oxides and its composition can be influenced by several factors. They are: nature of the ores and *gangue*, charcoal and wood ashes, furnace construction material (including lining, bricks, *tuyeres*, temper added to clays used as furnace linings, etc.), fluxes added, process condition (heat distribution, air intake, furnace profile and height, retention time of slag within furnace), cooling condition [Benvenuti 2004].

[2.2] During smelting, the ore is heated beyond the melting point, ordinarily in the presence of reducing agents (charcoal or coke). Thus a fuse composed by silicates is separate from the metal fraction, which forms as a solid in it. During the cooling of the fuse, impurities are separated from the metal and can be easily removed [Backmann 1968].

In particular, the Sumerians were the first to adopt tin bronze technology and the metallurgy of the *Early Dynastic period* (around 3000 B.C.) was well developed [Moorey 1994]. Despite the lack in ores, acquired from trade with the Near East, Mesopotamia was extremely rick in natural fuel. The advanced use and knowledge of the fuels and their properties made the Sumerian technology of bronze decidedly superior respect to contemporary cultures. Extending from India to Anatolia, the bronze metallurgy was spread spasmodically, appearing in the Indus valley in about 2500 B.C. and progressing westwards through Europe from about 2000 [Kaufman 2011].

Unlike copper, iron never appears in nature, in its native form. Iron ores are very widespread, but the extraction of the metal component is not simple, due to the high melting-point temperature at about 1500°C. On the other hand, the *Iron Age* could not develop until successful techniques for the reduction of iron ores had been devised and disseminated.

It is very likely that some attempts of iron working could have been attempted using the copper technology and meteoric iron. However, the erratic availability of the base material and the substantially inadequacy of the technique did not allow a regular production of iron objects, even though some findings of iron objects were exceptionally recovered in sites unequivocally attributed to the copper age [Grazzi 2012]. In addition, due the technology limitations, the quality of the first iron smelting attempts was not of immediate advantage to the Ancient World. Iron smelting seems to have been first developed, with some regularity and continuity, somewhere between the Caucasus and the Fertile Crescent early between the 3rd and the 2nd millennium B.C [Forbes 1964, Scott 1991].

Following the destruction of the Hittite Empire, in the 1200 B.C., the knowledge of iron-making spread fairly quickly around the Near East and it was exploited in a considerable scale by the Assyrian, which made a large scale use of iron. Greeks too used iron tools quite extensively, although they continued to employ bronze swords and armors. As a matter of fact, the Trojan war, also dated around 1200 B.C. was apparently fought using bronze weapons. According to some historians [e.g. Herodotus], Tyrrhenian populations, migrating from southern Anatolia around 12th XII century B.C., diffused the iron metallurgy in the Mediterranean area giving rise, likely, to the Etruscan civilization [Pallottino 1998]. In the northern Europe, north of the Alps, the westward movement of Celtic populations spread the knowledge of iron weapons and tools after the 5th century B.C. [Cleere and Scott 1984, Tylecote 1987].

The very low-carbon iron produced in the bloomery hearth furnaces, where bellows were used to force air through a pile of iron ore and burning charcoal, was inferior in hardness, as well as in corrosion resistance, to copper alloys. The success and upsurge of iron depended entirely on its ability to become carburized[2.3] and converted onto steel.

It has also been suggested that the transition to iron was due to shortage in the supplies of copper and, especially, tin. In addition, there was a fuel-saving incentive to change from bronze to iron and, moreover, the iron ore was much more widespread [Buchwald 2005].

Anyway, iron weapons and armors did not become superior to bronze until the fundamental discovery that quenching[2.4], after carburization, resulted in a dramatic increase in hardness. The process is difficult to manipulate, since the hardness is due to the formation of martensite[2.5], and an excess of this phase leads to embrittlements (and fragility) of the tool.

[2.3] Carburization is the process of increasing the carbon content of a metal.

[2.4] The act of quickly cooling a metal or alloy by plunging into cold water or oil.

[2.5] A non-equilibrium metastable phase resulting from the transformation, without diffusion, of austenite (see chapter 3–section 3.3.2).

Quenching is mentioned by Homer (perhaps in the 10th or 9th century B.C.) but the difficulties of controlling the carbon content in steel meant that quenching remained a hit-and-miss process, and therefore avoided by many smiths, for a long time to come.
The Roman army initially organized itself on the Greek and Macedonian models, also in terms of equipment, but contacts with the Celts and the experience of the Punic Wars led them to adopt the Celtic sword-making technology [Williams 2003].

In Central Europe ironworking developed within the Celtic sphere of influence from the 8th to the 7th century B.C. during a period that can hardly be determined. Iron soon became an important factor in everyday's life. The pulse for the development of iron-making in the Celtic area presumably moved from the Mediterranean and Near East towards Central Europe and could have taken several routes over the Alps and towards the western and eastern countries of southern Europe [Pleiner 1996]. According to the current school of thought, iron, in Europe, was exclusively produced in direct process before the blast furnace was developed at the end of the Medieval period. In this phase of the technological progress, iron was made in small furnaces, through the reduction of the ore into a pasty state, because temperature was not sufficiently high to melt iron [Shurmann 1958, Gassmann 1998]. In current use, a charge of ore and charcoal was placed in the furnace and, during the smelting process, some of the lighter impurities, i.e. the melted ones, were tapped off as slag until, at the end, cinders, slag and the so-called bloom[2.6] of iron remained at the bottom of the furnace. Repeated heating and forging of the bloom would be necessary to expel much of the slag and consolidate the metal part to produce a bar of wrought iron [Goodall 2012]. Then, the obtained product could be carburized. The process of carburizing wrought iron consisted in taking an iron or low carbon steel piece, packing it with carbonaceous material in a sealed vessel, and then baking at high temperature (at red heat) for a long period of time. Thus carbon would leech into the metal creating steel, eventually [Johnson 1999]. Pieces of iron (low carbon content, $C<0.2$ wt% C) and steel (higher carbon content, $C>0.2$ wt% C) could be welded together (by hot hammering) to form a sword, which was then hardened by some form of quenching. This procedure was adopted in both European and East Asian smithing techniques. In Europe, it led to the development of the piled and the pattern-welded sword. The subsequent development of large bloomeries[2.7] enabled to make steel in much larger quantities, so that the later European Middle Ages (14th century) saw the development of suits of steel plate armor as well as all-steel swords. In Japan this process was brought to its highest level, where it formed the basis of sword-making, almost until modern times [Williams 2003].

The date and origin of the introduction of iron artifacts and iron working into India remains a much debated problem, connected with the equally debatable question of its association with the supposed arrival, in the 2nd millennium B.C., of immigrants from the west. It is evident that iron first appeared in India between 1300 and 1200 B.C.. However, it is generally agreed that the beginning of the 1st millennium B.C. saw the advent of iron in India during a period of peaceful settlements and political stability (the Maurya period)[2.8] [Prakash and Tripathi 1986].
India was famed in literary and history accounts since Greek and Roman time for the traditional crucible steel. According to Will Durant, the technology passed to the Persians

---

[2.6] A roughly finished metallic product; specifically, the spongy mass of iron produced in a bloomery furnace in which the iron is reduced in situ and is not molten during reduction. The crude iron bloom must be extensively worked at red heat to consolidate the iron and remove excess slag and charcoal [Prakash and Tripathi 1986].
[2.7] The furnace for the extraction of iron from the ore.
[2.8] The Maurya Empire was a historical power in ancient India, ruled by the Mauryan dynasty from 322 to 185 B.C..

and from them to Arabs who spread it through the Middle East. In the 16th century, the Dutch carried the technology from South India to Europe, where it gave ride to steel mass-production [Porter 2003].

In this process, small pieces of iron can be separated from the bloom and then heated in a close crucible together with charcoal (which is almost entirely composed by carbon), until a partial or total melting takes place. Rapid absorption of carbon can lead to the formation of cast steel ("crucible" steel), with a very high (1.2-1.6 wt% C) carbon content, which needs further little hardening. Some steel of this type seems to have found its way into Europe during the early Middle Ages. Controlled cooling and forging can then develop a pattern, resembling watered silk, on the surface of the blade (*wootz steel*, misnamed *Damascus steel*). This was the procedure used in Iran, Central Asia and India, where it remained in operation until 19th century, with products that were high in quality but small in production scale [Williams 1963, Panseri 1965, Craddock 1995].

In China, bloomery-based ironworking was probably introduced through Central Asia [Pigott 1999]. However, from the 5th century B.C., a liquid product of the furnace was more usual. Such a furnace was called a blast furnace and differs from the bloomering only in a somewhat larger size and a different fuel over ore ratio. Owing to the sensible decrease of steel melting-point with increasing carbon content, a mixture over 2% carbon will melt at 1150°C, forming a liquid called cast iron or pig iron. This material can be cast into shape, but cannot be forged, nor hardened by quenching, and would seem useless for making weapon. Therefore, cast iron was converted into wrought iron by decarburization; to this aim, the steel was reheated and oxidized in air for several days in the finery. This technology, called the indirect iron process, was locally in use since the 1st century B.C.; The spread of this technique was favoured by the considerable scale economy it implied, allowing to work continuously, with a considerable saving in fuel per work unit, and avoiding the need to demolish the furnace for the extraction of the metal. Thus, large-scale production was favoured, while the bloomery gradually became uncompetitive, [Williams 2012, Craddock 1995].

In the late 12th century A.D. the indirect iron process became known in northern Europe, through Sweden, but it was spread, and commonly used in the resto of Europe, only during the 15th century A.D.. On the other hand, many scholars believe that blast furnaces have developed independently in Western Europe and China, albeit many centuries earlier in the latter [Buchwald 2005].

To be mentioned is the unique technology developed independently in Japan, where the traditional Japanese furnace, known as a *tatara* (Fig. 2.2), was developed. This is a hybrid type of furnace whose origin is still debated [Juleff 2009, Inoue 2009]. The *tatara* does not appear to be a Japanese invention and it may have come from Manchuria, by way of the Korean peninsula in the 6th or 7th century A.D.. By the 9th century, the *tatara* was in use throughout Japan, primarily by small groups of steelworkers, mining and smelting their own steel, and later evolving in mass production in selected centers [K. Nagayama 1997]. The *tatara* incorporated bellows, like the European blast furnace, but was constructed of clay; this furnace would eventually collapse after the first use [Wittner 2007]. According to existing archeological records, the first *tatara* were built during the middle part of the 6th century A.D. [Juleff 2009]. Due to the large scale of the *tatara*, as compared to its European, Indian and Chinese counterparts, the temperature at a given point would vary depending on the height in the furnace. Therefore, different types of iron could be found (with varying degrees of carbon content), at different heights, inside the furnace, ranging from wrought iron at the top of the *tatara* (furthest from the heat, lowest temperature), to cast iron towards the middle, and finally steel towards the bottom [F. Grazzi 2011]. Importantly, the *tatara* does not exceed 1500°C, so that it is unable to completely melt the iron. Obviously, the metal-workers could understand the differences between the various types of iron and they separated out and selected different portions of the "bloom" accordingly [Inoue 2009]. [2.9] From the early introduction of metal tools by the nearby Asia continents, during the Yayoi-period, the Japanese smiths evolved acquiring sophisticate skills that culminated in the forging of weapons, particularly swords [K. Nagayama 1997].

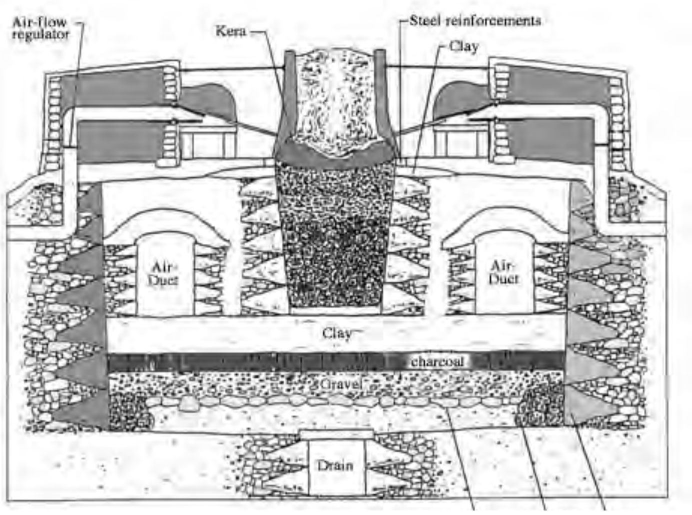

Figure 2.2: Cross section of a typical *tatara*. The complex structure below the ground is for the insulation, damp-proofing, and drainage. The clay driers are hollow; wood was burned in them at the time of construction [http://www.thejapanesesword.com/tatara].

[2.9] The metallurgy of others metals such as gold, silver, zinc, mercury and lead was avoided because out of the main themes discussed in this work.

Chapter 3

Materials

3 Materials

3.1 Metals

Materials in this group are composed of one or more elements (e.g., iron, copper, tin, zinc, silver, gold, nickel, ...), and often also non-metallic elements (e.g., carbon, nitrogen, oxygen, ...) in a relatively small concentration[3.1]. Atoms in metals and their alloys are arranged in very defined crystal structures and are relatively dense. Concerning the mechanical characteristics, these materials are relatively stiff and strong, yet are ductile and are generally resistant to fracture.

As is well known, metals contain large numbers of non-localized electrons, which are not bound to particular atoms. Many properties of metals are directly attributable to these electrons. For example, metals are extremely good conductors of electricity and heat, and are not transparent to visible light; a polished metal surface has a lustrous appearance. In addition, some metals (i.e., Fe, Co, and Ni) have desirable magnetic properties [Callister 2009].

3.2 Crystal structure

Solid materials may be classified according to the regularity with which atoms, or ions, are arranged with respect to one another. The distinct feature of a crystalline material is the placement of its atoms in a periodic array over large atomic distances, giving rise to long-range order where the atoms will position themselves in a repetitive three-dimensional pattern and each atom is bound to its nearest-neighbors. Under normal conditions, all metals form ordered and symmetrical arrangements called crystal lattice. Some of the properties of crystalline solids depend on the microscopic structure of the material, and therefore from the way in which atoms, ions, or molecules are spatially arranged [Callister 2009].

Every crystalline structure describing the regular position of atoms in a crystalline material may be considered in terms of a lattice of points in real space. Associated with each point is an array of atoms called *basis*. Thus, a structure comprises a lattice with its basis. The lattice of points can be described in terms of lattice vectors in real space, with every point on the lattice *l* given in terms of the fundamental translation vectors, or crystal axes, ***a***, ***b***, ***c***, which are chosen so that:

$$L=n_1\mathbf{a}+n_2\mathbf{b}+n_3\mathbf{c} \qquad (3.1)$$

where n_1, n_2, n_3 are integers. The lattice points can thus be said to have 3D translational symmetry. The values of ***a***, ***b***, ***c*** are called the *lattice constants*, which define the lattice together with the angles between these axis α, β and γ, where α is the angle between ***b*** and ***c*** and so on.

Associated with lattice is the concept of *unit cell*, a building block that, by repetition through linear translations, covers all points on the crystal lattice. The smallest unit cell is called the *primitive unit cell*, usually chosen to have one lattice point at each corner; the lattice points will then lie on what is called a *primitive lattice* [Hutchings *et al.* 2005].

The Bravais lattice is the set of all equivalent atoms in a crystal that is brought back onto itself when the whole set is displaced by the length of an integer value of a unit vector in a direction parallel to a unit vector [Kossevich 1999].

[3.1] The term *metal alloy* refers to a metallic substance that is composed of two or more elements.

In the three-dimensional space, the Bravais lattices are classified in a total of 14 possible lattices, according to the symmetry of rotations and reflections, and to the location of the lattice site [Kittel 1996].

Cubic and hexagonal lattices are of relevant interest here, since a large number of materials, especially metals, have this kind of lattice. Three relatively simple Bravais lattice are found for most of the common metals: face-centered cubic (*fcc*), body-centered cubic (*bcc*), and hexagonal close-packed (*hcp*), which, incidentally, represent the three most dense lattice configurations [Kittel 1996].

The crystal structure found for many metals has a unit cell of cubic geometry, with atoms located on each of the corners and on the centers of all the cube faces (*fcc*). The atomic packing factor[3.2] (APF) for this structure, is 0.74, which is the maximum possible packing value for spheres of the same diameter. The coordination number, i.e. the number of nearest neighbors, is 12 that is the same for *fcc* and *hcp* lattices. Metals typically have relatively large atomic packing factors, to maximize the shielding provided by the free electron cloud. Some of the most familiar metals, having this crystal structure, are copper, silver, and gold (Fig. 3.1-*a*).

Another common metal crystal structure is the *bcc* where the atoms are located on the corners and the center of a cubic cell. The coordination number this structure is 8 and, correspondingly, the atomic packing factor is 0.68. Iron, tungsten, and chromium exhibit a *bcc* structure (Fig. 3.1-*b*).

The *hcp* crystal structure, another close-packed structure like *fcc*, has a hexagonal unit cell (Figure 3.1-*c*). The coordination number and the atomic packing factor for this structure are the same as for *fcc*: i.e. 12 and 0.74, respectively. The HCP metals include cadmium, magnesium, titanium, and zinc [Callister 2009].

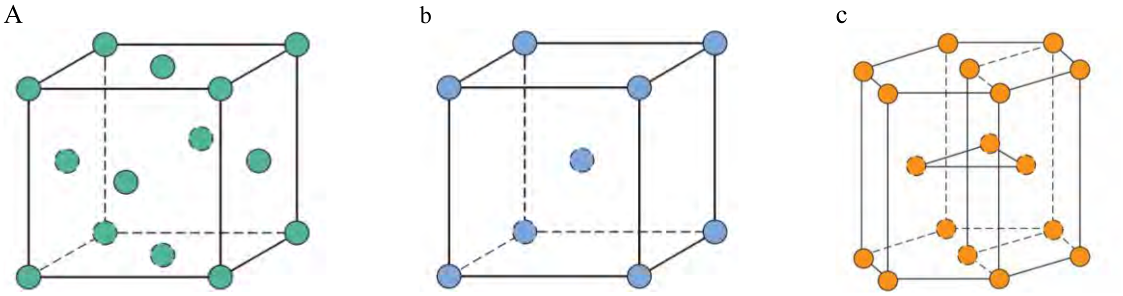

Figure 3.1: The reduced-sphere unit cell models for *a* the face-centered cubic crystal structure, *b* the body-centered cubic crystal structure, *c* hexagonal close-packed crystal structure [Callister 2009].

3.2.1 Cristallographic planes and directions

The orientation of crystallographic points, directions, and planes are specified in terms of indexing schemes. The basis for determining index values is the unit cell, with a right-handed coordinate system consisting of three axes (**x**, **y**, and **z**) situated at one of the corners and coinciding with the unit cell edges [Callister 2009].

The application of a set of rules leads to the assignment of the *Miller* indexes (*hkl*). The *Miller* indexes are conventionally defined as the reciprocal multiples of the axis intercepts, reduced to the smallest integers having the same ratios.

[3.2] The APF is the sum of the sphere volumes of all atoms, bordering one another, within a unit cell divided by the unit cell volume [Callister 2009].

In the single crystal, the periodic and repeated atomic pattern extends throughout the entire crystalline solid without interruption. However, this condition is very rare in real metals that, instead, are characterized by a generally polycrystalline structure composed by a collection of single crystal grains arranged together.

3.3 Alloys

A metal alloy is a solid mixture composed of two or more elements where the main component is always a metal. Most familiar alloys are those where impurity atoms have been added intentionally to impart specific characteristics to the material and to improve its properties. The addition of an impurity to a metal will result in the formation of a uniform solid solution and/or formation of a new phase, depending on the kinds of impurity, their concentrations, and the temperature of the alloy.

A solid solution may form when the impurity added atoms occupy substitutional or interstitial sites and are uniformly and randomly dispersed within the solid. In this case, the original host crystal structure is maintained and no new phase is formed, giving rise to a compositionally homogeneous resulting material. Several features determine the composition of substitutional solid solution: the atomic diameters, and electronegativities, should be similar; both elements should have the same crystal structure (or very similar ones, like *fcc* and *hcp*); the number of valence electrons in the impurity atoms should be equal, or smaller, than the host material [Pearson 1964]. In the particular case of interstitial solid solutions, impurity atoms fill the voids or interstices among the host atoms. For metallic materials that have relatively high atomic packing factors, these interstitial positions are relatively small. Consequently, the atomic diameter of an interstitial impurity must be substantially smaller than that of the host atoms. Normally, the maximum allowable concentration of interstitial impurity atoms is low (less than 10%). Since even very small impurity atoms are ordinarily larger than the interstitial sites, they introduce some lattice strains on the lattice of the host atoms. As an example, the alloy Fe-C is representative of an interstitial solid solution, whereas the alloy Cu-Sn (bronze) is substitutional.

The composition (or concentration) of an alloy can be expressed in terms of its constituent elements: weight (or mass) percent or atom percent. The basis of weight percent (wt%) is the weight of an element relative to the total alloy weight, whereas in the case of atom percent (at%) the calculation is based on the number of moles of an element in relation to the total moles of the elements in the alloy.

For some systems, discrete intermediate compounds rather than solid solutions may be obtained and these compounds have distinct stoichiometry and structure; for metal–metal systems, they are called intermetallic compounds. Intermetallic compounds exists as homogeneous, composite substances and differ discontinuously in structure from that of the constituent metals. Their properties cannot be transformed continuously into those of their constituents by changes of composition alone, and they form distinct crystalline species separated by phase boundaries from their metallic components and mixed crystals of these components. Although intermetallic compounds are noticed by chemical formulas, their composition is never well established on the sole basis of analytical data but can fluctuate in a very narrow range around the values indicated by the corresponding formula (Al_3Mg_4; Mg_2Si; CuZn, etc.).

3.3.1 Phases and phase diagrams

A phase can be defined as a homogeneous portion of a system that has uniform physical and chemical characteristics. In this respect, a single-phase system is termed *homogeneous*. Systems composed of two or more phases are termed *mixtures* or *heterogeneous systems*. Usually, the properties combination of the multiphase system is different from, and more attractive than, the ones of the individual phases [Callister 2009].

A phase diagram represents the limits of stability among the phases composing the alloy in its chemical equilibrium system, with respect to variables such as composition and temperature. For an alloy of specified composition, at a defined temperature, the analysis of the phase diagram allows to determine structural information at ideal equilibrium condition, i.e. following an infinitely slow relaxation process.

When two metals are mixed together, three different cases can occur. The first one is a solid alloy characterized by a complete solubility of the components. An example of this type of perfect miscible elements in a single phase is the silver-gold alloy.

The second possibility is that the solid alloy shows only partial solubility of the metals in each other. One example is represented by the silver-copper pair. In this case, three principal types of phase diagrams can arise. The most common is the eutectic type, the second is the eutectoid, and the third is the peritectoid.

An eutectic system has a single chemical composition, which solidifies at a lower temperature than single constituents. When an eutectic reaction occurs, a liquid phase transforms isothermally and reversibly into a two-phase microstructure resulting from the solidification of the liquid having the eutectic composition.

On the other hand, the decomposition from a solid solution into two finely dispersed solid phases creates a structure called an eutectoid of two new intimately mixed solid phases.

Finally, at the peritectoid composition, an isothermal reversible reaction of a liquid phase and a solid phase occurs to form a second solid phase during cooling.

The third case is the complete immiscibility of the two metals. As the temperature falls from the melt of these mutually insoluble metals, one of them will be precipitated, usually as globules of one phase in grains of the higher melting point metal. Examples of these microstructure are shown by the alloys of copper and lead, zinc and lead, iron and copper [Scott 1991].

A general dissertation about phase diagrams can be found in classical metallurgy books [Callister 2009, Scott 1991]. Here I will focus on the iron-carbide system, which is of interest for the purposes of the present study.

The thermodynamic equilibrium solid phases found on the iron–iron carbide phase diagram (Fig. 3.2-*a*) are ferrite (*bcc*), austenite (*fcc*), and the intermetallic compound iron carbide or cementite (Fe_3C).

On the basis of their composition, ferrous alloys fall into three classifications:

- Wrought Irons (C<0.25 wt%)
- Steels (0.25 wt% < C < 2.14 wt%)
    - hypoeutectoid steel (0.2-0.77% C)
    - eutectoid steel (0.77% C)
    - hypereutectoid steel (0.77-2.14% C)
- Cast irons (C>2.14 wt% C)[5.3] [Callister 2009].

[5.3] As a general definition, a steel is an alloy of iron, carbon (under 2% C), and other alloying elements that is capable of being hot and/or cold deformed into various shapes. A cast iron, on the other hand, is an alloy of

Moreover, three invariant reaction can be defined:

- eutectoid (727°C at C 0.77 wt%), the most important one from a technological point of view.
- eutectic (1147°C at C 4.3 wt%)
- perieutectoid (1495°C at C 0.17 wt%)

The development of microstructure for many iron–carbon alloys and steels depends on a eutectoid reaction in which the austenite phase (composition 0.76 wt% C) transforms isothermally, at 727 °C, to ferrite (0.022 wt% C) and cementite (6.67 wt% C) (Fig. 3.2-*b*).
The microstructural product of an iron–carbon alloy of eutectoid composition is pearlite, a microconstituent consisting of alternating layers of ferrite and cementite (Fig. 3.2-*b*).
The microstructures of alloys having carbon contents less than the eutectoid (i.e., hypoeutectoid alloys) are composed of a proeutectoid ferrite phase in addition to pearlite (Fig. 3.2-*c*).
Pearlite and proeutectoid cementite constitute the microconstituents for hypereutectoid alloys—those with carbon contents in excess of the eutectoid composition (Fig. 3.2-*d*).

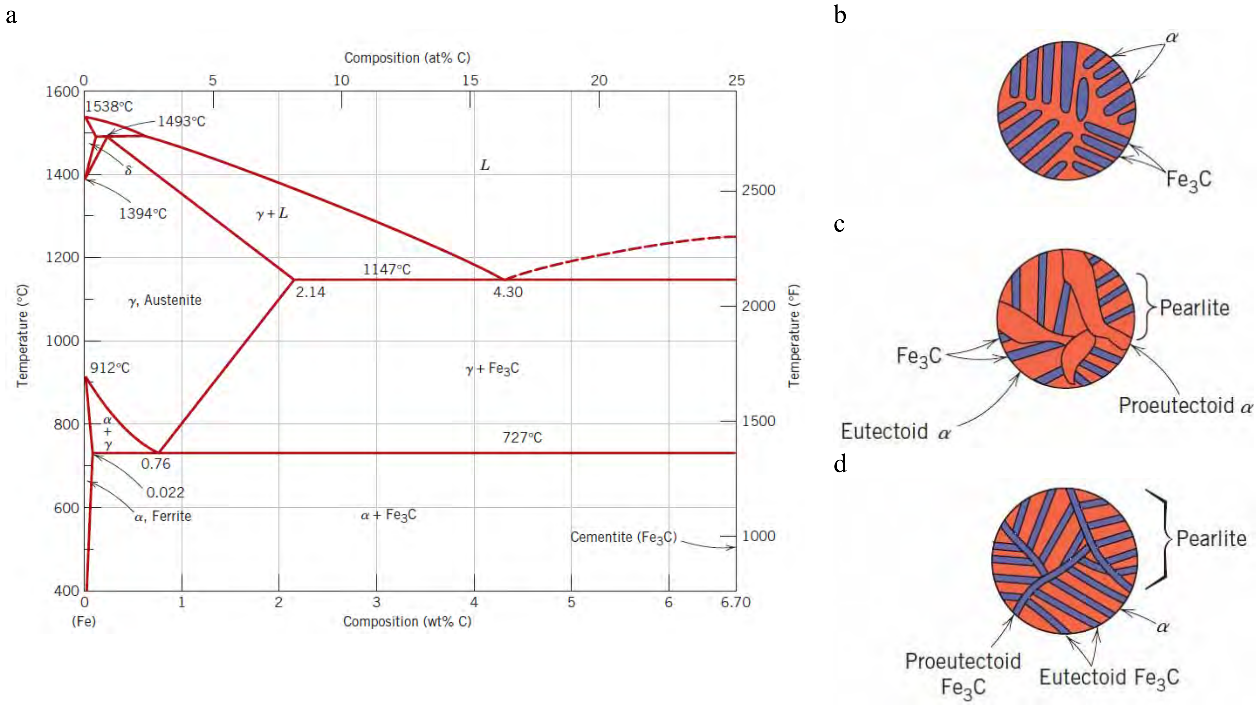

Figure 3.2: The iron–iron carbide phase diagram *a* and a schematic representations of the microstructures for an iron–carbon alloy of eutectoid composition *b*, hypoeutectoid composition *c* and hypereutectoid composition *d* [Callister 2009]

3.3.2 Continuous cooling transformation

Phase diagrams provide no information about the time-dependence of transformation progress. However, the time element is incorporated into isothermal transformation diagrams, plots of temperature versus time (usually on a logarithm scale), and similar. They are generated from a series of plots of percentage transformation versus the logarithm of time taken over a range of temperatures.
Conversely isothermal heat treatments are not the most practical to conduct because the process can be considered valid only for conditions of constant temperature in which an

---

iron, carbon (over 2% C), and other elements and is not normally capable of being hot and/or cold deformed. Various types of steels and cast irons are classified and defined [Bramfitt 2002].

alloy is rapidly cooled to, and maintained at, an elevated temperature from a higher temperature above the eutectoid. On the contrary, most heat treatments for metals involve the continuous and constant changing in temperature. For continuous cooling, the time required for a reaction to begin, and to end, is delayed. A plot containing such modified beginning and ending reaction curves is termed a continuous cooling transformation diagram (Fig. 3.3-*a*). These diagrams make possible the prediction of microstructural products for specified heat treatments. This feature was demonstrated for alloys of iron and carbon, such as perlite, bainite, spheroidite and martensite. Operatively, the rate of cooling can be influenced by the operative method, namely cooling the iron either in air, oil, or water.

In particular, the martensite phase is an important microstructural product. This is an iron–carbon solid solution with a body-centered tetragonal (*bct*) crystal structure. Martensite is a metastable single-phase structure, supersaturated in carbon, product of a diffusionless (athermal) transformation from austenitized iron–carbon alloys (Fig. 3.3-*b*). It appears by rapidly quenching austenite to a sufficiently low temperature so as to prevent carbon diffusion and the formation of pearlite and/or bainite.

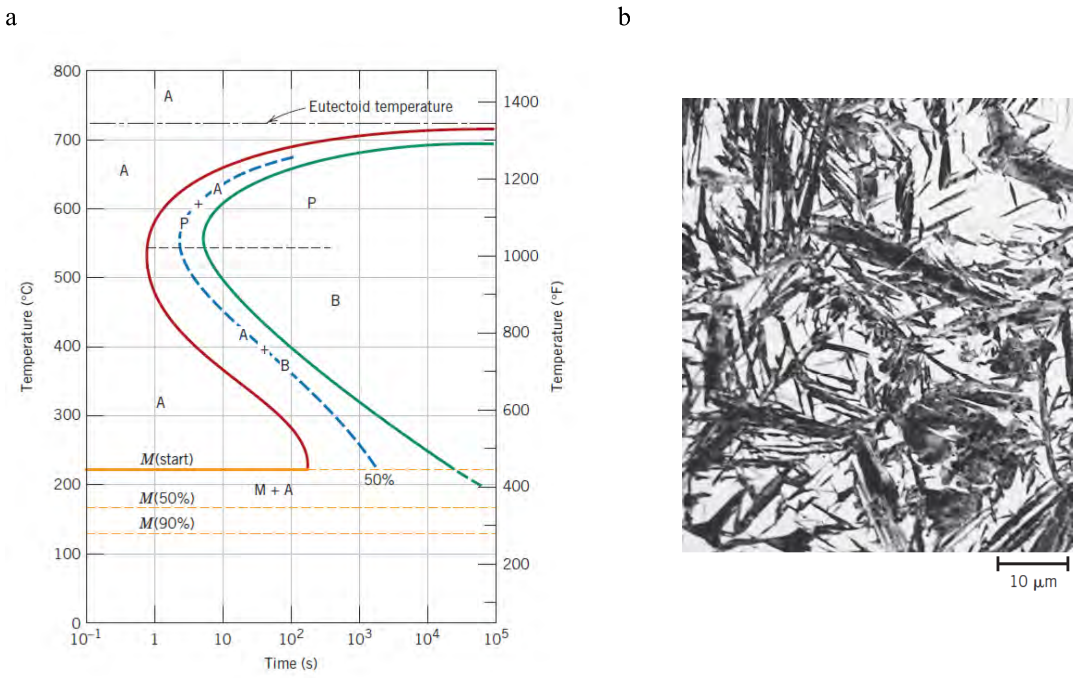

Figure 3.3: On the left, the complete isothermal transformation diagram for an iron–carbon alloy of eutectoid composition: A, austenite; B, bainite; M, martensite; P,pearlite. On the right, a photomicrograph at 1220x showing the martensitic microstructure. The needleshaped grains are the martensite phase, and the white regions are austenite that failed to transform during the rapid quenching [Callister 2009].

3.4 The microstructure of metals

There are two possible basic steps of manipulating metals or alloys: the first one is casting. After that, the metal can be left, as-cast, or subsequently worked.

3.4.1 Casting

The properties of the final metal product depend strongly on the quality of the original cast metal, which is therefore very important. The types of microstructure that can arise during the casting and cooling of a melt in a mold, regardless of the exact nature of the technology involved, influence the following properties of the cast metal. They are:

- The segregation of the alloying elements.
- The microstructure (grain size, phases).
- The soundness (porosity in the metal).

Segregation is the distribution of the solute product within the grains by solidification.
Dendritic growth is actually one form of segregation that can occur during casting. It is a segregation phenomenon that often arises in impure metals, or alloys, because one of the constituents usually has a different melting point. The faster is the rate of cooling, the smaller are the dendrites.
The other principal types of segregation are normal segregation and inverse segregation. Normal segregation occurs when the lower melting point constituent is concentrated towards the inner part of the mold, while inverse segregation can push the alloying element to the exterior of the surface of the mold.

Occasionally metal can be relatively free of impurities, on slow cooling no dendrites appears, and an equi-axial, hexagonal grain structure forms. An equilibrium structure of equi-axed hexagonal crystal structure, in which all the grains are roughly of the same size, randomly oriented, and roughly hexagonal in section, can be obtained by extensive annealing the original dendritic structure.

Cast metals often display characteristic holes, or porosity, which can be due to dissolved gases in the melt, or to interdendritic holes and channels that have not been kept filled with metal during solidification. As the metal cools, and the original gases dissolve, air can penetrate these cavities and create reactions with the metal itself to form oxides [Scott 1991].

3.5 Working

The mechanical properties of a metal are described in terms of stiffness, strength, hardness, ductility, and toughness. The behavior of the material reflects the relationship between its response, or deformation to an applied load. In particular, elastic deformation arises in the case of a temporary deformation that is totally recovered upon release of the applied stress.

Plastic deformation can occurs if, after release of the applied load, the deformation is permanent or non fully recoverable. It is accompanied by permanent atomic displacements [Callister 2009].

3.5.1 Plastic deformation in polycrystalline materials

3.5.1.1 *Slip system*

Plastic deformation corresponds to the motion of dislocations, linear crystalline defects in correspondence with atomic misalignment, in response to an applied shear stress. Edge, screw, and mixed dislocations are possible as the result of dislocation motion.
Dislocations move with different degree of ease in relation to the crystallographic planes of atoms and the crystallographic directions involved. Usually dislocation motion occurs along specific directions in a preferred plane called the *slip plane*; the direction of movement is called the *slip direction*. This combination of the slip plane and the slip direction is termed the *slip system*.
The crystal structure of the metal and the atomic distortion that accompanies the motion of a dislocation at a minimum position defines the slip system. Ordinarily the slip plane is the plane that has the most dense atomic packing for a particular crystal structure, while the

slip direction corresponds to the direction, in this plane, that is most closely packed with atoms.

The different possible combinations of slip planes and directions generate several independent slip systems for a particular crystal structure.

In general, *fcc* and *hcp* crystal structures are characterized by a relatively large number of different slip systems (at least 12), being the plastic deformation possible along the entire system and reflecting in a quite ductile behavior [Callister 2009].

These crystal imperfection, the dislocations, enable deformation to take place at lower applied stress than it would be possible if the lattice structure was perfect, give rise to the characteristic malleability of metals [Scott 1991].

5.5.1.2 *Mechanisms of strengthening in metals*

Since the macroscopic plastic deformation corresponds to the motion of large numbers of dislocations, the ability of a metal to plastic deformation depends on the ability of dislocations to move.

The mechanical strength of a metal may be enhanced by reducing the mobility of dislocations, being hardness and strength related to the ease with which plastic deformation can occur. On the other hand, the more unconstrained is the dislocation motion, the greater is the facility with which a metal may deform, consequently becoming softer and weaker. Virtually, all strengthening techniques restrict or hinder dislocation motions making the material harder and stronger. The main strengthening mechanisms for metallic materials are hardening, grain size reduction, and solid-solution strengthening.

Strain hardening is just the enhancement in strength and consequent decrease of ductility of a metal as it is plastically deformed. The process is also known as *cold-working* because the temperature at which deformation takes place is “cold” in comparison to the melting temperature of the metal itself. The treatment usually consists of rolling, hammering, or drawing at room temperatures where the hardness and tensile strength are increased with the amount of cold-work, but the ductility and impact strength are reduced.

During plastic deformation, the dislocation density increases, the average distance between adjacent dislocations decreases, and dislocation mobility becomes more restricted because dislocation–dislocation strain field interactions, are, on average, repulsive.

The size of the grains, or average grain diameter, in a polycrystalline metal influences the mechanical properties. During plastic deformation, slip or dislocation motion must take place across the common boundary among adjacent grains normally characterized by different crystallographic orientations. The grain boundary acts as a barrier to dislocation motion because the two grains are of different orientations, and the atomic disorder within a grain boundary region will result in a discontinuity of slip planes from one grain into the other. More grains produce a higher strength and, therefore, a fine-grained material is harder and stronger than a coarse-grained one, since the former has a larger total grain boundary area to block dislocation motion.

In a solid solution, the strengthening of the metals is also obtained by alloying impurity atoms which go into either substitutional or interstitial positions. Increasing the concentration of the impurities result in an increase in tensile and yield strengths because impurity atoms impose lattice strain on the surrounding host atoms. This results in an interaction between dislocations and these impurities, which restrict the dislocation movement.

As an example of the various microstructures that may be produced for a given steel alloy, martensite is the hardest and strongest one and, in addition, the most brittle. Its strength and hardness are not related to microstructure. Rather, these properties are attributed to the

effectiveness of the interstitial carbon atoms in hindering dislocation motion, and to the relatively few slip systems for the *bct* structure.
Concerning iron and steel, carburizing is a process for *case* (surface) hardening obtained by absorbtion of carbon freed when the metal is heated in the presence of a carbon bearing material, such as charcoal or carbon monoxide. Because carbon is almost insoluble into ferrite phase (0.02% maximum at 730°C) the metal is heated and moved to the austenitic phase, in order to solubilize a higher percentage of carbon in it (up to 2.1% at 1150°C). Heating longer (T> 750°C) in a closed environment of saturated carbon, the solid state diffusion of carbon in the austenitic matrix occurs.

The metal can be deformed by cold-working until it is too brittle to be worked any further. If further shaping or hammering is needed, then the metal must be annealed[3.4] in order to restore ductility and malleability. The properties and structures may revert back by appropriate heat treatment (sometimes termed as annealing treatment). During this process of heat-treatment carried out on a metal or alloy, usually to soften the material allowing further deformation, the material is exposed to an elevated temperature for an extended time period and then slowly cooled. The mechanical properties of the material that were changed during the cold-work process, are restored and the material becomes softer, weaker and more ductile. The extent of annealing depends both on temperature and time.
Together with temperature, time is another important parameter to be considered: a too long annealing can lead to grain growth and weakening of the structure, whereas a too short annealing may not be able to sufficiently eliminate heterogeneity and residual stresses.
The ductility and toughness of martensite may be enhanced and these internal stresses relieved by a heat treatment known as *tempering.* Tempering is accomplished by heating a martensitic steel to a temperature below the eutectoid for a specified time period. Normally, tempering is carried out at temperatures between 250 and 650°C.

3.6 Stress and strain

Cold-working a polycrystalline metal produces microstructural and property changes and some fraction of the energy expended in deformation is stored in the metal as strain energy, which is associated with tensile, compressive, and shear zones around the newly created dislocations. In defined environmental conditions, the mechanical properties of materials are ascertained by applying some load in tensile, compressive, or shear directions, constant with time or fluctuating continuously.

In the case of loading in tension and compression, stress is defined as the instantaneous load divided by the original specimen cross-sectional area.
The response of a metal to an applied force is a deformation, contracting when subjected to compression or stretching when under strain. The new configuration, assumed under the action of external forces, corresponds to a variation of the internal forces in the solid in order to balance the external ones.
As stated by Hooke's law, the degree to which a structure deforms or strains depends on the magnitude of the applied stress. The strain is expressed as the change in length (in the direction of load application) divided by the original length.
When most materials are deformed elastically, stress and strain are proportional. For tensile and compressive loading, the slope of the linear elastic region of the stress–strain curve is the *modulus of elasticity* (*E*), which can be seen as stiffness, or as material's

---

[3.4] Recovery and recrystallization processes are allowed to occur during annealing [Callister 2009].

resistance to elastic deformation. The elastic deformation is non-permanent and is totally recovered upon release of an applied stress.

If a critical value of applied stress is overtaken (*yield point*), a permanent deformation takes place in the material, which is not recovered after the releasing of the load. This type of deformation is called plastic deformation and it is accompanied by permanent atomic displacements. An important curve for the understanding of the response of the material under a load is the so-called *strain-stress curve,* which is experimentally constructed from the load elongation measurements (Fig. 3.4).

The shape and magnitude of the stress-strain curve of a metal will depend on its composition, heat treatment, prior history of plastic deformation, and the strain rate, temperature, and state of stress imposed.

When stress continues in the plastic regime, the stress-strain passes through a maximum, called the tensile strength, and then falls as the material starts to develop a neck and it finally breaks at the fracture point.

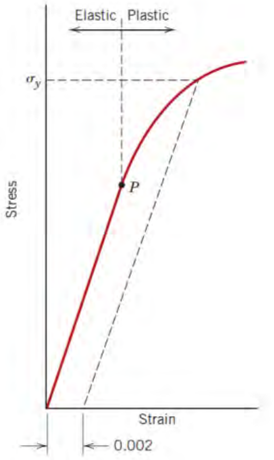

Figure 3.4: *a*) Typical stress–strain behavior for a metal showing elastic and plastic deformations, the proportional limit *P*, and the yield strength as determined using the 0.002 strain offset method [Callister 2009].

Heterogeneous plastic deformations, thermal contractions and phase transformations induced by the manufacturing process can produce permanent deformation in the metal.

When plastic deformation occurs, residual internal stresses forms, resulting in internal elastic strain of the material. The tension or compression remaining in the bulk without application of the external load is known as *residual stress*.

The residual stresses generated mechanically generally derived from non-uniform plastic deformation between the volume and the outer surface of the material; those from thermal processes are related to a non-uniform heating and cooling treatment; finally those associated with changes of volume or phase during chemical reactions such as precipitation or transformation of second phases.

Depending on the scale at which the matter is analyzed, three kinds of residual stresses are usually defined: the macro stresses, or stresses of first type, over a few grains; the stresses of second type over one particular grain; the stresses of third type across sub-microscopic areas, say several atomic distances within a grain. The stresses of second and third type are also called *micro stresses*. Residual stress is produced by heterogeneous plastic deformations, thermal contractions and phase transformations induced by the manufacturing process.

3.7 Texture

The crystallographic orientation refers to how the atomic planes in a volume of crystal are positioned relative to a fixed reference. This characteristic applies to all crystalline solids .

Almost all of these materials are polycrystalline and their component units are referred to as crystals or ‘grains’.

Grain orientations in polycrystals (whether naturally occurring or artificially produced) are rarely randomly distributed. In most materials, an orientation pattern is present and the occurrence of specific orientations is caused, firstly, during crystallisation from a melt or amorphous solid state and, subsequently, by further thermo-mechanical processes. This tendency is known as *preferred orientation* or, more concisely, *texture*. The importance and significance of texture to materials lies in the fact that many material properties are texture-specific [Randle and Engler 2009].

The knowledge and the measurement of texture in metals and in metal artefacts is very important. The orientation distribution is the result of the manufacturing or deformation process and thus texture contains information on the production techniques of a work piece [Scott 1991, Kocks *et al.* 1998, Nicodemi 1994]. Well-defined textures are produced by specific conditions during primary crystallisation from a melt, and by thermal and mechanical treatments of the cast such as annealing, drawing, hammering and rolling [Hatherly 1979].

Chapter 4

Methodology

4 Methodology

4.1 The Interaction of Neutrons with Matter

The neutron is a subatomic particle having no electric charge and a mass of 1.675 10^{-27} kg (1,839 times that of the electron). While bound neutrons are stable in an atomic nucleus, a free neutron decays into a proton, electron, and antineutrino with a mean lifetime of approximately 900 seconds. Neutron has no charge, it has a spin (½), and a magnetic dipole moment ($-1.913\ \mu_n$).

The neutron can be described as a classical particle with mass *m.* However, according to Quantum Mechanics, it can be associated with its de Broglie wavelength λ. According to their kinetic energy, neutrons are classified according to Table 1.

Neutrons	Energy range	Wavelength [Å]	Velocity [m/s]
ultra cold	≤ 300 neV	≥ 500	≤ 8
very cold	300 neV - 0.12 meV	52.2 – 26.1	7.5 – 152
cold	0.12 meV - 12 meV	26.1 – 2.6	152 – 1515
thermal	12 meV - 100 meV	2.6 - 0.9	1515 - 4374
epithermal	100 meV - 1eV	0.9 - 0.28	4374 - 13.8 10^3
intermediate	1eV - 0.8MeV		
fast	> 0.8MeV		

Table 4.1: Classification of neutron basing on their energy [http://www.psi.ch/niag/neutron-physics].

Differently from X-rays, and photons in general, which interact with the atomic charge distributions, neutrons interact directly with nuclei according to the so-called Fermi pseudo-potential. As a consequence, while the total X-ray cross-section grows monotonically as the square of the atomic number, the neutron cross-section appears as a much less predictable function, though not too much varying, among various nuclei. As a consequence, using neutrons we are able to distinguish between different isotopes and neighbouring atoms in the periodic table of the elements.

Moreover, thanks also to the overwhelming neutron cross-section of hydrogen, with respect to the average value of all the others, the presence of even a small quantity of hydrogen (or a hydrogen-based material) can be detected behind a thick metal wall.

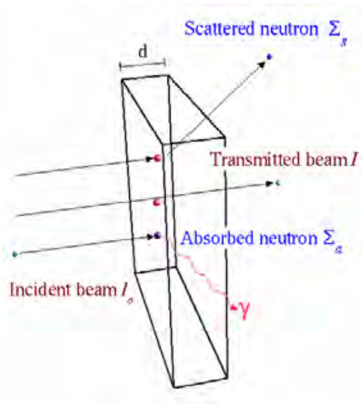

Figura 4.1: Neutron interactions with matter [http://www.psi.ch/niag/neutron-interaction-with-matter#].

The interaction of neutrons with dense matter is weak, (though not negligible) making them a highly penetrating probe. On the contrary, charged particles like electrons, due to their high charge/mass ratio, are characterized by a poor penetration power below the open surface of a sample. In this respect, thermal neutrons outperform other available probes, with a penetration range of the order of several cm, even in dense materials [Squires 1996].

Thanks to the generally weak interaction with the nuclei, thermal neutrons represent a truly non-invasive, non-destructive probe that generally leaves the samples unperturbed, apart from a weak radioactive activation that expires, typically, in one-week time or less [Siano *et al.* 2002, 2003]. Of course there are exceptions to this rule, e.g. strongly absorbing nuclei, but these cases are well known and samples can be tested in advance to avoid such

problems.
The average wavelength associated to a thermal neutron beam (E=25 meV) is around 1.8 Å, i.e. similar to the interatomic spacings. This feature, makes thermal neutrons an ideal probe for diffraction measurements.
When a neutron approaches a single nucleus, different events are possible:
a) Transmission: the neutron passes the atom without variation in its energy and direction.
b) Absorption: the neutron is absorbed transferring its energy and momentum to the nucleus, which undergoes a nuclear reaction, with the formation of a different nuclide and the possible consequent nuclear decay.
c) Scattering: the energy and direction of the neutron change. The scattering can be elastic with no energy transfer from probe to sample, or inelastic. The momentum transfer is the main variable entering in diffraction experiments.

The *microscopic cross-section* σ is used to express the probability, for a travelling neutron with a certain velocity, to interact with target nucleus [Rinard 1991; Markgraf and Matfield 1992]. The *total microscopic cross-section* σ_T sums up the probabilities of the possible interactions, mainly scattering σ_s and absorption σ_a [Beckurts and Wirtz 1964].

$$\sigma_T = \sigma_s + \sigma_a \tag{4.1}$$

Of these, the absorption cross section is generally linear in the wavelength value, while the scattering cross section can be further divided into coherent and incoherent components. It is appropriate to consider an *attenuation coefficient* when considering the attenuation of a neutron beam by a sample. This is designed by Σ and determines the power of removal of the neutrons from the selected beam due to both, absorption and scattering processes. In a simplified picture, the beam attenuation trough a flat slice of a homogeneous material is given by the Beer's law:

$$N_d=N_0 \exp[-\rho\ \sigma_T\ d] \tag{4.2}$$

where ρ is the atomic number density, σ_T is the total cross section, and d is the thickness of the selected slice.

Neutrons represent an ideal tool to probe the microscopic properties of bulk dense materials [Squires 1996, Sears 1992] and can be used to characterize the microscopic structure (at atomic level) of matter. For metal samples, neutron techniques are used to determine the qualitative and quantitative presence of different phases, as well as the presence and distribution of textures and residual stresses at the atomic level. From this wealth of data it is possible to obtain information on the conservation status of the artefact, as well as the smelting and smithing procedures, through identification of some peculiar signatures related to these processes [Lehmann and Hartmann 2010].

Hereafter, I will focus on Neutron Imaging and Neutron Diffraction methods adopted in the present study.

4.2 Neutron Imaging Methods

There are several possibilities how neutron imaging can be used for non-destructive evaluation. Basically, one can record single radiographic images or, by collecting several transmission images and applying suitable reconstruction programmes, build a 3D tomographic view of rigid objects.
In facts, the neutron transmission through material layers depends on the specific attenuation properties of that material. Neutron imaging is based on the degree to which an object, within the beam path, attenuates the incoming radiation according to the sample's removal cross section. The result is a shadow image of the object yielding information on

its inner structure and composition, consequent to the interactions between the incoming beam and the object and spatially depending on its elemental composition and density.
This simple technique, which is practically the neutron equivalent of an X-ray radiography or tomography, can be further improved, to achieve materials discrimination, by a proper selection of the neutron energy. By selecting an incident monochromatic neutron beam and changing its average wavelength gives the possibility of modifying the image contrast for different phases, taking advantage of the abrupt change of the attenuation coefficients in the proximity of the so-called Bragg cut-off [Josic *et al.* 2010]. Further information is given in the following sections.

4.2.1 Working principles of radiography and tomography

The neutron radiography method is based on the application of the basic law of radiation-attenuation [Lambert 1760, Beer 1852]. When the investigated object is exposed to the beam, neutrons interact differently with the nuclei of the atoms composing the sample, according to the total cross-section of the constituent elements and the flight path across the analysed object [Mannes 2009].
The degree to which a certain material attenuates a beam results from all interactions of the beam with an object. The transmission of a mono-energetic beam with characteristic energy E_0, can be described by the linear attenuation namely Beer-Lambert's law:

$$I = I_0 e^{-\Sigma d} \tag{4.3}$$

where I is the intensity of the transmitted beam, I_0 is the intensity of the incident beam, and Σ is the *macroscopic neutron attenuation coefficient* of the material, which is obtained by an obvious generalization of Eq. 4.2. The linear attenuation law is valid under the assumptions that the beam is mono-energetic and that the thickness is sufficiently small.
The emerging neutrons, generally detected by a two-dimensional position sensitive detector (Fig. 4.2), generate an image that contains information consisting of the integrated attenuation experienced by the beam on its way through the object, yielding information for every point in a two-dimensional plane [Domanus 1992].

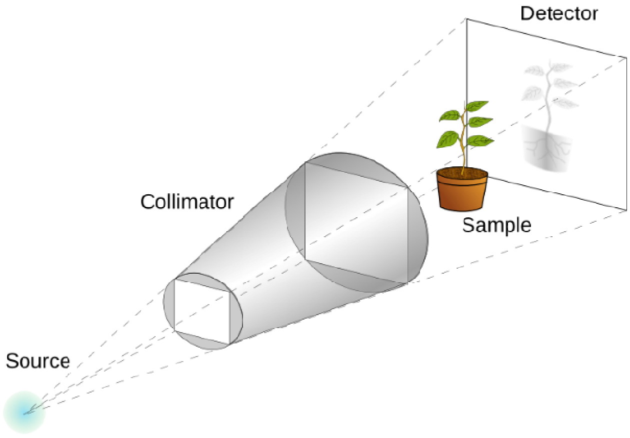

Figure 4.2: A schematic view of a basic neutron-imaging experimental set-up. The radiation is generated by a neutron source and is properly collimated. The achievable image resolution depends much on the collimator geometry: the L/D ratio, where L is the length of the collimator and D the diameter of its inlet aperture, is widely used as a measure for the beam divergence. The primary beam transmitted through the sample is recorded by a flat position-sensitive detector. The detector records a two-dimensional image which is the projection of the object on the detector plane [Mannes 2009, http://www.psi.ch/niag/neutron-imaging-setup].

Radiography makes possible a rough estimate of the position of an object's structural features in three dimensions. It is nevertheless still scarcely possible to make assumptions about the actual three-dimensional shape of these features. A step forward is represented by Computed Tomography (CT).
Tomographic techniques provide sliced images of an object from the transmission data, obtained by combining cross section measurements taken by irradiating the sample from many different directions. The method can be readily applied to bulk metal samples using

thermal and cold neutrons, which are detected using a proper scintillator plate[4.1]. In order to reconstruct the three-dimensional volume map of the sample, single 2-D parallel projections are measured during the rotation of the object around its vertical axis over a range of (at least) 180°. The larger the available information from varying viewing angles, the more defined will be the reconstruction on the internal structural features with respect to location and form (Fig. 4.3-*a*).

In practice, after correcting the raw images (neutron exposure, *flatfield* correction, bright spots filtering, rotation axis positioning), the tomographic slices are calculated using the inverse Radon transforms (filtered back-projection).
Applying the linear attenuation law, a frequency projection (line integral) of attenuation from a single slice projection is produced using the Radon Transform [Radon 1917; Brooks and Di Chiro 1975]. This procedure converts the spatial data into the frequency domain as a sinogram, where the y-axis represents a projection view or line integral, while the x-axis represents the detector channels, or the location of the impulse on the fixed detector. Once the projections are in the frequency domain, filters can be applied and then the projections can be transformed back into the spatial domain as reconstructed projections through filtered back projection (FBP) [Cormack 1963 and Hounsfield 1973, 1980]. FBP is a common reconstruction technique used in CT.

At the end of the process, tomographic slices reconstructed for every line within the detector are collected in an image stack representing a three dimensional matrix of the attenuation coefficients within the reconstructed volume. Then a virtual three-dimensional model of the object can be visualized, manipulated and evaluated using a proper 3D rendering software (Fig. 4.3-*b*) [Lehmann and Hartmann 2010, Dierick *et al.* 2004].

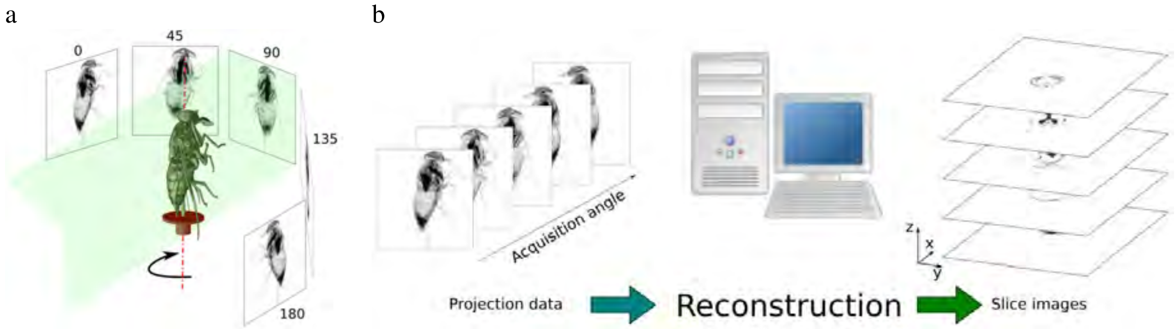

Figure 4.3: *a*) Tomographic data acquisition and *b*) Computed tomographic reconstruction [http://www.psi.ch/niag/neutron-tomography#].

4.2.2 Energy selective neutron radiography and tomography

Conventional neutron radiography is performed with a polychromatic spectrum of thermal or cold neutrons (depending on the beamline) and the interpretation of the image contrast is obtained by integration of the attenuation coefficients over the whole energy range. As a consequence, the energy-dependent features are lost in the averaging process.

[4.1] Detectors in use for neutron imaging purposes are those able to measure the neutron field in two dimensions perpendicular to the beam direction. Therefore, the detector area should be in the order or larger than the beam cross-section. Further boundary conditions are the spatial and time dependent resolution of the detector, which can be very different among the existing detectors systems. The inherent detectors properties are mainly given by the detection process, which is a nuclear reaction initiated by the neutrons. The primary detection reactions for thermal neutrons are mainly neutron capture by an absorbing material emitting secondary radiation, which can be used as the real neutrons proof. This is why neutrons have no electric charge and cannot make ionization directly which is needed for the detection [PSI].

On the other hand, for polycrystalline materials, the neutron attenuation coefficient decreases suddenly, for well defined neutron wavelengths where the conditions for Bragg scattering stop to be fulfilled – the so-called Bragg edges in the cross-section diagrams (Fig. 4.4). The neutrons with wavelength larger than the lattice constant of the investigated crystal cannot interfere coherently with it. Therefore a sudden drop in the total neutron cross-section is observed at a defined neutron wavelength. Since the position of the Bragg cut-off is related to the corresponding d_{hkl} spacing of the analysed phase, the drop in attenuation for the corresponding elements is significant and the image contrast is correspondingly enhanced. Thus, the conventional method can be greatly improved, to achieve phase discrimination in heterogeneous materials, by a proper selection of the neutron energy interval [Bücherl 1995, McDonald 1999, Santisteban 2001, Kardjilov 2011]. In order to take advantage of Bragg-edges, a polychromatic neutron beam must be monochromatized in a suitable range of wavelengths.

The conventional method can be greatly improved, using Bragg Edge techniques, to achieve materials discrimination, by a proper selection of the neutron energy interval. Moreover, exploiting the relationship:

$$\frac{\log I_{\lambda 2}}{\log I_{\lambda 1}} = \frac{\Sigma_{\lambda 2} d}{\Sigma_{\lambda 1} d} \tag{4.4}$$

the dependency from thickness (d) can be removed. Here, λ_1 and λ_2 are the neutron wavelengths, chosen respectively before and after the Bragg edge and Σ is the neutron attenuation cross section at the wavelength of analysis.

It is important to point out that, depending on the device adopted for the beam monochromatization, the wavelength distribution of the “monochromatic” neutron flux on the sample is not always perfectly homogeneous. This is not a problem, when tomographic reconstruction is applied, because the neutron flux is averaged during the rotation of the sample.

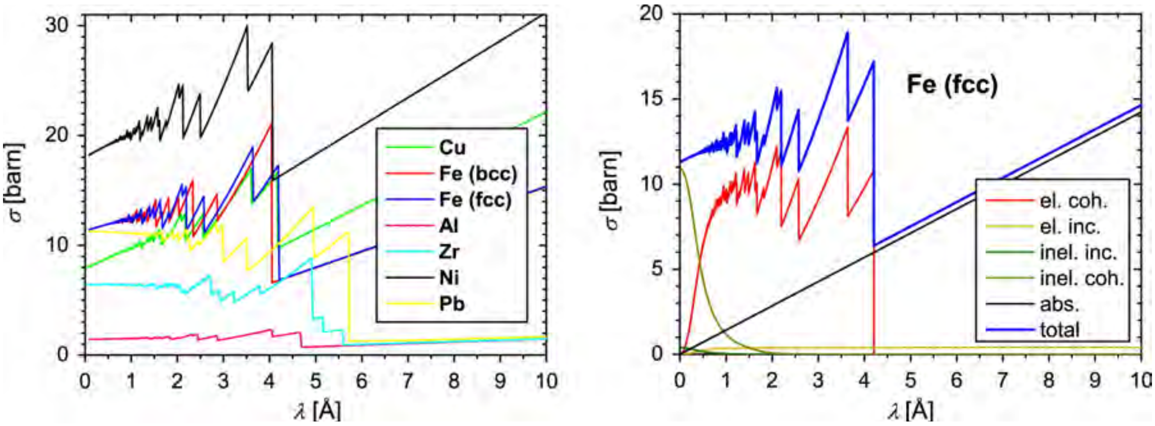

Figure. 4.4: on the left: total neutron cross-sections (σ) for different polycrystalline materials. On the right: the total neutron cross-section for Fe (fcc) and its components: elastic coherent (el. coh.), elastic incoherent (el. inc.), inelastic coherent (inel. coh.), inelastic incoherent (inel. inc.) and absorption (abs.). The elastic coherent component with characteristic peaks and Bragg edges enables a contrast change and a determination of the crystallographic structure in the energy selective neutron imaging [Josic 2011].

4.2.2.1 *Why cold neutrons*

Cold neutrons are usually produced by so-called cold sources in the existing facilities where a very low temperature moderator reduces the neutron energy to a few meV. The obtained neutron beam is characterized by a broad Maxwellian-like spectrum with an average energy value depending on the temperature of the cold source. The neutron transmission of different materials at these energies is very sensitive to the spectral characteristics of the neutron beam because of the above-mentioned Bragg cut off in their attenuation diagrams. Furthermore, the Bragg edges are most pronounced, and best separated, in the cold neutron energy range, which covers the low-indexed lattice planes of crystals [Josic *et al.* 2010, Santisteban 2001]. The use of cold neutrons, rather than the thermal ones, allows investigations with a high intensity flux near the Bragg cut off energies of the material.

4.2.2.2 *Beam monochromatization*

There are different ways to monochromatize the beam purposely for an energy-selective neutron imaging experiment.

In the case of pulsed neutron sources a time-of-flight technique can be applied for achieving a narrow neutron energy distribution. In this way short, intense neutron pulses allow a very sharp spectrum in combination with a high flux [McDonald 1999].

In the case of continues source, different solutions are available according to the experimental needs.

A double-monochromator device can be installed to scan through individual wavelengths by rotating and shifting two highly-orientated pyrolytic graphite (HOPG) single crystals according to the Bragg equation [Bücherl 1995]. The two crystals[4.2] are connected in series with their mechanical systems operating in tandem, so that they both select the same wavelength. With this setup a wavelength resolution of $\Delta\lambda/\lambda \approx 3\%$ is achieved but the intensity level, which depends on the Bragg reflections, is the most critical specification for the monochromatic beam.

Another way, for an effective monochromatization of the neutron beam in the context of radiography and tomography experiments, is the use of a neutron velocity selector [Kardjilov 2001]. This device consists of a rotating drum with a set of shaped curved blades, coated with a neutron absorbing material (^{10}B). Depending on the rotation frequency, only neutrons with the right speed are allowed to cross its length L, in the rotating helical path that is characterized by a pitch angle α. The neutrons that are too fast (short wavelength) or too slow (long wavelength) hit one of the lamellae, made of absorbing material, and are removed from the beam. Thus, the neutron wavelength, $\lambda = \frac{h}{mv}$, where h is the Planck's constant, m is the neutron mass, and v is the neutron speed, can be varied by changing the rotation speed, ω, according to the formula:

$$\lambda = \frac{h\alpha}{Lm\omega} \tag{4.5}$$

while the selector resolution (relative wavelength spread) is simply expressed by the ratio:

$$\frac{\Delta\lambda}{\lambda} = \frac{\alpha}{\beta} \tag{4.6}$$

where β is the angle subtending the transmitting window [Shurmann 1958]. Generally, a $\Delta\lambda/\lambda$=15 % monochromatic beam, much less energy-defined than using the crystal monochromator solution, but much more intense, is obtained [Friedrich *et al.* 1989].

In fact, the main advantages in using the MVS is in its good transmission rate for a defined neutron wavelength band and a sufficiently wide energy spectrum, yielding a high neutron flux, which allows the performance of tomography experiments in relatively short times.

As we mentioned, the limiting factor resides in its poor wavelength resolution. However, the energy-selective imaging instrument set-up based on MVS can be supplemented adding a set of crystals of different mosaicity, the so-called TESI device, to scatter out undesired

---

[4.2] Mosaic crystals are considered to be formed by a large number of small perfect crystallites of microscopical or submicroscopical size which are oriented almost but not exactly, parallel to one another. They show a much wider but lower direction profile as compared to perfect crystals [Tuffanelli *et al.* 1999].

parts of the spectrum and further reduce the pass band to an estimated wavelength resolution of 5% [Peetermans *et al.* 2011, Tamaki 2005].

4.2.3 White beam and energy selective neutron laminography

Neutron computed tomography has been demonstrated to be a powerful method for non-destructive investigation of metal artefacts [Schillinger *et al.* 1999, 2000; Lehmann *et al.* 2010; Kardjilov *et al.* 2011; Salvemini *et al.* 2012, 2013]. However, laterally extended specimens, like plate-like objects, are much less suitable to CT. In facts, the transmitted neutrons collected from orientations in which the plate is oriented parallel, or close, to the incoming beam, can be almost completely attenuated the thick materials with significant cross section. In this case, being the attenuation from very high to complete, the computed tomography reconstruction can produce serious streaking artefacts, affecting the data interpretation [Helfen *et al.* 2005].
In order to overcome this drawback, the Computed Laminography (CL) was recently developed as a method to complement computed tomography for three-dimensional imaging of laterally extended specimens [Helfen *et al.* 2007]. In the typical laminography set-up, the sample rotation axis is tilted with respect to the standard rotation axis that is oriented perpendicular to the beam in standard tomographic configuration. The sample is then arranged approximately perpendicular to the rotation axis as shown in figure 4.5. The specimen can laterally extend beyond the field of view of the detector, but is now limited in the direction of the rotation axis. One of the advantages of this scanning scheme is that the integral neutron transmission on the 2D detector doesn’t fall significantly during the scan, cause of the missing information from projections at angle closest to the sample surface. As a consequence, the integrity of laterally extended samples can be preserved [Helfen *et al.* 2011, 2012].

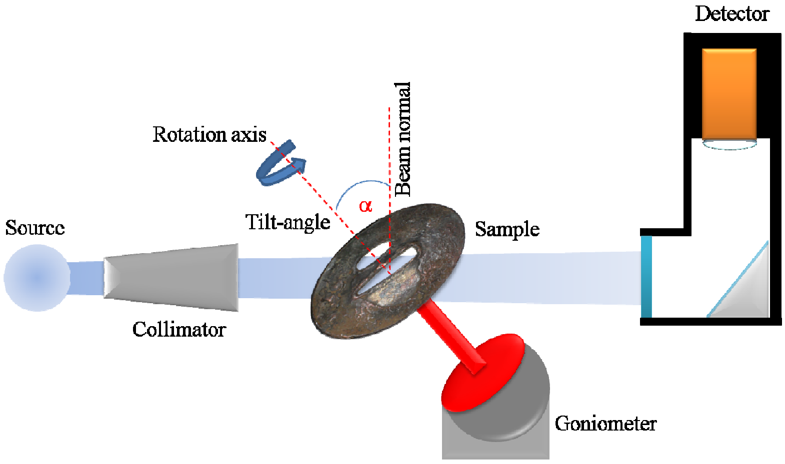

Figure 4.5: Scheme of the experimental set-up used for neutron laminography.

Early use of laminography was in the field of medical applications [Grant 1972]. Recently, laminography has been applied also to material science research [Helfen *et al.* 2007] and the interest in the application of the technique to art or archaeological objects rose up since such samples require investigation through non-invasive methods [Krug *et al.* 2008, Hai-Yen Nguyen 2011].

However, this technique can be further improved, to achieve materials discrimination, by a proper selection of the neutron energy. In fact, monochromatic neutron beams give the possibility of modifying the image contrast for different phases, taking advantage of the abrupt change of the attenuation coefficients in the proximity of the Bragg cut-off [Kardjilov *et al.* 2004, 2012; Josic *et al.* 2010].

4.2.4 Experimental Facilities

Hereafter the neutron imaging facilities involved in the present study are briefly described.

4.2.4.1 ICON

It is a dedicated beamline for imaging with cold neutrons situated at beam port 52 of the SINQ spallation neutron source at Paul Scherrer Institut (PSI) in Switzerland. Here, neutrons are generated by spallation when a quasi-continuous proton beam of 590 MeV and 1.5 mA impinges on a lead target. They are thermalized in a surrounding D_2O tank at room temperature, with a smaller tank of liquid D_2 at 25 K present to provide cold neutrons to a limited number of beamlines, one among them is ICON. A monochromatic beam can be produced by inserting a mechanical velocity selector in the beamline close to the aperture. This is permanently mounted on rails at the instrument front position. The second and third experimental positions are used for radiography and tomography with field of view from 30 mm to 250 mm, achieving a max spatial resolution of 20.3 µm. The neutron flux at the second sample position is 1.3×10^7 n cm^{-2} s^{-1} mA^{-1}(pin-hole aperture of 20 mm) [Kaestner *et al.* 2011].

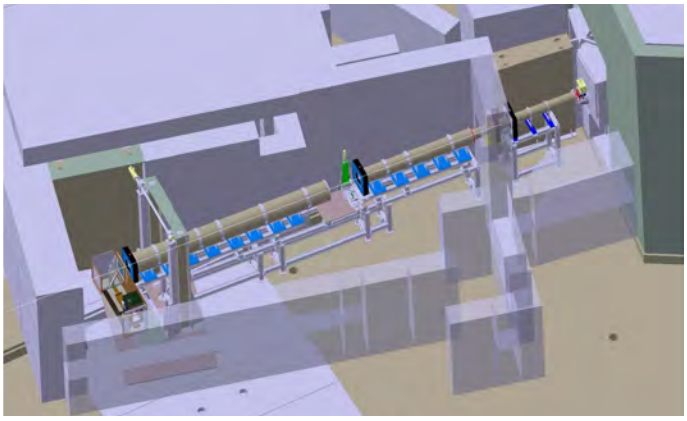

Figure 4.6: The ICON beamline at SINQ [http://www.psi.ch/sinq/icon].

4.2.4.2 NEUTRA

NEUTRA is the thermal neutron radiography station at the neutron spallation source SINQ at Paul Scherrer Institut (PSI) in Switzerland. It provides neutron radiography and tomography images of medium to large size objects using a thermal neutron energy spectrum characterized by a Maxwellian distribution and a flux of 5×10^6 n cm^{-2} s^{-1} mA^{-1} at the sample position. Special features available are a 320kV X-ray tube allowing dual modality imaging with an identical imaging geometry and a special setup for the investigation of highly radioactive materials [Lehmann *et al.* 2001].

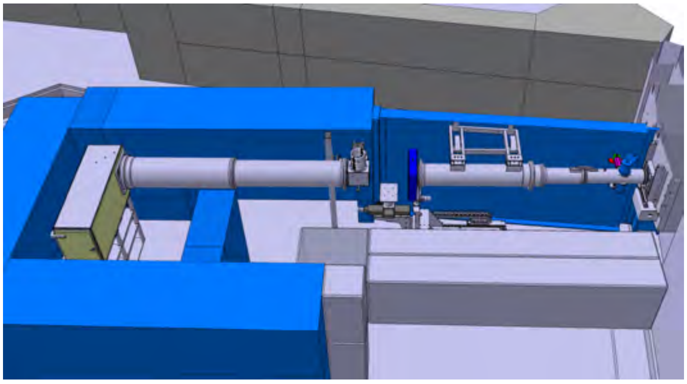

Figure 4.7: The NEUTRA bamline at SINQ [http://www.psi.ch/sinq/neutra]

4.2.4.3 CONRAD II

CONRAD II instrument is available at the Helmholtz-Zentrum Berlin (HZB). CONRAD II is a multifunctional facility for radiography and tomography with cold neutrons. It is located at the end of a curved neutron guide, which faces the cold-neutron source of the BER-II research reactor [Kardjilov *et al.* 2011]. The geometry provides a cold-neutron beam with wavelengths ranging from 2 Å to 12 Å. Two measuring positions are available for radiography and tomography investigations. The first one is placed at the end of the guide and it is optimized for in situ experiments in which a high neutron flux is required. The available flux at this position is approximately 10^9 n cm^{-2} s^{-1}. The second measuring position exploits a pin-hole geometry which allows better beam collimation (L/D up to 1000) and higher spatial resolution of the images. For energy-selective imaging a double highly-orientated pyrolytic graphite (HOPG) single crystals monochromator is available [Kardjilov *et al.* 2011].

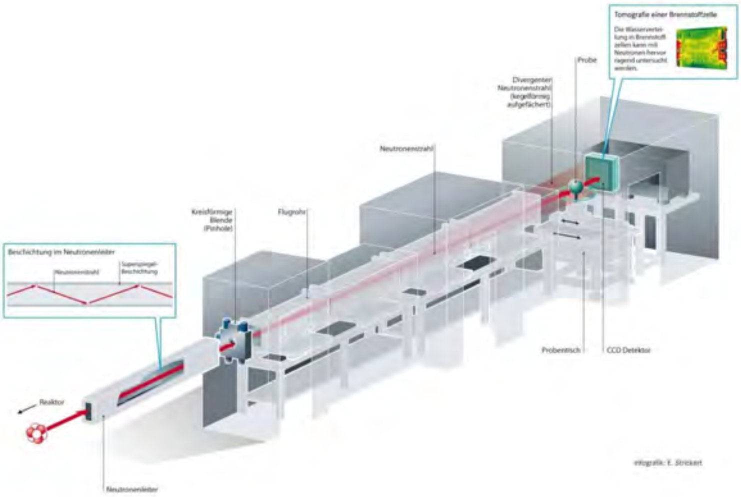

Figure 4.8: The CONRAD II beamline at HZB.

4.3 Neutron Diffraction Methods

Basing on the elastic scattering, neutron diffraction is a crystallographic method for the determination of the crystal structure of a material. The different type of radiation gives complementary information respect to the parental X-ray technique. However, neutron diffraction offers distinct advantages over X-ray techniques, which are more commonly used. To name one, neutron analysis with a beam size of several centimetres provides averaged information from the bulk sample. This is important, concerning archaemetallugy study, where neutron diffraction techniques can add useful information about the texture and the residual strain distribution (when present) related to the manufacturing technique of the analysed artefact [Paradowska *et al.* 2012].

Considering the scattering from two atoms neighbouring atoms lying in successive atomic lattice planes, vertically above one another and spaced at a distance *d*; each one will scatter neutrons coherently with a phase relationship maintained between the incident and scattered waves. If we consider the sum of their scattered amplitude at a diffraction angle θ, the two scattered waves will give rise to constructive interference if the extra path length for scattering from successive lattice planes is equal to an integer number *n* of wavelengths λ. This occurs when the Bragg condition:

$$n\lambda = 2d_{hkl} \sin\theta \tag{4.7}$$

is satisfied [Hutchings *et al.* 2005].

The diffraction peaks thus occur only under very special condition, i.e. when the Bragg's Law equation is satisfied and the planes are oriented correctly at the angle θ with respect to the incident beam. In describing diffraction from planes with Miller indices *hkl*, it is conventional to include the order *n* into the lattice spacing *d* [Hutchings *et al.* 2005].

Operatively, the investigated sample is placed in a beam of thermal or cold neutrons and the intensity pattern obtained from the sample gives information of the structure of the

material. As a result of the measurement the intensities of the peaks can be plotted versus the d-spacing. The task of the diffraction analysis is to evaluate the measured diffraction pattern in terms of peak position, peak widths and peak intensities.
While the peak positions are directly related to the crystal lattice spacing, the Bragg peak intensities and shape are determined by the atomic arrangement in the unit cell, giving information about the crystal structure.

The structure of a polycristalline material may be characterized at different levels [Bunge 1986, Kockelmann *et al.* 2004].

- The ”phase structure” describes the composition of a material.
- The ”crystal structure” deals with the atomic arrangement of each phase.
- The ”crystallite structure” represents size, shapes and mutual orientations (texture) of crystallites.
- The ”microstructure” describes structural deviations from an ideal crystal within a grain.

Sometimes the term microstructure is used to refer to both the crystallite and defect structure. The four structural levels are, of course, interdependent. Generally, direct evidence of working processes may be imprinted at one or more of the structural levels. Diffraction yields information on all four of them. Comparison with theoretical patterns, or with diffraction data from known and controlled samples, helps to interpret the measured patterns.
The variations in the intensities of the peaks may indicate a change of the phase mixture, a change of the crystal structure of one of the phases or can be due to texture in the material.
Peak shift may originate from changes in alloy composition or from residual strains deriving from material deformation.
Peak broadening generally indicates deviation from ideal structures within crystallites in terms of size and defects [Bunge 1999]. The line broadening increase comes essentially from three effects: the finite size of the crystallites [Scherrer 1918], the crystallite microstrains[4.3], the variation of composition in the irradiated portion of the sample.
Thermal treatments like slow heating and annealing at high temperatures eliminate the effects of cold working reducing crystal defects and relieving lattice strains whereas plastic deformations like hammering and quenching in water generate microstrain in the material.
The analysis of peak broadening may provide clues to understand the working processes to which the object has been subjected. To perform a more reliable analysis, it is often useful to compare the peak widths with those arising from suitable samples that are produced in a controlled way, i.e. that have been subjected to known working processes.

4.3.1 Experimental Facilities

Several configuration are developed for neutron diffraction analysis, according to the specific aspect to be investigated in a sample. Hereafter, the facility dedicated to non-destructive residual stress characterization and deformation behaviour, and involved in the present study is briefly presented.

4.3.1.1 POLDI

High resolution neutron diffraction measurements have been performed at the POLDI beam line [Evans *et al.* 2009; Stuhr *et al.* 2005, 2006], operating at the spallation neutron

---

[4.3] This broadening is defined by the crystalline non-uniform variation of d_{hkl}, which can be produced by external stresses or mechanical and thermal treatments, crystalline defects (dislocations for example) or local compositional variations.

source SINQ. POLDI is a multiple pulse overlap TOF-diffractometer [Windsor 1981] with a single chopper optimized for strain-scanning experiments.

By this method, a white pulsed beam impinges on a defined gauge volume of the sample. A highly collimated detector, fixed orthogonal with respect to the beam and covering a defined 2θ angular range, measures the arrival time of the neutrons in dependence of the scattering angle [Bragg 1852]. In a plot of intensity vs. arrival time and scattering angle each Bragg reflection is represented by a Bragg line (Fig. 4.9). The position of the diffraction peak is a measure of the average lattice spacing, while the width of the peak is related to the fluctuations in the crystal structure. In a strained material, the measured lattice spacing acts as a kind of strain gauge. If d_0 and d are, respectively, the stress-free and actual lattice constant then the strain is given by [Callister 2009]:

$$\varepsilon_{el} = \frac{d - d_0}{d_0} \tag{4.8}$$

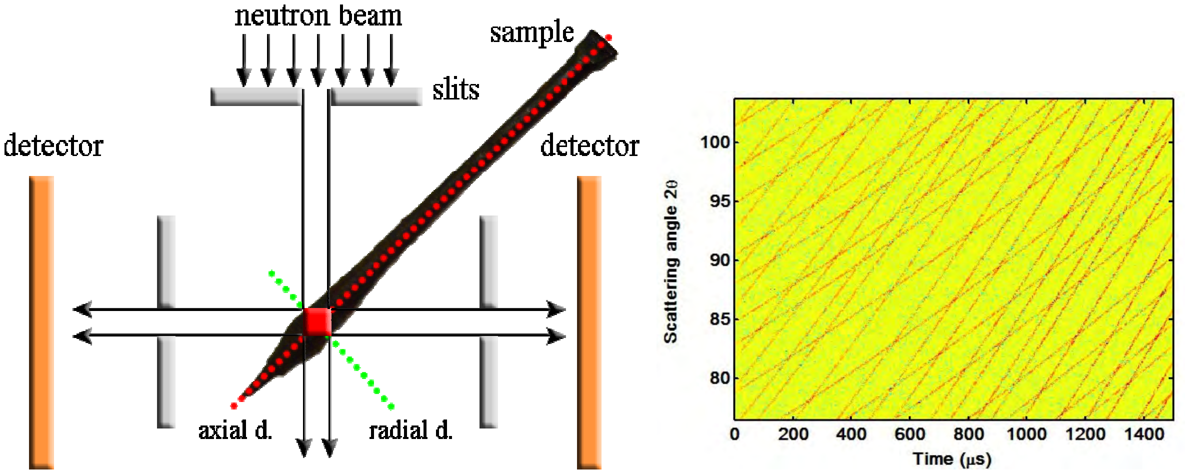

Figure 4.9: On the left, the principle of strain mapping. The scheme reports the positioning of the sample (over scaled), set with the flat side of the *stylus* facing up, and the indication of the axial and radial directions. On the right, a typical spectrum showing intensity vs. arrival time and scattering angle.

Chapter 5

Measurements and Results

5.1 The Samurai sword

Introduction

The forging techniques evolved by the Japanese smiths are somehow unique when compared with those in any other part of the world. From earliest times the functional attributes sought in a Japanese blade have been un-breakability, rigidity, and cutting power. The more purely aesthetic qualities sought by modern collectors might seem to be at variance with the severely practical requirements but in facts it is in the fulfilment of demanding technical norms that the essential beauty of Japanese sword lies. The combination of these qualities is the greatest achievement of Japanese forging and tempering techniques [Kanzan Sato 1997].

In Japanese traditional furnace, *tatara*, steel of different carbon content is produced. Crunches of steel are heated in the forge and hammered into flat sheets (Fig. 5.1). After cooling the sheets by quenching them in water, the smith uses a hammer to break them into small wafers. After visual selection of the steel pieces, the smith arranges them in a stack atop a plate of steel welded to a long handle. To hold the fragments together, the smith wraps the steel in clay and paper, and the pile is heated and hammered several times until forming a single block. When the elongated bar is ready, the smith scores lines with a chisel across the plate, folds the metal over itself, and then he hammers the piece out again into a flat plate of the same size as before. The process of lamination and folding is repeated many times in order to homogenize the carbon content and remove slag inclusions and defects. While heating the steel, the smith periodically removes it from the forge, quickly rolls it in rice-straw ashes, and covers it with a clay slurry before returning it to the fire. The clay and ashes help to protect the steel by preventing oxygen from reaching its surface, causing, in combination with temperature, an extreme loss of carbon.

In the case of Japanese medium- and full-size swords, they are formed in composite structures made of steel components of different carbon content. Japanese smiths assemble the different pieces into a block, weld them together, and then draw out the steel into a sword.

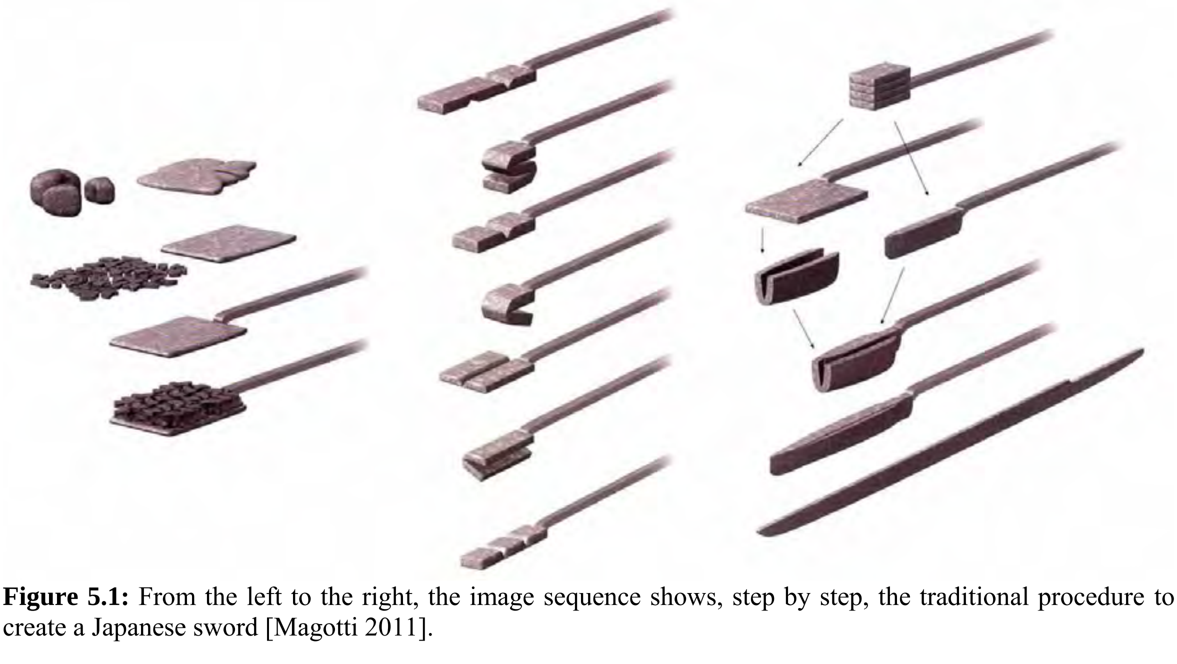

Figure 5.1: From the left to the right, the image sequence shows, step by step, the traditional procedure to create a Japanese sword [Magotti 2011].

After forging, the smith covers the entire blade in a heat-resistant mixture of clay and ash, which he then spreads away or thins along the edge with a metal spatula (Fig. 5.2).
The clay covering the blade is thoroughly dried and the smithy is made dark. The smith places the blade, with the clay still on it, in the furnace. At the moment when the metal glows red hot, the smith takes out the blade and plunges it briefly into a trough of water. The outline formed by the area of the edge thus exposed, results in the pattern of the temper-line, the *hamon*, of the finished sword [Kanzan Sato 1997, Kapp *et al.* 1987].

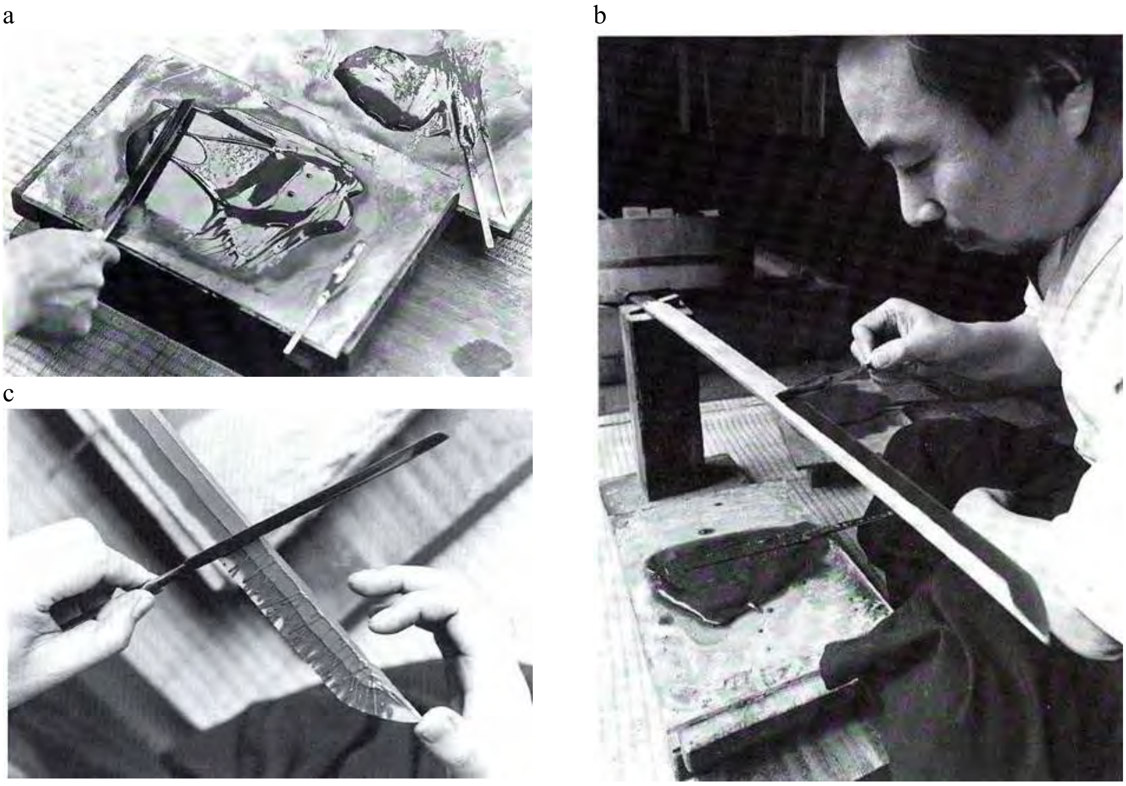

Figure 5.2: *a*) The smith mixes the clay with water, *b*) the edge of the blade is coated, c) the edge shape is created [Kapp *et al.* 1987].

According to history, the different styles of Japanese sword-making are divided into four periods [Sato 1997, Nagayama 1997]:

1) Koto (old sword): A.D. 987–1596
2) Shinto (new sword): A.D. 1596–1781
3) Shinshinto (new new sword): A.D. 1781–1876
4) Gendaito (modern era sword): A.D. 1876–present

The Koto age is further split into five traditions (Gokaden). These traditions derived from the common evolution of local replica of Chinese straight double-edge blades to curved one-edge blades. However, the fundamental techniques, like the smelting and smithing procedures, the forging, and the final treatments, were different and specific of the particular schools that each tradition started in a specific province and then diffused in the rest of the country. These provinces were either related to power centres or simply were in geographic areas rich in iron ore. Schools related to different traditions might co-exist in the same province.
The Shinto period was characterized by the unification and control of the weapon smithing techniques under the shogun control. As a consequence, the differentiation among various traditions slowly dissolved, only remaining as a sort of merely stylistic differentiation, with no real connection to the working process [Nagayama 1997].

The stylistic revival of the five *Gokaden* distinguished the production of the Shinshinto period. However, during the Meiji Restoration (1866-1869), the Emperor restored full power after centuries of shogun domain. Sanctioning the end of the samurai caste and banning the wearing of swords in public, the demand for swords declined.
When the mass production ceased, most of the smiths converted to other occupations; in consequence of the opening to the Western culture in the race for modernization, Japanese sword began to be considered an object pertaining to the past, a symbol of an obsolete culture.

During World War II (formerly Gendaito period), the Japanese army gathered the latest smiths necessary for a big mass production. The demand for military purposes was huge and sudden while the craftsmen were too few to produce all the blades traditionally used by the officers. So that the *gunto* sword was born: a blade of poor quality even made assembling industrial machinery and materials of second choice (mainly railway rails).
However, at the end of American Prohibition, the post-war production of swords was regulated by the government through the establishment of appropriate institutions to protect the ancient art of traditional Japanese swords [Nagayama 1997].

5.1.1 Test measurements on fragments of ancient Japanese swords

The samples

For the analysis presented in this work, five fragments of ancient swords, broken approximately at 10-20 cm from the tang and already analysed through time of flight neutron diffraction, have been selected [Grazzi *et al.* J. Anal. At. Spectrom. 2011]. All swords are assigned: four of them are attributed to the Koto Age forging traditions, and one is a more recent blade attributed to the Shinto tradition. The attributions were made through the analysis of the signatures (certain attribution) and, in absence of signature, through the stylistic analysis by our museum experts (hypothetical attribution). The transliteration of the signatures, as well as its translation and attribution is reported in the following (Sx labels the sample):

S0 Mumei (no signature)
Soshu-Kotō

S2 BIZEN no KUNI no JŪ OSAFUNE SHICHIBEI no JŌ SUKESADA/ KAMBUN SANNEN HACHIGATSU KICHINICHI
Shichibeinojō Sukesada inhabitant of Osafune in Bizen province/ a lucky day in the eight month of the third year of Kambun
Bizen (Okayama), 1663-Shintō

S3 BISHŪ OSAFUNE SUKESADA
Sukesada from Osafune in Bizen province,
Bizen (Okayama), middle of XVI century, Bizen –Kotō

S7 Mumei (no signature)
Soshu-Kotō

S8 NOSHŪ no JŪ KANESADA
Kanesada inhabitant of Mino province
Mino (Gifu), first half of XVI century, Mino-Kotō

The four swords of the Koto Age belong to three of the five traditions, while the Shinto one (S2) was produced in the same family of forgers as S3. These details are of strong importance in the data analysis. A picture of the blade fragments is shown in Figure 5.3.

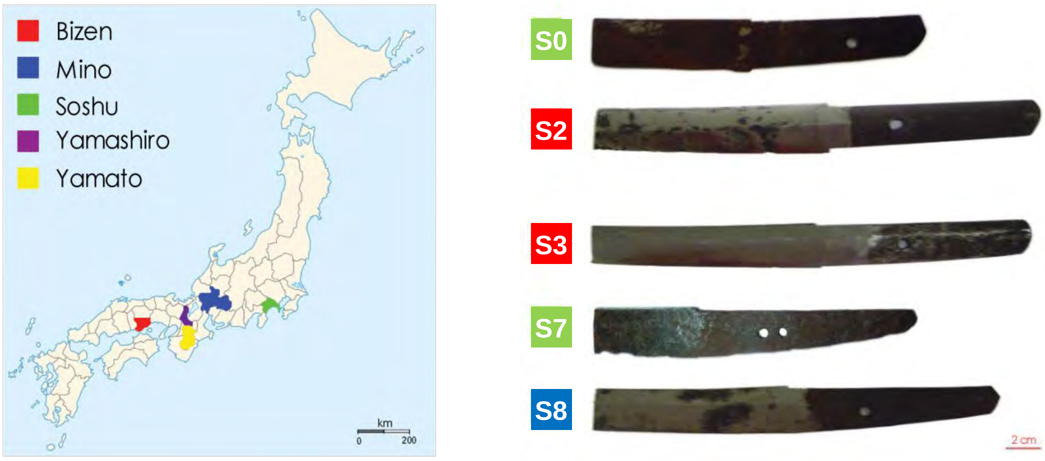

Figure 5.3: Map of Japan (Honshu is the main island) showing the location of the provinces where the five Koto age sword-making traditions were originated (left) and a picture of the five blade fragments (right).

Experimental set-up

The neutron imaging study has been performed using the ICON facility, which is collecting a neutron beam originating from the cold liquid D_2 moderator, at PSI.

The five Japanese blades where initially characterized using *white beam tomography* (WBT) whose instrumental set-up is reported in Table 5.1. The samples were gently wrapped using aluminium foil and then arranged in an aluminium cylindrical pipe; the very low microscopic cross section of aluminium makes this metal almost transparent to neutrons and avoids interference during the measurements. The data have been processed through the software package Octopus, developed at Ghent University [Dierick 2004].

In the second part of the experiment, it was exploited the *energy-selective tomography* technique (EST) whose instrumental set-up for this configuration is also reported in Table 5.1. The monochromatic neutron beam obtained from the mechanical velocity selector mounted on ICON gives the possibility of modifying the image contrast, in this case for ferrite, taking advantage of the abrupt change of the attenuation coefficients at the so-called Bragg cut-off. The tomographies were carried out at two different neutron wavelengths: 3.8 Å and 5.0 Å.

Preliminarily to EST measurement, theoretical data have been validated performing neutron radiography on one of the Japanese blade fragments, used as a test sample, to determine the effective monochromatic neutron flux distribution at different wavelengths. In order to obtain the greatest intensity variation and to select the proper wavelengths for the study, the sample with the highest average carbon weight percentage, i.e. S7 [Grazzi *et al.* J. Anal. At. Spectrom. 2011] has been chosen. Detailed information are given in Appendix A.

Imaging Method:	White beam and energy-selective tomography (S0, S2, S3, and S8)	Energy-selective imaging (sample test S7)
Neutron wavelength:	polychromatic, 3.8 Å, 5.0 Å	3.5 Å, 3.7 Å, 4.1 Å, 4.6 Å
L/D:	178	89
Scintillator:	^{6}LiF/ZnS (1:2) 100 μm	
Camera:	Andor DV434 - BV, 1024 x 1024 16 bit	
Field of View:	111.6 x 111.6 mm	
Object-Detector-Distance:	17 mm	
Pixel size:	160 μm	210 μm
Exposure Time:	5(WBT), 50-60 (ERT) s	6 s
Rotating Angle:	360º	360 º
Projections:	375	375

Table 5.1: The different instrumental set-up employed for measurements of the five Japanese blades.

Results

White beam tomography

In the figures reported below, the reconstructions of the neutron tomographies taken using white beam on four blade fragments (S0, S2, S3, S8) are shown. The present non-invasive analysis has permitted to identify some peculiar characteristics related to the forging methods used by the different schools and traditions in Japan (i.e. temper extension along the edge, defects, slag inclusions, internal cracks). The method also allows mapping the distribution of defects on the surface.

By the measurements, it is possible to detect differences, among the analysed samples, originating from different schools and traditions. In particular, in the following, I will concentrate on some specific points.

Beginning with the body blade of **S0** sample, we were able to detect the trace of a single internal crack extending from the tang to the cut edge. In addition, evidence of the diffuse presence of small slag-inclusions, elongated and parallel to the surface, could be revealed, in the tang (Fig. 5.4).

The absence of the *hamon* (the temper region typical of the japanese blade along the cutting edge) is connected to the incredibly high carbon content in this sample (average carbon weight: 1.05 %), in line with the usual belief that this tradition produced the hardest blades. Thus, the blade needed to be tempered, after quenching, in order to avoid a high fragility [Grazzi *et al.* J. Anal. At. Spectrom. 2011]. This blade is poorly conserved: in addition to the internal slag-inclusion observed by in the tomographic reconstruction, diffuse rust spots are also observed on the blade surface.

Sample **S2** is characterized by a homogeneous inner structure of the blade cross section. No trace of cracks or slags has been evidenced by the tomographic technique. However, a clear space pattern could be detected where the crystalline structure of the edge steel changes from hard martensite to pearlite, giving rise to the *hamon,* clearly delimited by the sharp *habuchi* line (red line in the figure). The tomographic method also allowed to map several rust spots that extend below the sample surface (Fig. 5.5).

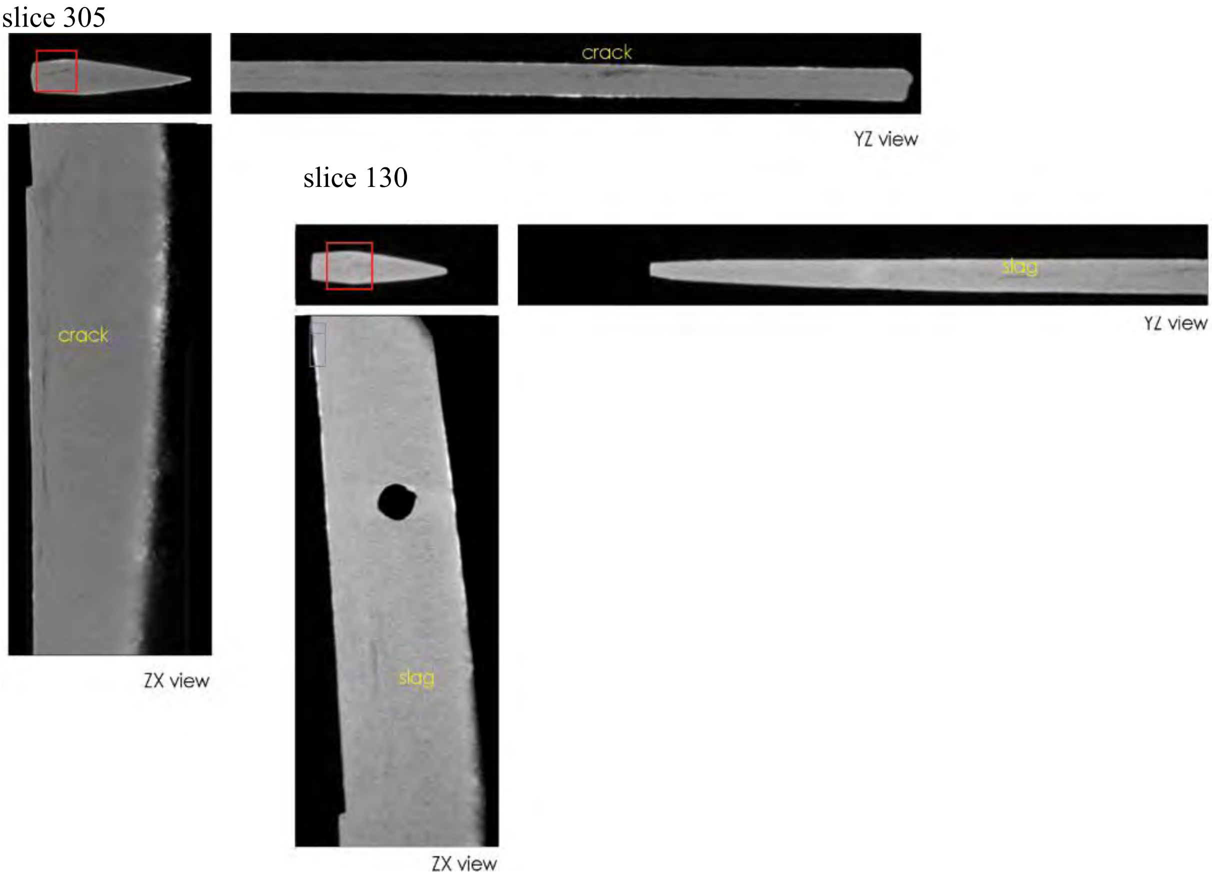

slice 305

slice 130

Figure 5.4: Selected slices and related orthogonal views from the neutron tomography carried out with white beam for the sample S0: a crack is clearly visible along the *Iori* (slice 305), while some slag-inclusions were localized in the tang (slice 130).

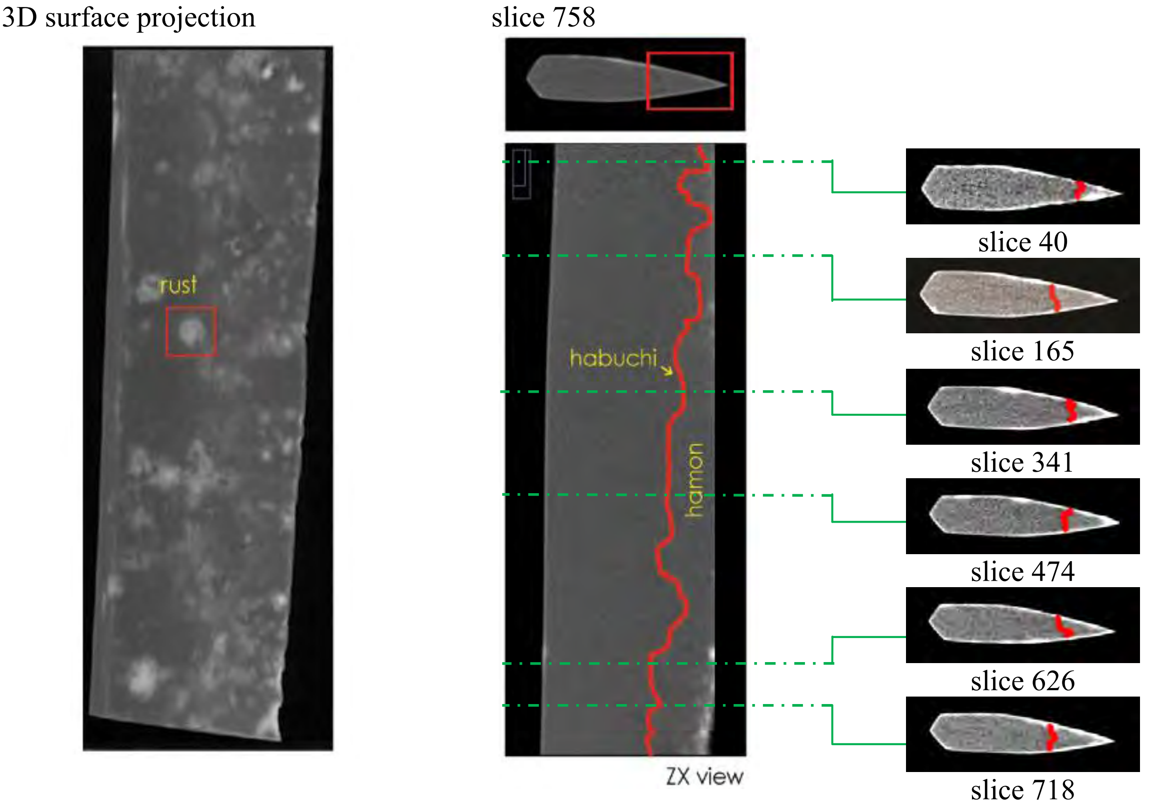

3D surface projection

slice 758

Figure 5.5: On the left, the 3D surface projection evidences the presence of rust spots diffusing below the surface of the fragment S2. On the right, the various slices, taken at different heights of the blade, show the progress of the *habuchi* line, delimiting the *hamon* along the fragment.

As samples **S3** and S2 were made by the same family, with the S2 younger than S3 by a few generations, the comparison between the two blades is very interesting. A rather large amount of slag inclusions has been detected and mapped along the body of blade S3 (Fig. 5.6). In addition, in this blade, the hardened edge of the *hamon* was sharper than in S2.

These results are consistent with a previous neutron diffraction analysis [Grazzi *et al.* J. Anal. At. Spectrom. 2011] where it was found that the average carbon content is slightly increased from the first sample (S3 average carbon content: 0.50 wt %) to the second (S2 average carbon content: 0.65 wt %). I would remind that this blade (S2) was manufactured during the Shinto period, when the steel production was under shogun control, but the used steel was highly carburised in either case. Even though older, the Koto Bizen blade (S3) was manufactured by the same high-rated family of craftsmen and its higher quality suggests that it was probably made for a high-rank samurai [Grazzi *et al.* J. Anal. At. Spectrom. 2011]

slice 638

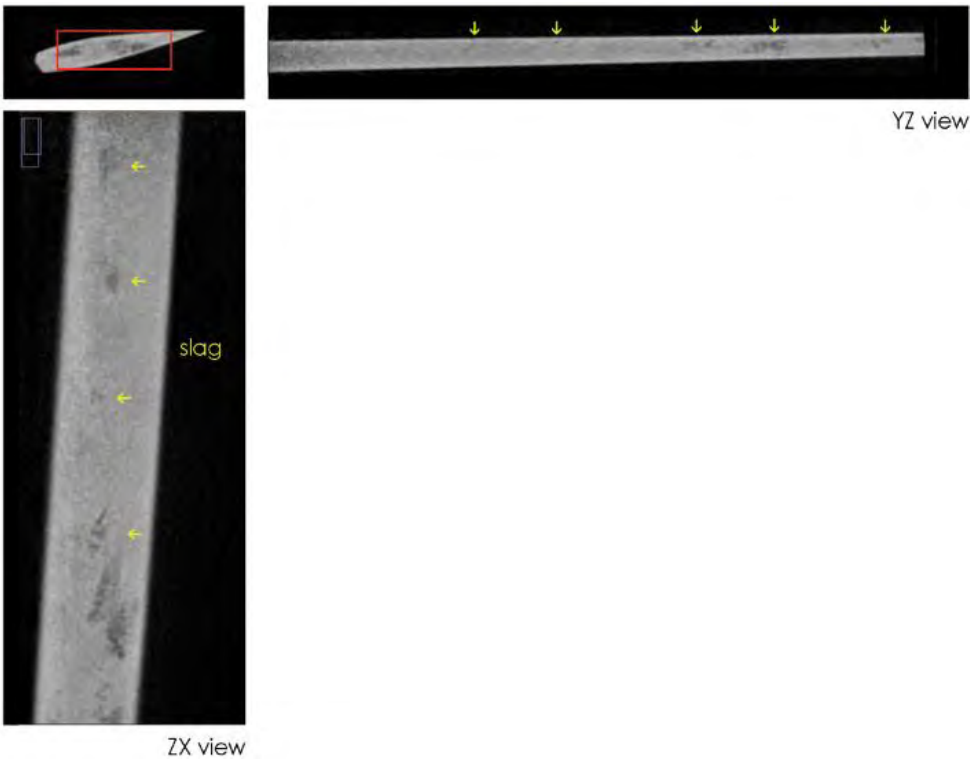

Figure 5.6: The white beam neutron tomography of the sample S3 has allowed mapping the distribution of the slag inclusions along the blade.

Sample **S8** (average carbon content: 0.25 wt %) evidences an inhomogeneous inner structure, probably due to the unequal distribution of the carbon content along the body blade (Fig. 5.7, slice 512): a careful analysis of the various tomographic slices allows to observe a "V-shaped" line in the sword cross section (Fig. 5.7, slice 514). Two long cracks parallel to the edge, as well as some small slag spots, are observed along the cutting edge (Fig. 5.7, slice 526), which is also characterized by a very sharp *hamon*.

Diffraction analysis and tomographies, as well as the fact that only one sample of this forging tradition has been analysed, does not allow to distinguish between high quality and mass production, in this case. In fact, the Koto Mino blade sample (S8) shows features that are intermediate between the so-called mass production blades, done in the warring states period (15th–16th century), and the high-rank production of the Bizen tradition. [Grazzi *et al.* J. Anal. At. Spectrom. 2011]

Energy-selective neutron tomography

In the second part of the experiment, energy-selective neutron tomographies were performed for all the samples.
For calibration purpose, a 6-mm-thick C40 steel plate has been analysed to map the ferrite contrast enhancement for the selection of two suitable neutron wavelengths to be used for imaging [Peetermans *et al.* 2013].
Two independent reconstructions have been carried out for each set of measurements, taken at the two different neutron wavelengths, namely 3.8 Å and 5.0 Å. The image stacks so obtained have been further processed, by subtracting the latter tomography from the former.

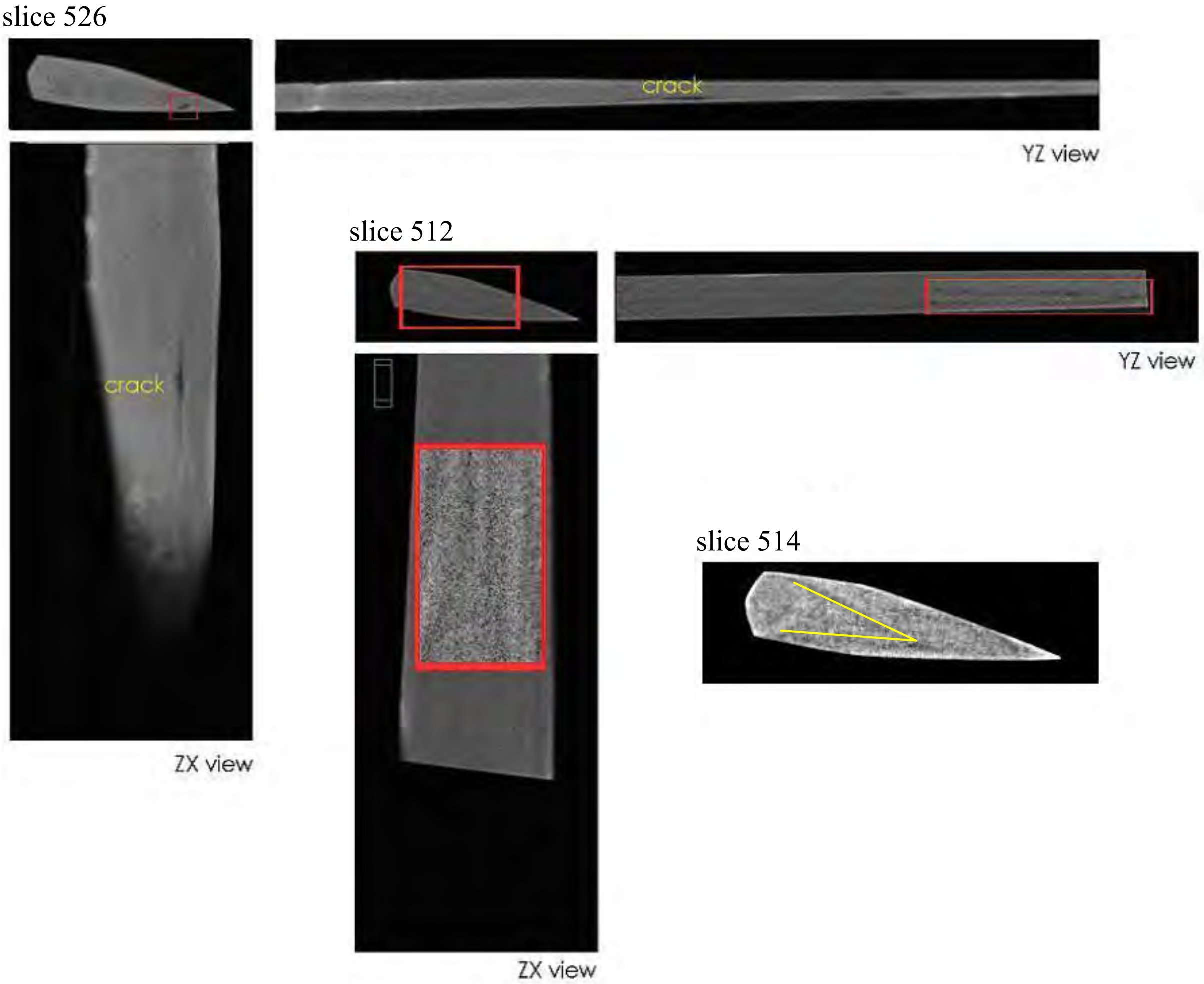
slice 526

slice 512

slice 514

Figure 5.7: Cracks (slice 526) and inner inhomogeneous structure, resulting from the particular manufacturing process (slice 512), were identified for the sample S8. Slice 514 shows some trace of the V-shaped line due to the unequal distribution of two different carbon content phases.

Referring to Figure 5.8, we can observe that the inner volume of the fragment is characterized by different distributions of dark areas (cementite) and light areas (ferrite). Thus, the present method allows us identifying the typical structure of a Japanese sword, which is known to be composed of two distinct sections of different types of steel. [Kapp *et al.* 1987] According to Kapp *et al.* 1987, Japanese medium- and full-size swords are composite structures made of a *kawagane* and *shingane* components. *Kawagane* (jacket steel) is the component forming the outer surface of the blade, including the sharp edge and the *hamon*. *Shingane* (core steel) is a slightly soften, low-carbon steel, which is embedded or wrapped into the high-carbon jacket steel along the entire length of the sword. Being more ductile than *kawagane*, it helps protecting the blade from cracking and breaking under stress. Still according to Kapp, Kapp, and Yoshihara [Kapp *et al.* 1987], Japanese smiths assemble the different pieces into a block, weld it together, and then draw out the steel into a sword. More complex structures might use four or more different pieces of steel for the core, the edge, the side, and the back of the blade. This great variety of forging methods reflects the way the various schools developed, in isolation from each other, over the country. However, this interpretation of the inner structure is not unique and other determinations have been proposed following a metallographic analysis [Tawara 1953; Notis 2000; Hoshi and Sasaki 2005].

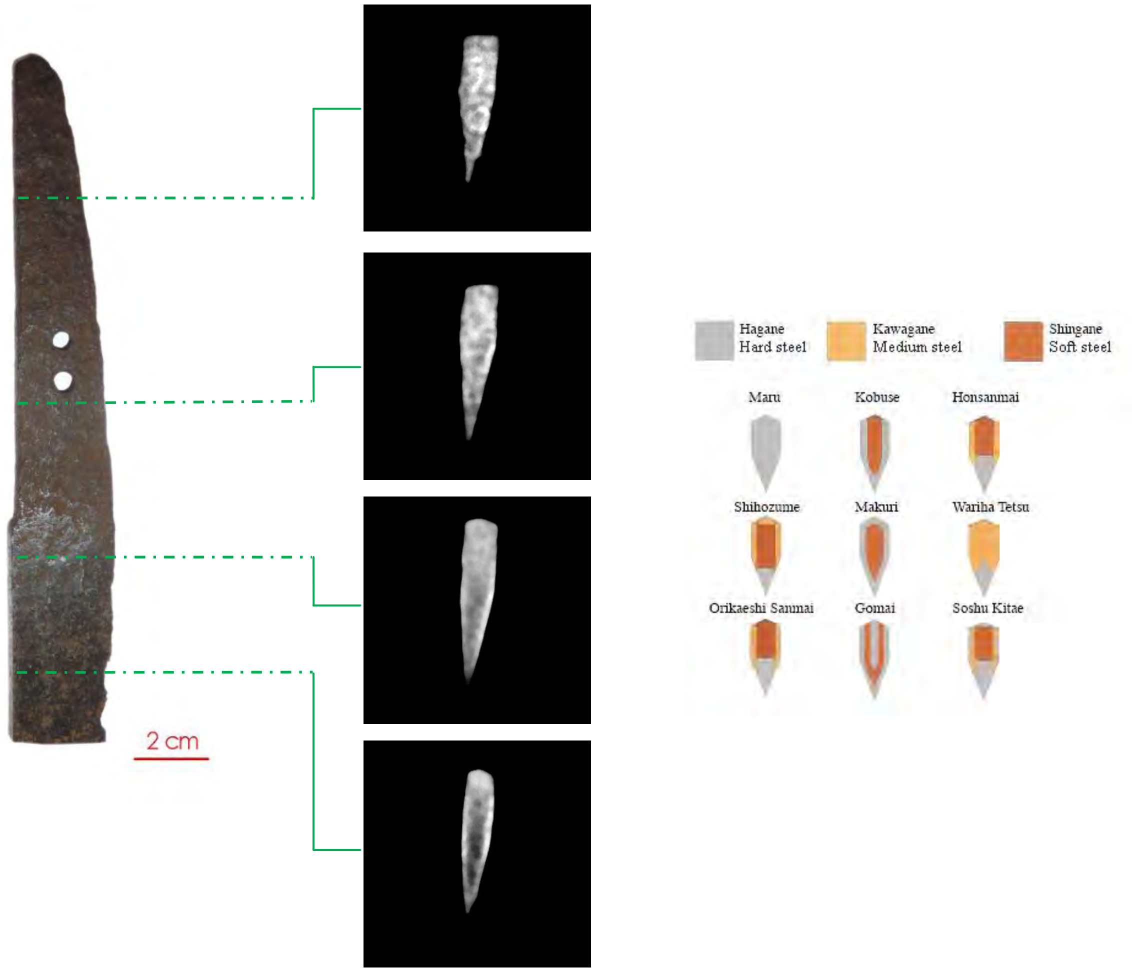

Figure 5.8: Reconstructed slices at different height along the sword S7. Energy-selective tomography have been able to evidence light areas of ferrite and dark areas of cementite. On the right, some different sword configurations, using steels with different carbon contents, typical of Japanese swords, are reported [Tawara 1953].

The tomographic slices, reported in Figure 5.9, suggest that the S7 blade has been probably manufactured by assembling a “jacket” (side and back) of low-carbon steel (*shingane*) around a very hard steel (the so-called *hagane*) composing the “core” and the “edge” of the sword. Thus, the present structure appears to be inconsistent with the one suggested in Ref. Kapp *et al.* 1987. Nonetheless, it is still possible to identify the present configuration among the various possibilities given by Tawara 1953 (cf. right picture in Fig. 5.9) and, consequntly, the sword should be assigned to one among the *Orikaeshi Sanmai*, *Soshu Kitae*, *Wariha Tetsu* or *Honsanmai* configurations. [Tawara 1953]

As it is apparent from the tomography slices shown in Figure 5.9, also the other samples, namely S0, S2, S3, and S8, are characterized by a structure similar to that of S7, with an outer soft-steel jacket (side and back of the blades) wrapped around an inner hard-steel core and edge. Thus, as far as the present samples are concerned, the found structures are more consistent with the analyses depicted in Refs. Tawara 1987; Notis 2000; Hoshi and Sasaki 2005.

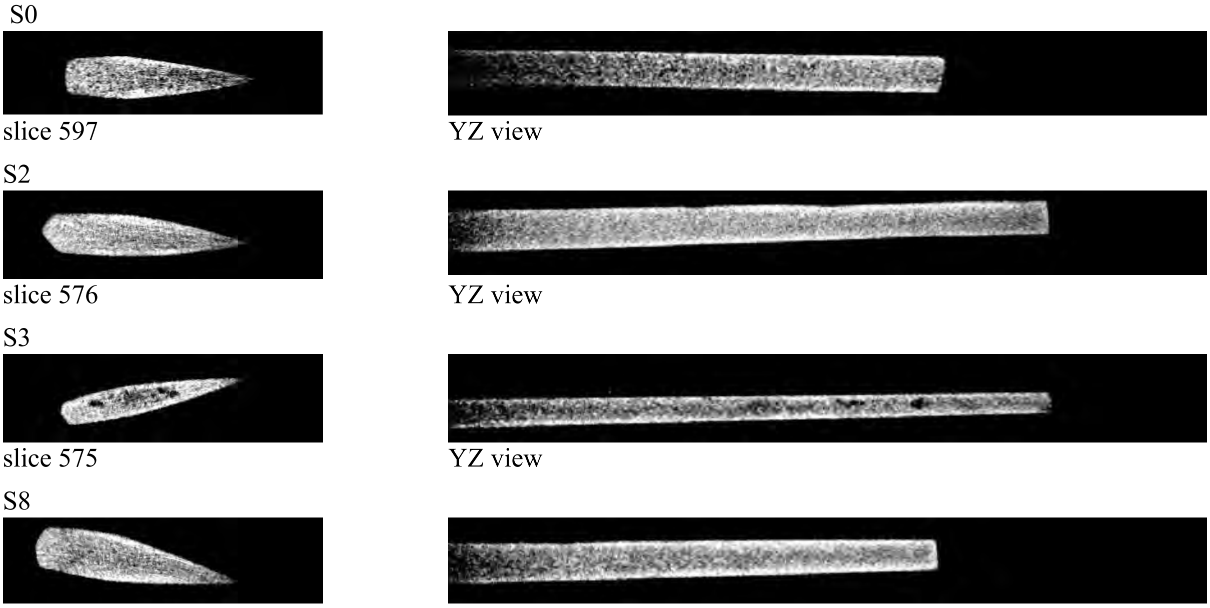

Figure 5.9: Selected slices, and related orthogonal views of energy-selective tomographies from the analysed samples, show areas of different types of steel: the lighter soft "jacket" and the darker hard "core" and "edge".

Conclusions

In the present work, five fragments of Japanese swords, pertaining to different periods and forging traditions ranging from 14th to 17th century A.D. have been studied. Even though an invasive approach could have been applied for this set of samples, it was deliberately chosen to apply a non-invasive technique to analyse all the samples, in order to show the validity of the proposed tomographic method.

White beam and energy-selective neutron tomographies have been used to investigate bulk metal samples and in a non-invasive way: the enhancement of contrast induced by the selection of an appropriate neutron wavelength has been exploited to enhance the image contrast for different component phases.

Tomographies, performed using white beam, have allowed identifying peculiar characteristics related to the forging methods and the thermal and mechanical treatments used by the different schools and traditions in Japan:

- slag inclusions and cracks were mapped and localized;
- inner structure, resulting from the particular manufacturing process, were analysed all over the samples;
- type of temper (*hamon*) has been evidenced along the cutting edge;
- alterations, originating from surface and extending in the body of the sword, have been identified for assessing the conservation status.

Concerning the energy-selective neutron tomographies, the present measurements clearly demonstrate that the proposed method can help to characterize the inner structure and composition of metal artefacts, non-destructively, in combination with other neutron inspection techniques.

5.1.2 Quantitative characterization of two ancient *katana*

Introduction

Considering the results obtained from the previous analysis, the application of neutron imaging methods, namely white beam and energy selective tomography, have been demonstrated promising in the non-destructive investigation of the inner structure and composition of ancient fragments of Japanese swords.
The investigation I'm going to focus, in this section, concerns a study performed to fully characterize two intact Japanese swords pertaining to Koto (987-1596) and Shinto (1596-1781) periods.

The samples

For the analysis presented in this work, two ancient Japanese swords, which are depicted in Figure 5.10, have been selected. Blade S1 evidences traces of a signature, which unfortunately cannot be univocally interpreted. Nonetheless, several surface features are visible and the specimen can be univocally assigned to Mino tradition of the Shinto period. Blade S2 is unsigned. However, from its shape and size, it can be univocally attributed to the Koto Age.

Figure 5.10: Picture of the two Japanese sword blades objects of the present study.

Experimental set-up

The neutron imaging study has been performed using the ICON beamline, which was described in the dedicated section 4.2.4.1.

Conceptually, the sample preparation was extremely simple. Each blade was gently wrapped using aluminium foil and its lowest part was partially inserted into an aluminium cylindrical pipe both for safety and for dealing with an object with cylindrical symmetry sitting on the rotating stage. Moreover, the tip of each blade was separately investigated setting a configuration for acquiring projections (both in white beam and in energy selective configurations) at higher spatial resolution than that taken on the whole samples.

The two Japanese blades were initially characterized using *white beam tomography* (WBT) whose instrumental set-up is reported in Table 5.2 (3rd column).

In the part of the experiment dedicated to the *energy-selective tomography* technique (the instrumental set-up for this configuration is reported in the 2nd column of Tab. 5.2), the tomographies were carried out using two different neutron wavelengths: 3.7 Å and 4.4 Å.

These values were optimized basing on the wavelength resolution of the neutron monochromator and the neutron imaging analysis conducted on the previous experiments on Japanese sword fragments [Grazzi *et al.* J. Anal. At. Spectrom. 2011, Salvemini *et al.* J. Anal. At. Spectrom. 2012]. To this aim, the neutron velocity selector, installed in front of the ICON neutron beam line and characterized by a 15% energy-resolving power, has been used to obtain energy selective tomography (EST) [Baechler *et al.* 2002, Lehmann *et al.* 2009, Hammouda 2009].

Aiming to map the ferrite density, the swords were analyzed by exploiting the contrast enhancement obtained using different neutron wavelengths. In particular, to fulfil this task, neutron wavelengths at values immediately below and immediately above the (110) ferrite Bragg edge have been used [Kaestner *et al.* 2011].

Imaging Method:	**High spatial-resolution white beam and energy-selective tomography**	**White beam tomography**
Neutron wavelength:	polychromatic, 3.7 Å, 4.4 Å	3.5 Å, 3.7 Å, 4.1 Å, 4.6 Å
L/D:	343	604
Scintillator:	^{6}LiF/ZnS (1:2) 100 [μm]	
Camera:	PCO 4000 2688×2688 14 bit	Andor DV434 – BV 1024 x 1024 16 bit
Field of View:	116 x 116 mm	232 x 232 mm
Object-Detector-D:	17 mm	
Pixel size:	126 μm	231 μm
Exposure Time:	30(WBT), 27 (EST) s	30 s
Rotating Angle:	360º	360º
Projections:	625(WBT), 375(EST)	375

Table 5.2: The different instrumental set-up employed for measurements of the two Japanese blades.

Results

White beam tomography

In the figures reported below, the reconstructions of the white beam neutron tomographies on the two blades are shown. The present non-invasive analysis permitted to identify some peculiar characteristics related to the forging methods used by the different schools and traditions in Japan (i.e. temper extension along the edge, defects, slag inclusions, internal cracks). As previously mentioned, a higher spatial-resolution tomography was acquired for the tip of both samples, in order to completely investigate the features of the temper in this critical area of the sword. By analysing the results of the present measurements, differences can be detected between the two samples, which can be univocally attributed to the different schools and traditions.

The orthogonal virtual section of blade **S1** evidenced the outline of a wide *hamon*, the temper region along the cutting edge, typical of the Japanese blade. As it is visible in the enlarged picture of the tip (Fig. 5.11, right side), the *hamon* pattern appears well defined also in the *kissaki*, the angled end part of the cutting edge, which forms the tip of the blade. As a matter of fact, Japanese sword-smiths had developed techniques for hardening only the cutting edge, leaving the body more flexible, able to absorb the shock of a blow or the stress caused by a sudden twisting [Kapp *et al.* 1987].
As the *hamon* was made by traditional quenching, and not using artificial etching process, these data allowed to confirm the authenticity of the sword. Moreover, it should be noted that the *hamon* of the tip, the so called *boshi*, appears still well preserved. As the tip is

likely the most damaged point in sword fight, a broken *kissaki*, could be often reshaped and polished, reducing the curvature and size of the *hamon* at this position.

A particular feature emerges analyzing the neutron tomographic reconstruction of S1 (Fig. 5.11). A dark area, running along the profile of the *hamon*, can be recognized. Typically the *hamon* is characterized by a high content of martensite (a non-equilibrium metastable phase resulting from the transformation, without diffusion, of austenite) with the rest transforming into ferrite. Indeed, martensite arises when austenitized iron–carbon alloys are rapidly cooled (or quenched) to a relatively low temperature (in the vicinity of the ambient) at such a high cooling rate that carbon atoms do not have time to diffuse out of the crystal structure in large enough quantities to generate cementite (Fe_3C). The face-centered cubic austenite transforms to a body-centered tetragonal form of ferrite, martensite, that is supersaturated with carbon [Callister 2009]. The polymorphic transition from the highly packed structure of the *fcc* structure to the *bct* one is combined with a variation in volume of the metal induced by the variation in temperature. The dilatation of the steel, during the transformation of the ferrite into austenite, and its following contraction, during the formation of martensite, depend on the competition between the thermal volume variation and the transformation process [Qui and van der Zwaag 1997]. If the thermal effect highly prevails, probably when temperature and cooling rate are not carefully controlled, it can cause the detachment of the interested area from the part of the blade that was kept thermally isolated during the process. This seems to be the best explanation of the phenomenon shown in Figure 5.11.

A careful analysis of Figure 5.11 (left picture) reveals the presence of small slag-inclusions, elongated and parallel to the back of the sword and to the *hamon* pattern. In addition, owing to the high resolution white beam tomograpy of the tip, the trace of a single internal crack starting from the tip and extending along the backside can be resolved (Fig. 5.11, right picture, red arrows). Last, but not least, the *kissaki* (tip) presents a very complex structure as it is evident in the high resolution section (Fig. 5.11, right picture) showing several strips and elongated spots with different neutron transmission density in the whole volume. They are probably related to the hammering work performed to shape the tip that is usually bent backward from a diagonally cut bar [Kapp *et al.* 1987] combined together with the effect of quenching.

Finally, the various cross sections, taken at different heights of blade S1 (Fig. 5.11, sequence of central images), evidence an inhomogeneous inner structure. The presence of a bright area, on each flat side of the sword, leads to two different explanations. The first hypothesis is related to a highly neutron attenuating material, i.e. goethite FeO(OH), diffusing from the surface to the inside of the blade. The second interpretation leads to the probable use of different types of steel characterized by different carbon contents. As the first hypothesis would imply the visible presence of rust traces onto the external surface (not detected in this case), I would be led to favour the second one. As clarified in detail, in the following section, also the variation of the gray tones in the core of the blade, visible in the cross sections images and in the orthogonal view, strongly suggest a preference for the second interpretation.

Figure 5.11: On the left, the orthogonal section virtually cut at the centre of the blade. At its side, different slices, selected at different heights of the sample, show the progress of the *hamon* line along the blade and the inner structure of the whole object. On the right, the high spatial-resolution image of the tip, whose location is marked by a red frame in the orthogonal view, evidences the presence of slag inclusions (red rectangle) and a crack (red arrows) in sample **S1**.

Concerning the sample **S2**, also in this case an inhomogeneous inner structure has been revealed by the analysis (see Fig. 5.12, left side and central images sequence).
The quenched region (*hamon*) along the cutting edge is visibly thinner than in sample S1. Moreover, it could be detected evidence of the diffuse presence of small slag-inclusions in the whole body of the sword. In particular, as visible from the orthogonal view of the high spatial resolution tomographic reconstruction (Fig. 5.12, right picture), a huge defect is recognizable near the tip and inclusions appear concentrated especially along the backside of the sample.

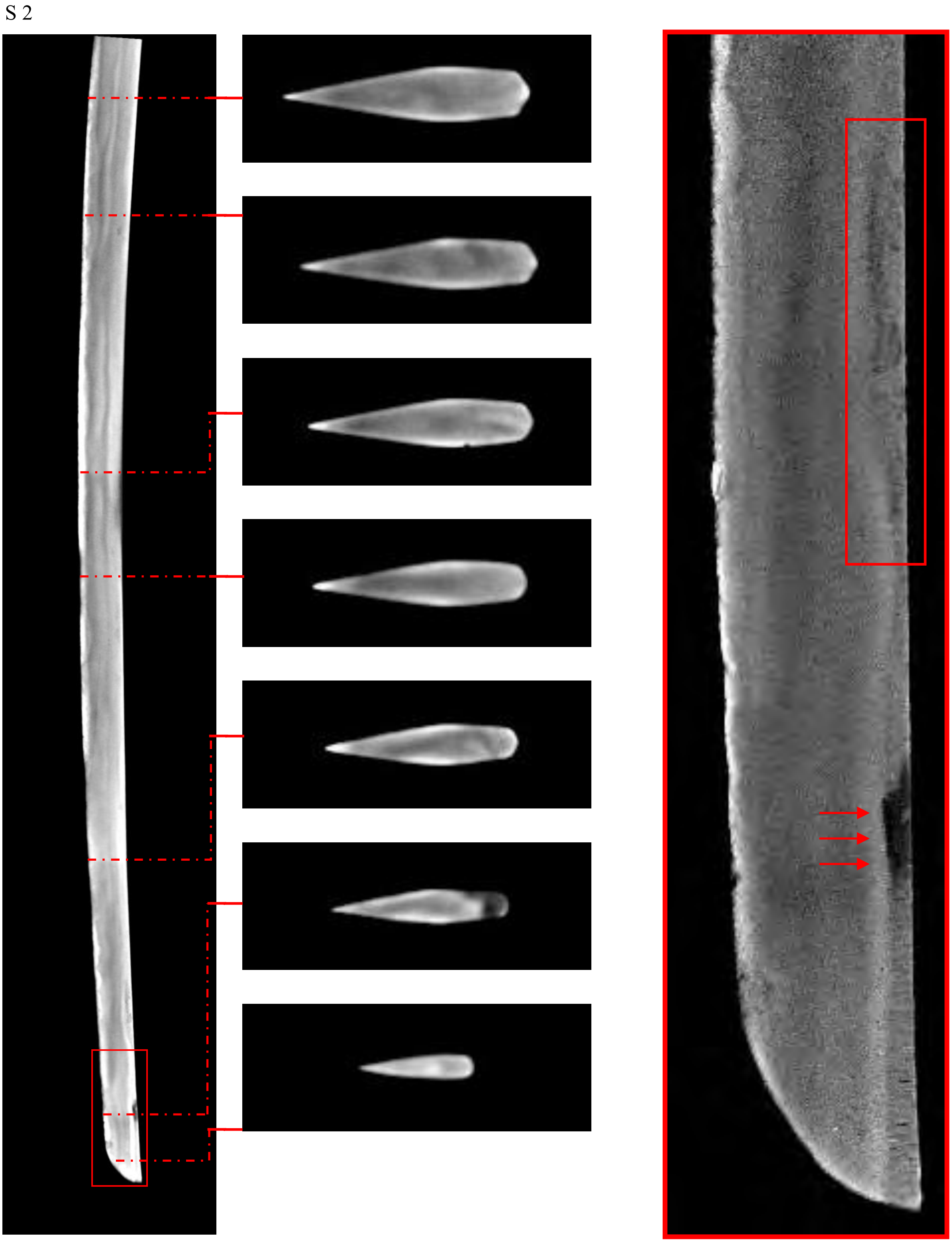

Figure 5.12: The orthogonal central view of sample **S2** is reported on the left. The red lines indicate the height of the shown axial slices. A red frame points out the location of the high spatial-resolution image of the tip, reported on the right side. In the enlarged picture, the presence of a defect (red arrow) and the cloud of slag inclusions (red rectangle) are visible.

The tang, also known as *nakago*, deserves to be mentioned. Three *mekugi-ana* are observed in the tang of the sample S2 (hardly visible in Fig. 5.10). The *mekugi-ana* are holes drilled in the tang for passing through a peg in order to stick the hilt. Most blades have one *mekugi-ana*, whilst some have two or more, generally due to a reshaping of the tang, as it seems to be the case in the presently analyzed sample, where three peg-holes are counted. The evident observation of the *hamon* line, well extending into the tang, suggests that the original blade was shortened, so that part of the original blade was transformed into the actual tang. This hypothesis is confirmed by the presence and spatial disposition of a third *mekugi-ana*. Indeed, comparing the shape and geometry of the holes, it can be distinguished a different direction in making the third hole, with respect to the others (Fig. 5.13).

Finally, it is worthwhile to mention that the black line facing the *hamon* on the inner side of the blade is not present in sword S2. The process of heating a sword until it is red hot, and then plugging it into water, is perhaps the most dramatic moment in the sword-smith's practice [Kapp *et al.* 1987]. So, the S2 blade was probably made following a more careful and accurate procedure than the Mino-Shinto sword (S1), where the procedure was, likely, more "industrialized".

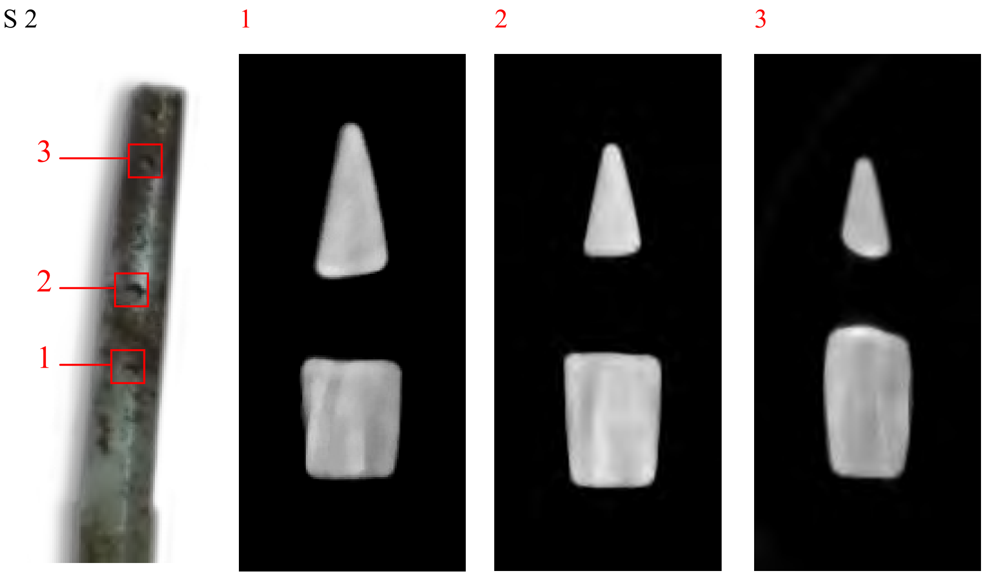

Figure 5.13: Axial cross sections are acquired at the centre of each *mekugi-ana*. The red numbers identify the location of the holes in the S2 blade.

Energy -selective neutron tomography

In the second part of the experiment, energy-selective neutron tomographies were performed on both samples. Basing on preliminary analysis conducted for test and calibration purposes on Japanese sword fragments, the same two suitable neutron wavelengths used for energy selective imaging have been used to map the presence of ferrite [Salvemini *et al.* JAAS 2012].

Two independent reconstructions have been carried out for each set of measurements, taken at the two different neutron wavelengths, namely 3.7 Å and 4.4 Å. The image stacks, so obtained, have been further processed, by subtracting the latter tomography from the former.

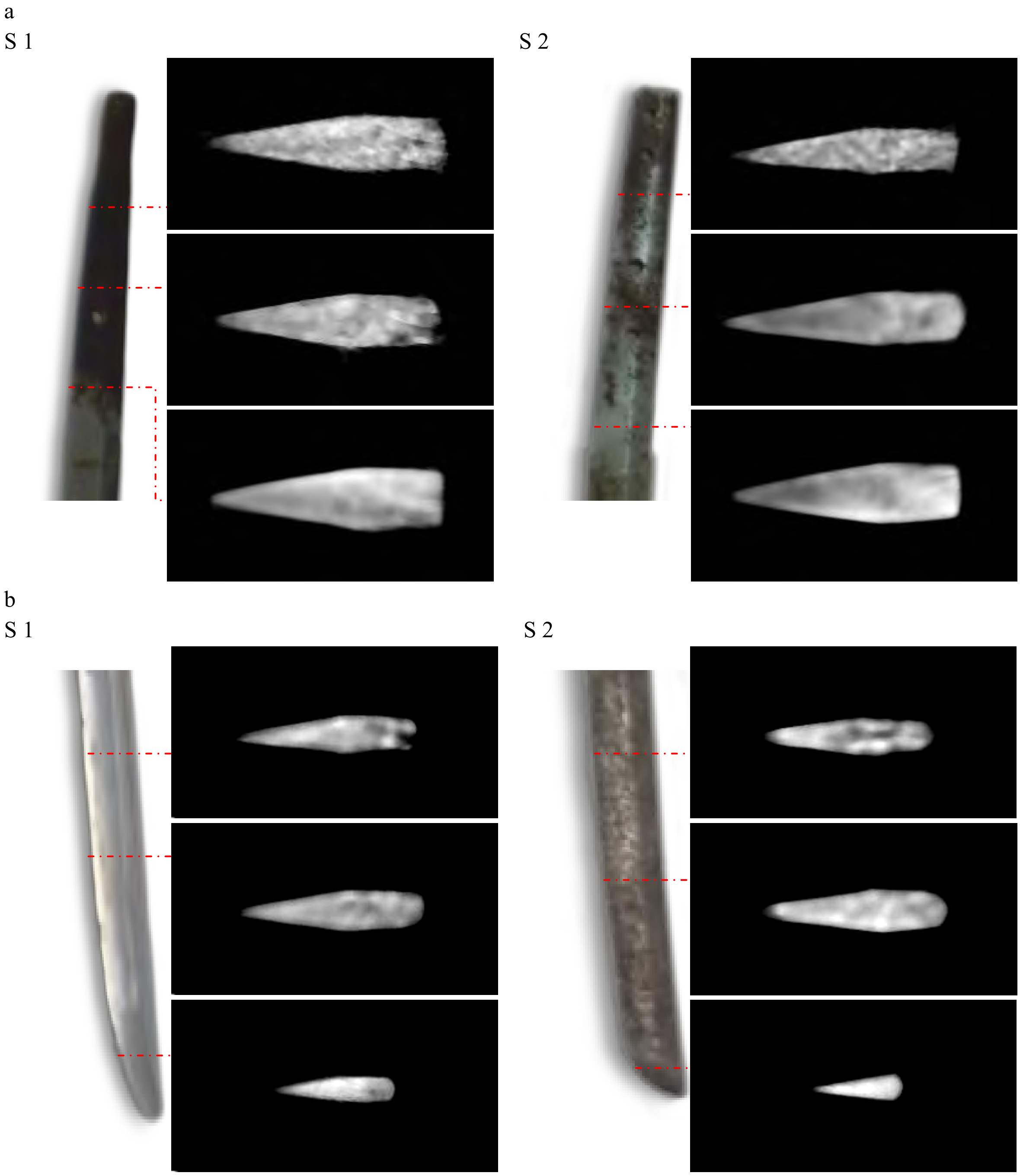

Figure 5.14: Selected slices of the analysed samples show the inner structure of the tang *a*) and the point *b*). Energy -selective tomography have been able to evidence light areas of ferrite and dark areas of cementite.

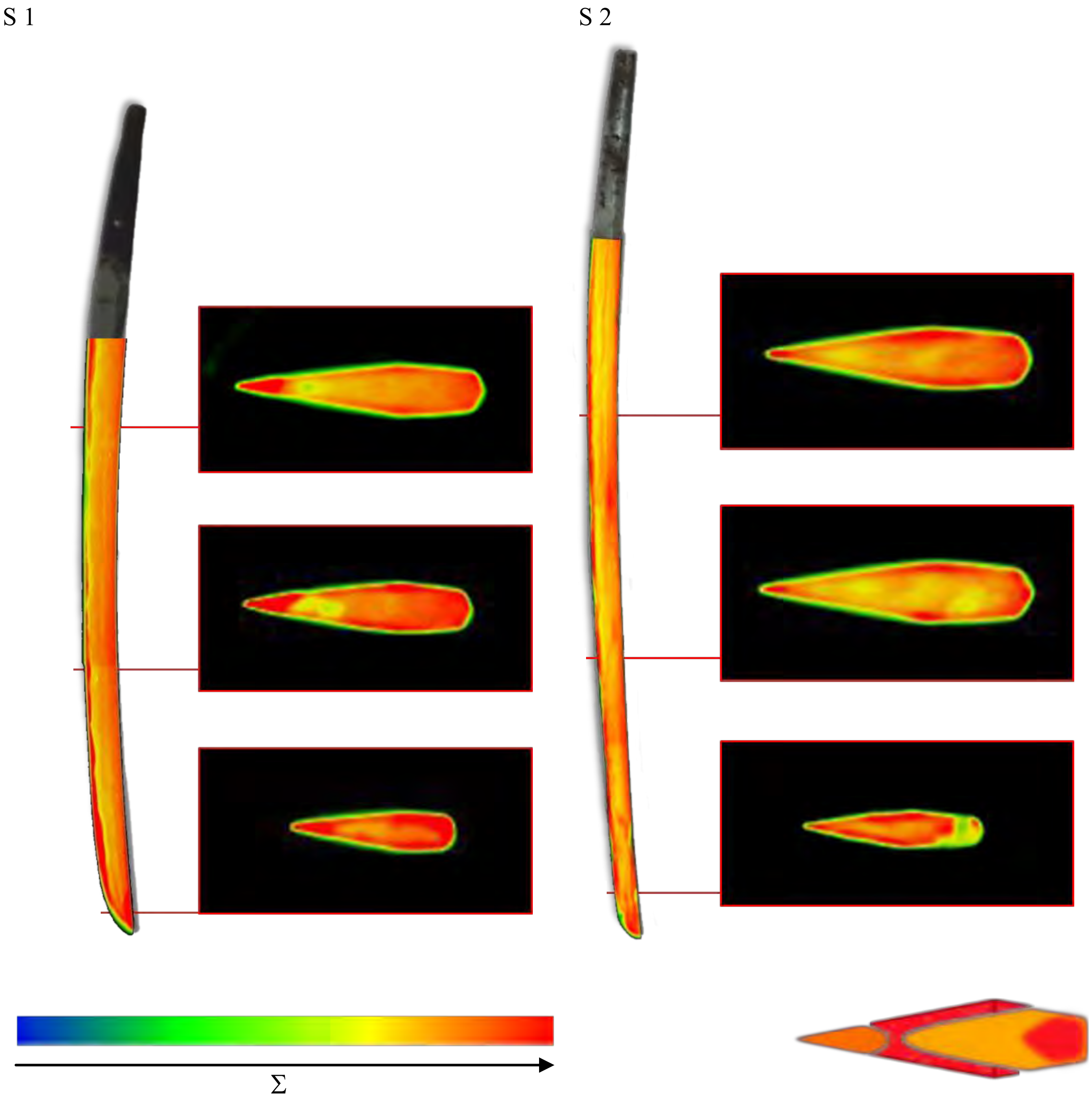

Figure 5.15: Reconstructed slices at different height along the two swords. The tomographic reconstructions are shown in false colour enhancing the contrast in order to help in detecting the structure. A gradient bar is placed at the bottom. On the bottom-right corner, it is reported the detected sword configurations, one of those typical among Japanese swords [Sato 1983].

As it is visible from the tomography slices shown in Figure 5.14-*a*, both tangs of **S1** and **S2** are characterized by a homogenous inner structure slightly changing to an ordered structure going towards the blade. This happens earlier for blade S2 due to the shortening and reshaping. Instead, above the quenched region of the tip, the contrast enhancement, induced by the selection of an appropriate neutron wavelength, allowed us to discern a certain differentiation in the swords structure (Fig. 5.14-*b*).

Indeed, referring to Figure 5.15, green-yellow colour area can be related to the presence of defect and inclusion (previously discussed in the *white beam tomography* section). Moreover, it can be observed that the inner volume of the sword is characterized by different distributions of orange areas (cementite) and red areas (ferrite). Thus, the present method allows us identifying the typical structure of a Japanese sword, which is known to be composed of, at least, two distinct sections of different types of steel [Kapp *et al.* 1987]. According to Kapp *et al.* 1987, Japanese medium and long swords are composite structures made of a *kawagane* and *shingane* components as detailed described in the previous section 5.2.1 on the test measurement conducted on the five fragments.

The tomographic slices, reported in Figure 5.15, suggest that also the **S1** and **S2** blades have been probably manufactured by assembling a “jacket” (side and back) of low-carbon steel (*shingane*) around a very hard steel (*hagane*) composing the “core” and the “edge” of the sword. Thus, the present structure appears to be inconsistent with the one suggested in Ref. Kapp *et al.* 1987 and identical to one detected in the test analysis. Nonetheless, it is still possible to identify the present configuration among the one given by Ref. Tawara 1953 (cf. bottom-right corner of Fig. 5.15) and, consequently, the swords should be assigned to *Shihozume* configuration [Tawara 1953].

Conclusions

In the present work, two Japanese swords, pertaining to different periods and forging traditions, have been studied. White beam and energy-selective neutron tomographies have been used to investigate bulk metal samples in a non-invasive way that is mandatory for this kind of artefacts.

White beam tomographies have allowed to identify peculiar characteristics related to the forging methods as well as the thermal and mechanical treatments used by the different schools and traditions in Japan:

- slag inclusions and cracks were mapped and localized;
- inner structure, resulting from the particular manufacturing process, were analysed all over the samples;
- the line of temper (*hamon*) and related care in the quenching process has been evidenced;
- marks of reshaping have been identified.

The present measurements even confirmed that energy-selective neutron tomography helps in characterizing, non-destructively, the inner structure and composition of metal artefacts. Thanks to the contrast enhancement induced by the selection of an appropriate neutron wavelength, the image contrast for different component phases has been exploited to define the assembling configuration of the samples.

5.2 Revealing the secrets of *kabuto*

Introduction

Japanese swords and armours have always been very attractive to the western culture because of their distinctive styles, which are considerably different from the corresponding objects familiar to western culture. I believe it is a peculiar duty of material scientists to widen this interest to include a deeper understanding of the technological differences behind the self-evident differences in style. This would help in elucidating the forging techniques, which were used by ancient Japanese craftsmen in the manufacture of sword blades and armours. Much literature exists about Japanese swords, but far less is known about the technology of armours. So, an international team of scientists and curators decided to work together, to investigate the construction of one of the most critical components of the Japanese armour, namely the helmet (*kabuto*). In the present section, I report the first, and to some extent surprising, results of such study.

The *kabuto* of the traditional samurai armour is a kind of helmet, typically made of steel components, assembled in ways peculiar to their particular manufacturing school. These objects are quite rare and, when found in museums, are usually in an excellent state of conservation, being considered masterpieces representative of Japanese culture. For this reason, any detailed study of these artefacts must rely on non-invasive techniques and it was decided that only thermal and cold neutron techniques should be employed for this investigation.

In parallel to the evolution of the offensive power of the *katana*, the celebrated and deadly sword of the samurai, there was a less apparent but still important improvement of the defensive qualities of the samurai's equipment. Among the various components of their armour, the helmet assumes, for obvious reasons, considerable importance. Here, the technological skill of the craftsman might reach the best results in joining lightness and effectiveness to defend the most important organ of the samurai's body: the head. In addition, being the most visible part of the warrior from a distance, the helmet assumed also the role of the distinctive sign of a leader in battle. Thus, not only effectiveness, but also elegance and visibility became necessary qualities for the samurai's helmet, the *kabuto*.

The *kabuto* became an important part of the traditional Japanese armour during the feudal period, and was initially worn only by high-ranking warriors [Kozan Sakakibara 1800, Sinclaire 2004]. During the Momoyama Period (1568-1603), armourers began to build fantastic shapes on top of the earlier simple helmets, in order to improve visibility and enhance the leader's presence on the battlefield. These *kabuto* were composed of a steel bowl, surmounted by a structure of papier-mâché and lacquer, or sometimes entirely of iron. These shapes mimicked forms taken from Japanese culture and mythology, including fish, shell, dragon, etc. [Sinclaire 2004]. These can be classified into three main categories: those made from a single sheet of metal, folded and welded; those assembled from a small number of sheets; and those assembled from a large number (varying between 8 and 128) of lamellar plates arranged in a circular fashion around the crown on top of the head [Sinclaire 2004]. From the mid 16th century, when a Portuguese ship first landed on Tanegashima Island, Japan came into contact with the European culture, tradition, art, and fighting techniques. As a result, armament production was strongly influenced and armour construction and design, including helmets, was modified in an attempt to resist firearms [Sinclaire 2004].

The samples

For the analysis presented in this section, two examples of ancient helmets have been selected. In fact, the two chosen *kabuto* are antithetical in their complexity: while the first one is characterized by a unusually complex shape, the second is made of a large set of relatively simple components, assembled in a very complex structure. Each one was dated by the museum experts using stylistic analysis and archive studies.

The helmet shown on the left side of Figure 5.16 is a *Horagai Bachi*, a peculiar example of a helmet of the 1st type (as previously defined). This is classified as a *tetsu bari shiki kawari-bachi* (wonderfully shaped steel helmet) and was made, in the form of a shell, by *Ryōei - Ohara Katsunari* from Hiroshima province at the end of the 17th Century. This helmet was made available by the Stibbert Museum in Florence.

The *kabuto* shown on the right hand side of Figure 1 is, according to our definition, an example of the third type. This is a signed *Saotome bachi* made in the 1st half of the 17th Century by *Saotome Ienari*. He was the third craftsman of the *Saotome* dynasty, so the helmet is one of the oldest surviving of this type. The sample is made of 64 lamellar plates, finished with a visor decorated with two facing gold dragons. It is a typical *suji kabuto*, or “flange helmet bowl”, presenting ribs at the edge of each plate. The various components are joined by rivets, which are invisible because the surface is lacquered on the inside and patinated on the outside. This helmet was kindly provided by a British private collector and was formerly part of the H. Russel Robinson Collection.

Figure 5.16: The picture on the left shows the unconventional shape of the *horagai bachi* helmet (shell shaped). On the right, the *suji-bachi* helmet is shown: this is a multiple-plate type of *hachi* (Japanese helmet bowl) with raised ribs on every plate and connection rivets hidden into the internal structure.

Scientific investigations

In the present experiment, the neutron radiography has been performed at the ICON facility.
The peculiar cold neutron wavelength of the ICON instrument allowed us to enhance the contrast between the different phases and the different thickness of the material, thanks to the large cross-sections for some elements and the consequent high sensitivity in thin layers.

Sample:	***Horagai Bachi* Helmet**	***Suji-Bachi* Helmet**
Instrument:	**ICON**	**NEUTRA**
Imaging Method:	Neutron radiography	Neutron tomography
L/D:	605	550
Scintillator:	^{6}LiF/ZnS (1:2) 100 μm	^{6}LiF/ZnS (1:2) 200 μm
Camera:	Andor DV434 – BV 1024 x 1024 16 bit	Andor iKon-L DW936N 2048 x 2048 16 bit
Field of View:	323.4 x 323.4 mm	309 x 309 mm
Object-Detector-D:	150 mm	148 mm
Pixel size:	310 μm	150 μm
Exposure time:	12 s	20 s
Rotating Angle:	-	360 °
Projections:	13	625

Table 5.3: The different instrumental set-up employed for measurements of the two Japanese helmets.

The neutron tomography study has been performed using the NEUTRA facility, the thermal neutron imaging station at SINQ.
In order to cover the whole volume of the helmet, within the field of view of the instrument (NEUTRA), the sample was placed diagonally over an aluminium cylindrical frame and gently fixed using aluminium strips. The very low cross section of aluminium makes this metal almost transparent to neutrons, thus avoiding the need of a complex data analysis to remove interferences between the two components during the data reduction. The acquired neutron tomography data were processed through the software package Octopus, developed at Ghent University [Dierick et al. 2004].

In Table 5.3 the different experimental configurations and instrument set-up for the two measured samples are summarized.

Dealing with precious museum objects implies taking extra precautionary measures preventing possible damage to the sample or somehow impairing its availability for a much too long time (e.g. because of a long-living residual radiation activity) [Fedrigo *et al.* 2013]. To this aim, the first *kabuto* (the shell shaped *horagai bachi*) was initially characterized trough a preliminary Neutron Activation Analysis test measurement. This analysis was used to evaluate the concentration of trace and major elements (and their isotopes) in the sample with the aim of testing its activation rate and decay time as a function of the exposure time [Alfassi 1990]. In order to limit the activation level induced by the presence of Cu and to avoid a decay time longer than a few hours, this helmet was investigated for a limited neutron exposure time and only 13 neutron radiographies were taken from different positions on the sample. No such problems emerged in the analysis of the second *kabuto* (the bell shaped *suji-bachi*) and therefore, in this case, a full tomographic study was possible.

Results

The following images show some of the neutron radiographies and neutron tomography reconstructions of the two helmets. The non-invasive analysis allows the identification of some peculiarities of the manufacturing methods used by the Japanese craftsmen. In particular, details of some specific structural elements shed some light on the assembly techniques of the objects.

Horagai bachi helmet (shell shaped)

The set of neutron radiographies allowed us to discover that this helmet is built of three different metal sectors and these were joined (by brazing) in such a way that it was impossible to see the seams due to the surface finish patina. The seams are shown in Figure 5.17 enhanced by the red lines. The first circular brazing, close to the top, is connecting the upper almost conical part of the helmet to the lower portion. The second brazing is linear and closes the seam of the large single-plate component bent to form the central part of the helmet. Finally, a third circular brazing was used to connect the body of the helmet with the circular plate on the bottom. It should be noted that the brazing was absolutely invisible, and could only have been detected by removing the original patina, which covers the *kabuto* surface both internally and externally. A careful analysis of the gamma emission spectrum originating from the brazing material allowed us to identify it as pure copper.

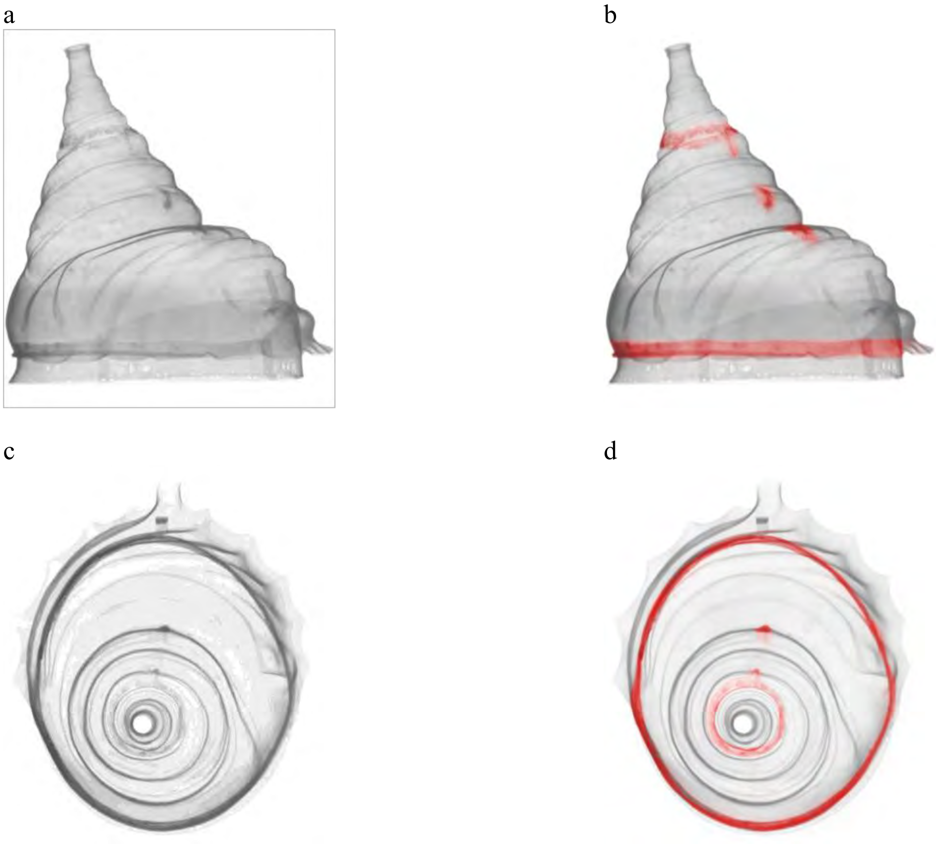

Figure 5.17: Selected neutron radiographies show the helmet structure. In *a* and *c* the transversal and bottom views, respectively; in *b* and *d*, the brazing positions linking the three different metal portions are marked in red (see text).

Suji-bachi helmet (bell shaped)

Concerning the *Saotome bachi* helmet, the tomographic reconstruction of the *kabuto* allowed us to acquire a wealth of information about the inner structure and assembly methods of this masterpiece. In the left half of Figure 5.18, the *kabuto* image and the reference system of the tomographic planes are reported. In the right part, the 3D tomographic image is cut along the selected planes and the resulting images are shown. From top to bottom we observe: 1) the horizontal (axial) section obtained by slicing along the blue plane; 2) the longitudinal section obtained by slicing along the green plane; 3) the transversal section obtained by slicing along the red plane.

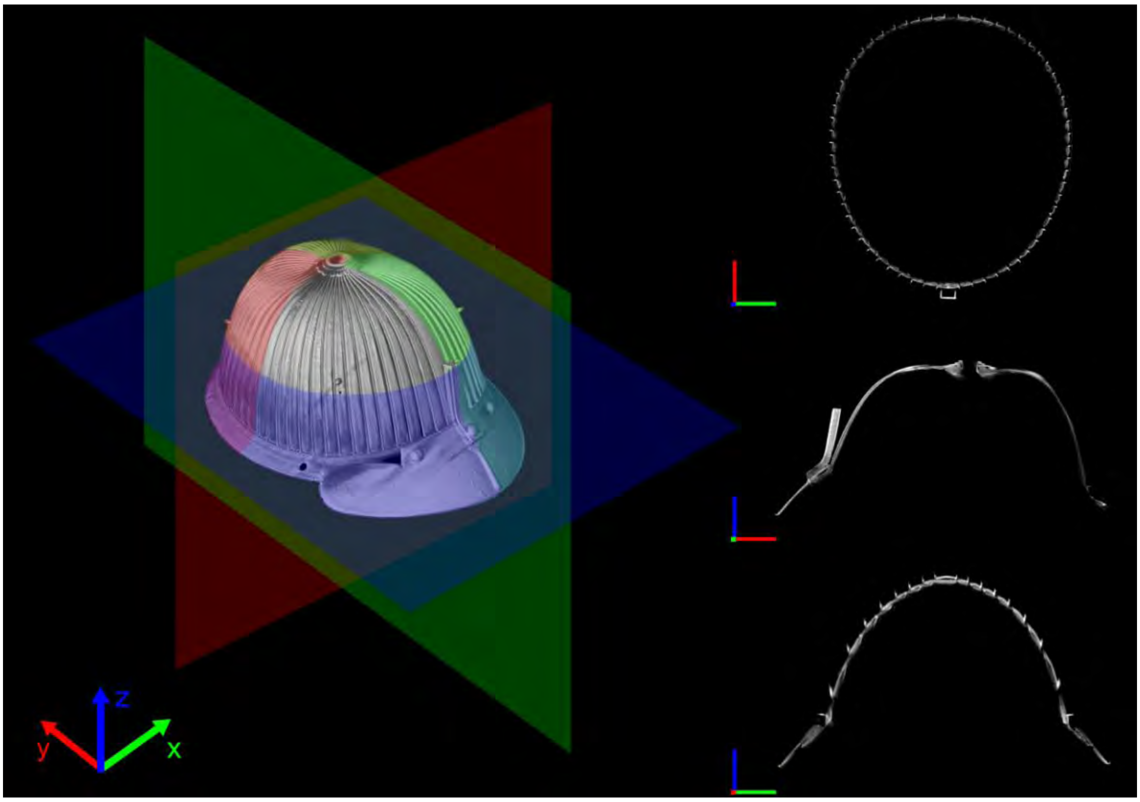

Figure 5.18: On the left, perpendicular sections trough the helmet (blue, green, and red planes) and their orientation (x, y, and z axis) within the virtual 3D space. From top to bottom on the right side, axial, transversal, and normal views clearly show how the tomographic images were used to gain information on the *kabuto* inner structure.

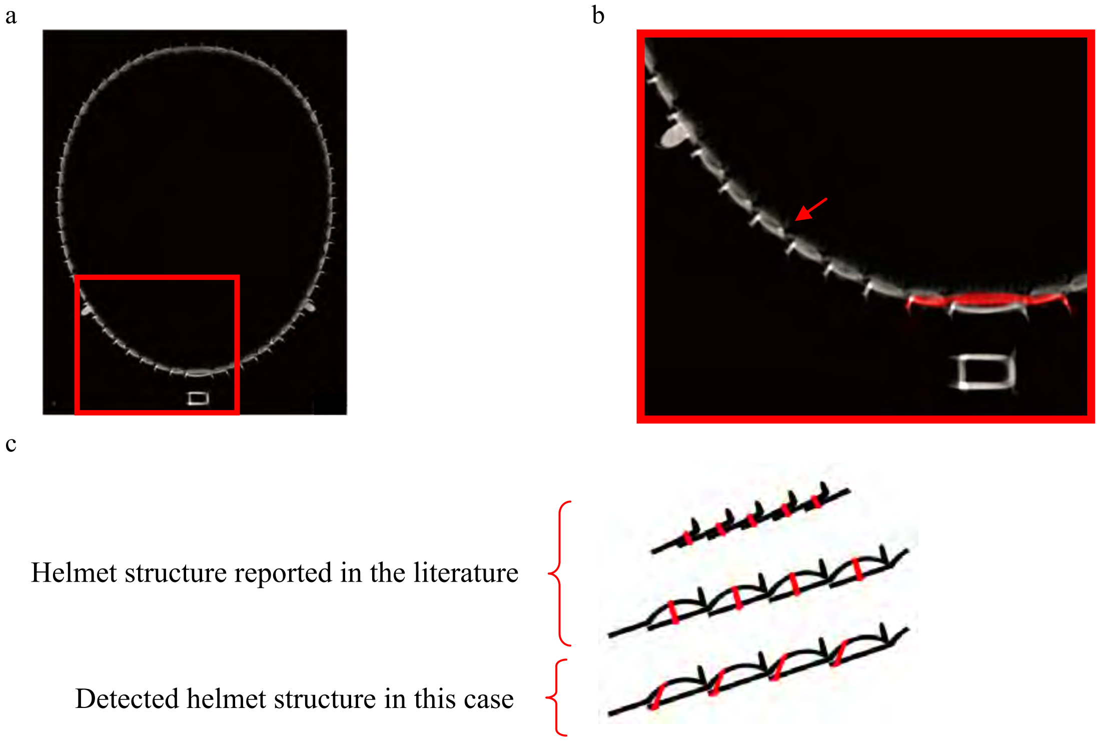

Figure 5.19: The image *a* is the axial cross section taken half way up through the helmet; the red rectangle marks the zoomed region reported in *b*. The enlarged image clearly shows the arrangement of the overlapped "S" shaped plates. The red arrow points out the position of a rivet, linking the extreme end of the lower plate with the central part of the upper one. The frontal area is manufactured superimposing a properly curved narrow metal sheet over a large 3-folded one, here coloured in red. As shown in picture *c*, the detected structure is of a new type with respect to the two kinds so far reported in the literature.

The helmet axial section, reported enlarged in Figure 5.19 *a*, is further zoomed in Figure 5.19 *b*. From these images (and from others, even further zoomed) the actual arrangement of the lamellar components in the *kabuto* was made visible. The construction starts from the central plate, in the back of the helmet. The "S" shaped vertical plates overlap one other, leaving an empty space in the centre of the superimposed area. This arrangement was invented to absorb the energy of a blow and was probably evolved from a simpler structure such as that one shown in the upper drawing of Figure 5.19 *c,* where flat plates are fixed to one another by rivets (*boshi*). According to the current literature [Kozan Sakakibara 1800], the vertical curved plates of the helmet (*tate hagi-no-ita*) are interconnected by orthogonal rivets as well. These are supposed to be inserted through the centre of a portion of each lower plate and connecting to the centre of the curved portion of the upper plate (see the intermediate drawing in Figure 5.19 *c*). Instead, in this case, the image reconstruction shows a different layout characterized by diagonal *boshi,* as reported in the bottom scheme of Figure 5.19 *c*.

This type of arrangement shows well in the orthogonal projections of the tomographic reconstruction of Figure 5.20. Such a structure allows the helmet to be more resistant to blows. In fact, if the helmet is struck, every plate involved tends to transfer the impact to the next ones. This permits the differently curved parts to contribute to the absorption of the impact energy. Moreover, the external ribs located in the side end of the plates are facing towards the back of the helmet. Thanks to this arrangement, most of the impact energy is transferred to these ribs in case of a frontal or diagonal hit. The diagonal orientation of the rivets helps in keeping the structure stable under the blows offsetting their tendency to deform. It is amazing how a simple modification in the alignment of the *boshi* improves all the intrinsic advantages of the curved structure by adding stability and hence strength to the entire structure.

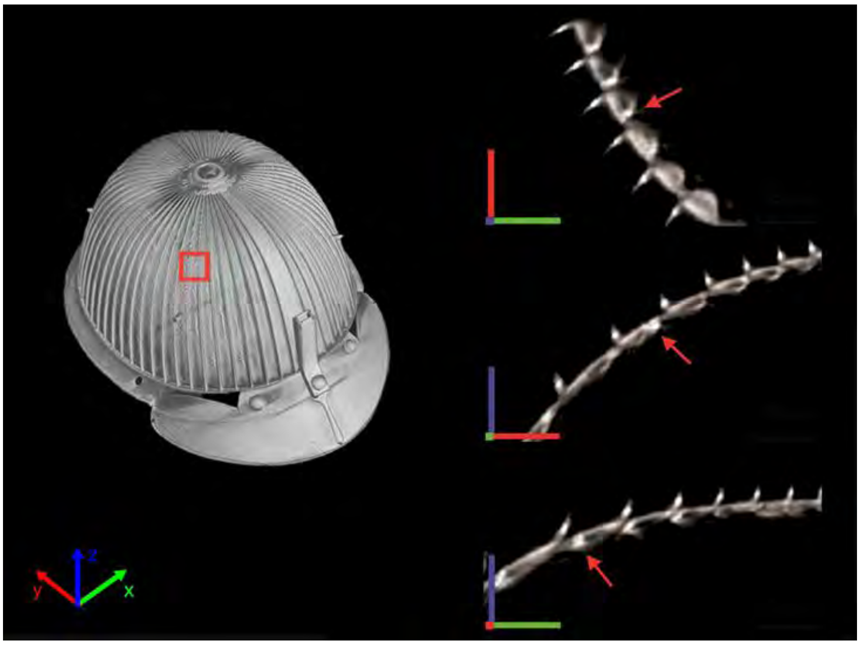

Figure 5.20: In the 3D reconstructed image, the red square marks the position of a hidden rivet. On the right, from top to bottom, the red arrows point its precise location in the axial, transversal and normal orthogonal views, respectively.

We can also observe that the central plate located in the back of the *kabuto* is composed by a single metal sheet whose edges are completely covered by the two adjacent sectors (see upper part of Figure 5.19 *a*). On the contrary, the frontal area was manufactured by superimposing a properly curved narrow metal sheet over a large 3-folded one that completes the round shape of the helmet, thus fixing and securing both sides of the *hachi* (helmet bowl) structure (see Figure 5.19 *b*). The rivets are arranged in six concentric rings running at different heights all around the helmet circumference joining adjacent plates, holding together and stabilizing the two-layers structure.

As it can be observed in Figure 5.21 (a zoomed view of the transversal section already shown in Figure 5.18) all the plates radiate vertically from a central opening at the top of the bowl, named *tehen*. This portion of the *kabuto* is marked with the upper red rectangle, while the lower one depicts a schematic view. In the same figure, we can note that the visor (*tsuke mabizashi*) and the front crest holder (*haraidate-dai*) were fixed together and anchored to the helmet body through a large and prominent rivet called *hachi tsuke-no-byo*.

The round plate at the bottom of the helmet is named *koshimaki* and is attached to the upper part (*hachi*) with a single line of rivets. This is depicted in Figure 5.22. On the left side, the tomographic image of this section is shown, while on the right, in the red frame, a scheme of the two curved portions of the *koshimaki* and of the *hachi* shows the connecting rivets in red.

Another important and unexpected feature revealed by the tomographic reconstruction of this *kabuto* is the presence of two *byo*, whose position is evidenced in Figure 5.23 by the two red circles (picture on the left) and by the rectangles (picture on the right). These two rivets have no structural function but were typically placed by the maker as his own signature. The number and position of these *byo*, characteristic of the *Saotome* school, confirmed the helmet attribution that was previously based only on the available documents and the stylistic analysis.

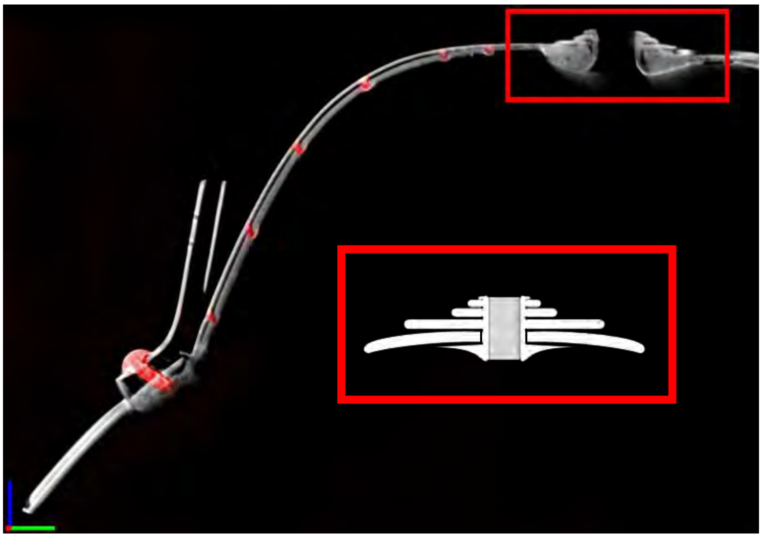

Figure 5.21: Normal section taken through the middle of the helmet: red spots map the rivets position along the two central superimposed lamellar plates. An anchor rivet, also in red, joins the visor and the front crest holder to the *hachi*. The upper red frame points out the position of the *tehen* with its idealized structure depicted in the lower red rectangle.

Figure 5.22: The axial cross section at the bottom of the helmet shows the arrangements of the *koshimaki* and the *hachi*. The light red spots mark the rivets positions, as shown by the scheme in the red frame on the right.

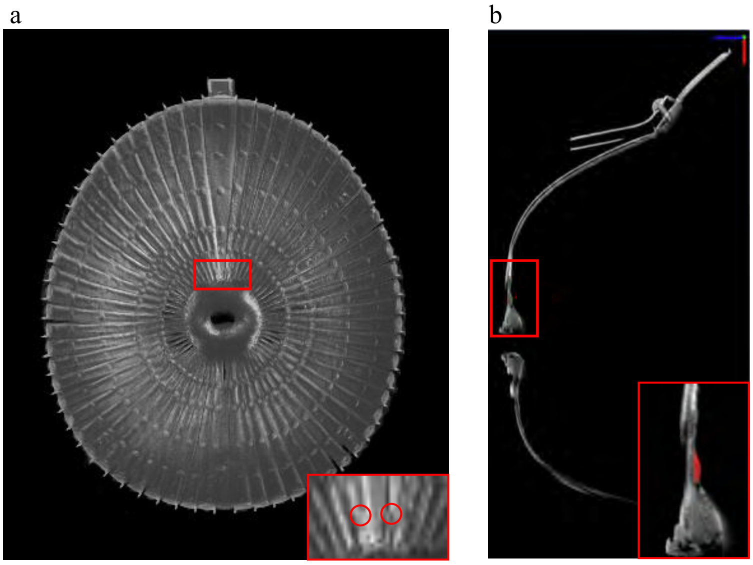

Figure 5.23: The axial 3D cross section *a* allows to define, looking from the bottom, the *byo* position in the inner-upper portion of the central plate. On the right *b*, the red rectangle points out the rivets location in the transversal section. At the right side bottom of each image, a zoom of the region of interest shows *byo* marked in red.

Conclusions

This work is the result of a collaborative investigation carried out on two Japanese helmets belonging to different structural categories from the 17th century. The present analysis could not have been carried out using traditional (invasive) analytical methods, which cannot be applied to such ancient and rare artefacts where a non-invasive, non-destructive experimental approach is mandatory.

Neutron imaging experiments were used to identify the peculiar characteristics of the construction methods used for two different types of *kabuto*. In particular, in the *horagai bachi* helmet more than one metal plate component was revealed and the invisible brazing lines were identified.

Concerning the *suji bachi* helmet, a truly complex assembly method was elucidated:

- the presence, the location, and the direction of insertion of hidden rivets were determined;
- the hidden lamellar plate shape was established and a novel arrangement discovered;
- the inner structure, resulting from the peculiar manufacturing process, was analysed and the assembly of *tehen*, *tsuke mabizashi*, and *hachi* was identified.

The present results show that the proposed investigation technique, using neutron imaging, allowed us revealing unexpected features with respect to the current literature reports. This opens new interesting perspectives and further work will be needed to gain a more thorough understanding of the ancient art of Japanese armour making. In particular, more samples need to be analysed to extend our knowledge to the wide variety of *kabuto* types, as well as of other armour components.

The success of the experiment was largely obtained through a close collaboration between scientists and museum curators. I strongly believe that this is the key to further progress in this kind of studies.

5.3 European blades

Introduction

The study of historical technology allows revealing methodological process that leads to the conception, development, and evolution of a specific artefact, trying to establish the relationship existing among people that implemented it, as well as the socio-economical context that characterized the circumstances of its production.

By the year 1300, after nearly four thousand years of continuous development, the sword in Europe reached its apogee as an instrument of war. The evolution of the sword and the dagger throughout the Renaissance period presents a fascinating and complex picture. Long-cherished forms were retained side by side with forms which changed from year to year, making exact chronologies sometimes difficult to establish. Blades, hilts and other features changed their form in response to change in body armour, new military tactics or simply the dictates of fashion.

Many sword types flourished from the mid 15th century when the sword, and in particular the rapier, became an accepted part of civilian dress. One of the most remarkable things about the evolution of the rapier was its swiftness, and the explanation for this probably lies in the fact that from the late 15th century onwards the sword become more and more important as costume accessories and *ipso facto* subject to the vagaries of fashion.

This is not to imply that a the civilian rapier become a mere ornamental bauble. Its development began at a time period when the need for a lighter and faster sword became mandatory thanks to the introduction of firearm use in warfare. Rather, the 16th century marked a parting of the ways between those swords and rapiers suitable for use on the battlefield and those intended for civilian war. Moreover, the sword served the knightly class not only in war and ceremony, but also in competitive sport.

The 17th century was a most important one in the evolution of the sword in Europe, from the 1603s the fashion for rapier and dagger play in fencing had considerably declined. A decade later the small swords, in effect a light rapier, was introduced. Yet throughout the period the sword remained an essential implement of war and was carried as an additional ornament with civilian costume with the wealthier classes. The small sword rapidly become the most commonly worn sword in Europe and in some countries continued its career into the 19th century.

In the 19th century of course the role of the sword on the field of battle was largely superseded by long-range tactics which relied on artillery and firearms. By the 1820s swords had been more or less abandoned as adjuncts to civilian dress, although they were retained for formal court ceremonies [Coe *et al.* 2012].

In this ongoing work, I focused on the technology to produce sword blades in Europe during a period ranging from the Late Renaissance to the Early Modern Age (about 16th to 18th centuries), comparing metallographic and neutron imaging data.

Coeval documentation regarding the manufacturing and commerce of sword blades includes references revealing how blades were valued depending on their place of manufacture, with Toledo blades scoring on top, and the other ones priced down to three times less. The present study was undertaken with the aim to quantitatively determine how much this huge price difference was related to effective quality variation, and to determine differences in actual manufacturing technology among different European sword blades. To this aim, two rapier blade fragments from the 17th and 18th century have been investigated (Fig. 5.24). This study, which should be considered preliminary, took advantage of two peculiar samples, which were not considered precious and therefore were expendable. Thus, in this particular case it was also possible to investigate the samples through standard metallography [Gener 2009] and then by means of the non-invasive technique using white beam and energy-selective neutron imaging thus benefitting of a direct comparison between the two techniques.

The samples

The two analyzed European sword blades are attributed to a period ranging from the 17th to the 18th centuries.

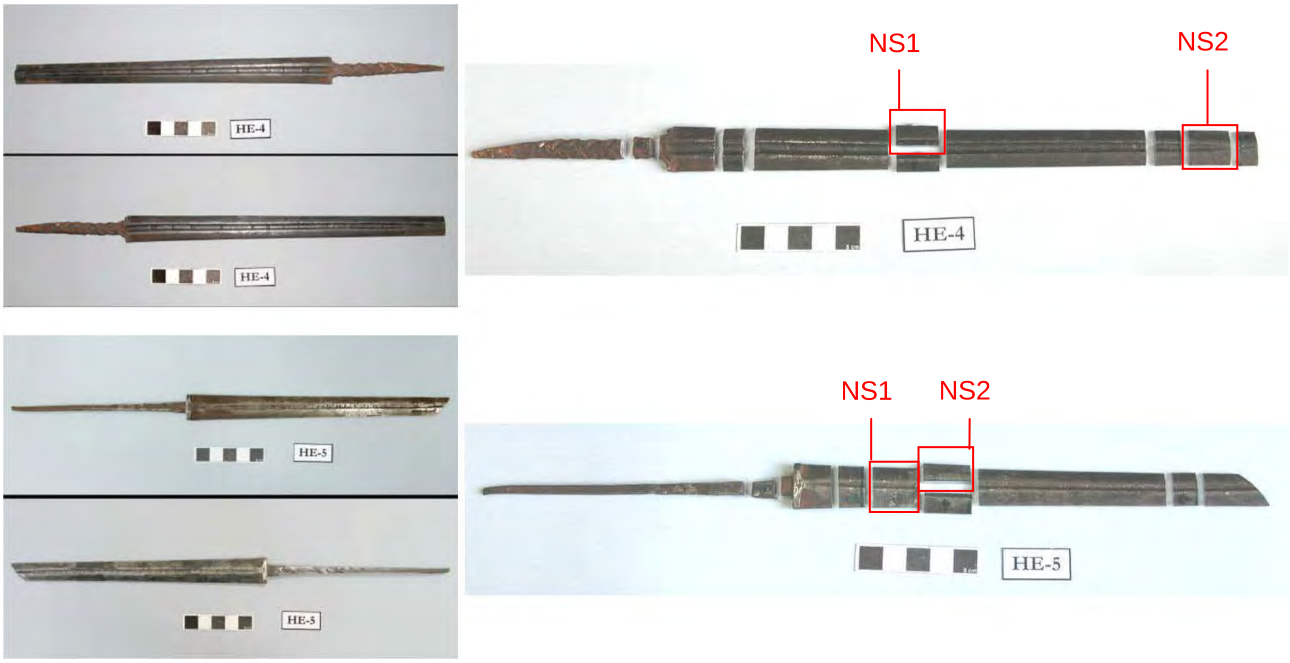

Figure 5.24: On the left, the integer sword blades are shown on their both sides. On the right image, the red frames map the original position of the analyzed cross section.

The first blade (labelled HE-4) is marked as being made in Solingen (actual Germany), while the second one (labelled HE-5), though subject to some debate, is marked as being made in Toledo (Fig. 5.24). It should honestly be pointed out that reasonable doubts could be raised about the second one's origin and that this blade too could be probably attributed to the Solingen production.

Period documents attested that the "old" Toledo masters (16th and 17th century) made their best sword blades by means of forge-welding two strips of steel sandwiching a third strip of wrought iron, that formed the core. The composite block was forged and shaped into a blade. Finally the blade was heated and quenched only in the upper 80% of its length, while the remaining 20% was simply tempered. The purposefully composite assembly and the obtained microstructure found their explanation into the need of containing the cost related to the purchase of steel, the typology of rapier blades, the kind of fighting techniques adopted at that time, the need of avoiding fragile fractures, and the easy fitting of the mounting [Gener 2009].

In the present work, the samples used for analysis were complete and half cross-sections that were cut in different points of the longitudinal direction. The purpose of this study was to observe the variations in construction and microstructure along the blade, testing advantages and limits of neutron imaging techniques, through validation based on previous metallographic investigation [Gener 2009].

Experimental set-up

For the present investigation conducted on ICON beamline at PSI, neutron white beam and energy-selective neutron imaging techniques were applied to characterize the inner volume of the sword blades.

Preliminarily, white beam neutron tomography was carried out to provide 3D information about the structure inside the sample (Tab. 5.4, 2nd column).
Further, in order to obtain information about the composition and material distribution, an energy-selective neutron imaging analysis (Tab. 5.4, 3rd column) of these samples was carried out too. The swords were analyzed using neutron wavelengths at values immediately below and above the 110 ferrite Bragg edge at 4.05Å [Lehmann *et al.* 2011]. These values were optimized basing on the wavelength resolution of the monochromator and the neutron imaging analysis preliminarily conducted on Japanese swords fragments, presented in the dedicated section 5.2.1. The combination of the mechanical velocity selector with the TESI device was involved in performing energy-selective imaging investigations in order to reach the highest possible wavelength resolution power [Lehmann *et al.* 2009, Santisteban *et al.* 2001].
In Table 5.4 the different experimental configurations and instrument set-up for the measured samples are summarized.

Imaging Method:	**White beam tomography**	**Radiographic energy scan**
Neutron Wavelength:	polychromatic	MVS + TESI: 3.9Å / 4.2Å
L/D:	343	350
Scintillator:	^{6}LiF/ZnS (1:2), 100 µm	
Camera:	Andor DW434- BV 1024x1024 16 bit-	
Field of View:	50X50 mm	
Pixel size:	60 µm	
Exposure Time:	15 s	200 s
Rotating Angle:	0°-360°	na
Projections:	376	na

Table 5.4: The different instrumental set-up employed for measurements of the four blade fragments.

Results

White beam tomography

In the fragment **NS1** of Solingen blade **HE4**, the reconstructed volume of the two cross sections, evidences a very homogeneous body (Fig. 5.25, left side). As a matter of fact, the metallographic study of fragment HE4-3, the twin half of sample NS1 and longitudinally cut along the central channel, confirmed a very homogeneous microstructure. The inclusions appear elongated in the direction of the longitudinal axis of the blade, showing the direction in which the original metallic block was forged, and they are distributed in layers, which can be due either to the construction of the core using various fragments of steel welded together or to the consolidation processes that were part of the production of steel (Fig. 5.25-*a*).

Moreover, along the two cutting edges, the presence of martensitic microstructure was revealed by the detection of a bright superficial area in neutron tomographies and confirmed by standard analysis where tempered martensite was observed (Fig. 5.25).
In the cross sections taken before and after the fragment **NS2**, the metallographic results were again coherent with neutron tomographic investigation (Fig. 5.25, left side). At this point it can be concluded that the blade is also composed of a single type of material, a heat-treated steel associated to tempered martensite microstructure (Fig. 5.25, *b* and *c*).

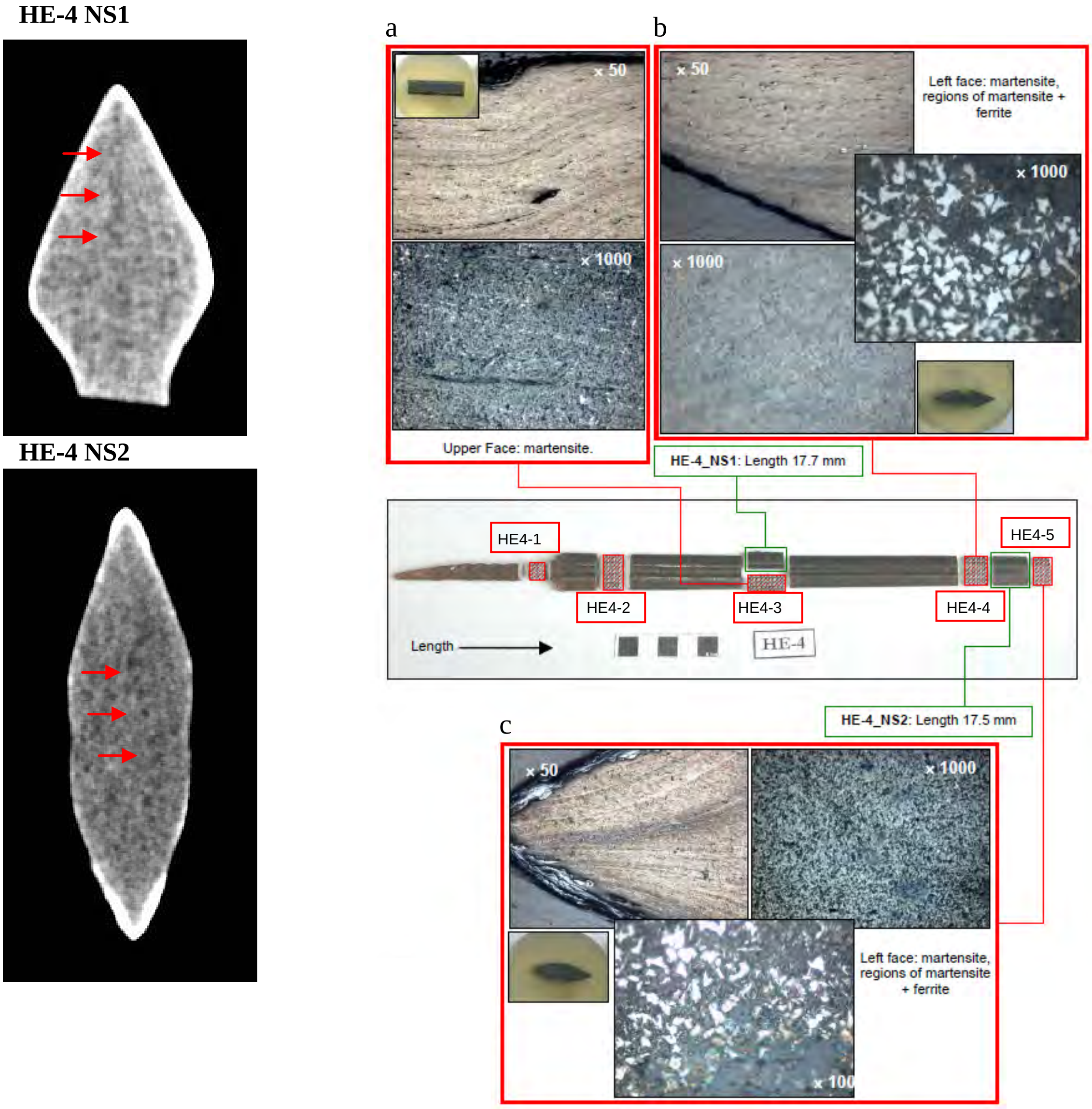

Figure 5.25: On the left side, selected slices from the reconstructed volume of the HE-4 fragments are shown. In sample NS1, the red arrows point out the mark of a welding, while in sample NS2 the distribution of slag inclusions. On the right side, the central image maps the original location of the cut fragments; the cross sections analyzed by means of metallography are framed in red, and the samples analyzed through neutron imaging are reported in green squares. The metallographies are shown. The windows correspond to overviews of the samples (*a*) HE4-3 Detail of the area around a mark (a letter, hot-punched inside the central groove -or "fuller"- of the blade), showing the layered structure of the slag and how it conforms to the deformation of the mark (×50) with detail of the microstructure (×1000) (*b*) HE4-4 Detail of the edge, showing the weld (×50) with detail of the microstructure (×1000) (*c*) HE4-5 Detail of the edge, showing the weld (×50) with detail of the microstructure (×1000).

The fragment **NS1**, pertaining to the sword blade **HE-5**, featured a composite construction instead, already visible in the white beam neutron tomographic reconstruction (Fig. 5.26, left side). These evidences have been confirmed by the metallographic investigation [Gener 2009].

The sample HE5-2, cut closer to the tang with respect to the fragment NS1 and analyzed through metallography, features the same construction. However, at this point the external layer has been ground off, at the edges of the blade, to the point of exposing the internal core in one of them. In this sample, the external strips feature ferrite, and the internal core shows a pearlite and ferrite microstructure corresponding to an approximate proportion of carbon around 0.5%, with the pearlite also partially spheroidised (Fig. 5.26-*a*) [Gener 2009].

Sample **NS2** is also from a longitudinal cut done along the central channel. At the end of the sample closer to the tang, two wedges of iron are visible, marking the end of the iron wrapping, which only reaches this point. Similar features can be observed and confirmed by the metallographic analysis conducted on the twin cross section HE5-3 (Fig. 5.26-*b*).

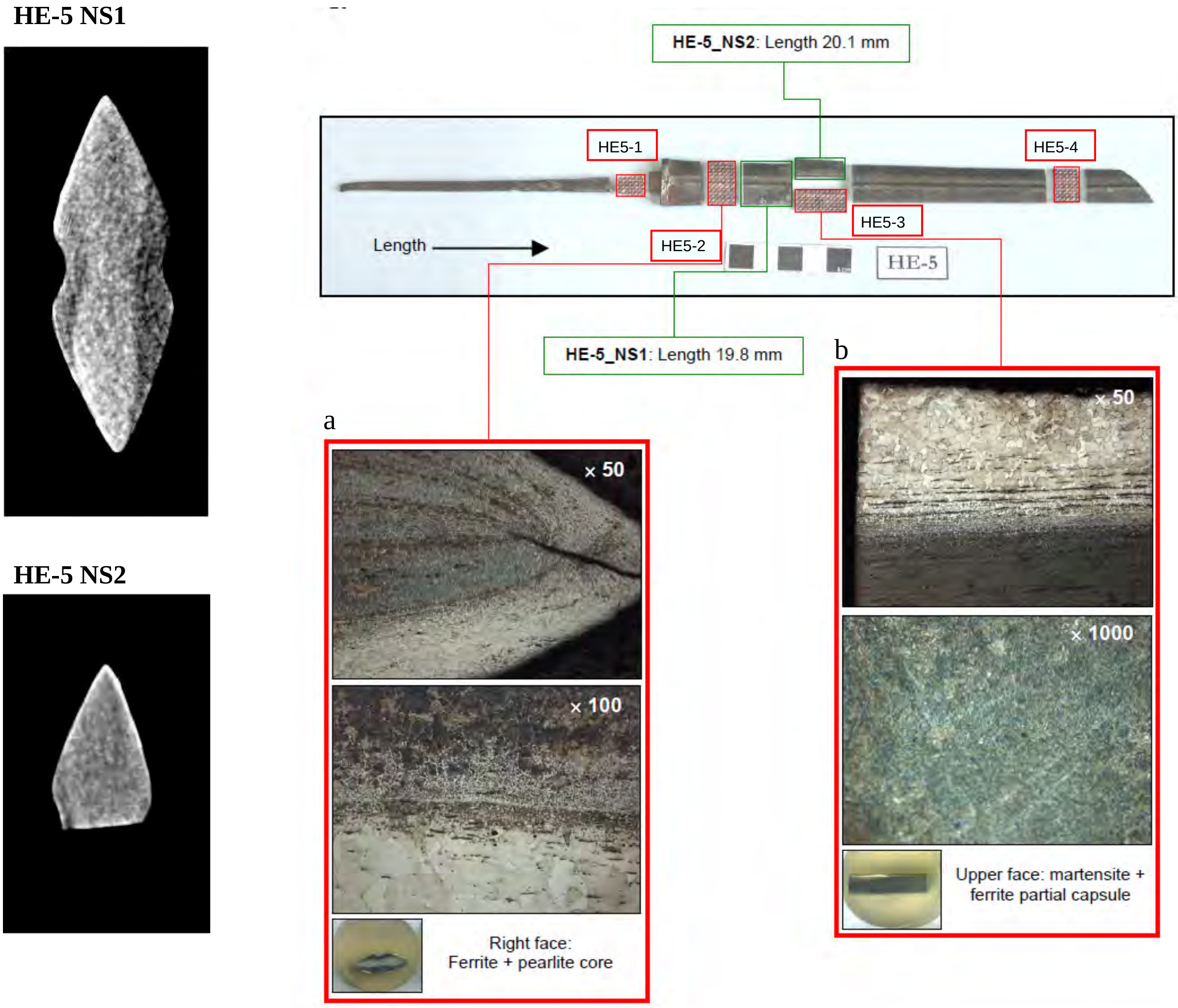

Figure 5.26: The inner composite volume of the HE-5 fragments is visible from the tomographic slices. The stretching of the dynamic range allows to enhance the contrast and to discriminate between iron (dark) and steel (light). On the right side, the original location of the cut fragments is documented by the upper image; the cross sections analyzed by means of metallography are framed in red, and the samples analyzed through neutron imaging are reported in green squares. The respective metallographies are shown in the bottom. The windows correspond to overviews of the samples (*a*) HE5-2 Detail of the edge area, showing the crack developed there (×50) with core microstructure, partially spheroidised pearlite (×100) (*b*) HE5-3 Construction detail, showing the weld area between the iron external strip and the core (×50) and microstructure of the steel core, tempered martensite (×1000).

Energy-selective imaging

In the second part of the experiment, energy-selective neutron imaging analyses were performed. For test and calibration purpose, several Japanese sword fragments, featuring a composite structure, have been preliminarily analysed to map the ferrite contrast enhancement for the selection of two suitable neutron wavelengths.
In the case of the energy radiography scan, two independent acquisitions have been carried out at the two different neutron wavelengths, namely 3.9 Å and 4.2 Å by taking advance from the combined use of the MVS and TESI device.
Owing to the symmetry of the sample and the homogeneity in their inner structure, only radiographies were acquired (Fig. 5.27).

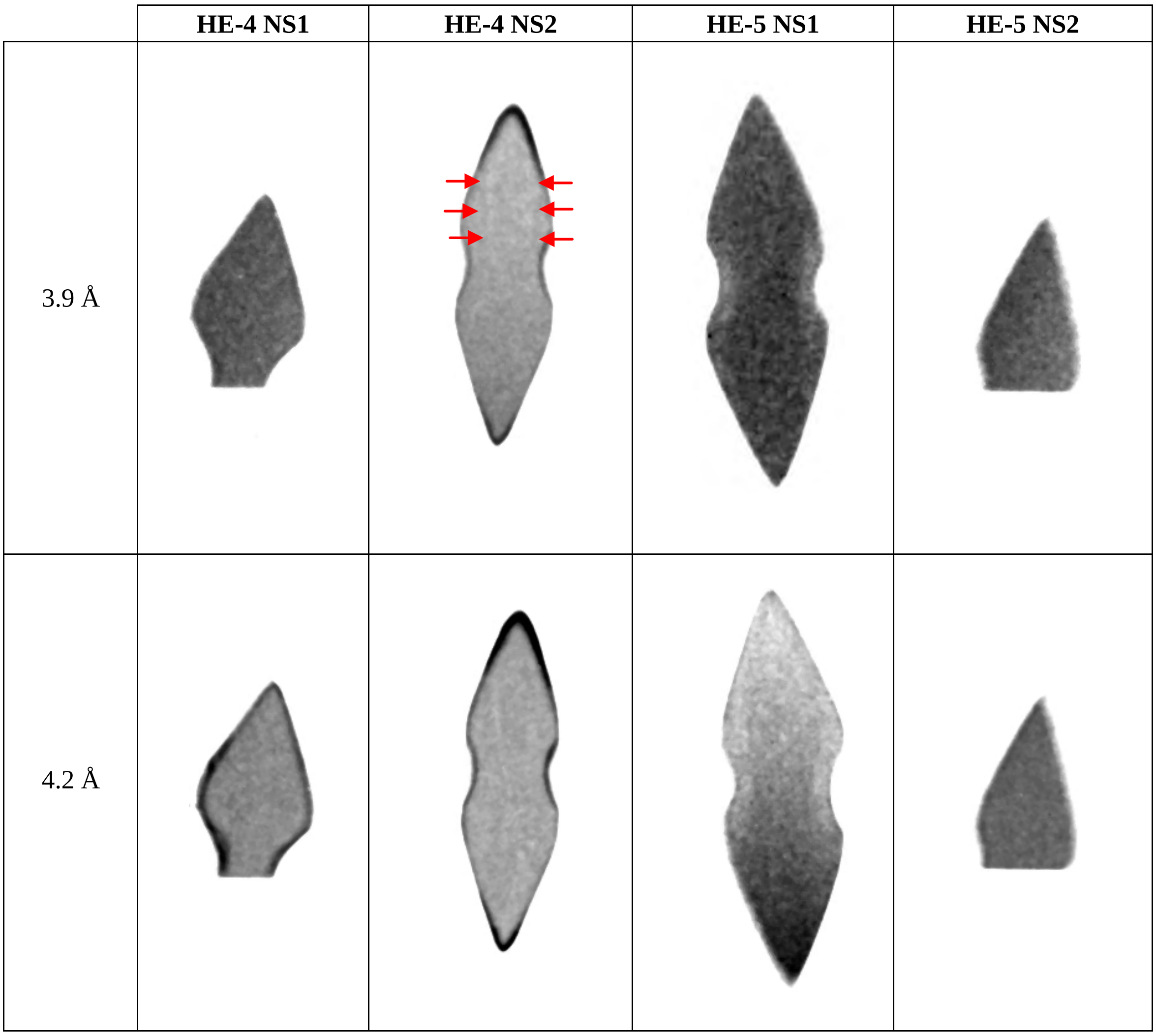

Figure 5.27: Monochromatic neutron radiographies taken at 3.9 Å and 4.2 Å are reported for each fragment that was labelled at the top of each image. In the case of sample HE-4 NS2, the red arrows indicate the weld of pieces of metal.

The radiography of the HE 4 cross sections confirmed the presence of a homogeneous body. In particular, sample NS2 (Fig. 5.27) evidenced a core that was probably made joining various bits of metal in order to have a piece of suitable steel big enough for the task [Gener 2009].
The presence of a dark region, outlining both fragments of the HE-4 sword blade can be related to the presence of martensitic structure, well detected and most extended with respect to the HE-5 samples. It cannot be excluded that this effect can also be related to the

presence of corrosion products on the surface of the sample and slightly diffusing inside the body.
In the fragment HE5, a variation in contrast has been recognized, as evidenced in sample NS1 of Figure 5.27. Crossing the 110 ferrite Bragg-edge (i.e. changing wavelength), the inversion of grey tones is visible and the obtained contrast enhancement allowed discerning between iron (low carbon content) and steel (higher carbon content). On the contrary, fragment HE-5 NS2 did not evidence any variation in composition of the used steel.
Gray gradient in the image (i.e. Fig. 5.27 sample HE-5 NS1 at 4.2 Å**)** can be attributed to the shift in the incoming neutron wavelength distribution over the acquisition window. Due to the small field of view, the limited side of the analyzed sample and the required neutron energy resolution, the wavelength shift can be ignored [Peetermans *et al.* 2013].

Small blurring in the contour (i.e. sample HE-5 NS2) are likely caused by slight misalignment in the positioning of the sample with respect to the neutron beam axis.
However, the result obtained from the energy-selective imaging study, gave coherent data with respect to the metallographic analysis. I would stress that the composite structure of European Renaissance blade, described in historical documents and detected through standard destructive analysis, was recognized using a non-destructive method. Thanks to the energy-selective radiography, the volume of samples was qualitatively and quantitatively characterized, allowing to detect the forge-welding strips of wrought iron sandwiching a third strip of steel, that formed the core.

Conclusion

In the present work, four fragments of two European rapier blades ranging from 17th to 18th century have been studied. Even though an invasive approach has been already applied for this set of samples, a non-invasive technique have been deliberately chosen to analyse all the samples, in order to show the validity and detailed level of information that can be reached by exploiting the proposed tomographic method and directly comparing it with metallographic results.
White beam and energy-selective neutron imaging have been used to investigate bulk metal samples in a non-invasive way: the contrast enhancement induced by the selection of an appropriate neutron wavelength has been exploited to increase the image contrast for different component phases.
White beam tomographies allowed identifying peculiar characteristics related to the forging methods as well as the thermal and mechanical treatments used by European sword-smiths:

- slag inclusions and cracks were mapped and localized;
- inner structure, resulting from the particular manufacturing process, were analysed all over the samples;
- the quenched steel area was evidenced.

Taking advantage of the metallographic studies, the present measurements clearly demonstrate that energy-selective neutron radiography allows characterizing the inner structure and composition of metal artefacts, non-destructively, obtaining results that are qualitatively and quantitatively confirmed by the classical well established complementary technique. The correspondence between the two methods, the non-invasive character and the possibility to obtain 3-D reconstruction, candidate neutron imaging as an important and quantitatively reliable technique for metal characterization.

5.4 *Kris*, weapon of the Malay world

Introduction

The *kris* (or *keris*) is the distinctive weapon of Malaysia and Indonesia. The *kris* is found in a variety of forms but, typically, it is an elongated dagger or short sword of slender proportions with a blade of rough damascened texture sharpened on both edges [Frey 2010]. The origin of the *kris* has long been a matter of dispute among arms historians. One early theory affirms that it was evolved from the *ko*, a Chinese halberd or pronged spear [Coe *et al.* 2012]. However, other theses on the origin of the *kris* exist. For example, it may be developed from the shape of the tip of the sting-ray. In early times fishermen used the poisonous tip of a sting-ray's tail as a weapon (spear-point or dagger), or to manufacture poison. It was called *ikan pari.* An alternative theory asserts that *kris* may have evolved from the *keris majapahit*[5.1], a small *kris* forged from a piece of iron. The question arises if these were used as weapons, or only as luck-bringing amulets and as protectors of field crops. Finally, according to the mythological tradition, the *kris* was introduced in Java by the hero *Pamij* [van Zonneveld 2002].

The shape and the size of *kris* changes with some variety, depending on the geographical area and on the aim for which the blade were designed. The Javanese *kris* is the most typical, usually from twelve to twenty inches long. Two unique features make the *kris* totally different from all other weapons: the sudden change in size of the blade just below the base and the fact that in all, but the earliest one-piece (blade-handle) models, the blade is not firmly connected to the handle.

The most valuable part of the *kris* is the blade (*mata kris*). For scholars the size and the shape of the blade are the only basic quality. Blades may be straight (*dopur bener*) or undulate (*dapur luq* or *dapur parung*). The former design represents a state of static rest; the latter, the action personified; both blade forms are representative of the serpent, a cannibalistic deity. All original old-model *kris* were forged with straight-line blades, a design feature adopted from the Indian weapons [Gardner 1936].

Another distinguishing feature of the *kris* that is imparted by the *pande* (sword-smith) is the rough, lacking-finish quality of the blade surface. This feature has been often mistakenly called damascening, but in reality it is a damascening lacks reliefs on the surface, representing the distinctive character of *pamor*. *Pamor* is a special design feature obtained by welding, in very peculiar fashions, metals of different composition to the core of the blade.

In order to create the base material for the blade, the smith assembles a multi-layered block. He starts with a central plate of steel: the core; to each side of this, he applies a bar of iron, which has been hammered and folded several times; then he completes the sandwich with two (sometimes more than two) outer plates of steel, making five (or more) discrete layers; the whole compound, so assembled, is then heated and hammered to weld it into one single metal piece[Coe *et al.*2012]. The number of strips used to forge a *kris* can be as high as twenty. These are welded together by hammering, around each side of the core plate. The smith carefully controls the order and the layering design, thus creating the *pamor* [Bronson 1987]. Not all *kris* are given this complex treatment, but those without it are not considered completely finished.

[5.1] The term *majapahit* stands for the Hindu-Javanese empire in East Java (1292-1522). In particular *keris majapahit* refers to a form of ancient *keris* originated during the *Majapahit* empire [van Zonneveld 2002].

Once the different strips are homogenized together, into the primitive shape of the blade, the final shaping starts, beginning from the handle and working towards the tip step by step. Holes and channels may be cut to expose metal veins showing different colour properties. At the end, some hand-polishing is used to smooth down the roughest edges, but the blade is never finely polished. In order to emphasize the pattern due to the different reaction of the several parts to an oxidizing environment, the blade is soaked for several days in a bath of boiling water containing a mixture of sulphur, rice and salt. Finally the blade is rubbed over with the acid juice of lime [Coe *et al.* 2012]. The blade is finally washed and oiled, ready for being fitted to its chosen and carefully made handle [Bronson 1987].

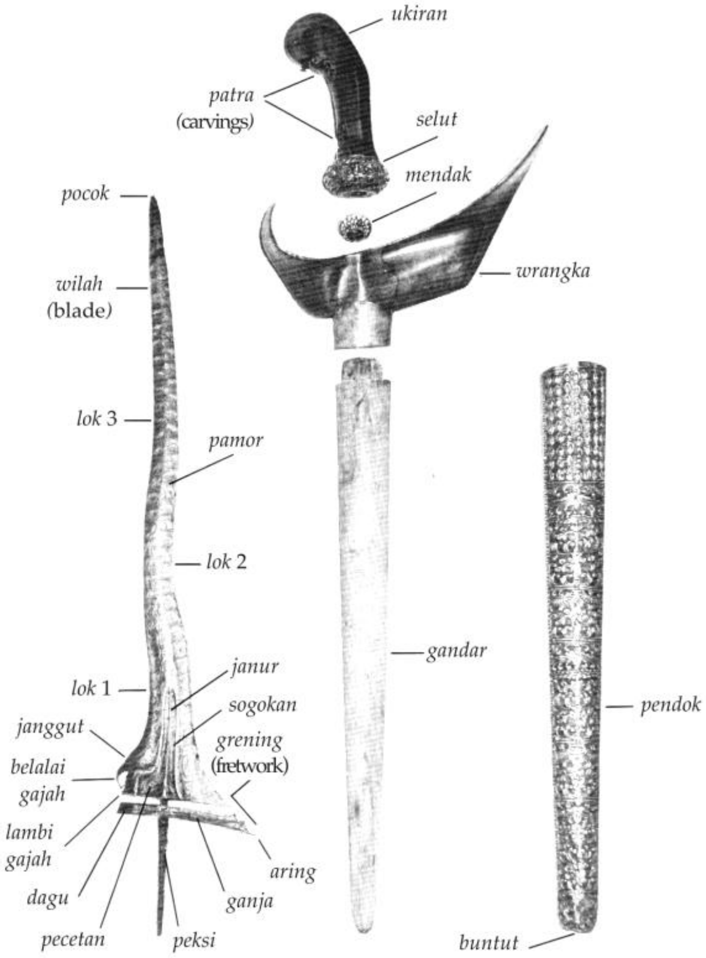

Figure 5.28: The components of a *kris* [Frey 2010].

All good Southeast Asian *kris* are made of two sorts of metal, iron (or steel) and *pamor*[5.2] welded together in intricate patterns that are subsequently brought out on the polished surface of the blade through the use of an etchant. In particular, *pamor*, is by definition the etch-resistant component, traditionally used in the blades, and comprehends an heterogeneous group of metals [Bronson 1987].

The most beautiful patterns are obtained by using normal iron in combination with iron containing nickel. Once coloured with acid containing arsenic, the normal iron turns black while the nickel-holding iron remains silver-coloured [van Zonneveld 2002].

[5.2] The word *pamor* is used indiscriminately to indicate both the mixture of alloys and the pattern obtained from the metal alloy decoration on the blade.

Before the middle 19th century, most part of *pamor* (and the only considered the "true" ones) came from the Indonesian island of Célebes, where large deposits of iron-nickel ore exist, of a type that could be smelted in simple furnaces. Anyway the most desirable kind of *pamor*, in the eyes of modern Javanese *kris* specialists, is the metal derived from a meteorite that in the 18th century was found near the ancient temple site of Prambanan, in central Java. Small amounts of this meteoric alloy were later used by *kris*-makers, mainly in the years around 1840-1860. Another kind of *pamor*, used more recently, is almost entirely composed by pure nickel foils, made by the Krupp company and introduced in Indonesia in late 19th century. A further more recent kind of *pamor* includes an European iron-nickel alloy, obtained from bicycle frames and ship propellers, that reached the Southeast Asia in the second half of 19th century. Miscellaneous class of scrap iron and steel were also used for making cheap *kris* during 19th and 20th century [Bronson 1987].
Beside, instead of iron combined with nickel-containing iron, some *kris*-makers simply used various pieces of iron, of different quality and hardness. After applying the acid treatment, the colour does not change, but the *pamor* pattern appears in relief [van Zonneveld 2002].

Concerning the morphology of a kris, it is related to both ritual and technical reasons. The deadliness of a *kris* in combat increases with the number of waves it possesses. A wavy blade makes a larger wound and can penetrate more deadly between bones. The number of turns in a blade along the longitudinal axis, from the base to its tip, is always odd ranging from three to thirteen. However, some exist showing as many as twenty-nine turns. The cross section of the blade may be elliptical, diamond-like, almost flat, or shaped with swallowed-stepped profile. Sometimes a narrow channel runs the length of the blade on both sides. The channel can be sometimes present on one side only and made by two grooves close each other, their distance is an index of the skill of the smith in chiselling tiny details in metals; the closer they are, the more skilled the smith is.
The raised strongly asymmetric collar guard (*ganja*) always forms the basement of the blade. In the earliest models, the *ganja* was forged out from the main body of the blade (*ganja menumpang*); in later models, the *ganja* is a separate piece. The shank (*paksi*) is a pin projecting through the *ganja* in line with the axis of the blade to be fitted into the handle.
The slant of *ganja* is deliberately proportional to the blade length and features one end sharp-pointed (*aring*), with the other one relatively blunt (*dagu*). The *aring* side of the *ganja* features, on its upper edge, a series of multiple serrations (*janggut*); the *dagu* side is instead shaped to show a stylized elephant including an upward and inward curved spike (*belalaigaja*, or elephant's trunk) and a short spike above it, called *lambaigaja* or elephant's tusk. This feature has a mystic significance. Between these spikes there may be a few tooth-like projections corresponding to the *janggut* on the opposite edge. In many models however, the spikes are reduced to symbolic protuberances or they may even be entirely absent (Fig. 5.28).

The handle (grip or hilt) offers a category of differentiation among *kris*. This important part of the weapon is called *ulu*. Different handles were designed for different classes of people and there may have been connections between handle design and geographical area. The importance of the *kris* handle is reflected even today when it is used to show the social status of the owner. As the social status of Javanese people alters, so does his *kris*-handle design. The handle is often hand-carved in meticulous details and made from various materials: from precious rare types of wood, to gold, or ivory. They resemble, in the older *kris*, human or animal figure, or Hindu gods and deities, but later, under the Islamic influence, it was reduced to geometrical shapes.

Kris were treated with much care and when a really old weapon was being handled it was raised up to the forehead as a mark of respect. They were also feared, for it was thought that they had magical power. Many Malays believed that a *kris* should always be pointed at nobody, even when sheathed, and it should always be kept with the point either down or up so that the risk of accidental magical harm to bystanders in line with the point was reduced [Coe *et al.* 2012].

The samples

In order to investigate the composite structure of this mystic weapon and the different types of *pamor* effectively used, four *kris* have been selected for a neutron imaging study. The samples have been provided by the Museo di Storia Naturale, Sezione di Etnologia e Antropologia of Università di Firenze. The *kris* were gathered by the Italian explorer Giovanni Battista Cerruti, visiting Indonesia at the end of the 19th century, and were donated to the Museum Collection before year 1913. Since they were probably made only a few years earlier, they can be made of any type of *pamor* previously described.
The samples are catalogued in the Museum diary as:

- K1: Inv 5142 - *kris* of *majapahit picit*[5.3] shape, made in Ambon Island or Ternate Island;
- K2: Inv 5143 - *kris* of early *majapahit* shape, made in Semarang (Java Island);
- K3: Inv. 5144 - *kris* of early *majapahit* shape, made in Semarang;
- K4: Inv 5145 - *kris* of *majapahit picit* shape, made in Ambon Island.

The *kris* have been intentionally selected since two of them are declared to come from Java, where the Prambanan meteorite was found and used, while the other two come from islands very closed to Célebes (a site rich in iron-nickel ore).

Pictures of the samples are shown in Figures 5.29 and their likely provenance in the map is reported in Figure 5.30.

[5.3] *Picit* indicates the oldest (*majapahit*) type of *kris* with an iron figure for a hilt and thumb-like marks on the blade [Stevens 2004]. Here the words *majapahit* and *picit* probably refer exclusively to the stylistic features of the weapon and cannot be strictly related to a date of production.

5142 5143 5144 5145

Figure 5.29: The *kris*, identified by their own inventory number, are shown.

Figure 5.30: A map of Indonesia is reported: the orange rhombus indicates Semarang with the yellow one pointing the site of Prambanan; the violet rhombus corresponds to the Ternate island, while the Ambor island is highlighted in red. In green it is indicated the area of Célebes while in blue the iron-nickel mines.

Experimental set-up

In order to characterize the composite structure of the four *kris*, a neutron imaging study was performed on CONRAD II at HZB.

Firstly a white beam tomography was carried out to investigate the morphology of the samples, leading to the identification of the metal layers composing the weapons, the quality of the making process and the condition of conservation.

This analysis was followed by a radiographic energy scan of the samples to select the proper neutron wavelength values for enhancing the material-contrast at the Bragg-edge correspondence during the subsequent energy-selective analysis.
According to the nickel content, iron-nickel alloys are mainly constituted by kamacite (metallic iron *bcc* structure with up to 7.5% nickel in solid solution) and taenite (metallic iron, *fcc* structure with nickel ranging from 25 to 70%). Moreover, the lattice parameter of the two phases changes according to the nickel content. In order to detect the presence of iron, steel, and nickel-iron phases, correlated to the use of different types of *pamor,* an energy-selective tomography was done.

Performing the white beam tomography and the energy-selective tomography, the samples have been mounted together to reduce the total measuring time. A special-purpose frame was made to fix each *kris* in a staggered position with respect to the others; adopting such a configuration the incoming neutron beam intercepts the sample one at time, avoiding the risk of too much attenuation (Appendix B - Fig. B2). Also for the radiographic energy scan a frame has been constructed to fix the *kris* all together. (Appendix B - Fig. B1).

The instrumental set-up for all the measurements is reported in the following table.

Imaging Method:	**White beam tomography**	**Radiographic energy scan**	**Energy-selective tomography**
Neutron wavelength:	polychromatic	from 2.0 Å-4.5 Å with a step of 0.02 Å	3.82 Å and 4.15 Å
L/D:	500	333	
Scintillator	^{6}LiF 400 µm		
Camera	andor DW436N-BV CCD3325 2048x2048 16 bit		
Field of View:	200x200 mm		
Object-detector-D:	145 mm max.	10 mm	
Pixel size:	109 µm		
Exposure time:	50 s	130 s	
Projections:	400		500
Rotating Angle:	0°-360°		0°-360°

Table 5.5: The different instrumental set-up employed for the measurements.

Results

White beam tomography

- K1: Inv 5142

The blade K1 appears to be characterized by a homogenously structured body (Fig. 5.31-*a*); however, stretching the dynamic range of the tomographic reconstruction image, very thin wavy metal layers turn visible in the considered volume (Figg. 5.32-*b* and *c*). A small crack, of 0.2 mm in thickness, can be seen at the position of the second radial section (starting from the hilt) and penetrating for 10 mm into the blade (Fig. 5.31-*b*). Few small slag inclusions are slightly visible as dark spherical spots diffused in the central portion of the *kris* (Fig. 5.31-*b*, third and fourth cross sections).

Also the *ganja*, the raised collar guard of the *kris*, reveals a composite structure constituted by layers of different type of metal, probably composing the original *pamor* subsequently worked by folding and hammering to create the typical pattern at the *kris* surface (Fig. 5.32-*a*). According to literature the *ganja* was provided by a piece cut-off from the bottom of the *pamor* while working. Referring to Frey [E. Frey 2010], the smith prepares a thick rectangle (strip) of iron which consists of three layers of thin *pamor* sandwiched with three layers of soft iron. While red-hot, the strip is worked with a hammer so all layers are thoroughly combined together. In the working, the strip becomes longer and thinner. The strip is then folded to provide a long U-shaped piece with the *pamor* side outside. The fold at bottom of the U is cut-off, providing material for the *ganja*. Because it was part of the blade material, the *ganja* will have the same *pamor* design as the blade itself. In this case, 6 layers about 1.7 mm thick can be identified basing on the different contrast and can be related to the welding of different types of iron and steel in the *pamor*. Moreover, the *ganja* is a distinct piece, confirming this *kris* as an example of later models.

Regarding the *paksi*, by inserting the blade into the grip, the piece, as prolongation of the blade, appears to be extruded from the main body of the *kris*. The cylindrical shape was probably formed by rolling the metal over itself as suggested by the detection of a crack, 0.8 mm in diameter, crossing the centre of the *paksi* in length (Fig. 5.31-*b*, first cross section).

Analyzing the axial and transversal virtual cuts at the tip position, the sheet appears secured by the bending of this portion (Figg. 5.33-*a* and *b*). This configuration could negatively influence the effectiveness of the penetrating power of the object. However it should be mentioned that *kris* were often used as luck-bringing amulets and as protectors of field crop, rather than weapons. Countless story are found about the supernatural powers of the *keris* [van Zonneveld 2002].

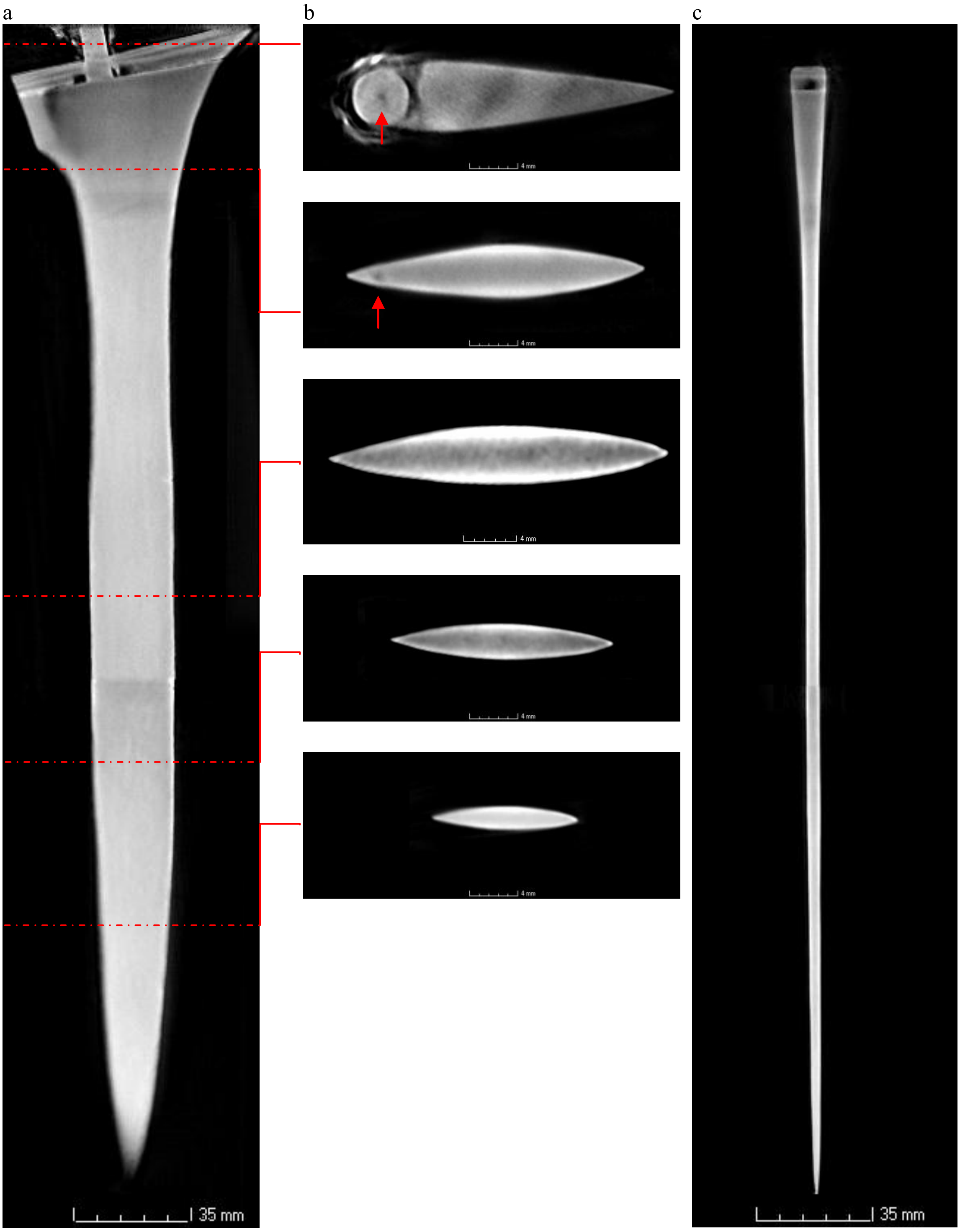

Figure 5.31: Considering the axis placed in the centre of the blade length, images *a* and *c* refer to the cross sections taken along the axial and transversal direction, respectively. Radial cross sections *b* are virtually cut at different high of the *kris* K1. The red arrows highlight the position of inner cracks.

Finally, the bright tone of the material constituting the surface can be related to the production of a patina due to the etching substance applied during the finishing to enhance the typical pattern of the *kris*. The reaction of the metal with the etchant mixture probably generated hydroxide compounds of the metal, also diffusing into the creeks between the *ganja* and the main body of the blade. Indeed, the presence of H, characterized by an high scattering cross section, appears as a bright grey area in transmission.

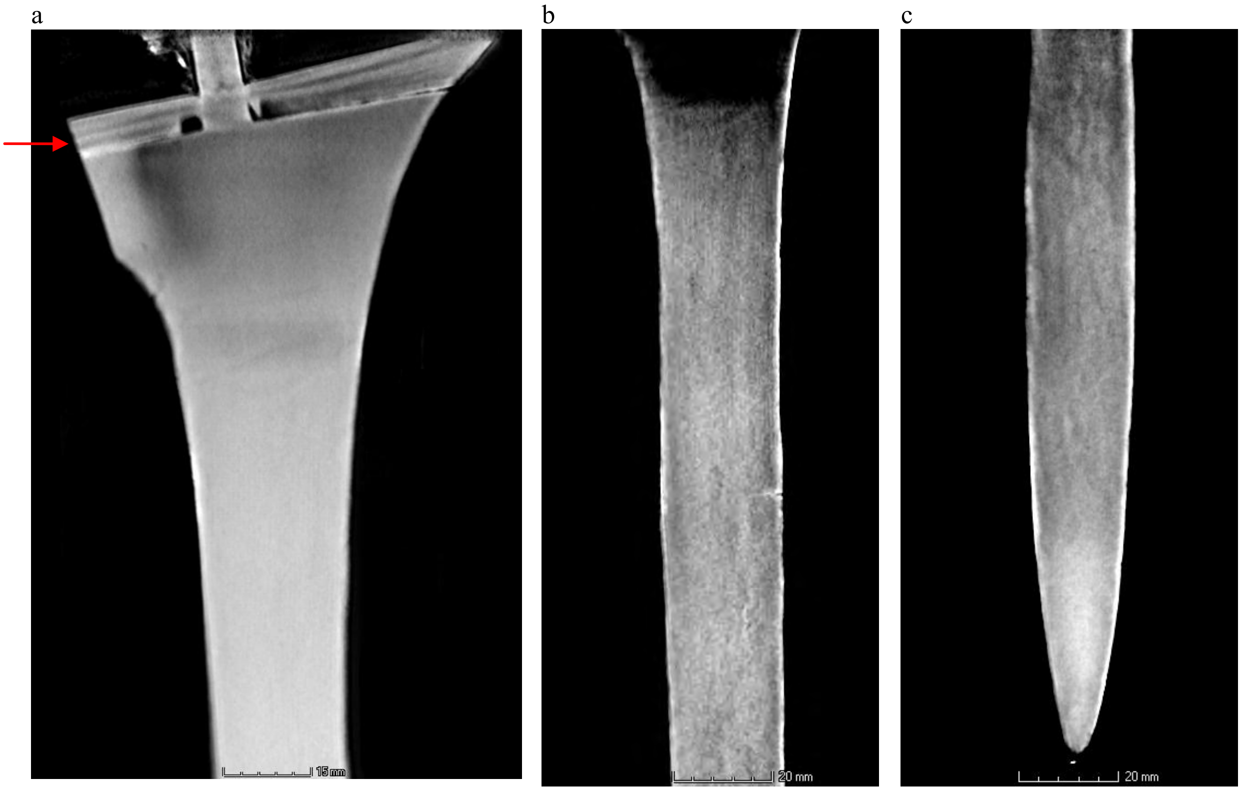

Figure 5.32: Images *a*, *b* and *c* are enlarged axial views cut at different height of *kris* K1. The cross section *a* shows the layered structure of the *ganja* pointed out by the red arrow. Stretching the dynamic range, the composite structure becomes visible inside the sample.

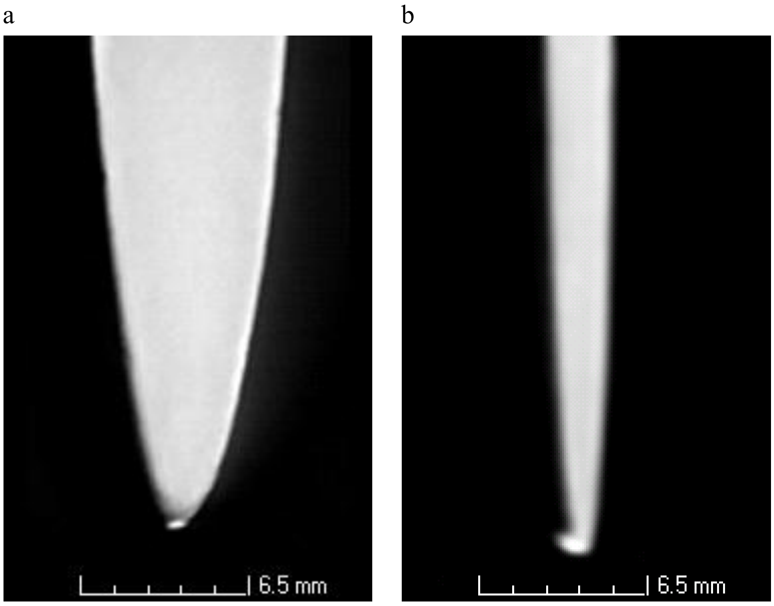

Figure 5.33: Axial *a* and transversal *b* cross sections are enlarged in order to highlight the folding of the metal in the area of the point.

- K2: Inv 5143

The tomographic reconstruction reveals a different making process for *kris* K2 compared with the previous sample. Basing on the morphological features and the difference in contrast, the blade body appears to be composed by a central block of metal wrapped by a multi-layered strap constituted by different types of iron and/or steel (Fig. 5.34-*a*).
As described by E. Frey 2010, the smith inserted thin pieces of steel, or hard-iron, between the two legs of the U-shape strip of metal layers. This hard core will provide a sharp point and hard edges to the *kris*. All is heated and forged again to a single rough blade. However, empty areas 0.3 mm thick are visible at the base of the blade K2 as displacements among metal pieces (Fig. 5.34-*b*, second slice). Contrarily to *kris* K1, in this case the *ganja* is formed by a homogeneous piece of metal.
The *kris* K2 was finally formed into a wavy shape and the surface was further etched creating the bright patina visible on the surface in the reconstructed image. Figure 5.34-*c* evidences the presence of wavy dark lines probably connected to an imperfect soldering of the layers constituting also the core.

Concerning the *paksi,* it appears to be a separated element that was pulled on the tang and anchored by applying a gluing material at the correspondence of its central hole. The bright tone of the substance, attributable to a high attenuation coefficient, suggests the use of an H-based material. The traces can be recognized along the profile of the piercing (Fig. 5.35); the thickness of this connecting layer ranges from 0.1 mm, along the rod, to 0.05 mm, at the contact with the raised collar guard (*ganja*) that usually forms the base of the blade as typical in later models.
Moreover, the *paksi* was shaped in the form of a cylindrical rod obtained by rolling a piece of metal over itself, thus creating a small crack 0.1 mm wide detectable through its centre. This component was inserted, through the funnel-shaped neck of the wooden grip, into a dedicated slot penetrating the wood for around 4.8 cm. The small area of the tang emerging from the main body of the handle was covered by a metal collar. According to low grey tone visible in Figure 5.35-*a*, related to a low neutron attenuation coefficient, the material of the decorative element could be made of a Cu-based alloy. However, not much can be said as no diffraction measurements could be carried out on these samples. Nevertheless, very bright spots are visible inside the collar and on its surface. The bright spots suggest the application of a decorative motif composed by a metal with a high neutron attenuation coefficient as gold or silver; the presence of gold was confirmed by Neutron Activation Analysis (NAA) performed after the imaging study in order to check the activation level of the sample.

The absence of slag inclusions and inner defects suggest a particular care in the manufacturing of this *keris.* This features, associated with the preciousness of the materials, can lead to the assumption that this weapon was probably designed for a high-ranking person.

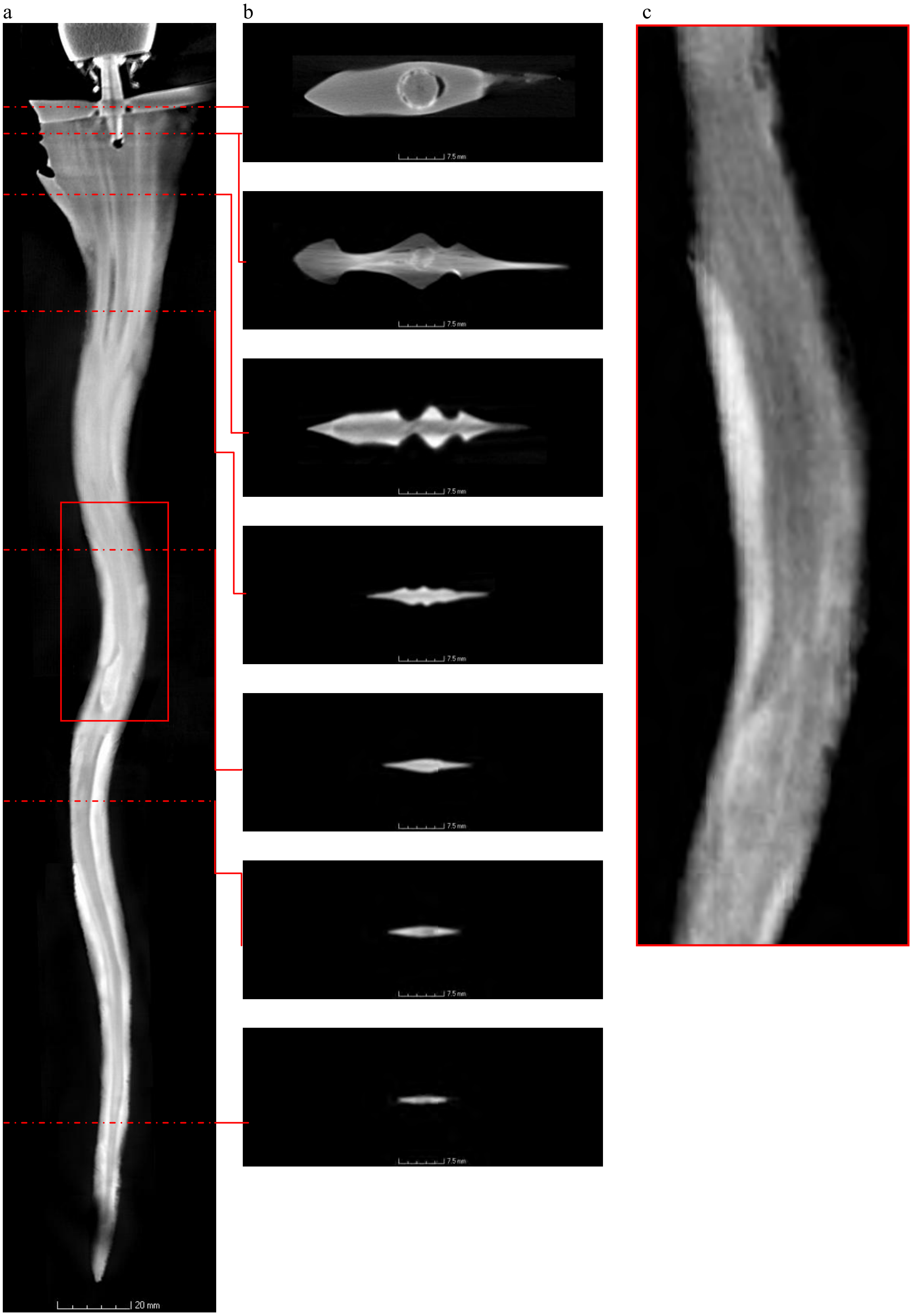

Figure 5.34: The axial view *a* of *kris* K2 is reported on the left. The red lines indicate the height of the shown axial slices *b*. The enlarged axial cross section of the region framed in red is reported in *c*. Here dark lines are present in the metal core, following the curved profile of the blade.

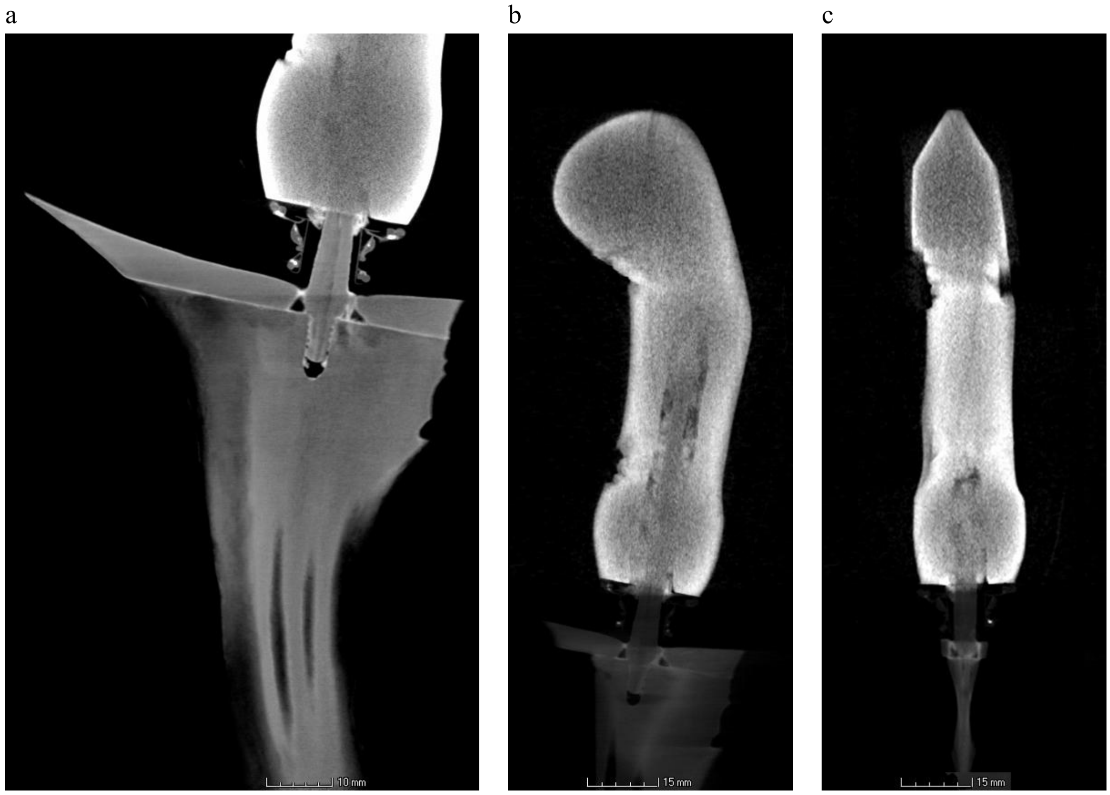

Figure 5.35: The enlarged view of the axial cross section at the base of the blade is shown in figure *a*. Images *b* and *c* are an enlarged axial and transversal views inside the hilt revealing its structure; the ring of the wood and the hole of the slot created to hold the *paksi* are visible.

- K3: Inv. 5144

Although the *kris* K3 appears quite similar in shape to the first sample here discussed, substantial differences emerged from the tomographic analysis.

Here the body is composed by a thin central piece of homogeneous metal welded between two strips of metal (Fig. 5.36). The core, starting from the tang and ending a few centimetres before the tip, doesn't reach the end point as in *kris* K1. Only few slag inclusions were detected in its whole length. The traces of welding among pieces are visible in the form of cracks and empty areas. Starting from the surface at the base of the hand-guard, a small crack diffuses for 1.50 cm inside the blade. At the tip, a dark line seems to outline the area of conjunction between the "jacket" metal plate (Fig. 5.36-*c*).

Contrarily to the other samples, in this *kris,* the *paksy* and the *ganja* were formed and fused to the body as typical in earlier *kris*.

When the blade was finally shaped, the surface was further etched creating the bright patina visible on the surface in the reconstructed images.

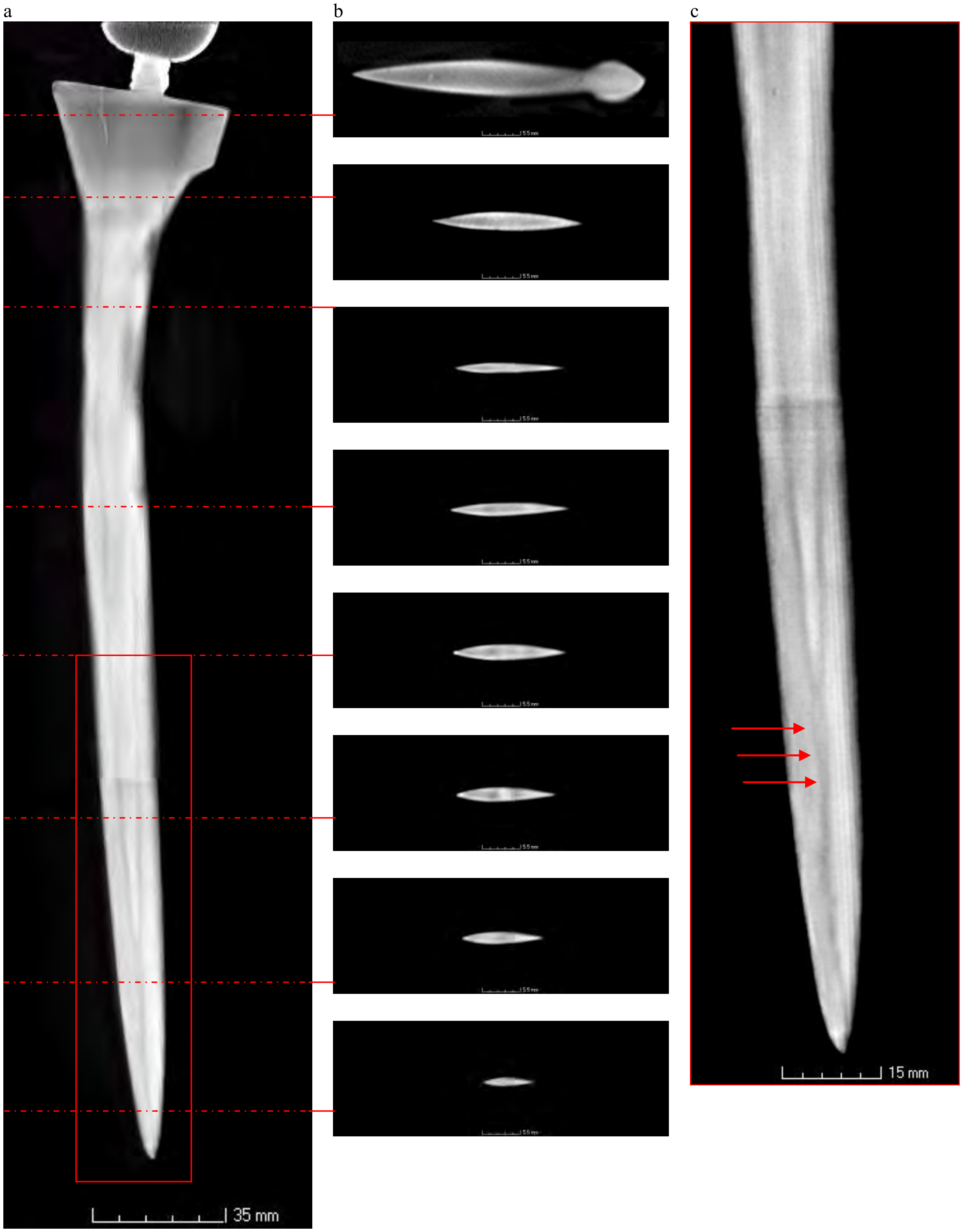

Figure 5.36: On the left, the orthogonal section *a* virtually cuts at the centre of the blade K3. At its side, slices *b*, selected at different heights of the sample, show the inner composite structure of the whole object. On the right, the high spatial-resolution image of the tip *c*, whose location is marked by a red frame in the orthogonal view, evidences the profile of the conjunction among metal layers (red arrows).

- K4: Inv 5145

Thanks to the neutron white beam tomography, the morphological analysis of the whole volume of the *kris* K4 was achieved, allowing to distinguish different composing elements and the assembling method. The whole volume of blade revealed a multi-layered structure quite similar to that detected for *kris* K2. Also in this case a core and a distinctive metal "jacket" can be identified, where the external strips are composed by a multi-layered structure (Fig. 5.37).

The *ganja* appears to be composed by superimposed pieces of metal probably originated from the "jacket" material. Here at least 3 layers can be recognized. The bright area outlining the hole of the hand-guard can be related to the etchant mixture used for the patination or to the application of a H-base gluing material. The *pesky* rises continuously from the core of the blade into the dedicated slot of the grip (Fig. 5.37-*a*).

A small crack, 1 mm wide and 1.5 mm long, is visible at the base, while at the edge few small cracks starting from the surface and penetrating for 20 mm inside the body of the blade follow the profile of the metal layers (Fig. 5.38-*b*). A blade with a wavy shape, such as *kris* K3, was created by working a raw straight multi-layered block. Progressively heating and hammering the starting piece, the final wavy profile was given to the weapon [Frey 2010].

Moreover, inclusions are elongated inside the body, outlining the curvature of the *kris* and denoting a lesser care in manufacturing the weapon. Many of them are present also in the core and oriented along the axis indicating the working direction. Moreover, strongly extended dark lines follow the profile of the core, probably due to an inaccurate welding process. Also, in the *ganja* the packing of the layers appears poorly welded as suggested by the presence of dark regions in between the metal sheets (Fig. 5.38-*c*).

At the correspondence of the tip (Fig. 5.38-*d*), the folding of the external layer is highlighted, where the brighter layer is twisted around the wavy profile of the blade, enclosing the core and forming the tip.

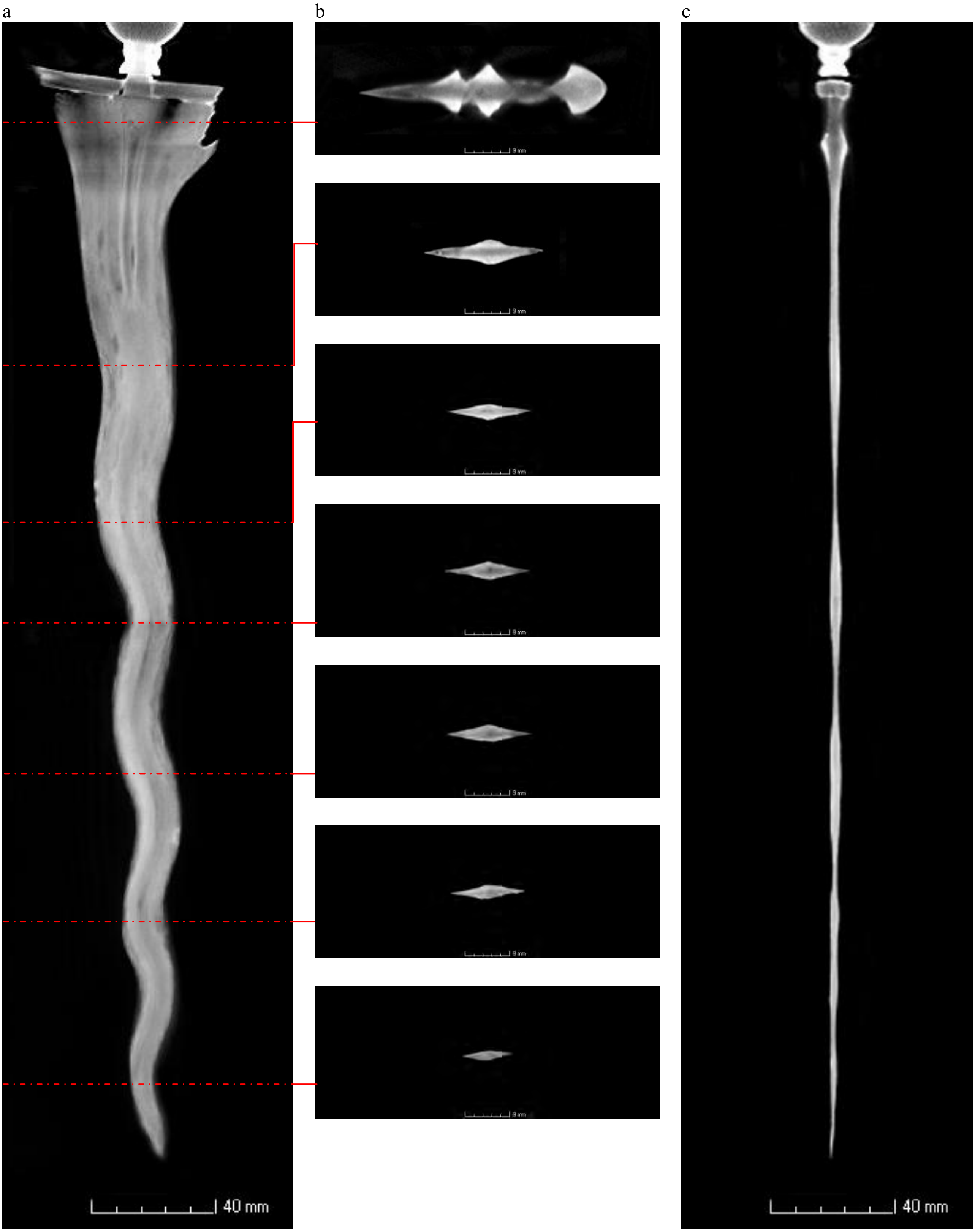

Figure 5.37: The *kris* K4 is shown sliced along the axial *a*, radial *b* and transversal *c* direction.

Figure 5.38: Small inner cracks are visible in the enlarged image *a* (red arrows). In the axial cross section *b*, the two red arrows indicate the presence of slag inclusions; other two arrows highlight cracks diffusing from the surface into the blade. The picture evidences the multi-layered structure of *kris* 4, and strongly oriented dark areas, enhanced by stretching the dynamic range in image *c*. The orthogonal view *d* shows a detail of the twisted layers pointed out by arrows.

Energy-selective tomography

The energy-selective neutron tomographic study was performed on all samples with the aim to identify the presence of iron, steel and nickel-iron phases, correlated to the use of different types of *pamor*. The *kris* were preliminarily analysed, for test and calibration purpose, to map the material contrast enhancement for the selection of suitable neutron wavelengths to be used for energy-selective imaging. Basing of the radiographic energy scan, the Bragg edge profile was reconstructed (Appendix C). Since the Bragg edges of ferrite, kamacite and tainite fall very close, in relation to the wavelength resolution achievable with the current device for beam monochromatization, the phases of interest cannot be discriminated. Thus, only the typical ferrite Bragg edge profile is recognizable. Two independent reconstructions were carried out for each set of measurements, taken at the two different neutron wavelengths, above and below the 110 ferrite Bragg cut-off, namely 3.82 Å and 4.15 Å. The image stacks, so obtained were further processed, by progressively subtracting the latter tomography from the former, according to the method already described in Chapter 4 (cf. section: *Energy-selective neutron radiography and tomography*). In order to improve the statistics, each stack was processed by applying a median filter, and a projection along the z axis was applied every 50 slices in the area characterized by the same dimension and geometry.

Hereafter, I reported only the computational tomographic reconstruction of *kris* K1 as representative sample. The results of all the other weapons are shown in Appendix C for the sake of completeness.
As it is visible, from the tomography slices, all the *kris* are characterized by the same inner structure. The arrangement of different types of metal was highlighted through the contrast enhancement, induced by the selection of an appropriate neutron wavelength.
Indeed, referring to Figure 5.39-*b*, bright area can be related to the presence of ferrite. On the contrary, the dark area, observable in the inner volume of the blade, are due to the segregation of cementite. Thus, the present method allows identifying the typical structure of a *kris*, which is known to be composed of, at least, two distinct sections of different types of steel. We remind, once more, that in order to make a *keris* the sword-smith makes a number of small bars. A central plate of steel or hard-iron, named *slorok,* provides a sharp point and hard edges to the *kris*; on each side of this, a layer of *pamor* was made of iron bars welded together, then beaten. [Gardner 1936].
The tomographic slices suggest that also the investigated blades have been probably manufactured by assembling a “jacket” of low-carbon steel around a very hard steel composing the “core” of the blade, as also confirmed by Frey [Frey 2010].
However, the low statistics due to the neutron beam monochromatization, combined with the effects of filtering and slice-merging processes (done to increment the signal over noise ratio), limited the possibility to discriminate, at the single layer level, compositional differences in the components of both the *pamor* and the core.

K1: Inv 5142

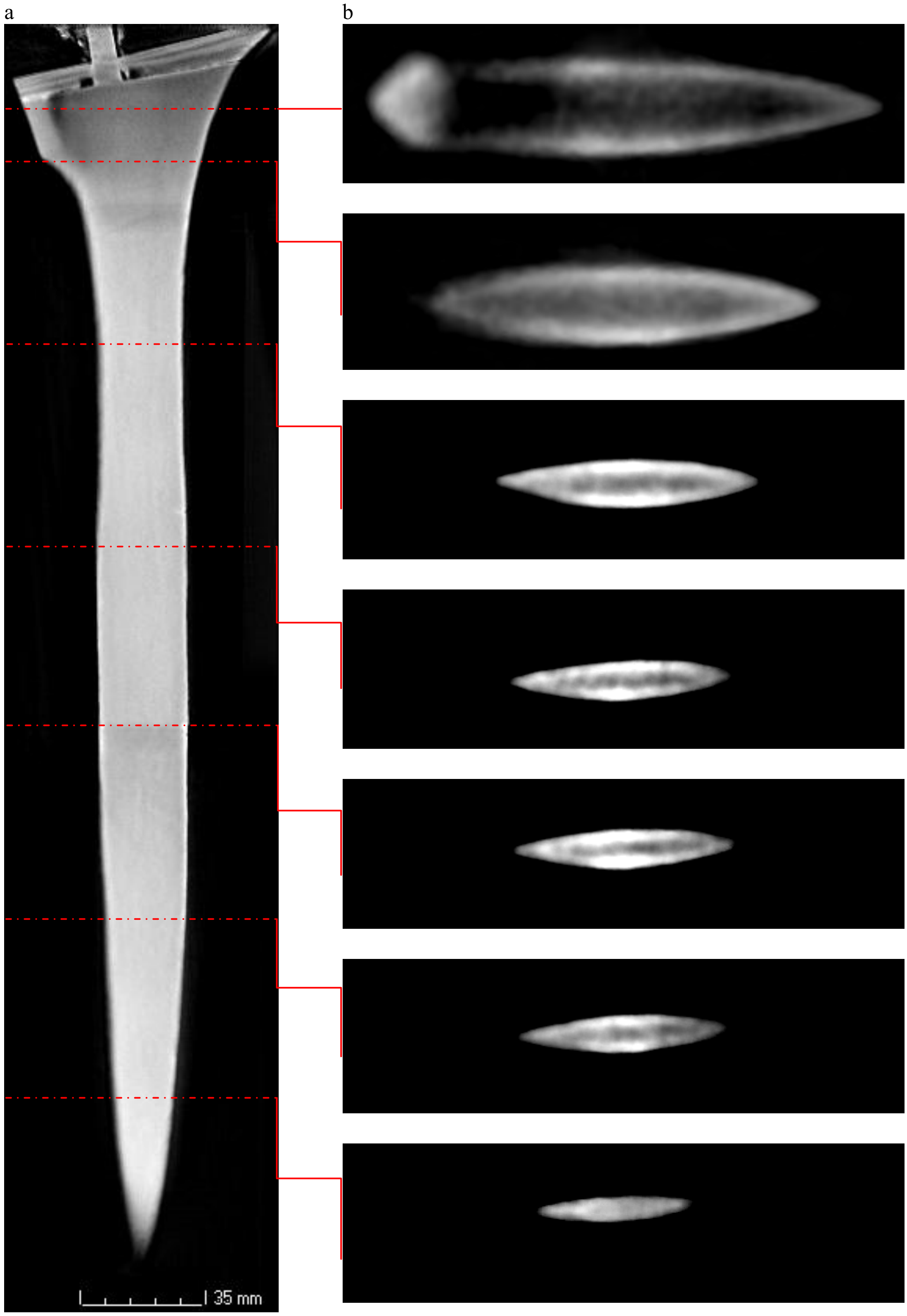

Figure 5.39: Reconstructed slices at different height along the *kris* K1. The cross section shown in *b* are taken at different heights of the sample at the position indicated by the red line in the white beam tomographic reconstruction reported as reference in *a*.

Conclusion

In the present section, four *kris* have been investigated in order to characterize, in a completely non-destructive way, such valuable objects made available from Museo di Storia Naturale, Sezione di Etnologia e Antropologia of Università di Firenze.

Contextually to the measurements that will be presented in Chapter 5.5, white beam and energy-selective neutron tomography have successfully applied to identify peculiar and complementary features related to the forging methods as well as the thermal and mechanical treatments used for the weapons.

The identification of slag inclusions, inner cracks and metal layers allowed to recognize differences and analogies in the working procedure. Although similar features emerged, such as the multi-layered structure, the configurations have shown variances in the number of metal layers, both into the jacket and the core portion, as well as in its distribution (i.e. the *ganja*). In particular, the energy-selective neutron tomographies allowed to qualitatively characterize the metal by mapping the distribution of the materials into the artefacts.

On the other hand, we had to face intrinsic technical limits in the present state of the art of the technique, related to the possibility to resolve the close Bragg-edges relative to different phases, or the ability to distinguish metal layers of different composition identified on the basis of the morphological features and the difference in contrast by means of the white beam tomography.

5.5 *Kris* and *kanjar*: an authentication study

Introduction

The authentication of artefacts is one of the major concerns in museum collections. Judgement on the genuineness or authenticity of a work of art or an archaeological object are established through examinations, including the characterization of the materials, the methods of manufacture and the age determination. For a long time the authentication was exclusively based on the evidences provided by documents proving the identity and the origin of the objects, or it was inferred by stylistic analysis, comparing the attributes of the object itself to what is known about corresponding objects of similar origin. Nowadays, non-invasive experimental methods are catching the attention of curators and private collectors and are playing an important role in the field of cultural heritage research with an increasing demand for authentication studies.

It has to be noted here that the scientific analysis data cannot provide definitive attribution, nevertheless, they can give useful information showing whether a particular property is consistent with other properties pertaining to a certain time period, from a well defined place of origin, and/or from a specific maker [Janssens and van Grieken 2004]. A close collaboration among scientists and humanists, sharing and joining knowledge from different fields of research, is the fundamental key leading to a reasonable and plausible determination.

This study takes advantage of two particular samples to demonstrate the potentiality of imaging techniques in the extensive investigation of objects of cultural and historical interest, also in the field of authentication. This chapter is focused on a *kris* and a *kanjar*, two weapons from ancient Asia. These objects were provided by private collectors to disclose the secrets of ancient technological manufacturing methods and, at mean time, to possibly confirm the authenticity of the samples.

In the past, collectors neglected Oriental weapons and very few top quality pieces fetched only a fraction of comparable European pieces. However, since the turn of 19th century there has been a gradual growth of interest and appreciation of Islamic and Asiatic art. Inevitably, this generated a raising demand of artefacts, which in turn pushed up prices, and not too much time had to pass until the craftsmen of India and Pakistan, encouraged by eager dealers, began to fill the growing gap in the market with modern reproductions. Today a considerable number of first-class modern copies of early daggers and swords are finding their way into the antiquity market. So good are these reproductions that it is often difficult to distinguish them from the original ones [Coe *et al.* 2012].

The sample

As already described in section 5.4, the *kris* is the distinctive weapon of Malaysia and Indonesia. It is found in a variety of forms but, typically, it is an elongated dagger or short sword of slender proportions with a relief texture on both edges [Frey 2010]. All good Southeast Asian *kris* are made of two sorts of metal, iron (or steel) and *pamor* welded together in intricate patterns that are subsequently brought out on the polished surface of the blade through the use of an etchant. In particular, *pamor* is by definition the etch-resistant component traditionally used in the blades, and comprehends a heterogeneous group of metals [Bronson 1987]. A more detailed description about this type of weapons is provided in *Introduction* of Section 5.4.

Kanjar is an Arabic word used in the Islamic countries for different weapons. In Persia and India the name is applied to a double-edged dagger with a slightly curved blade and, usually, a pistol-grip hilt made from metal, ivory, jade or some other hard-stone. *Kanjar* are commonly used in India since about 1600. Daggers with hilts of gold, silver, jade or ivory were worn at court or in cerimonies, they were too precious to be carried on the battlefield [Welch 1985].

A *kris* and a *kanjar* have been investigated, non-invasively, using a combination of different imaging methods: X-ray, neutron white beam and energy-selective neutron imaging were applied in order to qualitatively and quantitatively characterize the peculiar constructive features of these historical objects as tangible evidences of their cultural belongings and the related metallurgical technology.

Experimental set-up

The ongoing study was performed at the CONRAD II beamline at the Helmholtz-Zentrum Berlin (HZB).
In order to investigate the structure and the morphology of the *kris*, the sample was fixed to a purposely-constructed aluminium frame (Fig. 1, *a*) and preliminarily analyzed by means of low resolution *white beam neutron tomography* (Tab. 5.6, 2nd column). The very low microscopic cross section of aluminium makes this metal almost transparent to neutrons and avoids interference during the measurements.

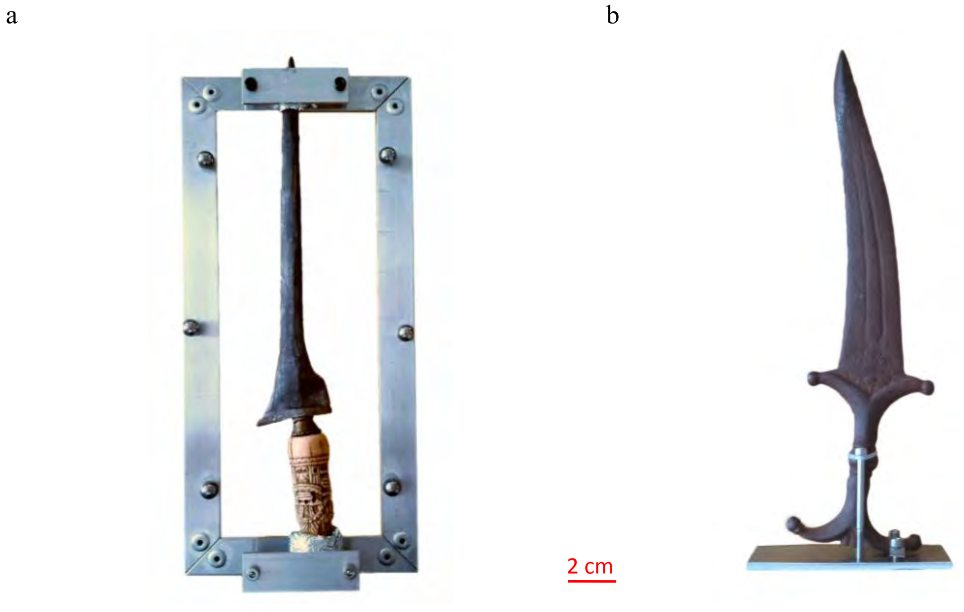

Figure 5.40: The sample set-up adopted for performing analysis on a) the *kris* and b) the *kanjar*.

For detecting the presence of possible hidden structures, related to the manufacturing procedure, the tip of both *kris* and *kanjar* was analyzed through neutron and X-ray tomography, setting a high spatial resolution configuration (Tab. 5.6, 3rd and 4th columns respectively).
Here, the high spatial resolution configuration for neutron tomography available on CONRAD was applied for a direct comparison with X-ray tomographic data. At the tip position, the material and the size of the chosen samples were suitable to fulfil the set task.
For the X-ray technique, a X-ray CT scanner, based on a micro-focus tube (Hamamatsu, L8121-03) available at HZB, was used.

Furthermore, aiming to map and discriminate materials in the inner volume of both samples, an *energy-selective tomographic* (EST) study was performed. I remind that in order to apply the Bragg-edge technique, the generally polychromatic neutron beam must be monochromatized through a well defined range of wavelengths. This has been accomplished at the CONRAD beamline using a double crystal monochromator (see Chapter 4-section *Beam monochromatization*).
Preliminarily to the EST, a *radiographic energy scan* was carried out aiming to discriminate the presence of ferrite by exploiting the contrast enhancement obtained using different neutron wavelengths (Tab. 5.7, 2nd column). In particular, neutron wavelengths at values immediately above and below the 110 *bcc* Fe Bragg-edge were used.

In the part of the experiment dedicated to the *energy-selective tomographic* technique (the instrumental set-up for this configuration is reported in Tab. 5.7, 3rd column), the measurement was carried out using two different neutron wavelengths that were selected, following the energy scan, at 3.94 Å and 4.12 Å and were defined as the optimal values for enhancing the image contrast for material discrimination. The *kris* was arranged into the beam using the same configuration adopted for the *High Spatial-Resolution Neutron Tomography* (HSRNT), while the *kanjar* was fixed from the hilt to an Al plate equipped with two aluminium rods (Fig. 5.40, *b*).

All data were processed through the software package Octopus, developed at Ghent University [Dierick *et al.* 2004] and visualized using VGStudio Max [http://www.volumegraphics.com/products/vgstudio/].

Imaging Method:	**White beam neutron tomography**	**High spatial resolution white beam neutron tomography**	**High spatial resolution X-ray tomography**
Neutron wavelength:	polychromatic		140 KV, 71 mA
L/D:	500	333	7 um source size
Scintillator:	^{6}LiF 400 μm	Gadox 10 μm	-
Camera	Andor DW436N-BV 2048x2048 16 bit		semiconductor plate 2316x2316 12 bit
Field of View:	200x200 mm	13 mm in diameter	-
Object-Detector-D:	90 mm max.	10 mm	390 mm
Pixel size:	106 μm	6.5 μm	6.4 μm
Exposure time:	35 s	20 s	2.5 s
Rotating Angle:	0°-360°	0°-180°	0°-360°
Projections:	300	600	1000

Table 5.6: The different instrumental set-up employed for the measurements.

Imaging Method:	**Radiographic energy scan**	**Energy-selective neutron tomography**
Neutron wavelength:	from 2.0Å to 4.5Å with step of 0.02Å	3.94 Å and 4.12 Å
L/D:	333	
Scintillator:	^{6}LiF 400 μm	
Camera	Andor DW436N-BV 2048x2048 16bit	
Field of View:	200x200 mm	
Object-Detector-D:	20 mm	100 mm
Pixel size:	106 μm	
Exposure time:	150 s	80 s
Rotating Angle:	-	0°-360°
Projections:	-	300

Table 5.7: The different instrumental set-up employed for the measurements.

Results

Neutron white beam tomography

- *Kris*

Thanks to the neutron white beam tomography, the morphological analysis of the whole volume of the *kris* was accomplished, allowing to distinguish different composing elements and the assembling method (Fig. 5.41). The whole volume of the blade was reconstructed, revealing a homogeneous metal body without inclusions and empty areas (Fig. 5.41, *c*-*e*). In particular, the construction of the handle deserves to be mentioned. The tang of the blade was shaped in the form of a cylindrical rod that was inserted, through the funnel-shaped neck of the grip, into a dedicated slot. The small area of the tang, emerging from the main body of the handle, was covered by a metal collar. According to low grey tone visible in figure 5.41-*b*, related to a low neutron attenuation coefficient, we estimated that the material of the decorative element could be made of a Cu-based alloy.

The sharp base of the blade appears as a separate element, with a hole in the centre, in which the tang was inserted and anchored by gluing. The traces of a bright material, characterized by a high attenuation coefficient, are recognizable along the profile of the hole (Fig. 5.41, *b* and *e*). The thickness of this layer ranges from 0.40 mm, along the rod, to 1.10 mm, at the contact with the raised collar guard (*ganja*) that usually forms the base of the blade. In Ref. Draeger 1992, it is mentioned that in the earliest models, the *ganja* was fashioned as one piece with the blade, while in later models the *ganja* was heated and hammered as a separate piece. Consequently, the gluing material, probably composed by an H-based material, could not be attributed to a traditional crafting procedure adopted by earlier Indonesian smiths.

Moreover, a semi-quantitative elemental characterization of the sample was performed. Taking into account the neutron wavelength distribution of the probing beam and the image slope value, the total neutron macroscopic cross sections (absorption and scattering) of the different elements have been estimated. On the basis of the evaluated threshold values of different materials, the segmentation of the image histogram allowed us to distinguish the aforementioned components of the *kris* (Fig. 5.41, *a*). By this method, the same attenuation coefficient was found for the material composing the glue and the ivory-like hilt. Indeed, ivory is manly composed by $Ca_3(PO_4)_2$, which features a lower neutron attenuation coefficient than iron. On the other hand, the gray value of hilt appears higher with respect to the blade body in the performed tomography. A resin, or a plastic material of inferior value and easier to be worked, was probably used for manufacturing the grip in order to resemble ivory.

The profile, the size, and the depth of the decorative holes in the ivory-like hilt suggest that the decorations were made using the same chiselling tool. The average diameter of the holes was 2.00 mm and the average penetration depth was evaluated around 3.50 mm. The importance of the *kris*-handle is reflected by its design, even today, when it is simply used as a status symbol. Contextualizing to the analyzed *kris*, the anthropomorphic decoration that could date the sample as an old one, appears in contrast with the assembling configuration of the *ganja* and the composition of the handle here investigated.

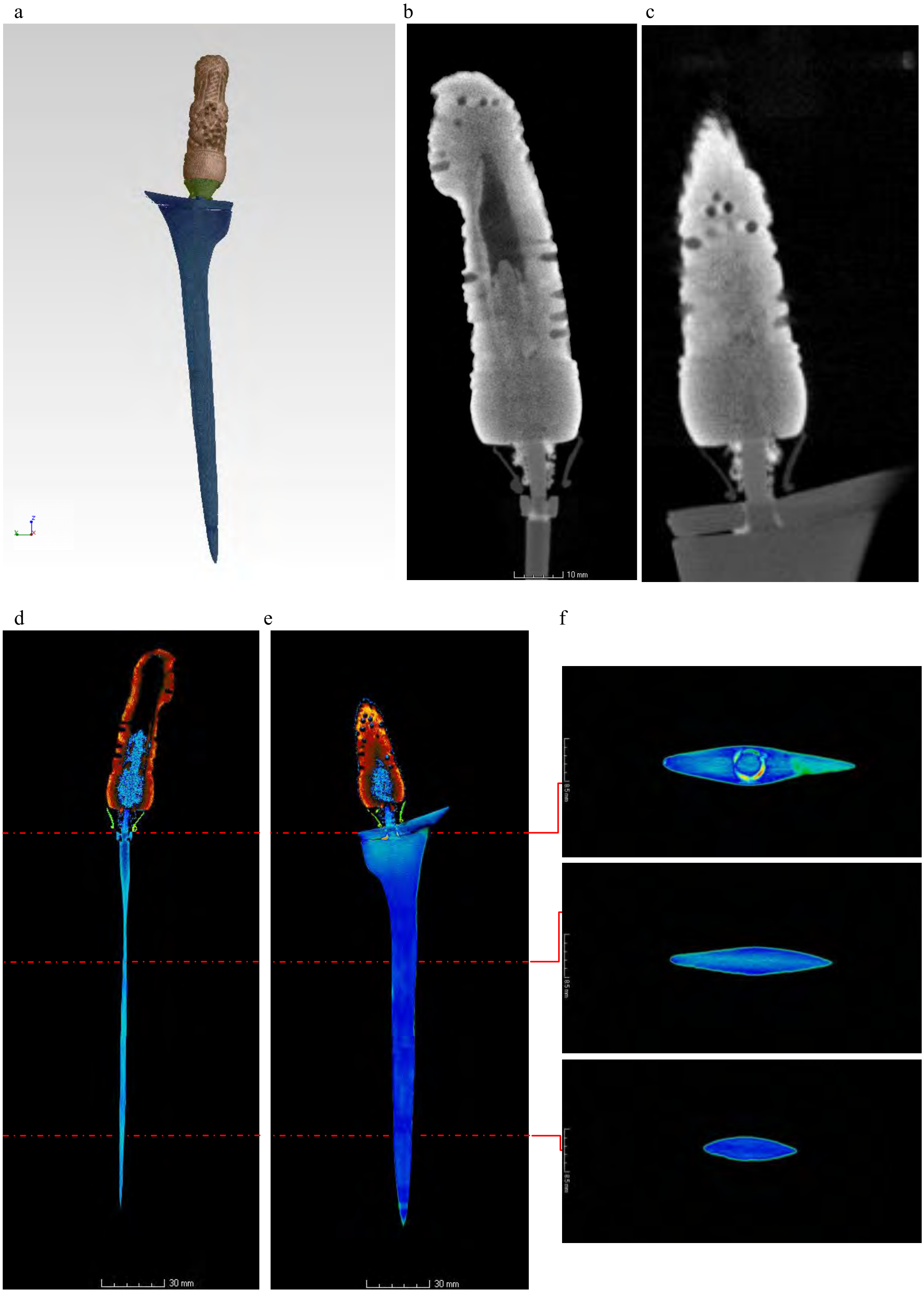

Figure 5.41: The *a* image shows the three dimensional reconstruction of the sample analyzed through white beam tomography. The whole volume of the sample was segmented in order to distinguish its constructive components. The ivory-like handle is reported in red-brow colour, the green tones are used for the metal collar, while the blade is visualized in blue. Considering the axis placed in the centre of the blade length, images *b* and *c* are an enlarged axial and transversal views inside the hilt revealing its structure. Images *d* and *e* refer to the cross sections taken along the axial and transversal direction, respectively. Radial cross sections *f* are virtually cut at different high of the *kris*.

High resolution neutron white beam tomography

- *Kanjar*

The high spatial resolution configuration, set for the tomographic investigation of the tip of the *kanjar*, permitted to characterize the inner structure of the specimen. The metal appeared to be a massive block of metal, crossed by very small cracks. The average thickness of the cracks is 0.07 mm while their length ranges from 0.16 mm to 3.76 mm. The presence of small non-homogeneous dark areas, probably due to the presence of a group of slag inclusions, was also visible (Fig. 5.42, *c* and *d*).

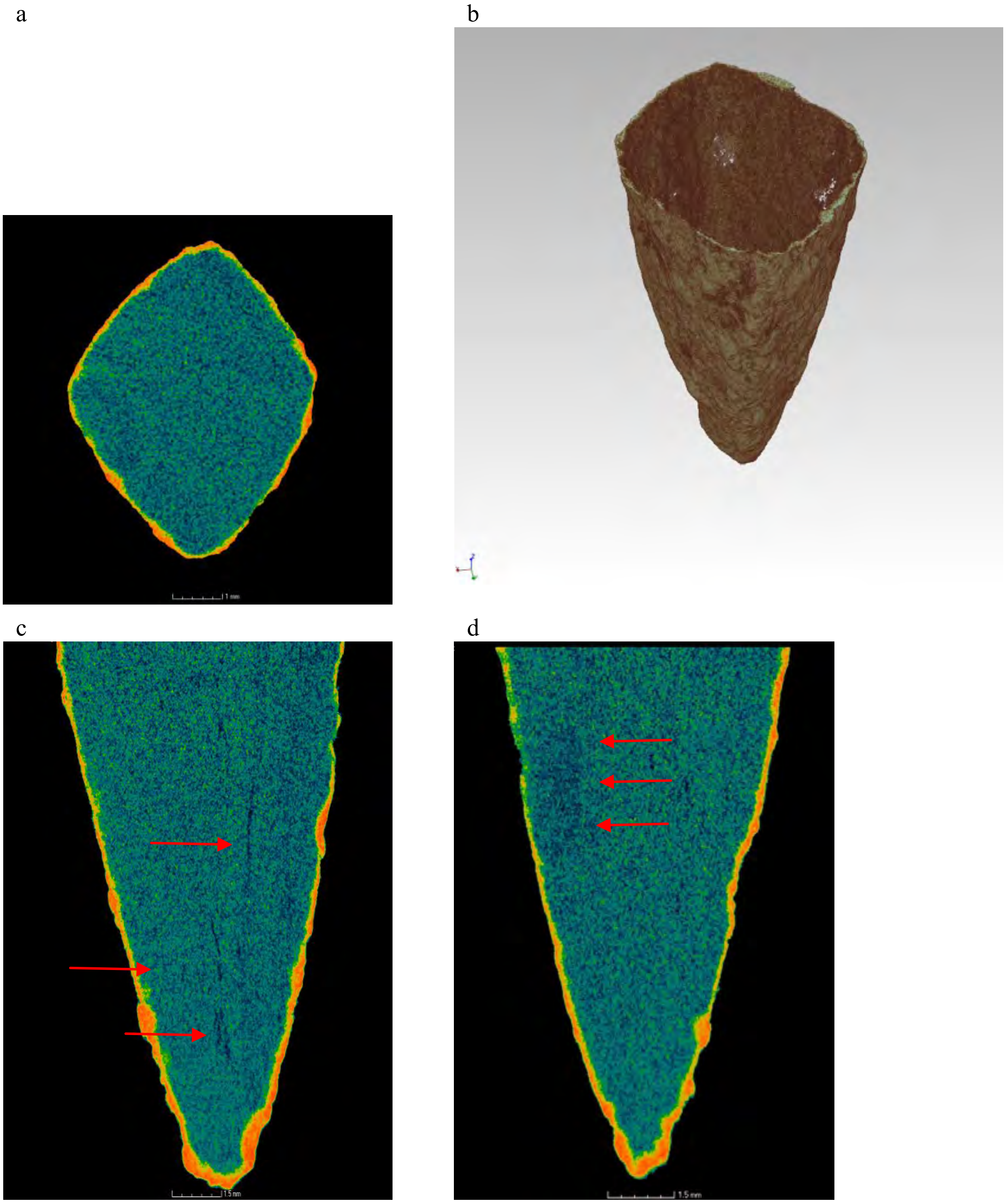

Figure 5.42: Images *a*, *c* and *d* are respectively the radial, axial and transversal cross sections of the *kanjar*, considering the axis placed in the centre of the blade main length. The red arrows indicate in figure *c* the presence of small crack, while in figure *d* a non homogeneous area. Moreover, the false colour visualization permits to distinguish the oxides (red-orange colour) covering the whole surface of the blade and shown in 3D in capture *b*.

Performing the segmentation of the histogram dynamic range, we were able to evidence the alteration of the surface. The oxides appear almost localized on the surface of the sample without deep diffusion into the body (average thickness of the layer is 0.20 mm), this is a sign of a good conservation condition.

- *Kris*

By this measurement, the constructive method adopted for crafting the *kris* was detected with a high-spatial resolution.

In Fig. 5.43 *c* and *d*, selected radial cross sections, taken in different positions of the acquired stack, are shown. They reveal that the weapon was composed using at least two sheets of metal, with one of them featuring a thickness of 0.10 mm and also showing the presence of a channel crossing the whole length of the blade. These elements are clearly visible also analyzing the transversal virtual cuts, especially at the tip position, where the sheet appears secured by bending it around the core (Fig. 5.43, *f*). This configuration could negatively influence the effectiveness of the penetrating power of the blade. On the other hand, the inner body appeared quite homogeneous, despite the detection of a dark area well visible from the axial view (Fig. 5.43, *e*).

Moreover, the segmentation allowed to highlight the presence of a patina, discernible from the few spots of rust, and localized on the whole surface with a thickness of 0.05 mm. In the three-dimensional visualization, reported in Figg. 5.43 *a* and *b*, the patina, the spot of rust, and the metal bulk are clearly mapped. This patina is related to the etching of the surface, adopted in order to enhance the pattern. Details about the surface patina are reported in section 5.4.

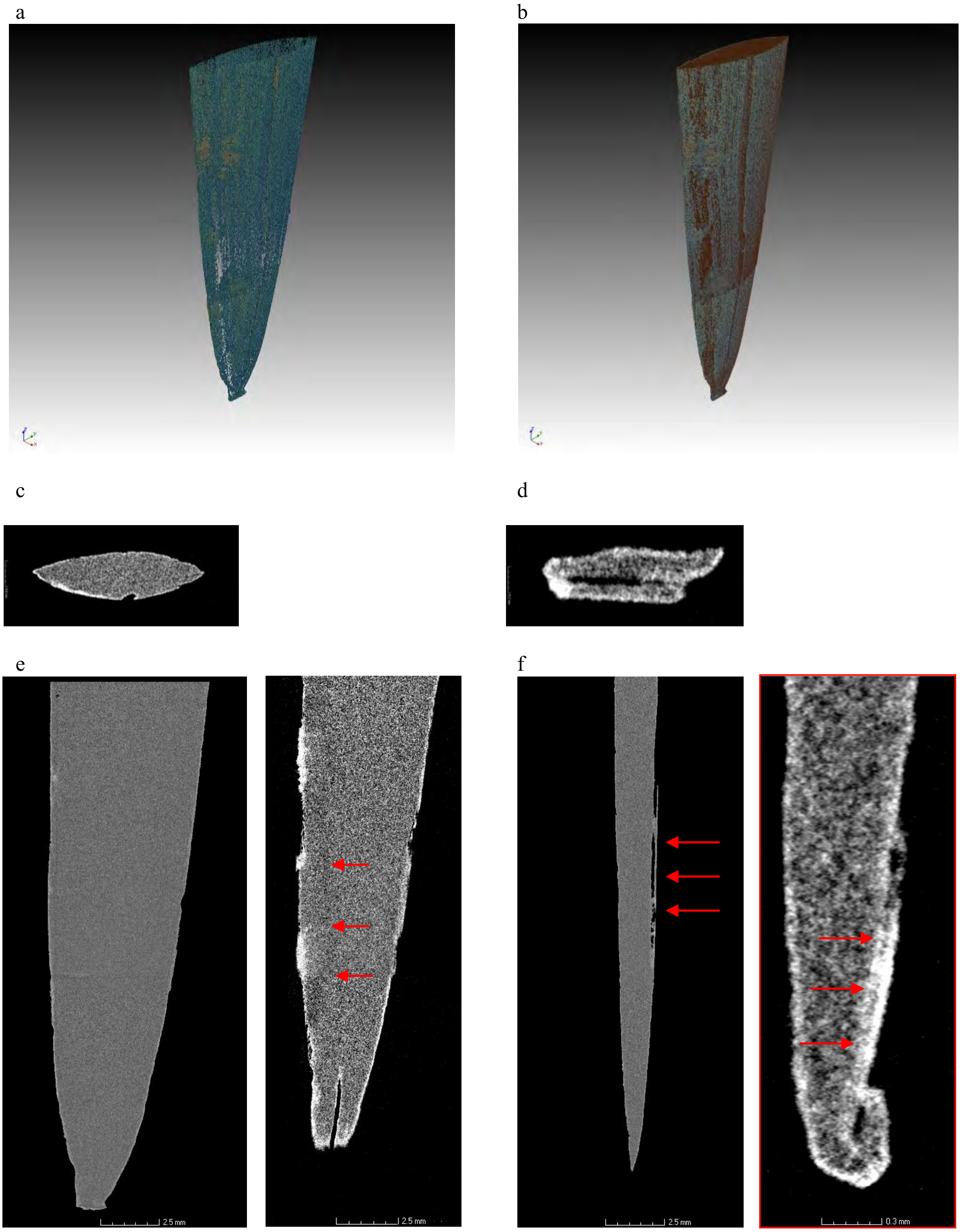

Figure 5.43: Images *a* and *b* show a 3D reconstruction of the *kris*: the first picture refers to the distribution of a patina all over the surface (green) with few spots of rust (orange), while the second one evidences the metal bulk in red-brown colour. Figures *c* and *d* are cross sections taken at the tip, showing the superimposition of two layers of metal, and at the centre of the first half of the sword (starting from the point), evidencing the presence of a channel crossing the whole length of the blade. Axial (*e*) and transversal (*f*) cross sections of the *kris* are reported. The presence of non homogeneous areas (right image *e*, red arrow) and a metal layer applied on the main metal, with an enlargement of the tip (right image *f*, red arrow), are visible.

High resolution X-ray white beam tomography

- *Kris*

Due to the high X-ray absorption from metal elements, the adoption of a high-spatial resolution configuration for the study of the tip allowed to shed light on the manufacturing techniques used to produce this sample. In particular, the weapon appears composed by more than two sheets of metal, like previously hypothesized from the neutron tomography data. Here the high contrast and spatial resolution permitted to map cracks as crossing the whole length of the blade and outlining the profile of the iron sheets. The thickness of the layers is around 0.2 mm for the whole volume. Cracks are visible between them, having a size from 0.01 mm up to a maximum of 0.07 mm. The roughness and the frequent discontinuity of the surface, visible in the 3-D rendering (Fig. 5.44, *a* and *b*), support the hypothesized layered structure.

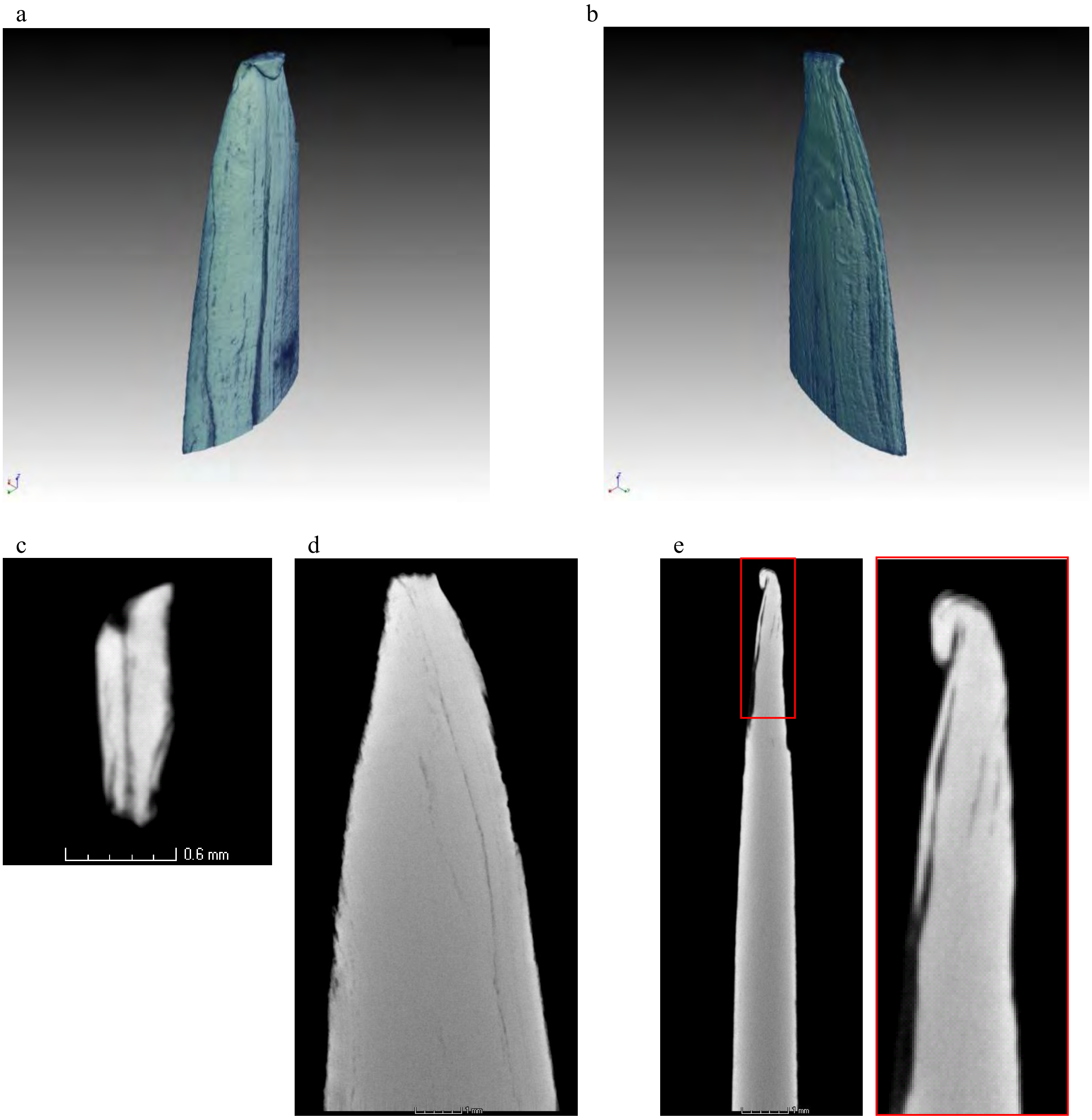

Figure 5.44: The three dimensional reconstructions of the X-ray tomography *a* and *b* show the relief surface of the *kris*, the central channel and the bent tip. The radial *c*, transversal *d* and axial *e* cross sections are reported in grey scale highlighting the presence of diffuse inner small cracks, following the profile of the assembled metal sheets.

In this panorama, the tip was probably bent to secure the sheets, being them poorly welded. Indeed, literature reports that one of the distinguishing features of the *kris,* which is imparted by the *pande* (swordsmith), is the rough, lacking-finish quality of the blade. This is related to a special design feature obtained by welding metal sheets of different composition in an ingenious manner to the ferrite core of the blade. Details about the layer structure assembly are reported in section 5.4.

Neutron energy-selective tomography

The energy-selective neutron tomographic study was performed on both samples. For the sake of completeness, I would remind that the *kris* and *kanjar* were preliminarily analysed, for test and calibration purpose, to map the ferrite contrast enhancement for the selection of two suitable neutron wavelengths to be used for energy-selective imaging. Basing of the radiographic energy scan, two independent reconstructions were carried out for each set of measurements, taken at the two different neutron wavelengths, namely 3.94 Å and 4.12 Å. The image stacks so obtained were further processed, by progressively subtracting the latter tomography from the former, according to the method described in Chapter 4-section *Energy-selective tomography*. In order to increment the statistic, each stack was processed by applying a median filter, and a projection along the z axis was applied every 50 slices in the area characterized by the same size and geometry.

- *Kanjar*

Referring to Figure 5.45, it can be observed that the inner volume of the fragment is characterized by different distributions of blue areas (lower ferrite content and then high carbon) and red-orange areas (high ferrite content and then low or no carbon). Thus, the present method allows identifying the inner structure of the *kanjar.*

Literature [Kapp *et al.*1987, Tawara 1953, Hoshi and Sasaki 2005, Notis 2000, Pleines 1993] and diagnostic investigations [Gener 2007, Tylecote and Gilmour 1956, Piaskowski 1964] attested the procedure of forge-welding different types of steel, purposely located in defined portions of the blade, as a manufacturing method developed by different cultures in time. As an instance, the composite assembly used for making European Renaissance rapier blade shape found its explanation into the need of containing the cost related to the purchase of steel, and the fitting to the kind of fighting techniques adopted at that time that means the need of avoiding fragile fractures, and the easy fitting of the mounting as detailed explained in section 5.3.

Furthermore, as described in section 5.2, similarly to the analyzed structure of the *kanjar*, Japanese medium- and full-size swords feature a composite structure that, in the easiest configuration, was constituted by a core of low-carbon steel, which is embedded or wrapped around the high-carbon steel along the entire length of the sword [Kapp 1987].

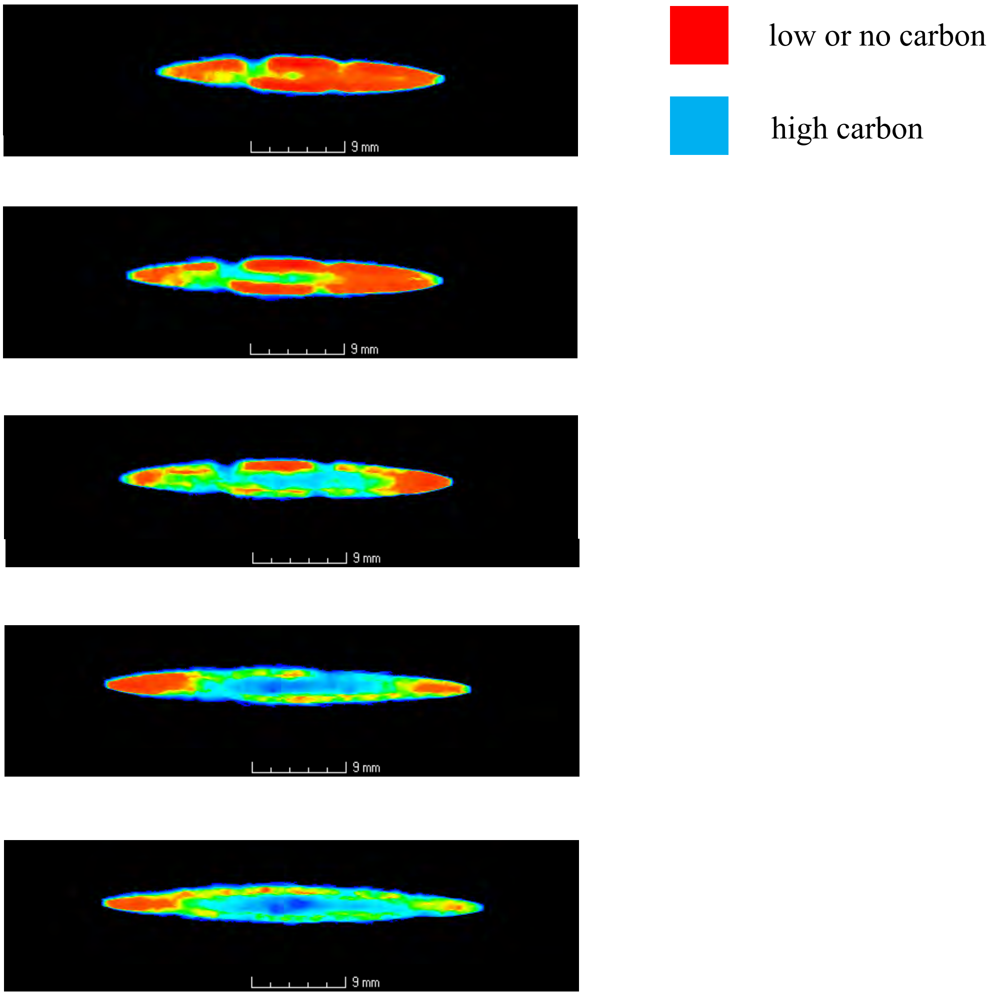

Figure 5.45: Starting from the point and going along the blade, radial cross sections are taken at different height of the *kanjar*. The tomographic reconstructions are shown in false colour enhancing the contrast in order to help in detecting the structure. On the right side, a legend explicits the meaning of the colours.

- *Kris*

Different distributions of dark areas (high carbon) and light areas (low or no carbon) can be observed in the inner volume of the *kris* (Fig. 5.46). The forging of *kris* blade, an intricate and extensive process, traditionally consists of combining several pieces, with different composition, of pre-shaped *pamor* around a low carbon iron core to create a multi-laminar sandwich which, when etched, reveals beautiful patterns. According to Frey [Frey, 2010] and Draeger [Draeger, 1992] and to the structure revealed by the study presented in section 5.4, well distinguishable blue and red coloured areas should be visible, with the latter forming the core all along the blade, due to the assembly of different types of metals. This feature is missing in the analyzed *kris* and the low or no carbon area is detected only in two large spots along the blade axis while the rest of the material is homogeneous and exhibit a higher carbon content.

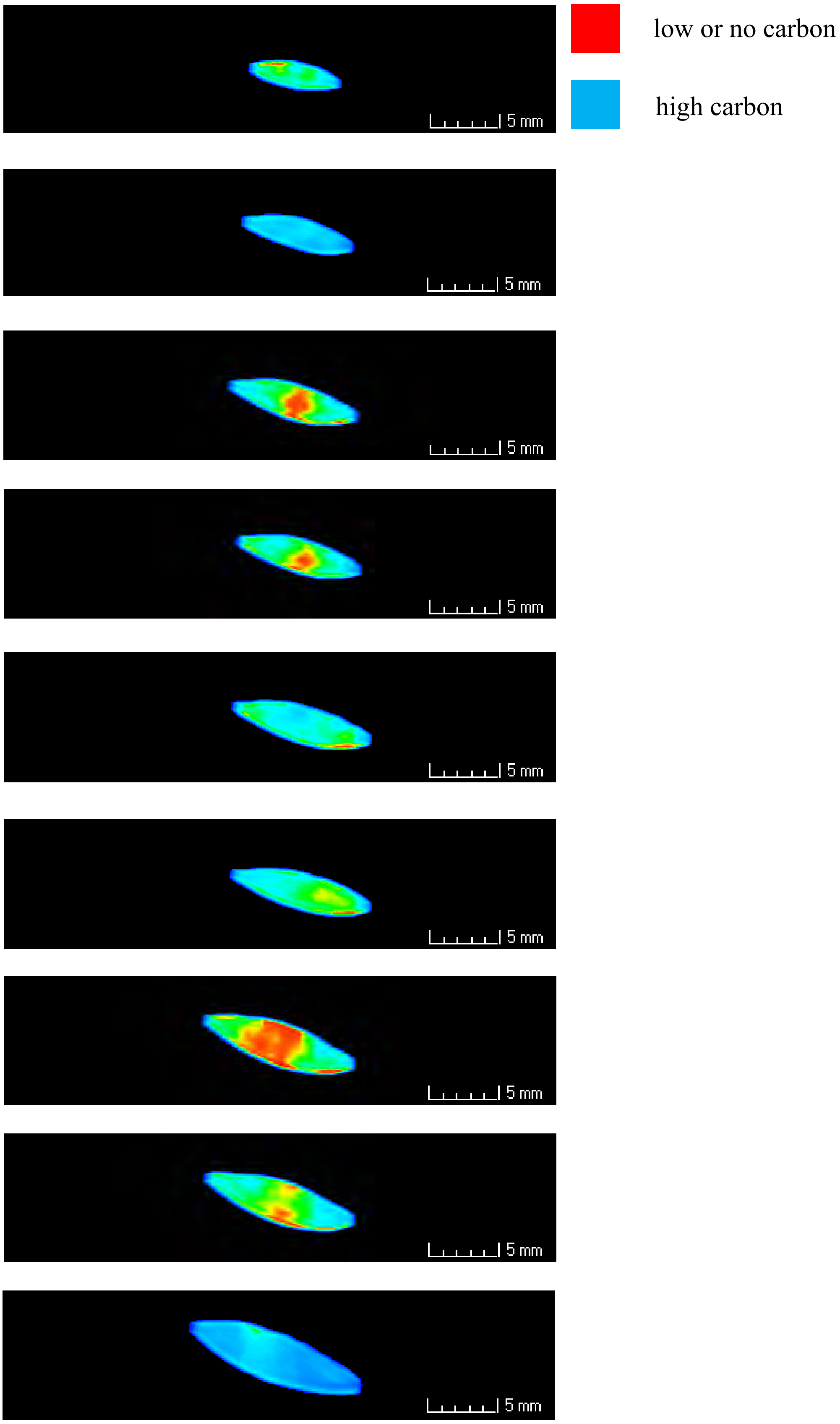

Figure 5.46: Selected slices of the analysed samples evidence the inner structure of the *kris*, starting from the tip and going along the blade,. The false colour visualization of the tomographic reconstructions enhance the contrast in order to help in detecting the structure. On the right side, a legend explicits the meaning of the colours.

Consideration about the authenticity of the samples

The combined information obtained from complementary diagnostic techniques allowed to understand the manufacturing procedure adopted for the making of the analyzed samples, *kris* and *kanjar*.
In the light of detailed data acquired on the morphology and composition of the *kris*, the evidences lead us to consider this specimen as a modern (1950-1980) production for what concerns the materials used to produce it, which are not appropriate for producing a *kris*. On the contrary, concerning the forging method, this follows the traditional working procedure, althoughit could be assigned to the latest one, known to be used for *kris* production in 19th century.
As mentioned before, the gluing material found at the base of the blade, probably composed by an H-based resin, could be hardly attributed to a traditional crafting procedure adopted by earlier Indonesian smiths. Considering the evaluation of the macroscopic cross section, the hilt can be referred to a resin or a plastic used for manufacturing the grip in order to resemble ivory; a huge set of possibilities are offered to the contemporary market providing materials in imitation of ivory but having an inferior value and being easier to work instead of the precious material.
On the other side, the anthropomorphic decoration that could date the sample as an old one, are incoherent with the assembly configuration of the *ganja*.
Finally, the detected distribution of phases inside the sample is in contrast with the expected layered structure of traditional *kris*, generally reported in literature and attested by previous analysis.
Instead, in the case of the *kanjar*, the material distribution in the volume of the sample, compatible to traditional metallurgical processes, allowed to consider this sample as an authentic one.

Conclusion

In the present section, different imaging methods were applied for a non-invasive investigation of a *kanjar* and a *kris*. The structure and the material distribution inside the weapon have shown the potentiality of the tomographic methods for the characterization of Cultural Heritage artefacts.
Neutron and X-ray imaging techniques allowed to identify peculiar and complementary features related to the forging methods as well as the thermal and mechanical treatments used for the two weapons (i.e. inner cracks and metal layers).
In high-spatial resolution configuration, X-ray tomography enhanced the presence of otherwise invisible details pointing the tip of the blade. On the other hand, neutron tomography provided information about the whole structure and clearly evidenced the presence of rust and patina.

Concerning the energy-selective neutron tomography, the present measurements clearly demonstrated that the proposed method can help in characterizing the inner structure and composition of metal artefacts, non-destructively, in combination with other neutron inspection techniques.
Moreover, each technique contributed in revealing evidences that may help in defining the authenticity of the investigated objects, basing on the reference data obtained from certified *kris*.

5.6 Neutron laminography

Test measurements on ancient metal artefacts

Introduction

From its introduction in the 1930s [Ziedses des Plantes 1932] until its intensive development in the 1970s [Grant 1972], the early use of laminography was in the field of medical applications. Nowadays, due to digital imaging detectors and increased computing power for reconstruction, laminographic methods encounter a revival [Helfen et al. 2005]. Recently, laminography has been applied also to material science research [Helfen et al. 2011] and the interest in the application of the technique to art or archaeological objects rose up, since such samples require investigation through non-invasive methods.

Computed Laminography (CL) was recently developed as a method to complement computed tomography for three-dimensional imaging of laterally extended specimens. The basic principle and the typical instrumental set-up were described in the dedicated section 4.2.3 *White beam and energy selective neutron laminography* in Chapter 4.

Considering the potential of the laminography for implementing the status of knowledge about ancient technology, the purpose of this study was to examine expanded applications of these non-invasive methods. These studies include the use of different neutron laminographic methods, which would allow the reconstruction and imaging of ancient metal artefacts. *Neutron white beam laminography* (WBL) and, for the first time, *energy-selective laminography* (ESL) were experimented on CONRAD II beamline at HZB.

The samples

For the present study a set of ancient artefacts, suitable for the designated aims, were collected as test samples and provided by private collectors. They are two hand-guards of Japanese sword (*tsuba*), two hilt collars of Japanese sword fitting (*fuchi*), and an archaeological bronze Celtic spiral (Fig. 5.47).

The first investigated object is a slightly elliptical iron *tsuba* (Fig. 5.47-*a*) with a rounded rim. This is carved with a tendril design (*sukashi* technique), including facing dragons, a jewel, and stylized flowers. The rim is rounded and gilded, and other gilding traces can be observed in other areas. The *tsuba* is not signed but can be dated to the first half of XVIII century, probably from Nagasaki (Hizen) area, in *namban* style. The Japanese word *namban*, which is literally translated as "southern barbarian", was used by Japanese people not only to indicate any foreigner who entered their country, but also to define a large number of artworks, where the decorations reflected a foreign influence in their appearance. From the relatively large diameter (8 cm), we presume that this hand-guard was created for a long sword (*katana*). It was equipped with a *nakago hitsu*, the central hole for fitting the tang of the blade, and a *kozuka hitsu*, the left side hole for accommodating the handle of a small knife called *kozuka*.

The second Japanese hand-guard, made of copper and copper alloy (Fig. 5.47-*b*), is of *sanmai* type: this is composed by three-layers with the central one made of a different alloy with respect to the others. The upper and lower layers are decorated through hammering. Decoration was typically made acting on the back of the layer and then fastening it to the central layer with adhesive or lacquer. A *fukurin*, i.e. soft metal-type rim, was hammered around to hold the three layers together. The rim profile is rounded and not decorated. The decoration theme is made of waves and imaginary animals (dragons). The piece can be dated either to the end of Momoyama period or to the beginning of Edo period. It was probably made in the Kyoto area. A relief decoration is in fact visible on the surface, even though the conservation conditions appear rather poor: detachments are recognizable at the edge and on the decorated surface. As in the previous sample, both a *nakago hitsu* and a *kozuka hitsu*, are present.

The other measured samples are: a bronze Celtic spiral, showing the typical alteration products of copper on its whole surface (Fig. 5.47-*c*), and two *fuchi* (Fig. 5.47 *d* and *e*) made of copper and copper alloys.

Figure 5.47: *a*) the iron *tsuba*, *b*) the copper *tsuba*, *c*) the Celtic spiral, *d*) and *e*) two *fuchi* are reported.

Experimental set-up

The neutron imaging study was performed at the CONRAD II instrument at the Helmholtz-Zentrum Berlin (HZB).

The two *tsuba* and the Celtic spiral were initially characterized using *white beam laminography*, whose instrumental set-up is reported in the first column of Tab. 1. In order to place the samples in the beam, an aluminium threaded rod was gently passed through the main hole (*nakago hitsu*) of the two *tsuba* and fastened with iron bolts. Small Al plates were placed between the sample surface and the bolts, in order to avoid direct contact that could affect the data processing and damage the objects. Concerning the Celtic spiral, due to its bad conservation conditions and to the shape, this sample was wrapped in aluminium foil and fixed on an Al plate mounted on the top of the rod (Fig. 5.48-*a*). The rod, with the samples fixed along it, was mechanically fixed to the rotating table and placed on a goniometer.

At the next stage, the copper *tsuba* and the two *fuchi* were investigated for phases discrimination applying the *energy-selective laminography* method.

As already mentioned, monochromatic neutron beam gives the possibility of modifying the image contrast, for different phases, taking advantage of the abrupt change of the attenuation coefficients at the Bragg cut-off, specific of each phase. This has been accomplished at the CONRAD beamline using a double crystal monochromator (DCM) [Treimer *et al.* 2006].

Preliminarily to the ESL, an *energy radiographic scan* was carried out aiming to discriminate the presence of copper and copper-alloy materials by exploiting the contrast enhancement obtained using different neutron wavelengths (Tab. 1, central column). In particular, to fulfil this task, neutron wavelengths at values immediately above and below the 111 Bragg-edge for Cu and Cu-alloys have been used [Giller *et al.* 2008], according to the lattice parameter defined by previous neutron diffraction analysis (tab. 2). Indeed the copper alloys maintain the same crystal structure of pure copper (*fcc*) while the lattice parameter changes according to the amount and type of solute mixed in it [Pearson and George 1958].

In the part of the experiment dedicated to the *energy-selective laminography* technique (the instrumental set-up for this configuration is reported in Tab. 1, fourth column), the measurement was carried out using four different neutron wavelengths. Thanks to the energy scan, 4.15 Å, 4.19 Å, 4.22 Å and 4.30 Å were defined as the optimal values for enhancing the image contrast for material discrimination. Similarly to the WBL experiment, also in this case, all the samples were fixed to an aluminium threaded rod (Fig. 5.48-*b*).

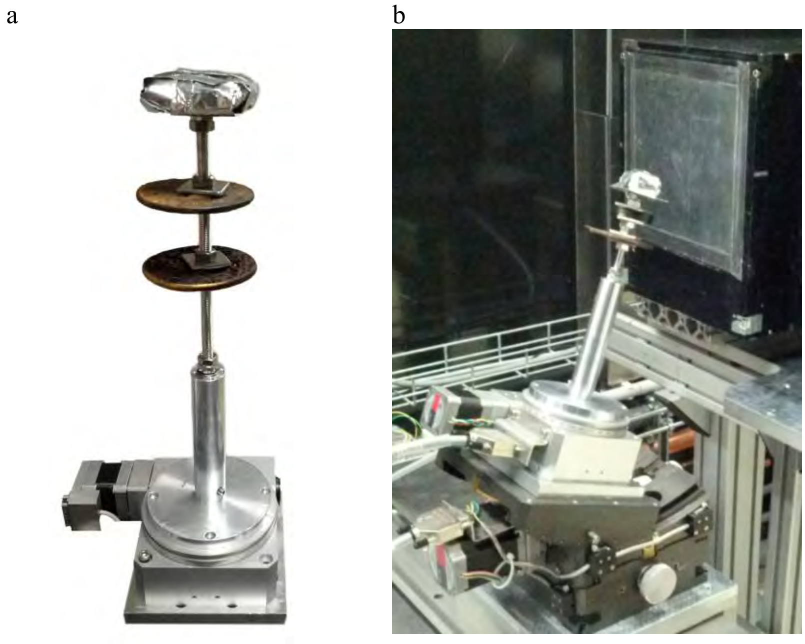

Figure 5.48: The instrumental set-up adopted for performing a) the WBL and b) the ESL.

Imaging method:	**White beam laminography**	**Radiographic energy scan**	**Energy-selective laminography**
Neutron wavelength:	polychromatic	from 2.0Å to 4.5Å with step of 0.02Å	4.15Å/ 4.19Å/ 4.22Å/ 4.30Å
L/D:	500	333	
Scintillator:	^{6}LiF 50 µm	^{6}LiF 400 µm	
Camera:	Andor DW436N-BV CCD3325 2048x2048 16 bit		
Field of View:	110x110 mm	200x200 mm	111.5x111.5 mm
Object-detector-D:	90 mm max.	20 mm	90 mm max
Pixel size:	53.8 µm	106 µm	54.45 µm
Exposure Time:	60 s	150 s	130 s
Rotating Angle:	0°-360°	-	0°-360°
Projections:	600	-	300
Tilt angle:	20°	-	20°

Table 5.7: The different instrumental set-up employed for measurements.

hkl	**2d=λ(Å)**
111	4.18
200	3.62
220	2.56
311	2.18
222	2.09
400	1.81

d(111)	
Cu	2.087
Cu-alloy	2.091

Table 5.8: On the left, the typical wavelength values of the Bragg-edge reported for the lattice plane (hkl) of the FCC copper crystalline structure. On the right, the lattice parameters defined by previous neutron diffraction analysis are shown for the investigated specimens made of copper.

Results

White beam laminography

The white beam laminography revealed a homogeneous body for the iron *tsuba*, probably filed starting from a single piece of iron (Fig. 5.49). As a matter of fact, starting from the *Muromachi* period, the *sukashi* technique evolved over time. The iron plate, prepared as the ground metal, was uniformly forged to produce a relatively soft material to successfully cut out the fine designs but hard enough to avoid breakage during use. Any void, or significant irregularity in the iron body, would have made impossible the shaping of continuous decorative lines. Extra effort in the preparation of the plate was then necessary, as observed in the inner volume of the sample, which was free from any cracks, pores and inclusions [Kanzan Sato 1983]. Evidences of welding weren't identified in the design motifs involving plants and animals figures, apart from the gilded ring outlining the profile of the *kozuka hitsu*. Brighter areas detected on the surface were probably due to the application of a patina or to the early formation of alteration products [Eitoku Sugimori 2004].

Virtual cross section taken at different heights of the copper *tsuba* revealed three layers of copper and copper-alloys (Fig. 5.50). The external sheets of metal were probably applied over the inner core by heating and slightly hammering, while their rather soft surface was worked with a punch to give texture. The composite structure was finally tightened by applying, all around the rim of the *tsuba* and the pierced hole, a thin ring appearing detached and lost in some areas.

The laminography allowed reconstructing the whole inner volume of the Celtic copper spiral, which appears entirely covered by alteration products (Fig. 5.51). A qualitative elemental characterization of the sample has been performed. Taking into account the neutron wavelength distribution of the probing beam and the image slope value, the total neutron macroscopic cross sections (absorption and scattering) of Cu and H have been estimated. On the base of the calculated threshold value between copper and hydrogen, the segmentation of the image histogram allowed us to distinguish the still integer metal, inside the sample, and the alteration, covering the surface and diffusing inside the metal. The integer metal is visible inside as well as the dark areas probably related to the presence of slag inclusions. The detected structure of the artifact is simple and was obtained by folding a copper wire over itself.

- Iron *tsuba*

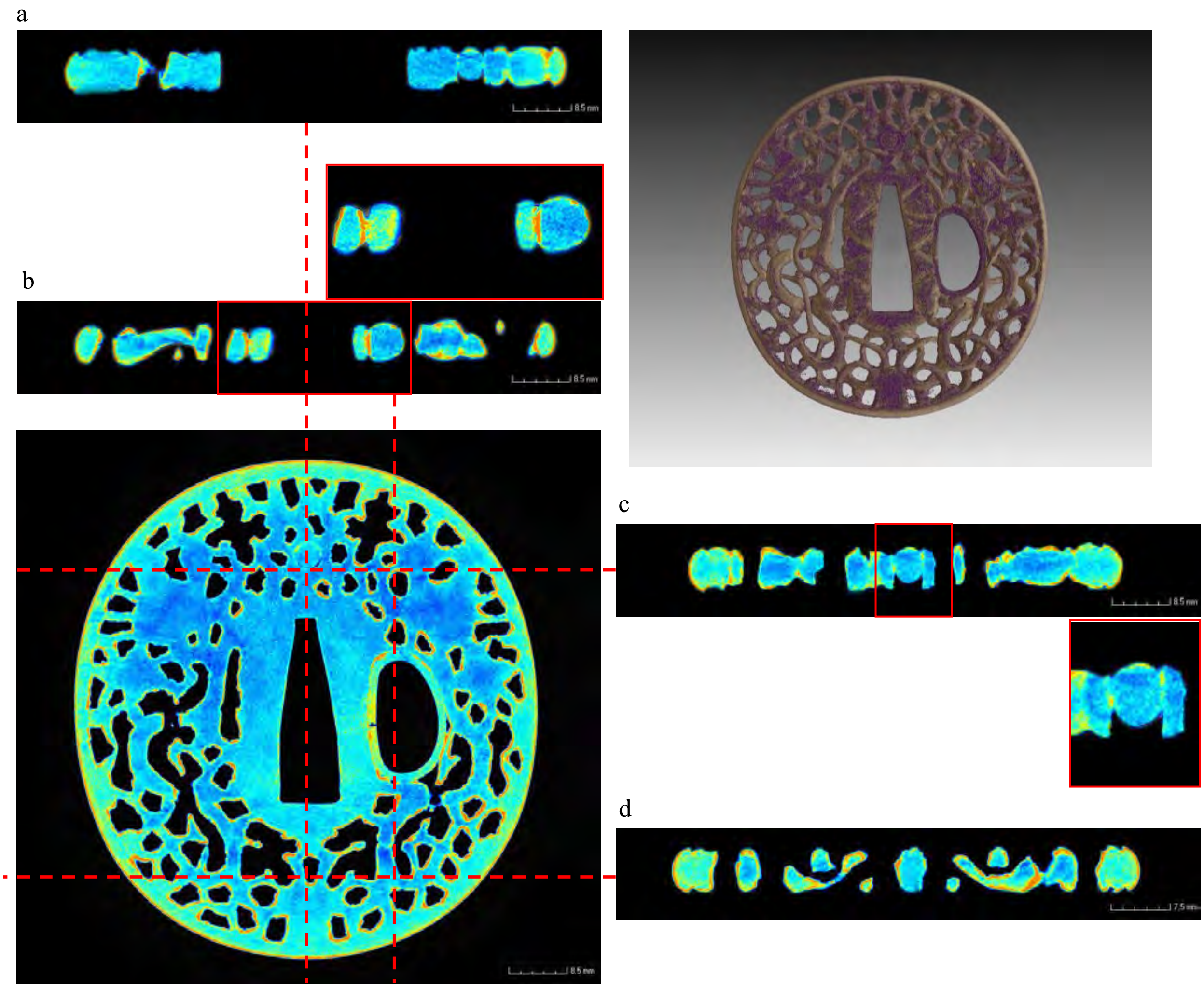

Figure 5.49: On the left bottom side of the capture, a virtual cross section of the iron *tsuba* is reported in false colors. The red dotted lines define the position of the orthogonal views shown alongside (*a*, *b*, *c* and *d*). The red squares map the area of interest inside the views and their respective enlargements. In the cross section *a*, the evidence of soldering are visible in red-orange tone at the edge of the ring. While images *a* and *b* allow to observe the absence of such soldering and the brighter spots are conducible to the patination or alteration of the surface. The view *d* gives an idea of the complicate arabesque-structure made by piercing a single metal disc. The right top image refers to a 3D rendering of the sample.

- Copper *tsuba*

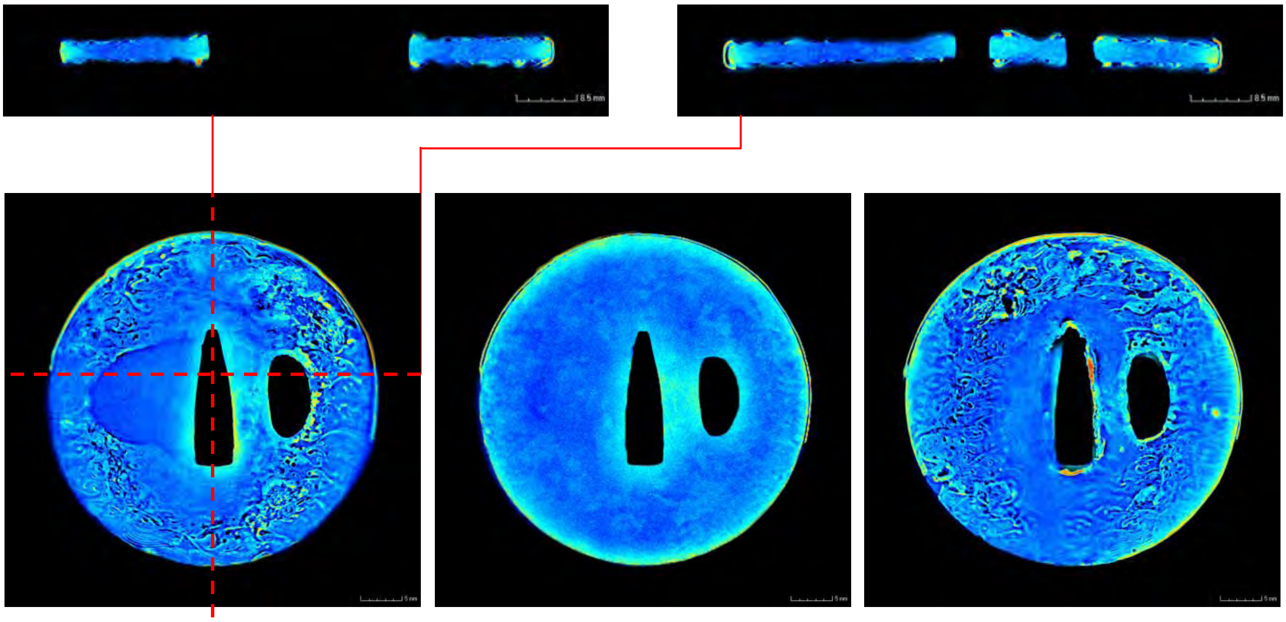

Figure 5.50: The three bottom images refer to cross sections taken at different depths of the copper *tsuba*, starting from one side of the metal disk and progressively emerging on the other one. The layers closer to the surface (the first and the third ones) feature the decorative pattern and the lacking area (red arrow in the first image), enhanced by the false colour visualization. Moreover, the remaining of a ring around the border of the *tsuba* is visible (red arrow, second image). The red dotted lines map the position for the orthogonal views, reported above, where the decorated layers soldered to the bulk sheet and the enclosing ring can be observed.

- Celtic spiral

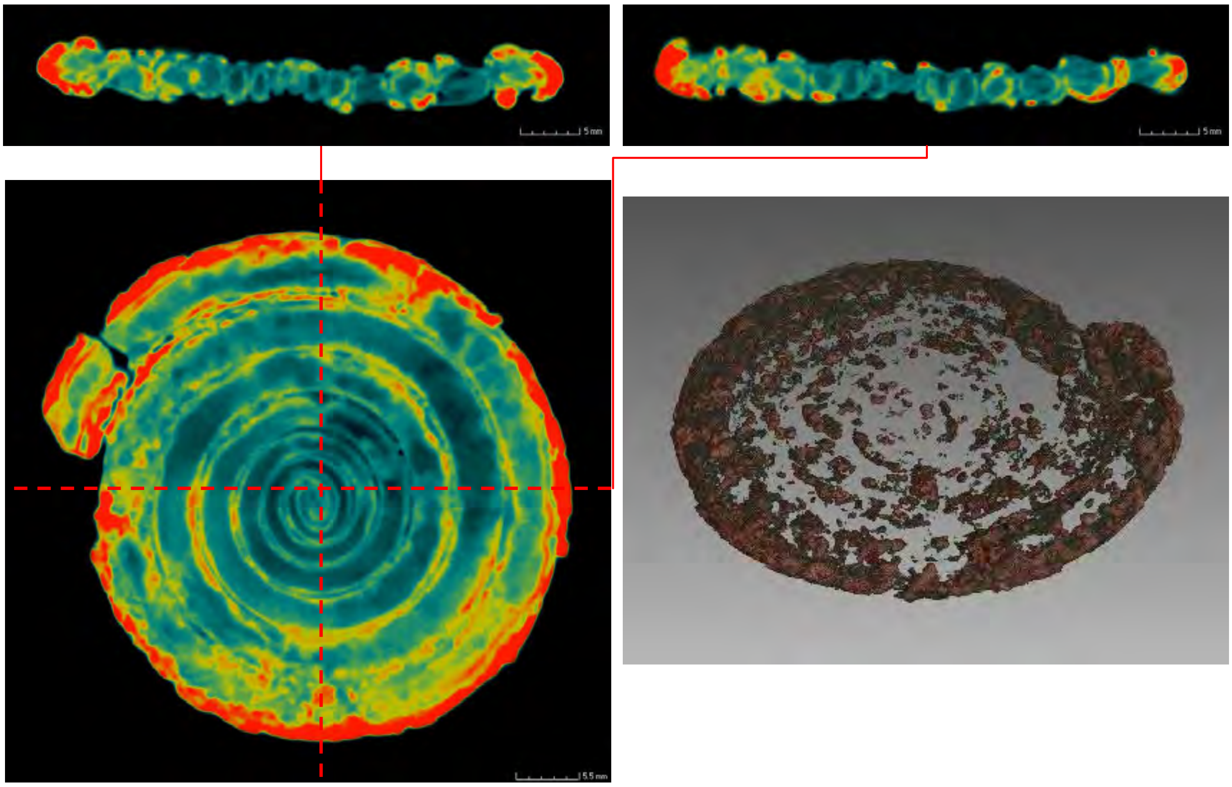

Figure 5.51: Here the three orthogonal views acquired cutting the Celtic spiral along the main directions are shown. The red dotted lines indicate the virtual cutting position. In the false colour visualization, the red-orange color referrers to the altered area, flowing the profile of the object, while the blue-green colour stands

for the still remaining metal inside the volume of the sample. The bottom-right image visualizes in 3D the products of alteration.

Energy radiographic scan

Preliminarily to the energy-selective laminography, a radiography energy scan was performed to correctly choose the proper neutron wavelength values for enhancing the phase-contrast at the Bragg-edge cut-off. To fulfil this task, measurements were performed from 2.0 Å to 4.5 Å with steps of 0.02 Å, crossing the 111 *fcc* Bragg edge for copper and for copper alloys. Figure 5.52 reports the optimum neutron wavelength values above and below the chosen edges for both samples.

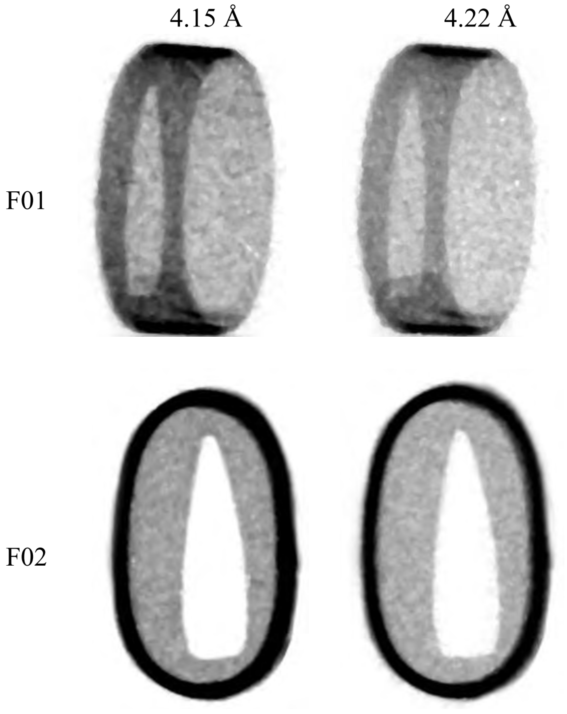

Figure 5.52: Radiographies of the *fuchi* taken at different neutron wavelengths, showing the variation of intensity due to the crossing of the 111 (FFC) Cu Bragg-edge.

Energy-selective laminography

Basing on the radiographic energy scan, three independent reconstructions have been carried out for each set of measurements, taken at the three different neutron wavelengths, namely 4.15 Å, 4.22 Å and 4.30 Å. The image stacks so obtained have been further processed, by progressively subtracting the latter tomography from the former. The images acquired at 4.15 Å are placed above the 111 Cu Bragg-edge, while the ones at 4.22 Å and 4.30 Å are located below the edge for Cu and Cu-alloy respectively.

In order to increase the statistics, each laminographic stack was processed by applying a median filter, and a projection along the z axis was applied every 50 slices.

The contribution due to the presence of Cu has been highly evidenced by subtracting the 4.15 Å from the 4.22 Å image, while Cu-alloy based elements were mapped by subtracting the 4.22 Å from the 4.30 Å image, according to the method described in Chapter 5.

The same procedure was applied to both *fuchi*. In the case of sample F01, the image resulting from subtracting the stack above and below the copper Bragg-edge (Fig. 5.53, F01, first sequence – image 4.15-4.22 Å) evidenced, in brighter grey tone, the presence of a flat plate made of Cu. A collar surrounded by decorative elements of a Cu-alloy based material can be pointed out in brighter area of the image 4.22-4.30 Å (Fig. 5.53, F01, second sequence).

Similar results were evidenced for the sample F02, featuring a copper collar outlined by a Cu-alloy material (Fig. 5.53, F02).

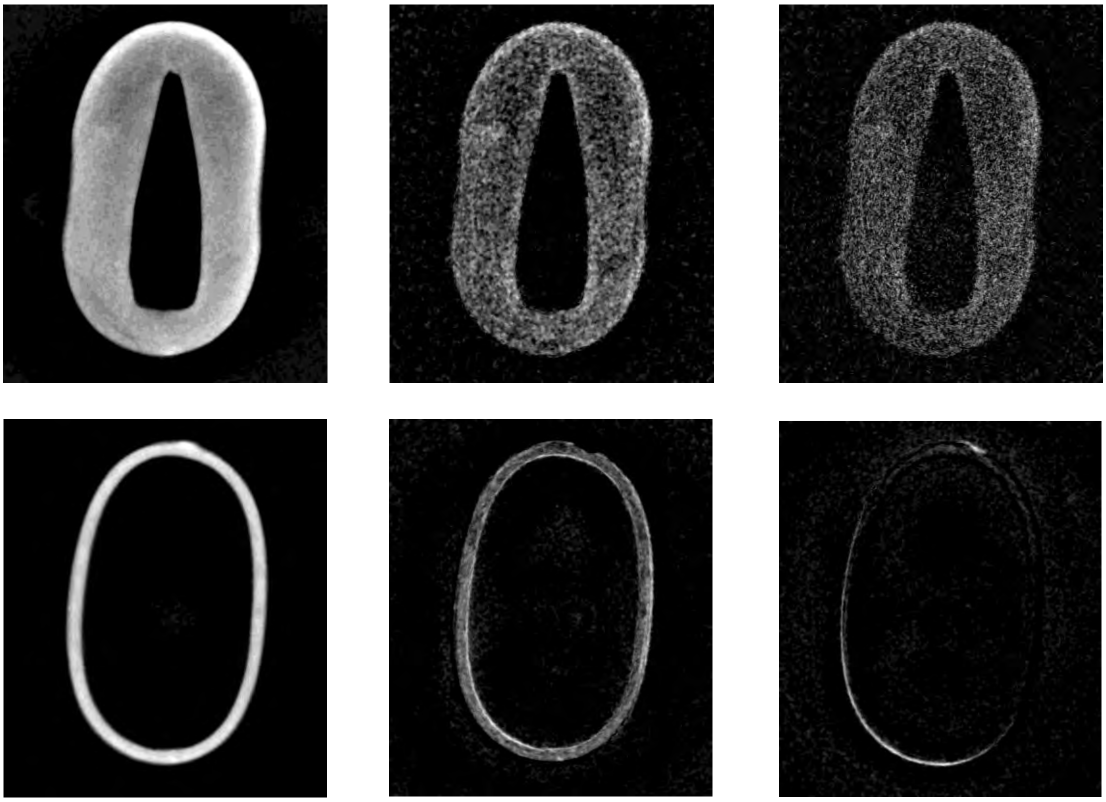

F01

4.15 Å 4.15-4.22 Å 4.22-4.30 Å

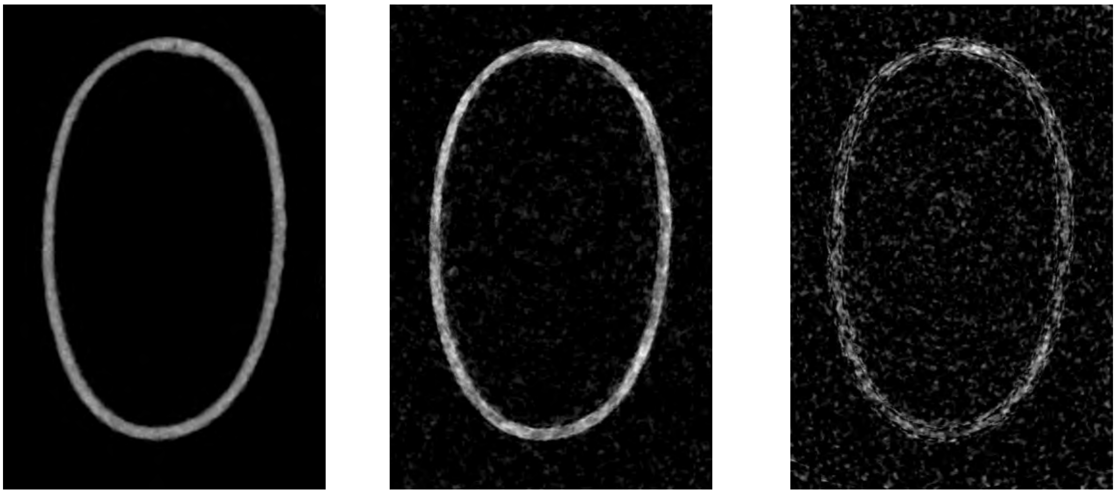

F02

4.15 Å 4.15-4.22 Å 4.22-4.30 Å

Figure 5.53: On the left of each sequence, slices taken at different high of the *fuchi* F01 and F02 are shown. On the right, we can see the results of the subtraction process at wavelength values above and below the Cu and Cu-alloy Bragg edge, respectively.

Finally, a laminographic analysis was conducted on the copper *tsuba* (Fig. 5.54). The experiment was carried out at the same wavelength values of the previous analysis but, at a glance, the method does not seem to lead a material-contrast improvement. This effect is explained by the neutron beam angular divergence, which produces an uncertainty in λ that is larger than the lattice parameter difference between Cu and Cu-alloy inside the acquisition window. In addition, the effect is further enhanced by the larger extension of the *tsuba* with respect to the *fuchi*.

This explanation is supported by the observation that, in correspondence to the centre of the rotation axis, where the wavelength shifts inside the field of view is smaller than the change of position of the Bragg-edge of interest, a certain increment in contrast can be detected between the Cu and Cu-alloy layers composing the sample (Fig. 5.54, red circles).

For the sake of completeness, the energy selective laminography was performed also at 4.19 Å. This value is located after the Bragg edge for the *shakudo*, a typical Japanese ternary copper alloy containing Arsenic and Gold up to 2%. However, due to the non-homogeneous distribution of the neutron wavelengths inside the acquisition window, and the narrow wavelength displacement among the Bragg-edges of the *shakudo* and the other Cu-alloy composing the sample, it was not possible to clearly detect this component, which however had been already evidenced by previous neutron diffraction analysis [Barzagli 2013].

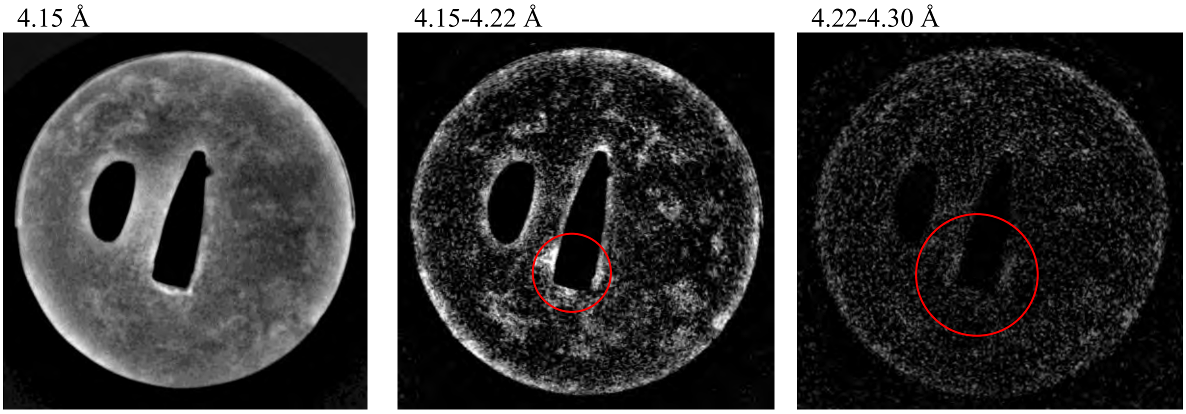

Figure 5.54: On the left, a projected slice taken above the Cu Bragg-edge is reported for the copper *tsuba*. On the right, we can see the results of the subtraction process at wavelength values above and below the Cu and Cu-alloy Bragg edge, respectively. The red circles point out the position of the rotation axis, where a slight increment in contrast is detectable.

Conclusion

In the present section, five different historical metal artefacts, chosen as test samples pertaining to different periods and forging traditions, have been studied.

Neutron white beam and energy-selective laminographies were used for the non-invasive investigation of laterally extended specimens and for showing the validity of the proposed laminographic methods. Moreover, the contrast enhancement induced by the selection of an appropriate neutron wavelength was exploited to increase the image contrast for the different material composing the analyzed specimens.

White beam laminography allowed identifying peculiar characteristics related to the forging methods of these flat objects:

- inner structure, resulting from the particular manufacturing process, were analysed all over the samples;
- presence of soldering was mapped;
- patination of the surface was established;

- alterations, originating from surface and extending in the body of the sample, have been identified for assessing the condition of conservation.

Concerning the energy-selective laminography, the present measurements clearly demonstrate that the proposed method can help to characterize the inner structure and composition of metal artefacts, non-destructively, in combination with other neutron inspection techniques.

However, further work is needed to improve the methods. In particular, more homogeneous neutron wavelength distribution in the whole field of view is needed to quantitatively characterize the phase distribution in the case of flat samples made of Cu and Cu-alloys.

5.7 *Koshirae*, components of Japanese swords

Introduction

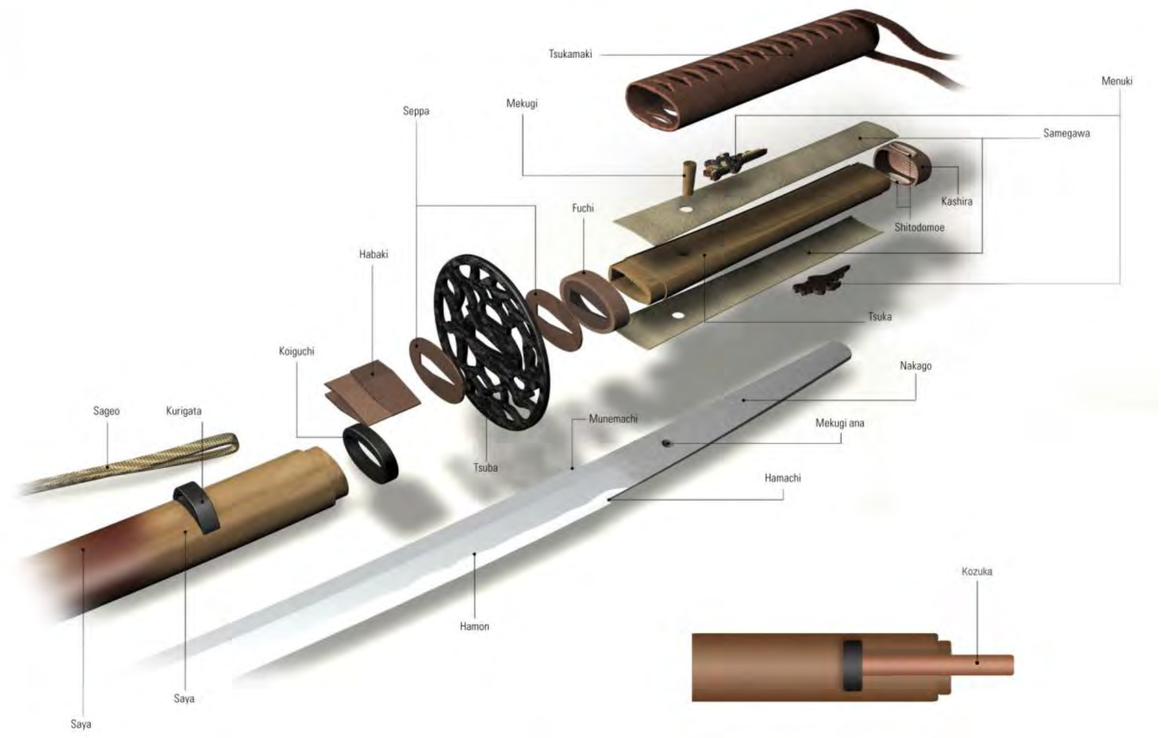

Figure 5.55: The components of the mounting of a *katana* are shown [Magotti 2011].

Japanese sword mountings are the various housings and associated fittings that hold the blade of a Japanese sword when it is being worn or stored. *Koshirae* refers to the ornate mountings of a Japanese sword (Fig. 5.55).
The sword-fittings that are most admired today were made for *uchigatana*[5.7] and date from the late Muromachi onwards, the majority of them being made during Momoyama (1573 - 1603) or Edo (1603 - 1868) period. Such components were considered to be adequate if practical function, and also aesthetic criteria, were fulfilled. These features were applied to their design or manufacture, thus leading to the evolution of more elaborate decorative techniques and the emergence of specialist sword-fitting makers [Kanzan Sato 1983].

Briefly tracing the development of Japanese sword-mounts from the earliest times to the modern age, *koshirae* evolved according to the needs and trends of the moment defined by the historical events and the cultural contest. In the 6th century the Chinese sword arrived in Japan, with its quite simple type of hand-guard, separated from the sword body, that was called *tsuba*; the Japanese craftsmen gradually enlarged and developed it to a totally different level of aesthetic. In particular, around the 9th century, the rise of the military class and the growing political disturbances conducted to the increasing demand for weapons. The modern curved type of blade and the modern guard were developed reflecting the changing form of warfare in Japan. The new curved sword was a far more

---

[5.7] A long sword worn with a guard, later becoming the *katana*, preceding the development of the *daisho* pair of long and short swords during the Momoyama period (1573-99) [Kanzan Sato 1983].

efficient weapon when wielded by a warrior on horseback where the curve of the blade adds considerably force to the cutting action.

The change in military tactics, following the Mongol invasions of 1274-1281, spurred further evolution of the Japanese sword. Often forced to abandon traditional mounted archery for hand-to-hand combat, many samurai found that their swords were too delicate and prone to damage when used against the thick leather armour of the invaders. In response, the huge *no-dachi*, worn at the back and wielded with both hands, replaced the lighter strongly-curved blade of the horseman. The guards increased proportionately in size and strength, and the material used for them was the finest wrought iron and steel, often forged by sword-smiths and armourers. In the 15th century, decorations were applied to the iron guard in the form of simple piercing (*sukashi*) or else of primitive inlay (*zogan*) of brass and copper. Around the same period, the other mounts came into use or received decorative treatment for the first time.

Towards 1500 the influence of Buddhist thought and idealism, propagated by the Zen sect, gradually elevated the minor crafts, especially metal working, to the dignity of the higher arts. The estimation for the sword itself increased, and an immense impetus was given to the decoration of the guards and other appurtenances of the now idealized sword. The artist was, for the first time, proud to sign his work and the execution beauty of such artefacts rapidly grew from this time onwards.

The bloody struggles between the feudal lords during the 16th century, culminating in the rise of Oda Nobunaga, led to a further reformation in military tactics. Elaborated *tsuba,* made lighter by extensive perforations, or else made brighter by coverage with plated brass wires, were favoured by the famous war-lord *Takeda Shingen*. The former decorative type was also adopted by the Tokugawa shogunate, and enjoyed a great vogue in the Edo period.

As long as the possibility of war was in front of man mind during the early years of the Tokugawa Shogunate, swords remained mostly practical tools, and their guards and other mounts were of severe and efficient type. However, the continuing years of peace and the lessening prospect of civil conflict led to a general shortening of the blades, accompanied by a gradual elaboration of the guard and mounts. Great armourers and sword-smiths worked at the Shogunal Court and many craftsmen of note are recorded, in direct affiliation, as having made sword-furniture during this period. These masters were probably grouped under more than sixty distinct schools, characterized by their individual style and technical qualities. From this period bold relief-sculpture, as an adjunct to the simple silhouette piercing or coarse brass inlay of earlier work, was widely adopted. The *ye-fu* (pictorial) style, characterized by elaborate incrustation of precious metals and coloured alloys, gradually yielded in popularity. This style became the most fashionable in the 18th century, and reached its decadence in the 3th quarter of the 19th century. However, as it usually happens, even the decay period , was illuminated by brilliant works [Robinson 1970].

The commonest basic material for sword-mounts, especially among the earlier examples, is iron, usually of fine quality. The other metals employed, commonly known as *soft metals*, include silver, bronze, brass, copper, and the three special copper alloys, namely *shakudo*, *shibuichi*, and *sentoku*, which are peculiar of Japan.

Shakudo is perhaps the best known copper alloy of the special Japanese alloys group; it is made by melting together 3-5% pure gold with copper and some arsenic. When the gold component raises between 5 and 7%, the alloy is called *murasaki-gane*.

Shibuichi (the word literally means *one quarter*) is an alloy consisting of one-fourth silver and three-fourths copper, sometimes with a low amount (1-2%) of pure gold added. For casting works, the percentage of silver might go as low as 7-15%.
Brass, called *shinchu* in Japanese, is an alloy of copper and zinc. By altering the proportions of the standard commonly used alloy (70% copper and 30% zinc), many variation of brass are possible [Eitoku Sugimori 2004].
The important fact is that none of these alloys is strongly different in colour from the unalloyed copper itself, and each one obtains the beautiful coloration, giving rise to its peculiar charm, thanks to treatments with special etching baths, whose result is to produce a rich palette of pigmentation to the different alloys. Although these colours are only skin-deep, they are practically permanent, as long as they are not subjected to scratching or rubbing with abrasives, which will rapidly destroy them and reveal the raw metal beneath .

Also pure iron was treated to produce a surface varying in colour from a russet chestnut tint to the deep violet-black (magnetite). Some guards are made of grained iron (*mokume-tetsu*), corresponding to watered or damascened steel, with the surface etched, so as to bring the different textures into relief.

Especially in late works, *koshirae* may be decorated using different metals applied in different portion of the object. Others, are compositely structured using different metals, in the styles known as *mokume* and *guri-bori*. The former term is applied to the result of a process in which layers of various copper alloys, as well as silver, and sometimes gold, are soldered together into a single sheet, which is then folded, crumpled, or dented. The resulting uneven surface is then cut or smoothly filed and treated with the necessary etchants so that the resulting surface may be compared to that of wood (which, incidentally, is what the word *mokume* means). Sometimes this *mokume* is only used as a thin sheet applied on a solid copper core, but some pieces are made of bulk *mokume*. In *guri-bori* (a technique borrowed from lacquer-work) several sheets of metals and alloys are flattened and welded together. The treatment consists merely in cutting deep V-shaped grooves into the metal layers sandwich; their slopes, after etching, reveal the alternation of patina-colours.

Several other decorative methods were employed: surface pattern and finishing, piercing and openwork, relief-modelling and etching, inlay, overlay, and incrustation, engraving and chasing, to mention a few.

The samples

The characterization of the inner structure of composite artefacts, made according to the *mokume* and *guribori* techniques, can lead to a deep comprehension of the Japanese metallurgical technology, which reached its highest artistic peak during the Edo period. As I have already demonstrated, in section 5.6 of this Chapter, white beam and energy-selective neutron imaging represent the ideal suitable techniques, actually available, in order to investigate, non-invasively, such valuable objects.
In order to achieve these goals, we have analyzed the *guri-bori* structure of the whole set of metal components in a *koshirae* (*fuchi*, *kashira*, and *tsuba*) and the *mokume* structure of a *kozuka* and a *tsuba* (see Fig. 5.62 below). All samples were made available from the Japanese section of the Stibbert Museum in Firenze (Italy),

The *tsuba,* or hand-guard, is the most important component of the fittings and is generally in the form of a flat disc. Its shape is usually regular and always rather compact, with a wedge-shaped opening, located in the centre, to insert the tang. Around the tang hole there is a wide flat area, where the *seppa*[5.8] usually stands, known as the *seppedai* (washer-stand). The *seppedai* is normally plain and used to engrave the signature placed on the side next to the hilt and rarely on the exposed part. On either side of the *tsuba* there may be holes for the insertion of knives or pins.

Tsuba are almost always made of metal, though in parade swords they may be also manufactured with lacquered leather, leather combined with wood, or *papier-mâché*. The usual metals employed for *tsuba*, or at least the background material on which the decoration is placed, are iron, steel, copper, and copper-alloys (always patinated) [Robinson 1970].

As already mentioned, two *tsuba* have been investigated in the present study (Fig. 5.62 *a* and *b*). The samples are approximately 80 mm in diameter and 5 mm in thickness. Both components are in copper-alloy and, probably, *shakudo*; one has a *mokume gane* decoration, the other one is made in *guri-bori.*

The *fuchi* (collar) and *kashira* (pommel-cap) have the mechanical function to strengthen the hilt at both ends. The term *kashira* means literally ‘head’; *fuchi* is a general term for a border.

The ordinary *fuchi* consists of a flat band of metal up to half an inch wide that encircles the hilt at the guard end and is easily removable. Its base is filled with an oval plaque, usually copper, pierced with a hole to insert the tang.

The *kashira* ordinarily comprises a similar flat band surmounted by a flat or gently rounded top, but also *kashira* with completely rounded form are common. The whole of *kashira* and the band of the *fuchi* are normally decorated, often *en suite*, sharing the same subject [Robinson 1970].

The analyzed *fuchi is* approximately an oval-shape disk 30 mm major axis, 15 mm minor axis and 10 mm thick (Fig. 5.62 *d*). Its corresponding *kashira* has a similar form and a thickness of 10 mm (Fig. 5.62 *c*). Both the objects are examples of the *guri-bori* technique made of copper-alloy and probably *shakudo.*

The *kozuka*, is the handle part of a small knife, carried in a slot placed on one side of the scabbard of certain swords. The *kozuka* is exposed and just rising above the upper surface of the *tsuba*, which is pierced to allow the *kozuka* to pass through it. Although a *kozuka* may very occasionally be found on a sword mounted as a *katana*, it was more often found in the *koshirae* of smaller weapons.

The word *kozuka* means, literally, ‘little hilt’, and there has been some differences of opinion on whether the term should be used for the complete knife, or only for its hilt. The latter hypothesis seems to be supported by the etymology of the word, and will be followed here. The whole knife may be called *kogatana*, a term applicable to any small knife. Its place is always on the *ura* side of the scabbard, and its most familiar form, which dates back to the 16th century, is a thin flat pointed blade thrust into a fat long handle. The latter, the proper *kozuka*, measures up to 10 cm in length and 15 mm in width.

Besides the usual metals and alloys, also wood (polished, carved, or lacquered) is found, as well as ivory and kindred materials. Because of its placing, the *kozuka* decoration is necessarily confined to the outer face, and is often set within a narrow raised border [Robinson 1970].

The studied *kozuka* is 80 mm long, 15 mm wide and 5 mm thick (Fig. 5.56 *e*). The artefact has a *mokume gane* decoration made in copper-alloy and *shakudo*.

[5.8] The *seppa* is a washer used in front and behind the *tsuba* to tighten the fittings.

Figure 5.56: *a*) the *guri-bori tsuba*, *b*) the *mokume tsuba*, *c*) the *kashira*, *d*) the *fuchi,* and *e*) the *kozuka* are reported.

Experimental set-up

Since some of the samples (*tsuba*, *fuchi* and *kashira*) feature a plate-like shape, which limits the applicability of ordinary tomography, neutron laminography technique was applied in order to reconstruct their whole volume structure. Standard neutron tomography, instead, was used to characterize the *kozuka*. The imaging study was performed at the CONRAD II instrument at the Helmholtz-Zentrum Berlin (HZB), basing on the configuration optimized during the test measurements already discussed (Chapter 5-section 5.6).

In Table 5.9, 2nd and 3rd columns, the set-up for white beam tomography and laminography, applied at first to determine the distribution and the density of the different alloys used to forge the *koshirae*, is reported.

At the next stage, the two *tsuba* and the *fuchi-kashira* set were investigated for phase discrimination through the *energy-selective laminography* method (Tab. 5.10, 2nd column). Taking advantage of the abrupt change of the attenuation coefficients at the Bragg cut-off, specific of each phase, the method gives the possibility of modifying the image contrast to map different phases.
I would point out that samples very similar to the investigated ones, all composed by copper and copper alloy layers, were previously characterized by time of flight neutron diffraction, obtaining information on the quantitative amount of copper and *shakudo* phases thus demonstrating that the different surface colours are due to *mokume* or *guri-bori* structure and not just to different patination [Barzagli *et al.* 2013].
The copper alloys maintain the same lattice structure as pure copper (*fcc*) while the lattice parameter changes according to the amount and type of solute mixed in it [Grazzi *et al.* 2010, Pearson 1958]. The monochromator available on CONRAD II (DCM) [Treimer *et al.* 2006] is good enough to discriminate copper and *shakudo* alloys since the lattice parameter difference is larger than its resolution.
Moreover, in order to ensure a homogeneous neutron energy distribution in the horizontal direction inside the acquisition window, a new arrangement was given to the

monochromatic device. Basing on the results of previous test measurements, the configuration has been improved by simply rotating the device of 90°.

Preliminarily to the ESL, a *radiographic energy scan* was carried out from 3.5 Å to 4.5 Å with a step of 0.02 Å, crossing the 111 FCC Bragg edge for copper and copper alloys (Tab. 5.10, 3rd column). The radiographic energy scan has been exploited to correctly choose the number and value of the neutron wavelengths to be used for the subsequent laminography.

Performing the measurements, the samples have been wrapped in aluminium foil and inserted into a purposely prepared aluminium holder (see Appendix B).

Imaging method:	**White beam laminography**	**White beam tomography**
Wavelength:	polychromatic	
L/D:	500	
Scintillator:	^{6}LiF 50 µm	^{6}LiF 100 µm
Camera:	Andor DW436N-BV CCD3325 2048x2048 16 bit	
Field of View:	130x130 mm	
Object-Detector-D:	90 mm max.	30 mm
Pixel size:	67 µm	
Exposure Time:	40 s	20 s
Rotating Angle:	500	
Projections:	0°-360°	
Tilt angle:	20°	-

Table 5.9: The different instrumental set-up employed for white-beam measurements.

Imaging method:	**Radiographic energy scan**	**Energy-selective laminography**
Wavelength:	from 3.5Å to 4.5Å with step of 0.02Å	4.15Å/ 4.18Å/ 4.25Å
L/D:	333	
Scintillator:	^{6}LiF 100 µm	^{6}LiF 400 µm
Camera:	Andor DW436N-BV CCD3325 2048x2048 16 bit	
Field of View:	130x130 mm	
Object-Detector-D:	20 mm	90 mm max
Pixel size:	65 µm	67 µm
Exposure Time:	80 s	130 s
Rotating Angle:	-	300
Projections:	-	0°-360°
Tilt angle:	-	20°

Table 5.10: The different instrumental set-up employed for energy-selective measurements.

Results

White beam laminography

- *Guri-bori tsuba*

A multi-layered structure emerged from the analysis of the computational laminographic reconstruction of the *tsuba* decorated in *guri-bori*. Observing the axial (Fig. 5.57-*a*) and the transversal (Fig. 5.57-*b*) cross sections, distinct sheets are delimited and outlined by bright spots aligned in layers parallel to the flat surface of the *tsuba*. Clouds of spots are spread among sheets that are around 0.30 mm thick (Fig. 5.57-*d*).

All samples were characterized trough a preliminary Neutron Activation Analysis test measurement. This analysis was used to evaluate the elements (and their isotopes) in the samples with the aim of testing its activation rate and decay time as a function of the

exposure time [Alfassi 1990]. Other than the expected copper and gold, traces of silver, arsenic, and antimony were detected which can be easily attributed to impurities in the metals used to produce the various alloys.
The traditional components employed in these decorative techniques were relatively malleable metal sheets (pure elements and alloys), which would form a thin molten layer on their surface. This was very useful in the traditional welding techniques to connect the layers together [http://www.silversmithing.com/1mokume.htm]. Moreover, the possible colour combinations made gold, copper, and silver alloys particularly eligible for metal-smiting.

On the other hand, considering the high attenuation coefficient of the revealed white spots, the necessity of using a soldering material with a melting point lower then copper and copper-alloy, and the good wettability of the employed metals, then we are led to take into account the possibility that an organic soldering material was probably used for joining the laminae. In facts, according to literature [Toshikatsu Nakasato 1998, http://www.nippon-kako.co.jp/patent.html; http://nekotani.lix.jp/diary/index.php?e=345], *urushi*[5.9], the traditional Japanese lacquer, was employed for manufacturing metal artefacts.
Even though several experts have been involved in the discussion, this aspect still remains debatable. Although controversial opinions were expressed about the assembling method, it should be considered that some traditional metallurgical procedures have been transmitted orally to the present, while others have been lost and often recovered by contemporary craftsman on a personal level, usually referring to partial information reported in old written documents, whose reliability is uncertain. In conclusion, we not able to exclude that, in this case, the application of the *urushi*,as soldering material, was applied.
Each lamina was probably stacked over another, spreading a thin layer of lacquer on the contact surface and repeating the procedure to assemble the desired number of plates into a single block. The whole work-piece was probably heated, causing the filling organic material to rapidly harden and the metallic components to bond. Pressure and heat were applied to stably solder the sheets forming one homogenous mass of distinctive layers. Thus, the thin layer of lacquer, between metal sheets, is likely responsible of the visible bright spots in the tomographic reconstruction.

Finally, a bright patina is observable on the surface of the *tsuba* at the correspondence of the chiselled decoration. We mention, here, that in order to increase the contrast between the laminated layers, many *guri-bori* items are coloured by the application of a patina (a controlled corrosion layer) aiming to accentuate, or even totally change, the colours of the metal surfaces.

[5.9] The term *urushi* has been used to define the lacquer derived from the sap of a tree indigenous to China and Japan, species Rhus verniciflua, commonly known as the “Lacquer Tree” [Gettens and Stout 1966]. From a more scientific point of view, the *urushi* can be defined as a colloidal system of a water-in-oil emulsion. Drops of water, containing polysaccharides and an enzyme, are dispersed within an oily phenol phase (*urushiol* and its polymers) in which insoluble glycoproteins and soluble gummy matter act as emulsifiers. The phenols oxidize in laccase enzyme and polymerize: upon evaporation of the water content the lacquer is hardened [Brommelle and Smith editors 1988].

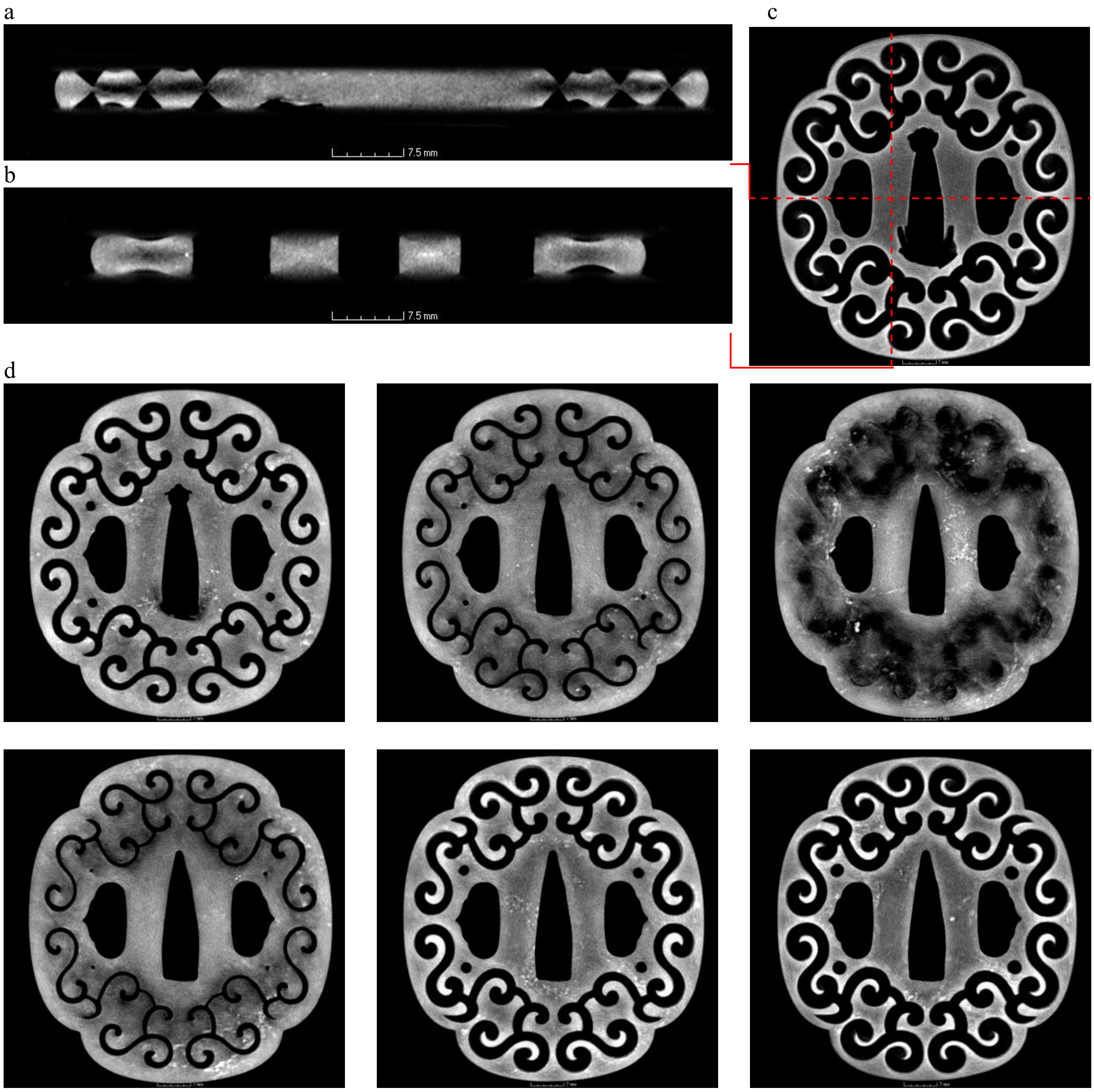

Figure 5.57: Images *a* and *b* are orthogonal views of the *guri-bori tsuba*. Their position is shown by the red dotted lines in the virtual cross section in *c*. The sequence *d* is composed by slices taken a different levels of the sample going from one face to the opposite one.

- *Guri-bori fuchi*

The constructive procedure of the *guri-bori tsuba* was applied also for the *fuchi*. The collar appears to be made by bending a multi-layered plate of copper and copper-alloy. Since the attenuation cross section of the material composing the sheets is similar, also in this case, the single laminae can be distinguished basing on the bright spots visible in between. The spots are likely due to the application of a filler joining the structure, even though little displacements among layers are visible (Figg. 5.58-*c*, cross sections 1st-3rd).

The ends of the collar were joined to one extremity and soldered together (Fig. 5.58-*b*, 2nd cross section). The structure was secured and fixed by a further plate (0.28 mm thick) placed on the inner surface. Here the junction is imperfect and some voids are visible in between (Fig. 5.58-*c*, cross section 4th).

The low gray value of the top covering layer respect to the material constituting the collar suggests the use of a different Cu-alloy. The flat pierced plate (2.57 mm thick) was probably joined by heating and solderingto the bent plate. Also in this portion, empty round areas and the bright soldering material can be recognized at the junction. Elliptical voids are elongated parallel to the junction showing a minimum diameter of 0.25 mm and a maximum diameter of 0.90 mm (Fig. 5.58-*a*).

The element detected by means of NAA attested the use of copper in alloy with gold. Apart from As, the other trace elements detected in the *guri-bori tsuba* are absent (Sb and Ag). We explain this fact suggesting that, in this case, a more accurately refined alloy was probably employed.

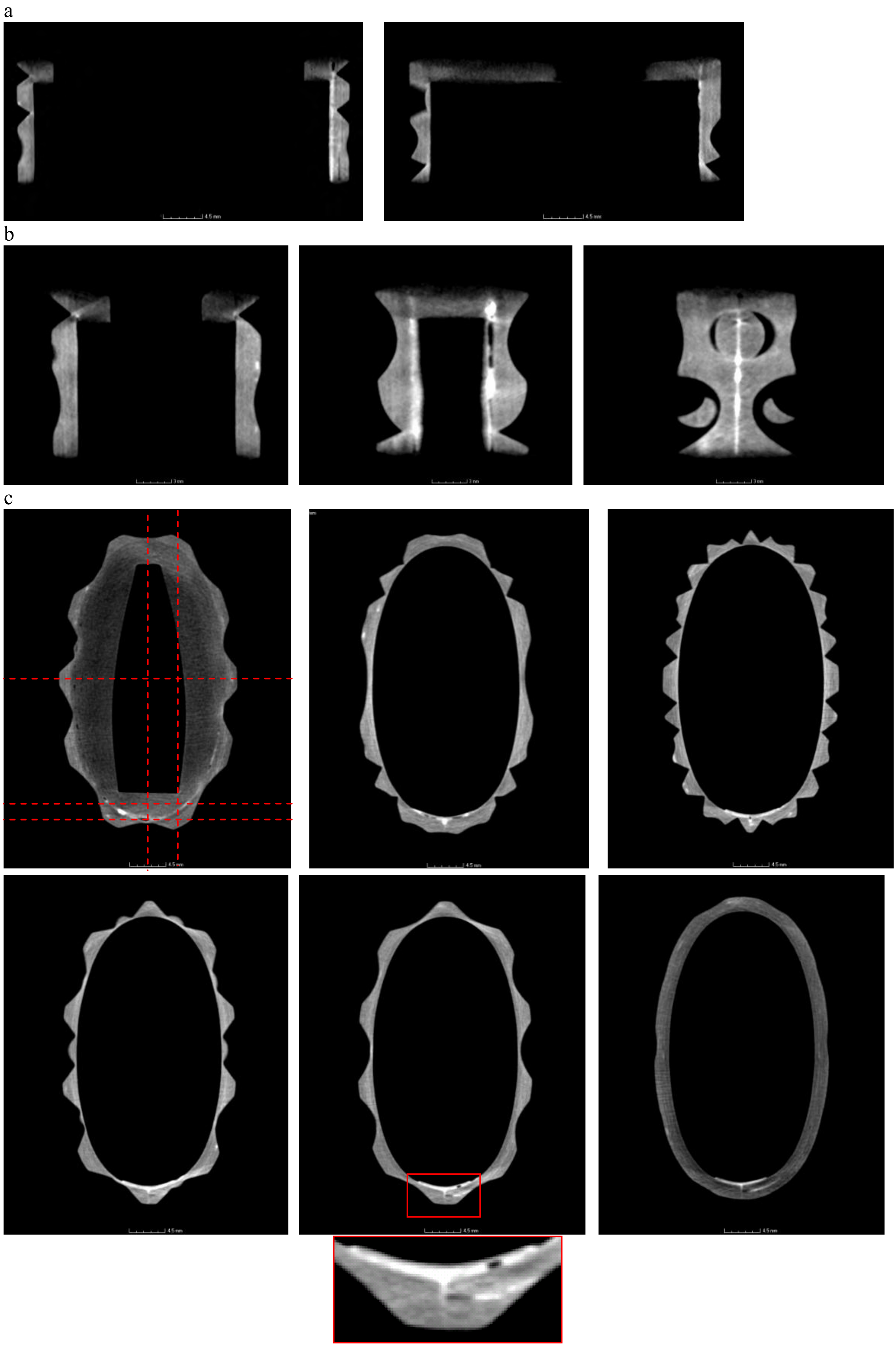

Figure 5.58: Here the orthogonal views acquired cutting the *fuchi* along the three main directions are shown. The slices presented in *a* and *b* are obtained by virtually cutting the object at the position indicated by the red dotted lines and reported in the first cross section in *c*. Crossing the sample from the upper surface to the back, the orthogonal views in *c* clearly shown the multi-layered composition of the collar. In the 5th section, the red frame enlarges a detail of the soldering between the two ends of the structured border; the soldering material, the fastening plate and the voids are visible.

- *Guri-bori kashira*

The *kashira* was made by giving a hemispherical shape to a multi-layered block constituted by laminas around 0.25 mm thickness, arranged and joined in the same structure detected for the other *guri-bori* samples. Inner surface with bright drops of a high absorbing material are visible as traces of the soldering material flowed during the making (Fig. 5.59).

The same elements found into the *kashir*a are detected for the *fuchi* (Cu, As, Au). So that, this two components probably belonged to the same original set, while the *tsuba* probably pertains to another mounting.

We conclude noting that a bright finishing patina was revealed for both *fuchi* and *kashira*.

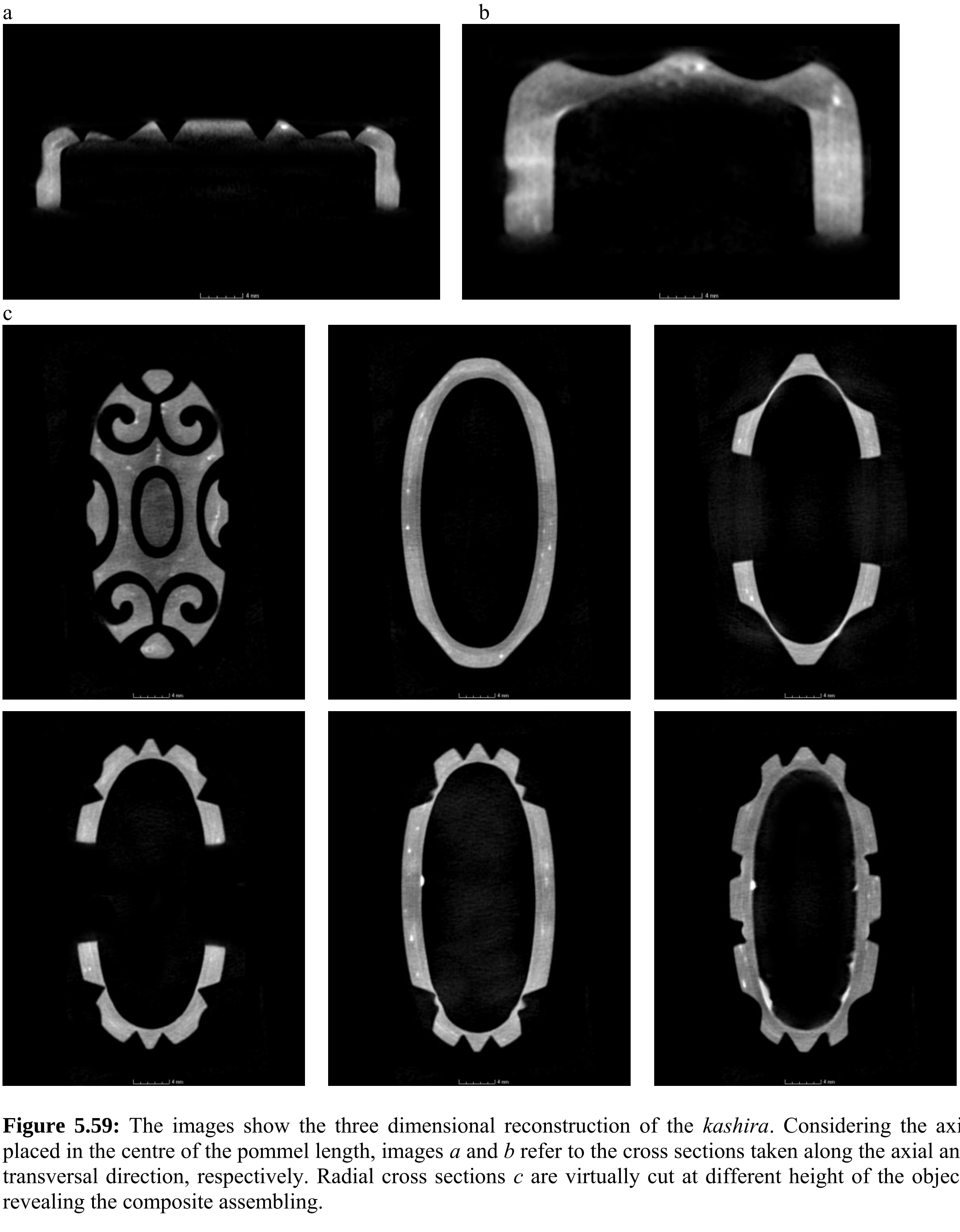

Figure 5.59: The images show the three dimensional reconstruction of the *kashira*. Considering the axis placed in the centre of the pommel length, images *a* and *b* refer to the cross sections taken along the axial and transversal direction, respectively. Radial cross sections *c* are virtually cut at different height of the object, revealing the composite assembling.

- *Mokume tsuba*

A different assembly was observed for the *mokume* decoration of the *tsuba* (Fig. 5.60). Here a base-plate around 2.06 mm thick was joined to a decorative layer 0.23 mm thick attached to one side. Its pattern is obtained by repeating a multiple step process of folding and shaping a multi-layered block of copper and copper-alloy.

The two sheets are fixed together by a soldering material presenting the same features already detected for the other *koshirae*. A bright layer is visible in between, and little round voids, large at least 0.46 mm in diameter, can be detected (Fig. 5.60-*a*).

The cloud of bright spots is more dense at the proximity of the pierced portion of the *tsuba*. The two layers are probably worked separately and joined later. When the soldering was applied and the layer attached, the filling diffuses, flowing out through the edges.

Moreover a piece of metal of different composition is visible at the extreme edge of the central piercing, probably applied to fix and secure the structure (Fig. 5.60-*c*, cross section 2nd).

Copper, gold, arsenic and antimony are detected thought NAA, suggesting the adoption of a different copper alloy for the making of the *tsuba*.

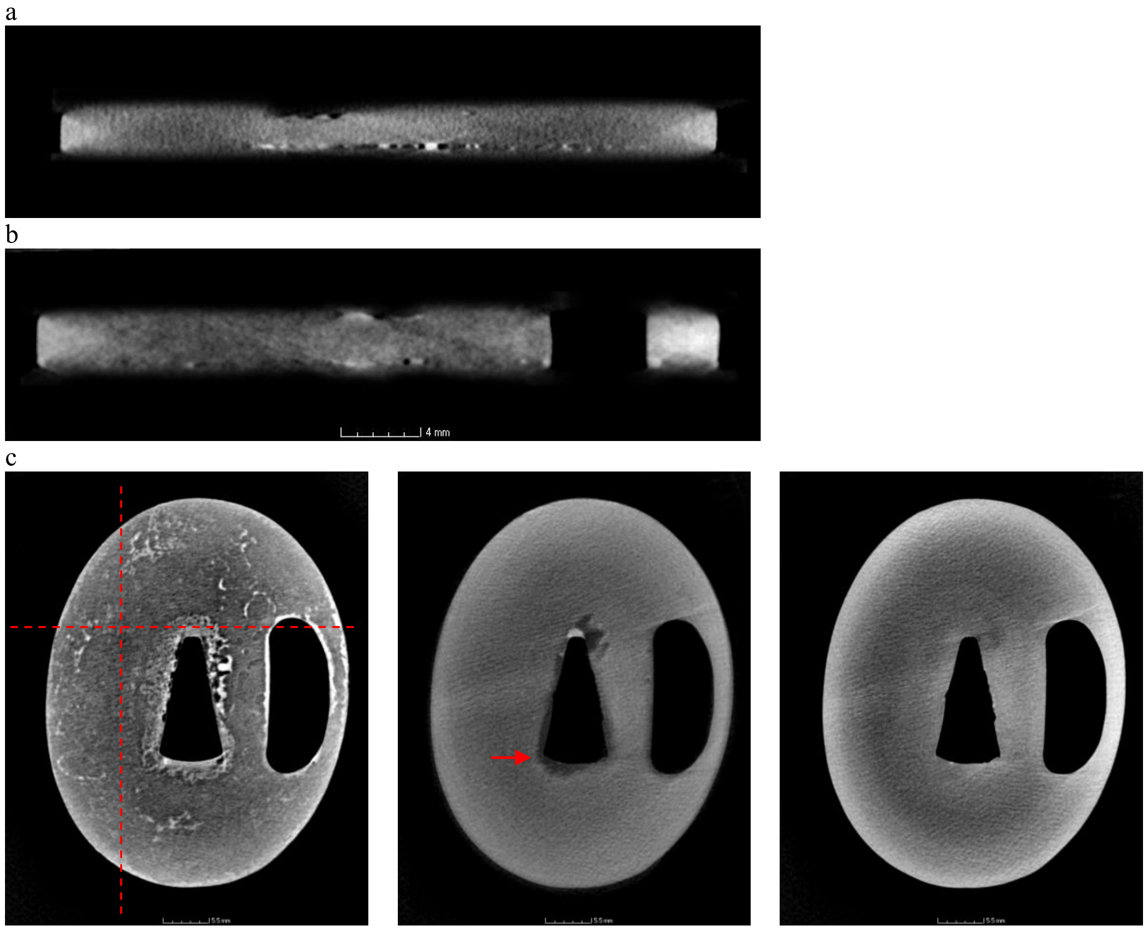

Figure 5.60: Images *a*, *b* and *c* are respectively the radial, transversal and axial cross sections of the *mokume tsuba*, considering the axis placed in the centre of the sample main length. In the first section in *c*, the red dotted lines indicate the virtual cutting position of the slices presented in *a* and *b*. The red arrow indicates in the 2nd figure in *c* the presence of a piece of metal of different composition, probably applied to fix and secure the structure.

- *Mokume kozuka*

The tomographic reconstruction of the *kozuka* revealed a composite assembling. It was constituted by a main sheet with a "U"-shaped radial cross section (Fig. 5.61-*c*). The ends of the "U" arms are joined to a second lamina by applying a soldering substance. According to the attenuation value, the filling substance can be considered of the same composition of that found in the others samples. On the external surface of this second sheet, a further plate was fixed. This lamina, featuring the typical *mokume-gane* decorative pattern is visible from the front projection in Fig. 5.61-*a*, 2nd cross section. Here, no trace of soldering material was identified, suggesting that the decorative layer was obtained using at least two different coloured metals or alloys, compatible in their properties of ductility and malleability, and welded together. The decorative plate was subject to further forging and shaping in order to create the desired pattern and finally soldered to the body of the handle.
The presence of voids and bubbles, visible between layers, suggests a lesser care spent in the making procedure. Moreover, the two plates present a displacement of 0.25 mm and a brush-like stroke profile is visible in between where the soldering material was applied for joining (Fig. 5.61-*a*, 2nd cross section). One of the bases of the grip was closed by soldering a properly shaped plate 1.96 mm thick. The inside surface shows a slightly bright layer probably due to the diffusion of the filler. At the soldered edges, the bonding material flowed out the junction, aggregating in spherical bubbles. Voids are visible between junctions and are characterized by a max diameter of 0.89 mm and min detectable diameter of 0.1 mm (Fig. 5.61-*c*, 1st cross section).
The external decorated surface was probably patinated to enhance the typical *mokume* pattern, as suggested by the brightness of its surface. On the decorated surface, the filler diffused among the badly soldered layers of the decoration.
Basing on the morphological feature and the attenuation value, some remains of organic material can be recognized inside the hilt.
This structure is consistent with the description provided by B.W. Robinson 1970; the *kozuka* decoration is worked on a separate plaque (*ji-ita*) and usually confined to the outer face within a narrow raised border. The back may be composed of two or even three different alloys joined together [Robinson 1970].

Finally, the NAA measurements revealed the same elements detected for the *tsuba* in *mokume*. This result, together with the similar making procedure of the *mokume* pattern, suggests the belonging of this *mokume* sample to the same mounting.

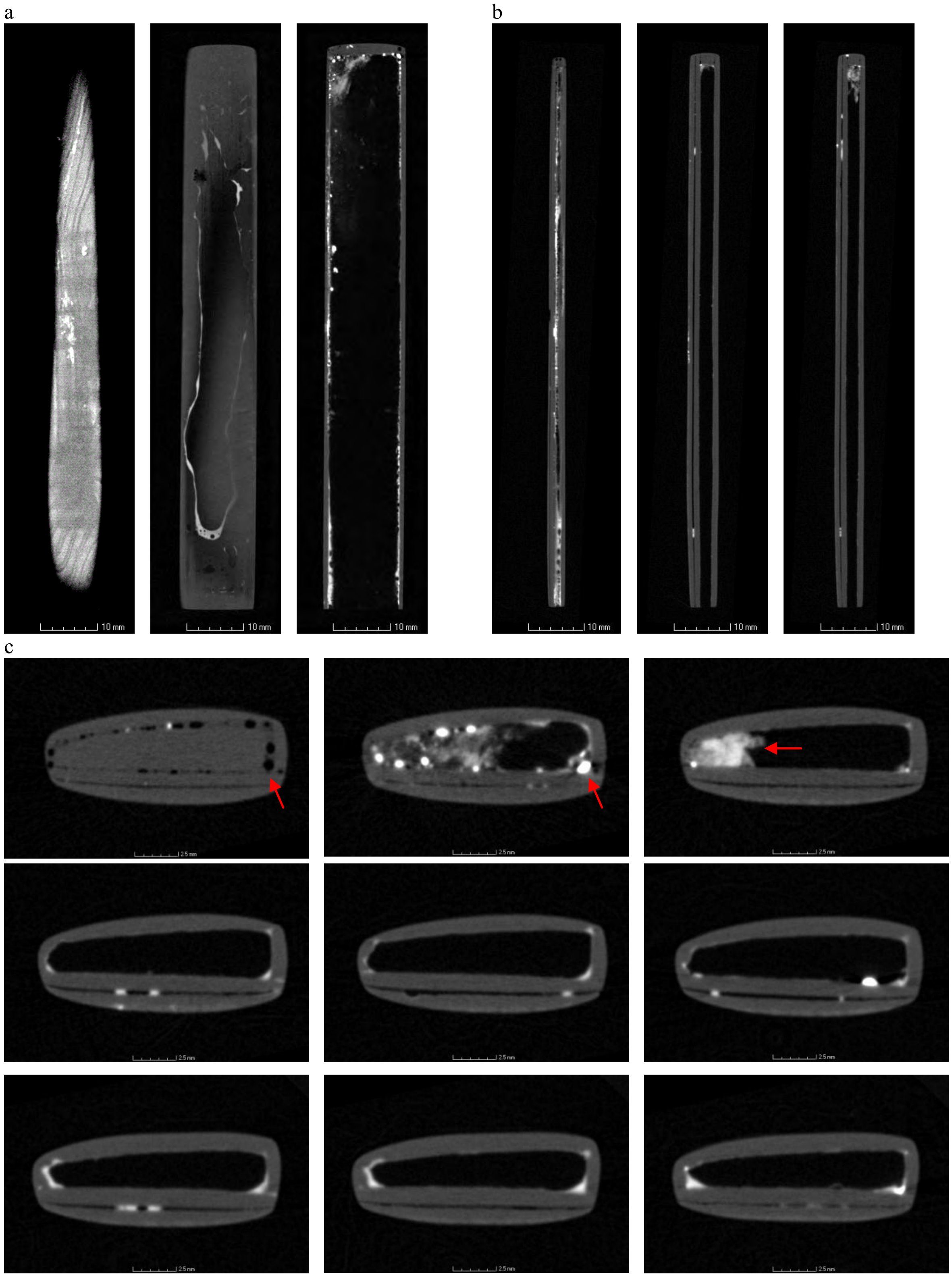

Figure 5.61: Considering the axis placed in the centre of the handle length, images *a* and *b* refer to the cross sections taken along the radial and transversal direction, respectively. Axial cross sections *c* are virtually cut at different height of the *kozuka*. In *c* the red arrows highlight the presence of voids in the 1st slice, the soldering material in the 2nd section and the organic material in the 3rd image.

Energy-selective laminography

Aiming to obtain material discrimination, a radiographic energy scan was carried out in order to select the proper wavelengths to enhance the contrast at the Bragg cut-off for copper and copper-alloys. Three independent reconstructions were performed for each set of measurements, taken at the three different neutron wavelengths, namely 4.15 Å, 4.18 Å and 4.25 Å. The image stacks so obtained were further processed, by progressively subtracting the latter tomography from the former. The images acquired at 4.15 Å were above the 111 Cu Bragg-edge, while the ones at 4.22 Å and 4.30 Å were placed below the edge for Cu and Cu-alloy respectively.
The contribute due to the presence of Cu was evidenced by subtracting the 4.15 from the 4.22 Å image, while Cu-alloy based elements were mapped by subtracting the 4.22 Å from the 4.30 Å image, according to the method described in Chapter 5.

A typical drawback of the neutron beam monochromatization is a sensible reduction in the flux. Before subtraction, in order to increase the statistics, each laminographic stack was processed by applying a median filter, and a projection was applied every 50 slices along the axis orthogonal to the flat surface of the layers. This procedure has been done for all samples.
In the case of the energy-selective laminography of the *guri-bori tsuba*, no material-contrast improvement was evidenced, both staking the slices parallel (fig. 5.63) or orthogonal (Fig. 5.62) to the flat surface of the layers. Even though a homogeneous distribution of the neutron wavelengths is present inside the acquisition window, the narrow wavelength displacement among the Bragg-edges of the copper and the other copper-alloy composing the sample, the thickness of the sheets and the low statistic did not allowed to detect different components. The same consideration can be applied to the result from the *mokume tsuba* (Fig. 5.64).

On the contrary, sheets of different composition have been observed on both *fuchi* (Fig. 5.65-*a*) and *kashira* (Fig. 5.65-*b*). The image resulting from subtracting the stack above and below the copper Bragg-edge (Figg. 5.65-*a* and *b*, slices 4.15-4.18 Å) evidenced, in brighter grey tone, the presence of a plate made of Cu. The brighter area in the image 4.22-4.30 Å can be attributed to the presence of copper-alloy based material (Figg. 5.65 -*a* and *b*, slices 4.18-4.25 Å). In this case, due to the shape of the samples, it was possible to merge a more relevant number of slices of the stack, thus improving the statistics.

- *Guri-bori tsuba*


4.15-4.18 Å

4.18-4.25

Figure 5.62: Here reported, the results of the subtraction process at wavelength values above and below the Cu and Cu-alloy Bragg edge, respectively. The *guri-bori tsuba* is stacked and projected orthogonally to the flat surface of the layers.

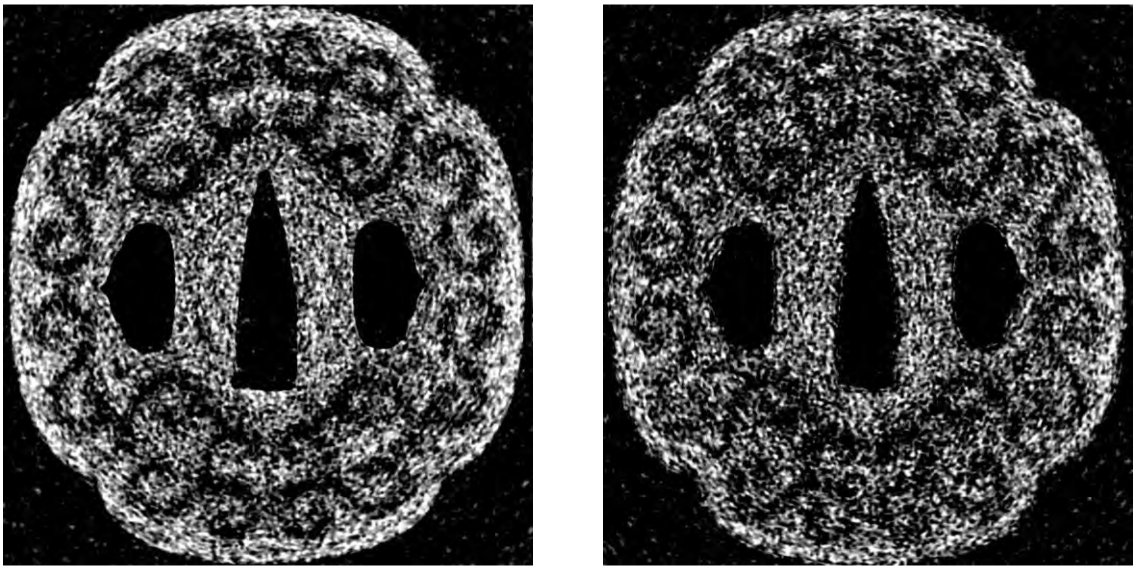
4.15-4.18 Å

4.18-4.25 Å

Figure 5.63: The results of the subtraction process at wavelength values above and below the Cu and Cu-alloy Bragg edge, respectively. The *guri-bori tsuba* is stacked and projected parallel to the flat surface of the layers.

- *Mokume tsuba*

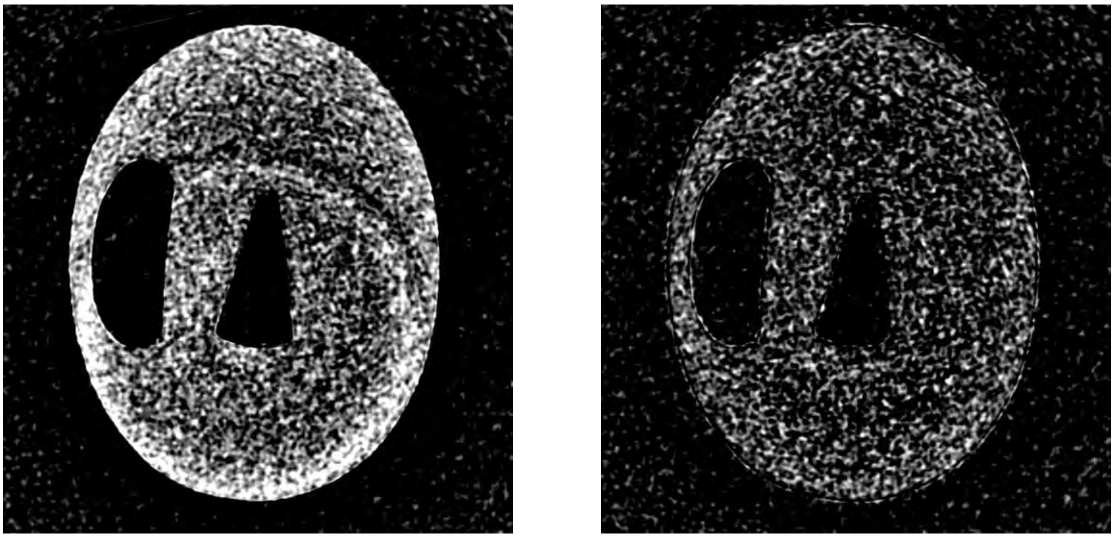
4.15-4.18 Å

4.18-4.25 Å

Figure 5.64: The processed slice are reported for the *mokume tsuba*, showing the results of the subtraction at wavelength values above and below the Cu and Cu-alloy Bragg edge, respectively.

- *Guri-bori fuchi and kashira*

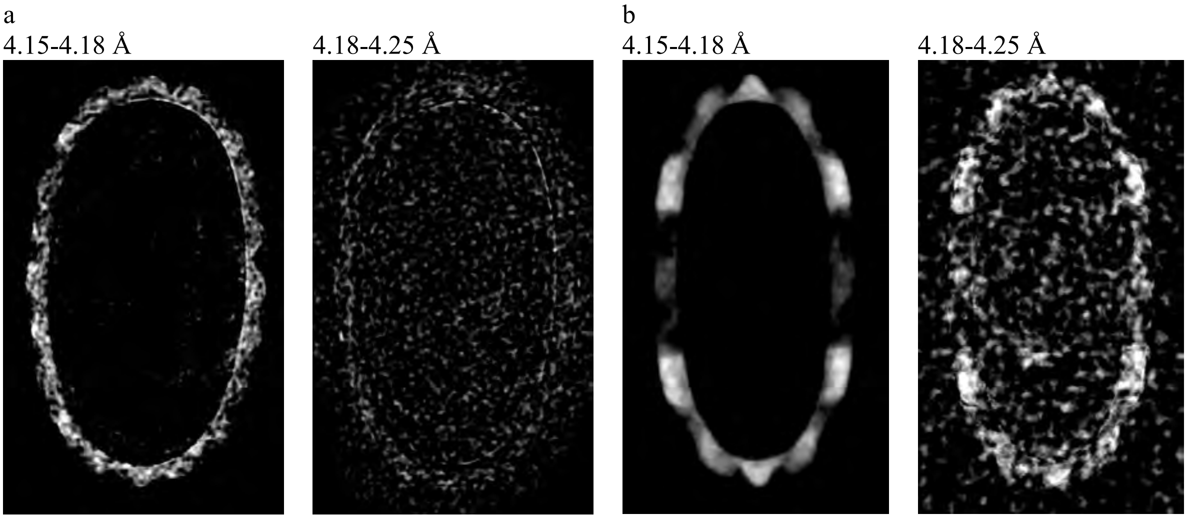

Figure 5.65: The processed energy-selective laminographic stacks for the *fuchi a* and the *kashira b* are shown.

Conclusion

Koshirae, the mounting components of the Japanese sword, pertaining to the Edo periods forging traditions, were studied in the present section.

Neutron white beam and energy-selective imaging were used to investigate, non-invasively, the *mokume* and *guri-bori* decoration of two *tsuba*, one *kozuka* and a set of *fuchi* and *kashira*. In the case of flat samples, the laminographic method was applied proving again its validity in morphological characterization. Moreover, the contrast enhancement induced by the selection of an appropriate neutron wavelength was exploited to increase the image contrast for the different materials composing the analyzed specimens.

White beam tomography and laminography allowed identifying peculiar characteristics related to the forging methods of these flat objects:

- inner structure, resulting from the particular manufacturing process, were analysed all over the samples;
- presence of soldering was mapped;
- patination of the surface was established;
- defects originated from the assembling procedure were identified clarifying the working method.

Concerning the energy-selective laminography, the present measurements clearly demonstrate that the proposed method can help to characterize the inner structure and composition of metal artefacts, non-destructively, in combination with other neutron inspection techniques.

Even though a homogeneous distribution of the neutron wavelengths was achieved inside the acquisition window, the narrow wavelength displacement among the Bragg-edges of the copper and the other copper-alloy composing the sample, the thickness of the sheets and the low statistic represent limiting factors in the possibility to distinguish different components made of copper and copper-alloys.

5.8 The Roman Settlement of *Iulia Concordia*

Introduction

Iulia Concordia is an important Roman settlement (presently *Concordia Sagittaria*, Venice - Italy) founded at the North-Eastern boundary of the Roman Empire. The settlement was located near the main roman road that led to the *Noricum* region, a prominent location for iron ore supplying (Fig. 5.66).

Due to its geographical position, the city developed and assumed an important strategic role during the barbaric invasions in 2nd - 4th century A.D.. *Iulia Concordia* was well-known to have hosted important military forces and at least one workshop for weapon production, although the exact location of the archaeometallurgical site is still undetermined. During the last excavations of the site, evidence of metal working activities and a huge number of arrowheads (*sagittae*) and *styli* were found [Di Filippo Balestrazzi and Vigoni 2009; Vigoni 2006], which are now part of the *Museo Nazionale Concordiese di Portogruaro* collection (Venice, Italy) [Brusin *et al.*1960, Zovatto *et al.* 1971].

Figure 5.66: On the left, the map reports *Regio X*, one of the *regiones* in which the Emperor Augustus divided the Italian territory around 7 A.D.. The location of the settlement of Iulia Concordia is highlighted by a red square. On the right, a reconstructive hypothesis of the Roman colony of *Iulia Concordia* is shown. A distinctive feature of the urban topography was a navigable artificial channel that in the southern part of the town replaced one of the main roads. Connecting the rivers that flow through the city, the channel created a waterway for the transfer of goods and people. [http://www.rufinoturranio.it/ita_concordia_sagittaria_romana_associazione_culturale_onlus_rufino_turranio_provincia_venezia_veneto_italia.asp]

5.8.1 Morphological characterization of Roman *styli*

The samples

During excavations in the end of the 18th century a huge number of metal artefacts were discovered in the bottom of the main channel of the city of *Iulia Concordia*; among them about one hundred of iron *styli* were found. The *stylus* is a small bar, made from either iron, bronze or bone, usually round in cross section, shaped with a sharp point on one end and surmounted by a *spatula* on the other one: it was used for writing, with the pointed end, and for erasing characters, with the opposite flat end, onto the wax coated surface of wooden flat tablets. Even though few typological studies have been conducted, *styli* are characterized by several different shapes, hypothetically related to their age and provenance [Manning 1985]. Furthermore, there is no evidence of previous investigations about the production processes and the working techniques used by Roman for *stylus* manufacturing.

In order to investigate composition, assembly method, and structural variations among different *styli* typologies, as well as their conservation *status,* an archaeometallurgical study has been developed in cooperation with the *Soprintendenza dei Beni Archeologici del Veneto* (E. Pettenò, F. Rinaldi and V. Tinè).

Due to their small size, *styli* are usually excavated strongly corroded; on the contrary, the ones found from *Concordia* are exceptionally well preserved: thus, traditional (invasive) analytical methods cannot generally be applied and a non-invasive approach is mandatory. Neutron techniques, which are able to identify the morphology and the inner structure of artefacts have been applied in order to determine their manufacturing methods.

For the analysis presented in this section, 91 examples of Roman *styli* from *Iulia Concordia* settlement, pertaining to different typological categories assigned through the stylistic analysis by archaeological experts, have been analysed (Fig. 5.67).

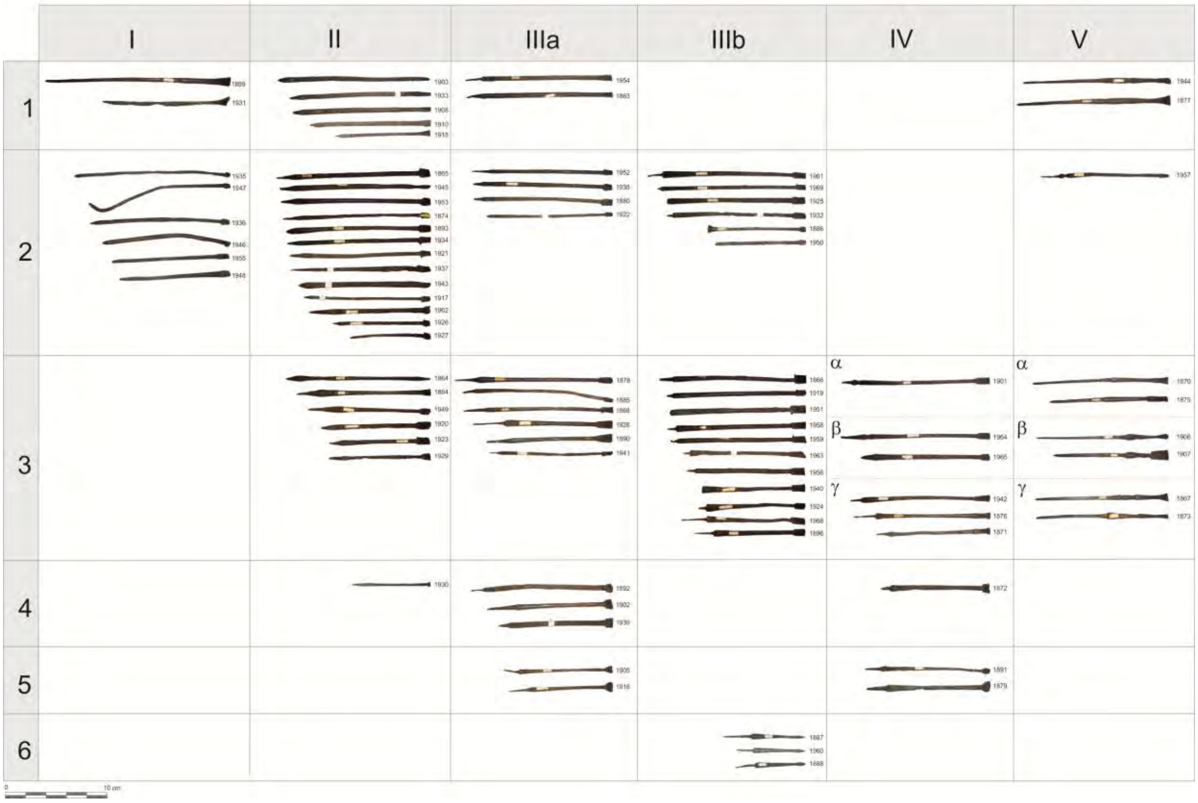

Figure 5.67: Distribution map of *styli* found in the excavated area, differentiated on the base of the typological classification.

Experimental set-up

The neutron imaging study has been performed at the NEUTRA beam line, operating at the spallation neutron source SINQ at PSI. The measurements were carried out at the midi position, with an aperture size D of the diaphragm at 29 mm, in order to achieve a L/D ratio of 350. The radiographies were acquired by irradiating the sample for 45s with a step-angle of 0.57° over 360° for tomographic reconstruction. Performing measurements, 5 open beam and 3 dark current images were taken for subsequent normalization and correction. A high performance 2048 x 2048 pixel-16 bit CCD camera system from Andor Technology and a ^{6}LiF/ZnS neutron scintillator screen (50 μm thickness), were used. In addition, the samples were positioned at the minimum possible distance from the scintillator plate (50 mm). The employed set-up resulted in a spatial resolution of ~100μm. The samples were divided in four groups of about 23 elements: they were wrapped in Al foil and placed in an Al pipe with a Gd strip marker at the bottom (Fig. 5.68).
Data acquisition was performed at two subsequent transmission windows with a vertical superimposition of few centimetres for each group to help merging the two blocks (apart from the group composed of the shortest *styli* in which the measurement was taken performing a single scan).
The data were processed through the software package Octopus for tomographic reconstructions [Dierick 2004].

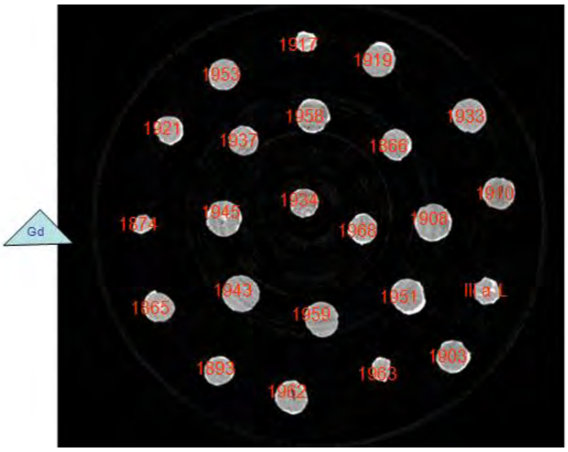

Figure 5.68 A tomographic reconstructed slice showing the *styli* arrangement and the position of the Gd marker placed for the samples identification after measurements.

Results

The tomographic reconstructions of *styli* allowed to identify peculiar structural components connected to the forging method and the burial conditions: well preserved residual iron metal, iron oxide alterations, internal cracks, and slag inclusions. It is important to evidence the presence, in many samples, of a crack crossing the whole length of the body and dividing it in two halves approximately of the same size. Relationships among the different structural typologies of the *styli* have also been identified.
According to imaging analysis, *stylus* structures can be grouped in two main classes.

ID	Typological classification			Integer	sectional crack			Rust	Inhomogeneities
					Body	Spatula	Tip		
1889	I	1			x	x	x		x
1931					x		x	x	
1935		2			x			x	x
1947					x	x		x	x
1936				x					few
1946					x	x	x	x	
1955					x				
1948					x		x	x	x
sac	II	1			x	x	x	x	few
1903					x				x
1933					x	x	x	x	few
1908					x		x	x	few
1910					x			x	x
1918					x	x		x	x
1865		2			x		x	x	few
1926				x					
1945					x	x	x	x	few
1953					x				few
1874					x			x	
1893					x	x	x	x	
1934					x		x	x	x
1921					x	x	x	x	few
1937					x	x	x	x	few
1943					x		x	x	few
1917					x		x	x	few
1962					x		x	x	
1927					x				few
1864		3			x	x	x		V few
1884					x		x		few
1949					x		x	x	x
1920					x		x	x	x
1923				x					x
1929					x			x	
1930		4			x				few
sac	III	a	c		x	x	x	xs	
sac			L		x	x	no	x	no
1954			1		x		x	x	few
1863				x					x
1952			2		x		x	x	few
1938					x		x	x	few
1880					x	x		x	few
1922					x				few
1878			3		x		x		few
1885					x	x		x	x
1868					x	x	x	x	few
1928					x	x		few	
1890					x	x	x	x	x
1941				x					
1892			4		x				x
1902					x				x
1939				x					
1905			5		x	x		xs	x
1916					x		x	x	
1961		b	2		x		x	s	
1969					x		x	x	x
1925					x	x		x	x
1932					x			x	few
1886					x			s	
1950					x		x	x	x
1866			3		x	x	x	x	x
1919					x		x	x	x
1951					x	x	no	x	few

1958					x	x		x	x
1959					x			x	x
1963					x		x	x	few
1956					x	x	x	few	x
1940					x			x	x
1924					x		x	xs	x
1968					x				few
1896					x				x
1887			6		x			x	x
1960					x				
1888				x					few
1257	IV	2		x					x
1901		3	α		x		x	x	
1965			β		x	few	few	few	few
1964					x	x	x	x	x
1942			γ	x					few
1876					x				x dec
1871					x	x	x	x	xs
1872		4			x			x s	x
1891		5			x				X dec
1879					x	x		x	few
1944	V	1			x	x	x	x	
1877					x		x		
1870		3	α		x		x	x	few
1875					x		x	x	x
1906			β		x		x	sx	few
1907					x				
1867			γ		x		x	x	x
1873					x				few

Table 5.11: Here, results from the neutron tomographic study are summarized. Each sample is reported with its own inventory number and it is referred to the stylistic classification attributed by the archaeological team. The *styli* are divided into groups basing on the body inner characteristics disclosed by tomographies: integer and cracked iron bar. Three different subsections are distinguished according to the extension of the break in the different components. Finally, the last two columns on the right side, define the inner presence of rust and dark non-homogeneous areas in the inside. Colours point out the attribution to a specific technological group and or subgroup, explained in the text here below.

The first main type consists of bars with integer body (Tab. 5.11, light-blue colour). This kind of *stylus* was probably made by simply hammering out a piece of iron into a proper shaped object. Among the 9 detected artefacts of this type, a huge amount of non-homogeneous dark portions are visible from cross sections (Fig. 5.69-1863). They are dark extended areas that can be interpreted as mixed volumes containing metal and poly-dispersed small slag inclusions and pores at different extents. It is important to underline that the pixel size is about 0.0548 mm while typical size for inclusions or pores can be smaller [Dillmann 2007, Blakelock 2009]. Among these samples, small diffuse large size inclusions are also visible, and their presence testify the use of a less accurate purified raw metal for the production of this *stylus*. On the contrary, samples 1926, 1941, and 1939 are characterized by a homogeneous inner body, probably produced following a more accurate metal refinement procedure, as deducible from Figure 5.69-1926.

The second main group of *styli* consists of samples all showing the presence of large size inner cracks located in the body. Subcategories are defined basing on the extension of the sectional crack, that is always crossing the whole body, in the tip and/or in the *spatula*, and according to the presence of slag inclusions and rust. Here the tomographic reconstructions of the first subcategory, characterized by samples exhibiting the presence of the crack crossing the *stylus* body only, are reported in Figure 5.70. (Tab. 5.11, white colour). A detailed description of the other subcategories is provided in Appendix D.

Taking into account the results obtained from the neutron tomography, the morphological study suggests two possible working processes adopted for the making of the second group *styli*. Concerning the first hypothesis, they should have been created by shaping twin halves of iron bars and soldering them together by hammering. Otherwise, *styli* should be made rolling up an iron flat thin long plate. When the cylindrical bar is formed by hammering, the extreme portion, tips and *spatula*, are shaped either extruding from one side or just shaping the combined parts into a different form. The presence of inner cracks confirm these hypotheses since the cracks are empty spaces, resulting from the process of soldering or rolling the iron plate over itself.
The presence of slag inclusions and rust inside the artefacts can be related to the care spent into the smithing process and to the burial conditions, respectively.

The following image-stacks are cross sections taken from the computed tomographic reconstruction of a selection of the analyzed *styli*. Each sample is virtually cut along three orthogonal directions: the upper image is always referred to the axial section, whose position is defined by the horizontal red line crossing the normal and transversal views, placed side by side on the bottom. Red dotted lines are linked to extra axial section, showed on the side of the image. The normal and transversal slices are acquired at the centre of the axial one. At the top of each slice-group, the sample reference number is reported. Moreover, the tomographic reconstructions are shown in false colour enhancing the contrast in order to help in detecting structural features: the green colour stands for iron, the dark-blue for slag inclusion rich areas, the yellow-orange for rust and decorations, finally, black stands for empty areas. As a matter of facts, a gradient bar is placed at the bottom of each figure: from blue to red, colours are associated to a rising macroscopic total attenuation cross section. The enlarged areas, framed in red, are filter-treated to point out specific structural characteristics inside the volume of the sample.

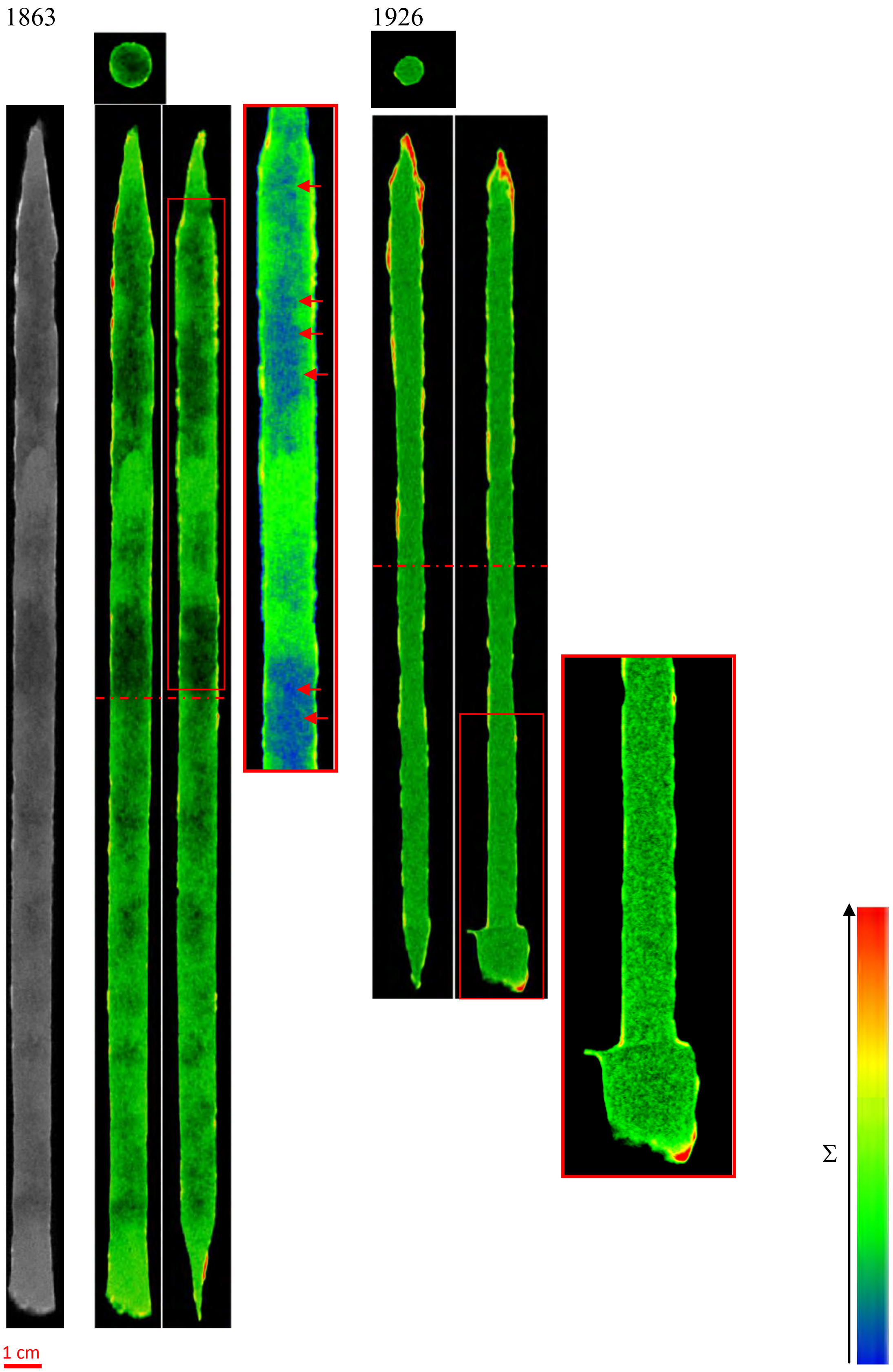

Figure 5.69: *Stylus* 1863 without inner fractures: non-homogeneous dark area and dark little ellipsoidal slag inclusions (indicated by arrows) are visible in the black and white image and evidenced in the false color one of this sample. On the contrary, they are missing in *stylus* 1926, as pointed out by the enlarged area on the right side of each image stack.

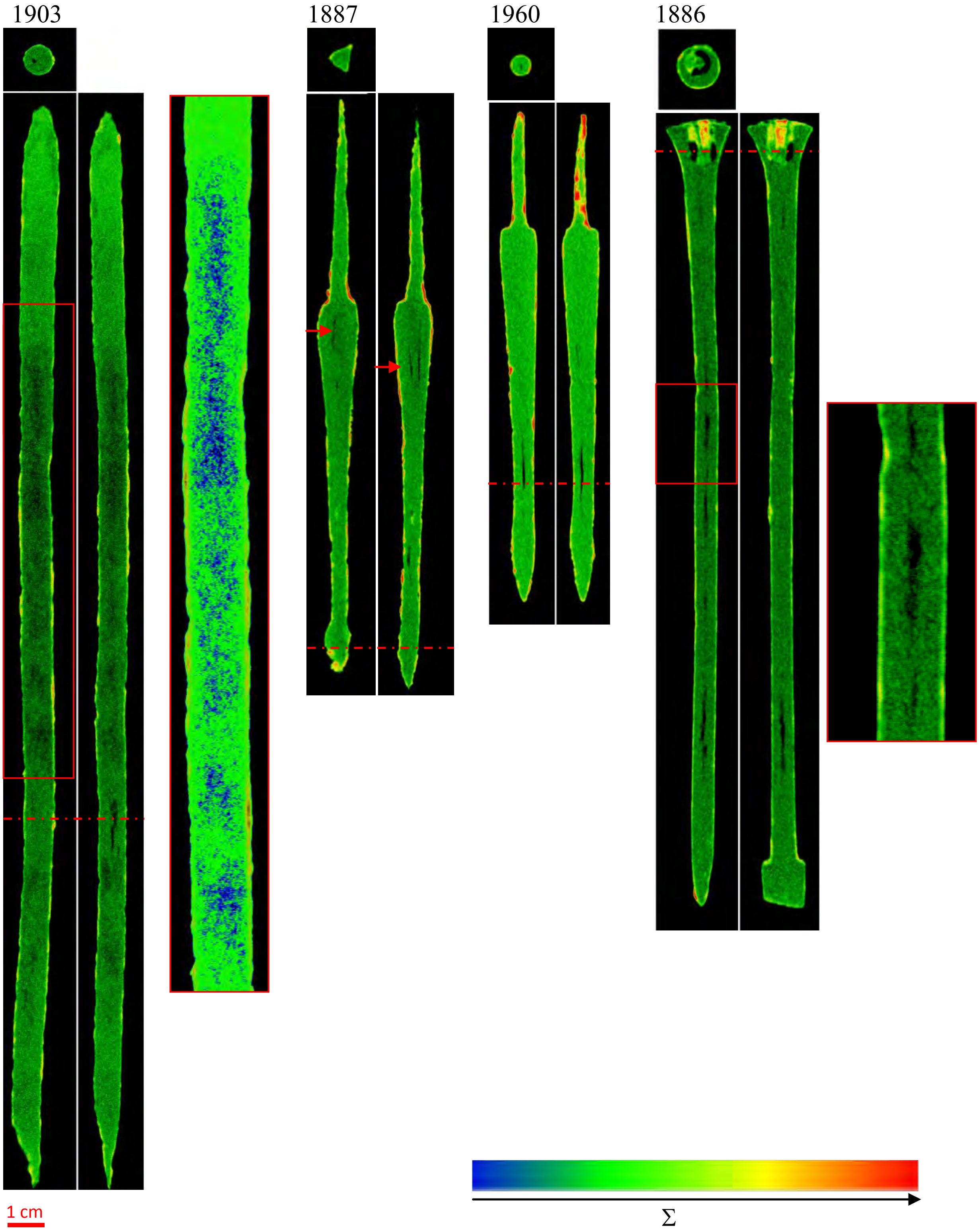

Figure 5.70: *Stylus* with inner cracks crossing only the body: in sample1903 clouds of inclusions are visible in the enlarged view. The artifact 1887 shows inclusions and spots of rust inside the inner fracture (red arrows), both features missing in 1960. The sample 1886 is unique: its axial cross section evidences an empty area at the tip insertion. In the enlarged image, a continuous light-colored coating is visible on the surface of the *stylus*.

Conclusions

Neutron tomography allowed to gain information about composition and assembly methods of the ancient Roman *styli*, belonging to different stylistic categories. The technology of the making of these artefacts is provided through the observation of the morphological characteristics:

- slag inclusions, non-homogenous areas and cracks were mapped and localized;
- inner structure, resulting from the particular manufacturing processes, were analysed all over the samples;
- alterations, on the surface and/or extending in the body of the samples, have been identified for assessing the conservation status;
- presence, type, extension and shape of decorations were detected.

Although a correlation between stylistic categories and technology was not evidenced, two main technological categories were identified.

Moreover, the results of this study indicate the potential sites for micro-sampling on a few selected samples for subsequent mineralogical, chemical and metallographic analyses.

In particular, a residual stress study helps in clarify the ancient Roman working techniques adopted in making *styli*.

5.8.2 Residual strain mapping of Roman *styli*

Basing on the neutron imaging investigation, for the analysis presented in this section, 11 examples of Roman *styli* from *Iulia Concordia* settlement, pertaining to different typological categories, have been studied (Fig. 5.71).

Figure 5.71: Pictures of the 11 analyzed *styli*. The identification number is reported on the left of each sample.

Experimental set-up

High resolution neutron diffraction measurements have been performed at the POLDI beam line, operating at the spallation neutron source SINQ (Paul Scherrer Institute, Switzerland). POLDI is a multiple pulse overlap TOF-diffractometer with a single chopper optimized for strain-scanning experiments.

The measurements on POLDI were taken on several points for each of the 11 selected samples, which are representative of the different categories previously identified through neutron tomography.

Neutron tomography results evidenced a difference between the stylistic categories (related to the shape) and the technological ones (related to the working process). The tomographic reconstruction of some of the 11 samples selected for strain measurements are shown in section 5.8.1.

Strain analysis has been performed using a neutron collimator with a spatial resolution of 2.5 mm and a motorized slit which shaped incident neutron beam to 1.5x5.0 mm^2 beam cross section. Styli are placed in a proper designed frame (Fig. 5.72) in order to measure strain in two directions, namely axial and radial (Fig. 4.9). The samples are divided in three regions of interest (ROI): the spatula, the body, and the tip. At least one spot per ROI was acquired for each sample (Fig. 5.73).
In addition, Fe powder in V can was measured as reference for strain determination.
The experimental diffraction data were refined (Rietveld) by applying the correlation procedure of full diffraction pattern, followed by a Gaussian fit of each diffraction peak independently. The data treatment routines are realized as a software package available at POLDI [Stuhr 2005].

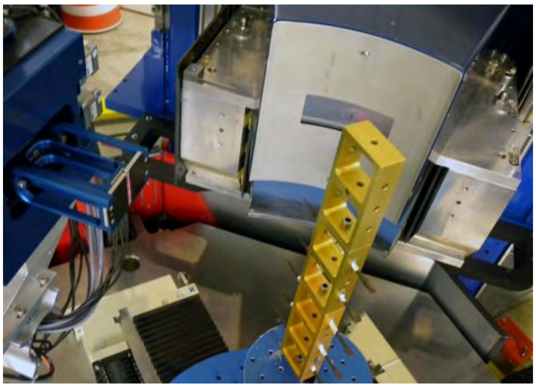

Figure 5.72: Instrumental set-up on POLDI.

Figure 5.73: The picture (sample 1878) is an example of the typical position of the gauge areas investigated on the *styli*.

Results

The residual strain analysis allowed to identify peculiar features connected to the forging process: method and direction of working are defined basing on the evaluation of the lattice parameter. From a preliminary data analysis, it turned out that the use of pure iron powder, as general reference for unstrained lattice parameter, was not viable due to the different composition of the iron used to forge *styli*. Then, making the assumption that a single sample is composed by iron with the same impurity composition, we have considered the average value of the lattice parameter, measured on the whole data set of the sample, as the d_0 reference. The same process is applied independently to all the samples.

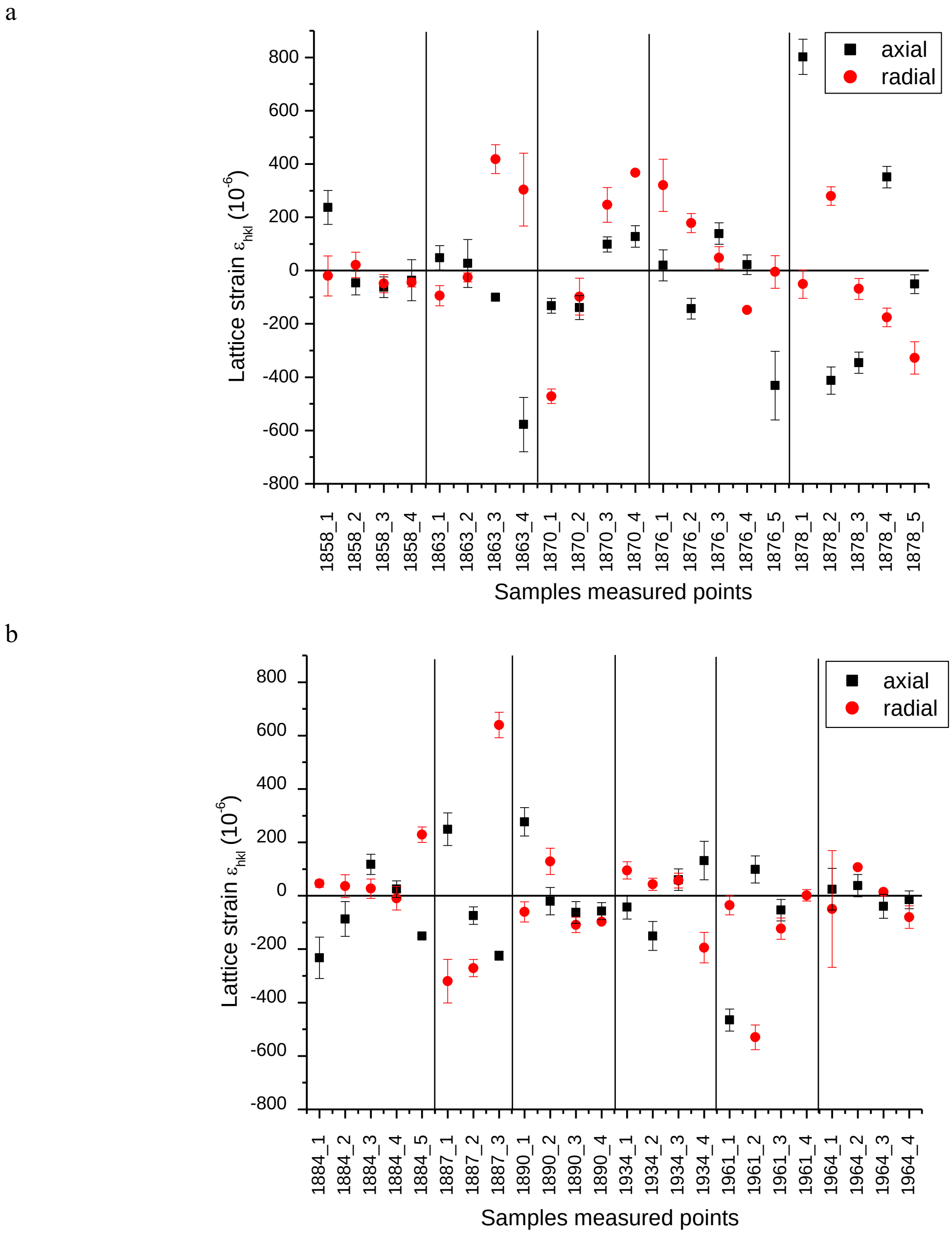

Graph 5.1: The two graphics report the values of residual deformation expressed as lattice micro-strain in ordinate, and the sampling points in abscissa. Vertical lines delimit the values obtained by analyzing, in the axial and radial directions, different spots for each sample. The notation progressively goes from the *spatula* (the first spot) to the tip (as reported in the example of Fig. 4). The intermediate spots are referred to the body or, if present, to decorative portions.

According to the classification of the *styli* obtained through the tomographic analysis, there are two main classes: the first one presents a solid homogeneous cylindrical body while the second one (the largest one) features the presence of two half cylinders welded together.
The sample **1863** is the only one, analysed with diffraction, pertaining to the first category. Data from this sample show a low radial stretching along the body, in the region closed to the tip (points 3 and 4). On the contrary, along the axial direction, the lattice strain value suggests the application of a compression force in the crowning end, increasing in the tip. Evidences are related to the working process; the *stylus* was probably obtained by low

level radial hammering of an iron bar in order to shape the *spatula*, while the tip area was enlarged and formed by preferentially working the metal along the axial direction.

As previously mentioned, taking into account the results obtained from the neutron tomographic reconstruction, the morphological study suggests that the remaining samples should be created by shaping twin halves of iron bars and soldering them together by hammering. When the cylindrical bar is formed, the extreme portion, tips and *spatula*, are shaped either extruding from one side or just shaping the combined parts into a different form. The presence of inner cracks confirms this hypothesis since the cracks are empty spaces, resulting from the process of soldering or rolling the iron plate over itself. The residual strain study allowed clarifyimg the procedure applied for creating each single *stylus,* as it will be discuss in the following. First of all, the data acquired in the body of the samples will be taken into account, while the tips and *spatulae* will be described together in the end.

Concerning the samples **1858** and **1964**, the data indicate that the objects were formed by slightly working the metal bar equally in both directions since the amount of residual strain is negligible in all body. A high residual strain, instead, can only be detected in correspondence with the *spatula* .
The close axial and radial micro-strain values of *stylus* **1870** suggest that the sample was made by shrinking the metal bar along the radial and axial direction (spot 2) and stretching the handle (spot 3) in order to create a drop-shape.
Also on spot 2 of sample **1876** it can be observed a procedure similar to that found for the previous *stylus* though with a larger intensity. Spot 3, measured in the swelled up part of the body preceding the point, is indicative of the starting size of the *stylus* due to the absence of strain.
The data acquired on spot 2 of sample **1878** reveal how the body was made, by applying a compression force along the axial direction. The micro-strain values on spots 3 and 4, referred to the decoration, show an inversion in the trend, being characterized by the growth of the compression along the radial direction, combined to a stretching effect along the axial one.
Sample **1884** shows negligible microstrain values in both directions in points 2-4.
The residual strain map of *stylus* **1887** allowed to hypothesize that the artefact was produced by hammering the body and the *spatula* normally to the surface, while the long and thin tip was preferentially worked along the axial direction.
In the case of *stylus* **1890**, the *spatula* end of the metal bar was manufactured by applying a low compression along the axial direction (spot 2) probably to enlarge the diameter at that position for the subsequent shaping of the *spatula*. The tip region was, instead, obtained hammering the object equally in both directions (spot 3).
The body of sample **1934** (spot 2 and 3) features a different level of compression along the metal bar axis going from the tip to the *spatula*; the object was probably hammered along this direction to enlarge the section of the body, creating a flared shape in the area facing the tip.
Sample **1961** was unstrained in spot 3, corresponding to the thick part of the bar preceding the point. On the contrary, taking into account the value at spot 2, it can be hypothesized that this area was obtained by hammering the iron bar in order to increase the length and to reduce the diameter size of the bar in proximity of the *spatula*.

Concerning the end portions of each *stylus*, different types of manufacturing methods can be distinguished for both *spatula* and tips. All the samples were measured, for gauge volume definition issues, with the *spatula* vertically oriented, so that the radial direction in *spatulae* corresponds to the residual strain measurement along the thicker section of them.

The lattice strain values of samples **1858**, **1878**, **1887,** and **1890** suggest the iron bar was compressed in the normal direction in order to flatten and broaden the *spatula* (spot 1 of each sample). After that, the object was worked by hammering, to reduce the size, only along the radial direction.
On the contrary, the *spatula* of *styli* **1884** and **1961** was obtained by compressing the metal bar along the axial direction, after flattening the metal along the normal one.
Unique sample appears the *stylus* **1870**; the microstrain values denote a compression along both the radial and the axial directions. The end of the metal bar was worked in that way in order to elongate the shape and sharpen the *spaluta*.
Styli **1863**, **1934,** and **1964** seem to evidence absence of strain, denoting a low intensity in the working process. However, concerning the last mentioned one (**1964**) the large error bar did not allow a precise estimation.
Finally, sample **1876** features the stretching along the radial direction. After hammering the *spatula* in the normal direction, the side was probably restrained only in the axial one.

The residual strain mapping analysis allowed to define the working procedures applied for shaping the tip. Some samples (**1890**, **1858,** and **1964)** exhibit no residual strain in the tip. A second group, including samples **1934**, **1878** and **1961** is characterized by the common feature that the writing ends were probably created by hammering the iron bar along the radial direction, thus axially elongating at a different extent the tip.
For a third group of samples (**1863**, **1870**, **1876**, **1884,** and **1887)**, the analysis reveals an intense compression in the axial direction and consequent stretching in the radial direction. An explanation of this feature, which represents the largest group, could be that the *styli* manufacturing implies a complex procedure for the final shaping of the tip. The first step is the hot working to extrude the tip from the body, shaping the tip without much precision. The following step is the final shaping of the tip (a shortening according to the experimental results), performed at low temperature so that this is the only residual strain that is identified.

Conclusions

The neutron TOF diffraction analysis allowed to gain information about the ancient Roman forging method of iron *styli*. In particular, the way and direction of working procedure applied for making *styli* belonging to different stylistic categories was clarified through the study of the residual strain map of several portions of the samples.
Moreover, the results of this study allowed answering some questions remained unsolved, even after the neutron imaging study. One more time, the combination of neutron imaging and diffraction techniques is demonstrated to be the ideal combination for investigating, non-destructively, ancient metal artefacts.

6 Conclusion

Individual conclusions have been drawn about the different aspects of this study, but the main aims of this research project should be addressed considering the results of the whole set of experiments.

The application of neutron imaging and diffraction techniques clearly demonstrated their potential for the characterization of metal artefacts of historical, archaeological and industrial interest. In particular, neutron-imaging techniques, namely radiography, tomography and laminography, both in white beam and energy-selective configuration, have been proved and exploited as a non-destructive approach for the study in the field of Cultural Heritage, necessarily linked to material science. In the current work, a comprehensive research has been developed on the metallurgy of artefacts of historical and archaeological interest, pertaining to different cultures and historical environments.

The morphology, the qualitative and the quantitative presence of different phases, the presence and distribution of texture and residual strain has been detected revealing the smelting and forging procedures as well as the conservation status of such valuable object provided by Museum Institutions.

White beam tomography, and laminography, allowed identifying slag inclusions, inner defects, structural variation, soldering, patination, alteration products on the surface and in the bulk.

Concerning the energy-selective neutron method, the present measurements have been exploiting the contrast enhancement induced by the selection of appropriate neutron wavelengths to increase the image contrast for mapping the distribution of the materials in the bulk of the artefacts.

The comparison of the results, obtained from preliminary standard metallography and neutron imaging techniques conducted on expendable samples, turned out to be satisfactory and testify for a nice complementarity between the two methods. Indeed, the present study demonstrates to what extent the agreement of the results can be obtained. Metallography has been considered up to now the method of choice for metal samples characterization. The good quantitative correspondence between the results of the two methods, the possibility to obtain 3-D reconstruction, and the non-invasive character of neutron imaging, candidate the neutron technique as the best investigation method for non-destructive metal characterization.

However, further work is needed to improve the energy-selective methods. In particular, a more homogeneous neutron wavelength distribution, in the whole acquisition window, would greatly improve the quantitative characterization of the phase distribution. Moreover, intrinsic technical limits are emerged, related to the possibility to resolve close Bragg-edges relative to different phases, or the ability to distinguish metal layers of different composition, identified on the basis of the morphological features and the difference in contrast by means of the white beam tomography. One of the most important future projects would be to improve this aspect of the method.

From the archaeometallurgical standpoint, at the present stage of the investigation, interesting relationships have been found, especially considering weapon and their composite assembling procedures. Metal of different composition have been used and assembled in order to obtain specifically desired technical and mechanical performance as well as esthetical design.

Some of the obtained results have been reported in the international literature for the first time; neutron-imaging techniques, in a combination with neutron diffraction, provide an attractive approach but are very rarely applied to help conservation and diagnostic of museum objects. By presenting the obtained positive results, this work will ideally encourage further study and application of the neutron techniques to different types of objects or a more in-depth look at their application to metal artefacts, whose current problems, or open questions, cannot be solved with the current, often invasive, commonly used techniques. These studies could reveal a sympathetic overview of the lost traditional metallurgical procedures, manly transmitted orally to the present, and often recovered by contemporary craftsman on a personal level referring to partial information reported in written documents not always fully reliable.

A possible focus for future experiments should be on further studies to better document the relationships among different material cultures evolved in time, as well as to determine variation in quality and differences in technology development within a specific contest.

In the perspective of a wide-ranging research, the study of historical technology allows revealing methodological process that leads to the conception, development, and evolution of a specific artefact, trying to establish the relationship existing among people that implemented it, as well as the socio-economical context that characterized the circumstances of its production.

Appendix A

Calibration measurements

In order to quantitatively determine the monochromatic neutron flux distribution, an analytical model was used to reproduce the measured cold neutron spectrum at the ICON facility, setting the mechanical velocity selector at different wavelengths of interest for material investigation (Fig. A1, left).

A calibration curve between the rotation frequency of the monochromator and the desired neutron wavelength was also produced [Kaestner 2011].

Theoretical data have been validated performing neutron radiography on the Japanese blade fragments S7 presented in Chapter 5.2 and used as a test sample. In order to obtain the highest intensity variation, the sample with the highest average carbon weight percentage (sample S7) was chosen [Grazzi *et al.* Anal. Bioanal. Chem. 2011].

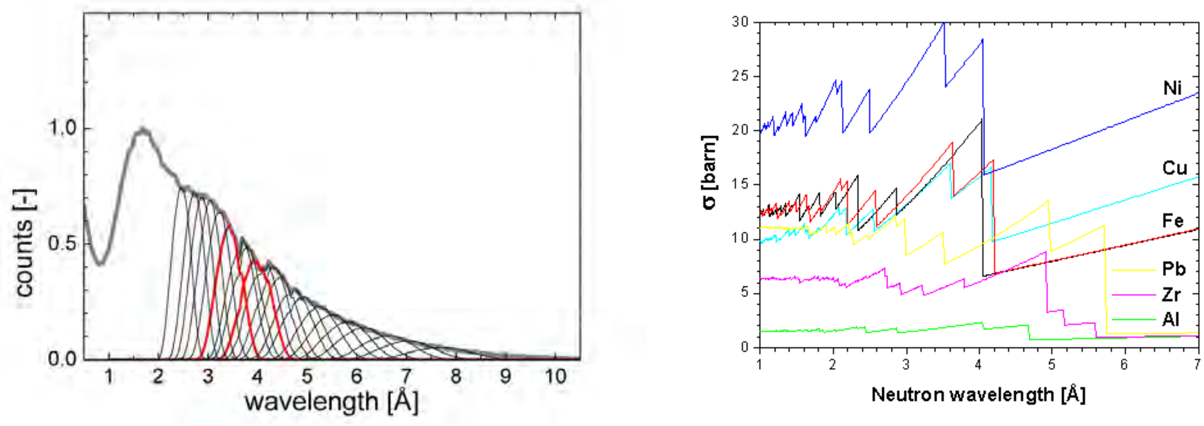

Figure A1: On the left, wavelength spectrum of the neutron-imaging beam-line ICON in the range from 0 to 10 Å in different configuration as white polychromatic beam (thick grey line) and energy selective monochromatic examples (thin grey and red lines): Gaussian distributions of the monochromatic flux, changing with the selector rotating frequency, were evaluated at different neutron wavelengths. On the right, total neutron cross sections (*σ)* for six different polycrystalline materials.

Using the monochromator calibration diagram, we have measured several radiographies changing the rotational frequency of the velocity selector. Thus, the fragment was analysed, aiming to map the ferrite density by maximizing the contrast enhancement obtained using different neutron wavelengths. In particular, to fulfil this task, neutron wavelengths at values immediately above, and below, the 110 ferrite Bragg edges were used [Giller 2008].

In Figure A2, the processed radiographies, taken at different frequencies and showing the variation in intensity due to the Bragg-edge enhancement, are reported. Owing to the Lambert–Beer exponential law, the intensity is also function of the sample thickness, *d*. However, exploiting the relationship (4.4) the *d* dependency can be removed. The results of this operation are shown in Figure A3.

Stretching the dynamic range in the radiography visualization, the ferrite phase can be identified with the dark area. However, due to the relatively broad band of neutron wavelengths transmitted by the velocity selector, the neutron beam does not appear to be sufficiently monochromatic to produce a sharp difference across the Bragg edge region. As a consequence, the contrast factor turns out be less than optimal. In the same context, it is also important to point out that the wavelength distribution of the ‘‘monochromatic’’ neutron flux impinging on the sample is not perfectly homogeneous. In facts, the diagonal yellow line shown in the picture is indicating the position of the 110 ferrite Bragg edge, thus meaning that the intensity peak of neutrons with wavelength about 4.1 Å is likely crossing the image in correspondence with it.

This is not a problem, when tomographic reconstruction is applied, because the neutron flux is averaged during the rotation of the sample.

Imaging Method:	**Energy-selective imaging (sample test S7)**
Neutron wavelength:	3.5 Å, 3.7 Å, 4.1 Å, 4.6 Å
L/D:	89
Scintillator:	^{6}LiF/ZnS (1:2) 100 µm
Camera:	Andor DV434 - BV, 1024 x 1024 16 bit
Field of View Length:	111.6 x 111.6 mm
Object-Detector-Distance:	17 mm
Pixel size:	210 µm
Exposure Time:	6 s

Table 1: The instrumental set-up employed for measurements.

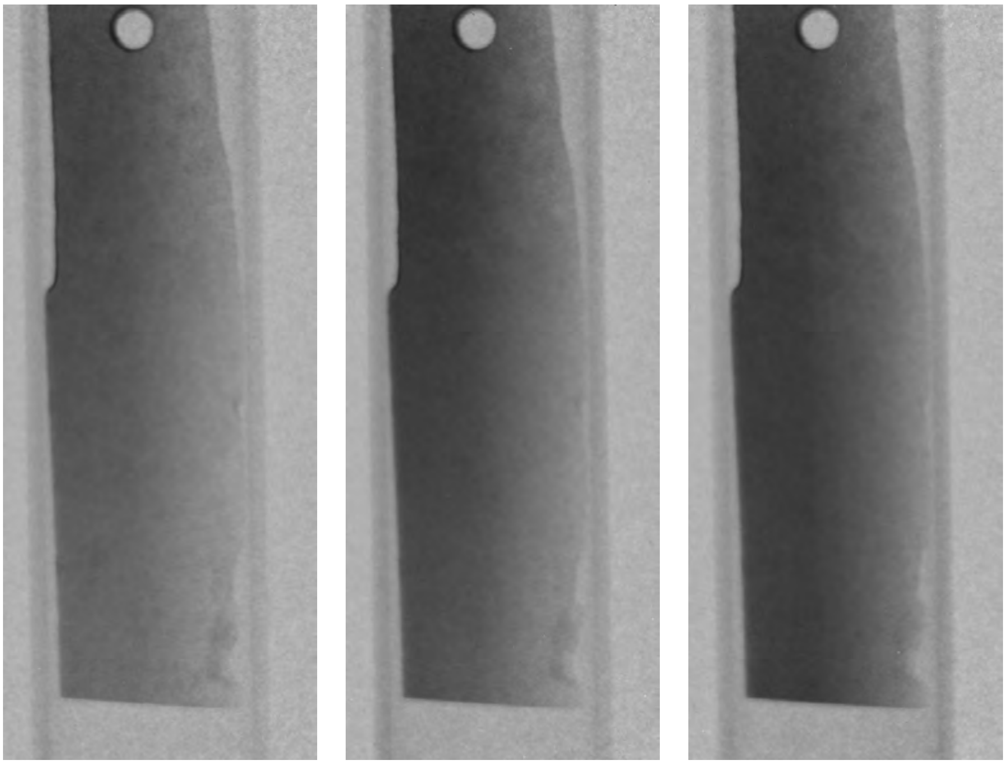
4.6 Å 4.1 Å 3.5 Å

Figure A2: Energy resolved neutron radiographies of the Soshu blade S7 (test sample) taken at different rotation speed ω of the mechanical velocity selector, showing the variation of intensity due to the Bragg-edge.

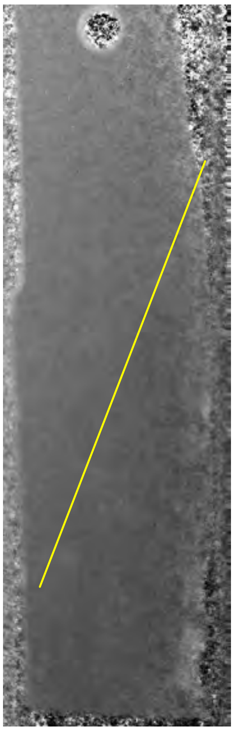

Figure A3: Image obtained by dividing the logarithm of radiographies of the sample S7 taken at 4.6 and 3.7 Å. The diagonal trend of the Bragg edge (evidenced by the yellow line) is slightly visible (see text for details). I should also point out that bright spots correspond to broken portion of the cutting edge, revealing a phases composed structure for the blade (a detailed explanation is provided in 5.1 *Result-Energy selective tomography* section).

Appendix B

Sample Environment

The technical features of neutron instruments were sometimes pushed to their limits by the shape and the size of cultural heritage objects. Performing neutron imaging experiments, purposely designed holders and special experimental set-up are often required, especially to permit to investigate the whole volume of the samples and to optimize the allocated beam time. Furthermore, handling such valuable and rare samples, a particular care must be ensured to safeguard the sample safety without preventing the success of the measurement.

Here, the two sample-holders used for the study presented in section 5.4 are described. In Figure B1, the frame adopted for the radiographic energy scan is shown. In order to perform the scan in a single measurement and optimizing the beam time, the frame was created to fit the *kris* all together covering the entire field of view of 200x200mm available on the instrument.

Particular attention was given to the materials: the frame, the screws and the plates are all in aluminium, while teflon buffers are placed at the contact points between the plates and the samples, carefully avoiding accidental scratches to the samples. We remind that teflon is sufficiently soft to safeguard the blade surface and almost transparent to neutrons .

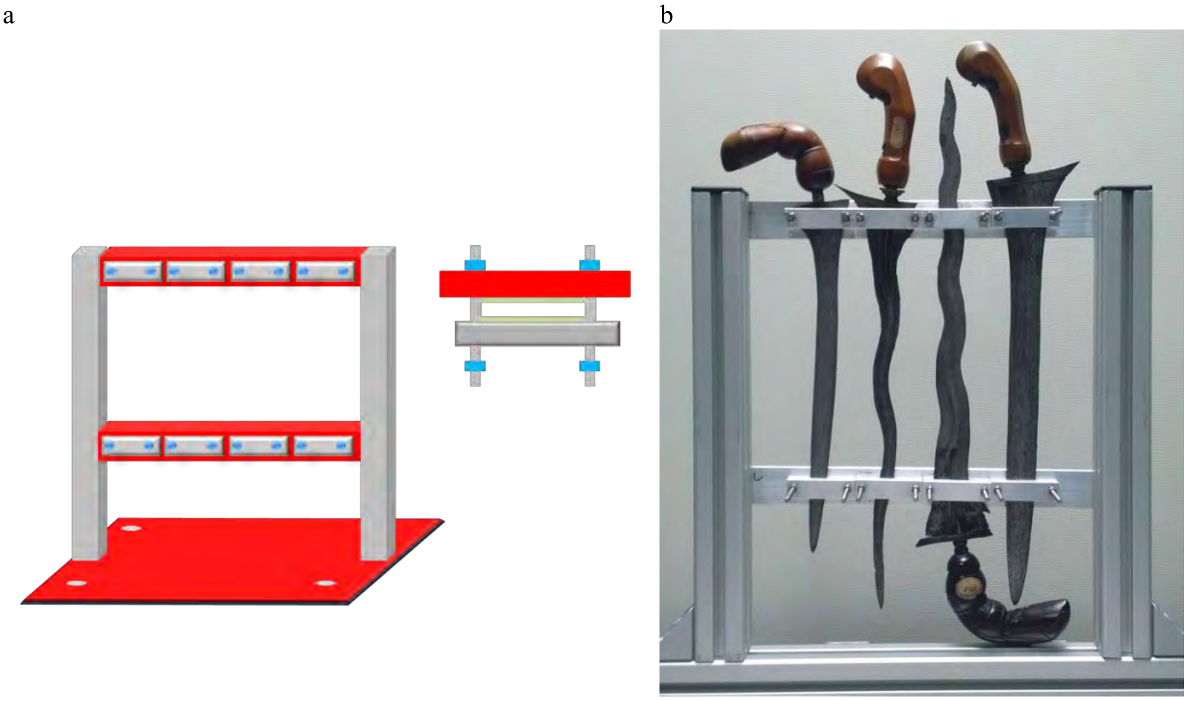

Figure B1: On the left: sketch drawing of the holder with a top view of its fastening system made for the radiographic energy scan. On the right: the *kris* are put in place.

In Figure B2, the mechanical mounting for the neutron tomography is shown. Performing the white beam tomography and the energy-selective tomography, the samples were mounted together to reduce the total measuring time. The purposely-made holder fixes each *kris* in a staggered position with respect to the others; adopting such a configuration the incoming neutron beam can intercept the samples one by one, avoiding the risk of too large attenuation. The pipe, the arms, and the screws are all made in aluminum and the contact with the sample surface, is covered by teflon.

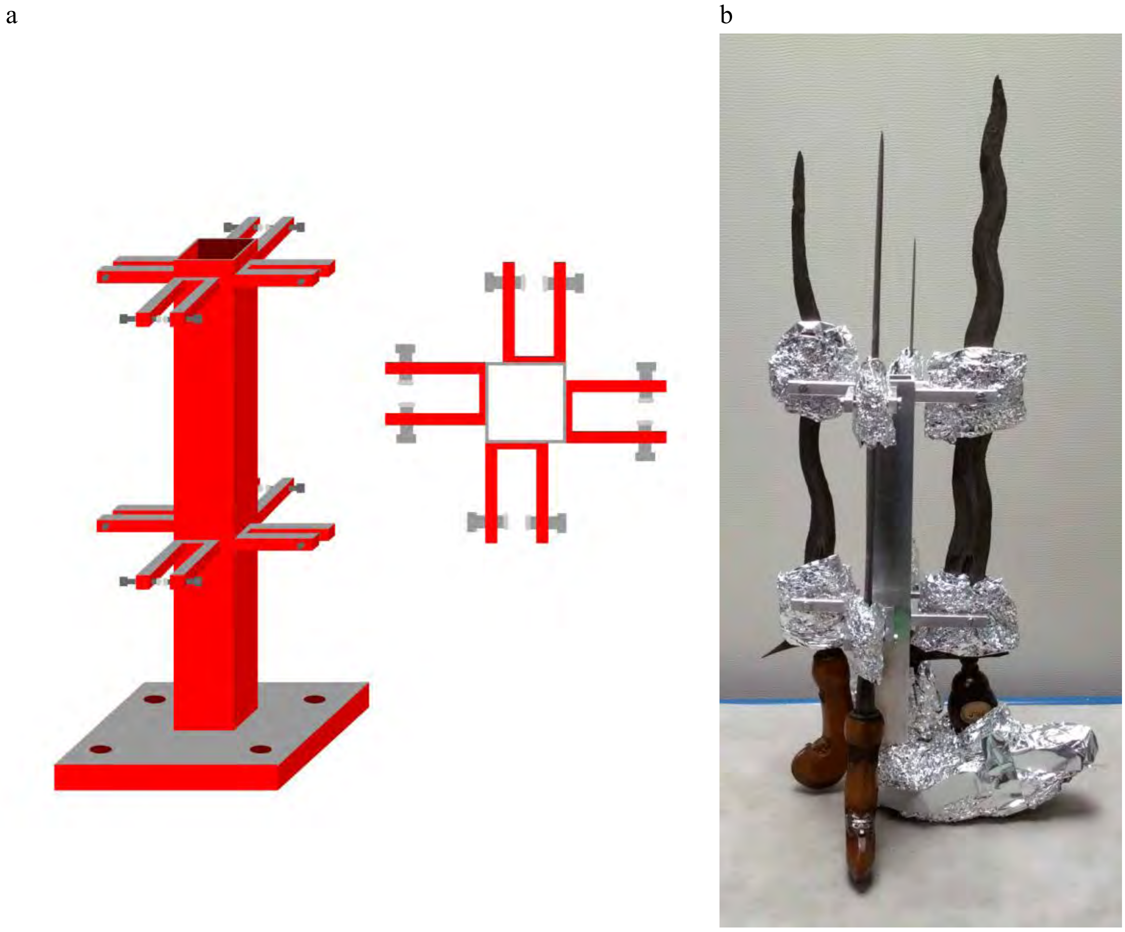

Figure B2: On the left, a sketch (side views) of the frame for the neutron tomography energy is shown with a top-view of the sample-fastening system. On the right, the samples are mounted. Additional wrapping with Al foils was required to fasten the *kris* and to support the handles.

The sample set-up for the neutron laminography is shown in Figure B3. The holder, all made in aluminum, was designed to host one samples at each level. he have Threaded end spacers were used to easily mount and dismount each component, to position the sample, and to regularize the gap between adjacent sectors.. All samples are wrapped into aluminium foil and secured with aluminium tape to the wall of its containing plate.

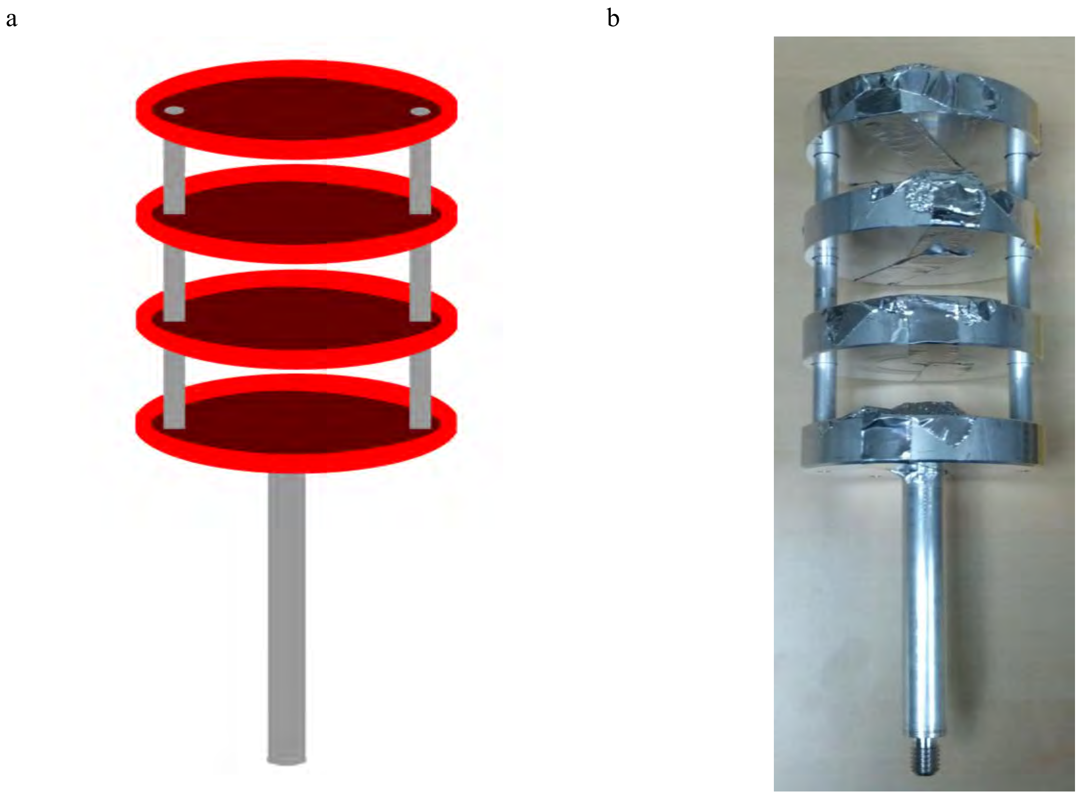

Figure B3: On the left, a frontal view of the sketch drawing the holder designed for the neutron laminography. On the right, the samples are arranged.

Appendix C

Energy-selective imaging on Indonesian *kris*

Before running the energy-selective tomography of the *kris*, a radiographic energy scan was carried out aiming to determine the optimal neutron wavelength for contrast enhancement in correspondence of the material Bragg-edgefor
Theoretical data, evaluated on the basis of the lattice parameter of the expected phases composing the sample, namely ferrite, taenite and kamacite (Tab. C1), have been validated performing neutron radiography on all the *kris* presented in Chapter 5.4.

Phase	Crystal structure	Lattice parameter *a*	Lattice plane $_{hkl}$	λ=2d [Å]
Ferrite	BCC	2,8668	110	4.0543
			200	2.8668
			211	2.3407
			220	2.0271
Kamacite	BCC	2,8690	110	4.0574
			200	2.8690
Taenite	FCC	3,5820	111	7.1640
			200	3.5820
			220	2.5329

Table C1: The phases expected to constitute the *kris* are listed in the first column. Here, the correspondent crystal structure, the lattice parameter *a*, lattice planes $_{hkl}$ of interest and the position of Bragg edges are reported for all phases.

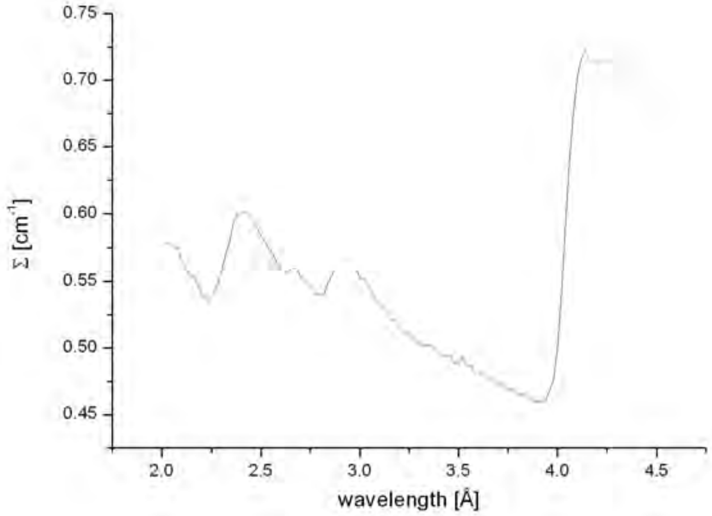

Figure C1: The profile evaluated basing on the radiographic energy scan is reported, showing the typical Bragg-edge of ferrite. I point out that the weak edge observed at 2.64 Å is artificial; this was verified by taking a stack-profile through an area outside the sample.

Several radiographies were carried out from 2.0 Å to 4.5 Å with a step of 0.02 Å. Since the Bragg edges of ferrite, kamacite and taenite fall very close to each other, in relation to the wavelength resolution achievable with the current beam monochromatization device, the phases of interest cannot be discriminated. This can be easily verified by looking at the values reported in the last column of Table C1. The crystalline structure for kamacite and ferrite is quite similar ($\Delta\lambda \cong$ 2-3 10^{-3} Å), resulting in an almost perfect superimposition of

the expected Bragg-edges, while the taenite signal is foundered into the ferrite-kamacite profile.
Consequently, only the typical ferrite Bragg edge profile is recognizable (fig. C1). Two independent reconstructions were carried out for each set of measurements, taken at the two different neutron wavelengths, above and below the 110 ferrite Bragg cut-off, namely 3.82 Å and 4.15 Å. The image stacks so obtained were further processed, by progressively subtracting the latter tomography from the former, according to the method already described in Chapter 4, section *Energy-selective neutron radiography and tomography*. In order to increment the statistics, each stack was processed by applying a median filter, and a projection along the z axis was applied every 50 slices in the area characterized by the same dimension and geometry.

Hereafter, I reported the computational tomographic reconstruction of *kris* K2 (fig. C2), K3 (fig. C3) and K4 (fig. C4).

- K2: Inv 5143 - *kris* of early *majapahit* shape, made in Semarang (Java Island)

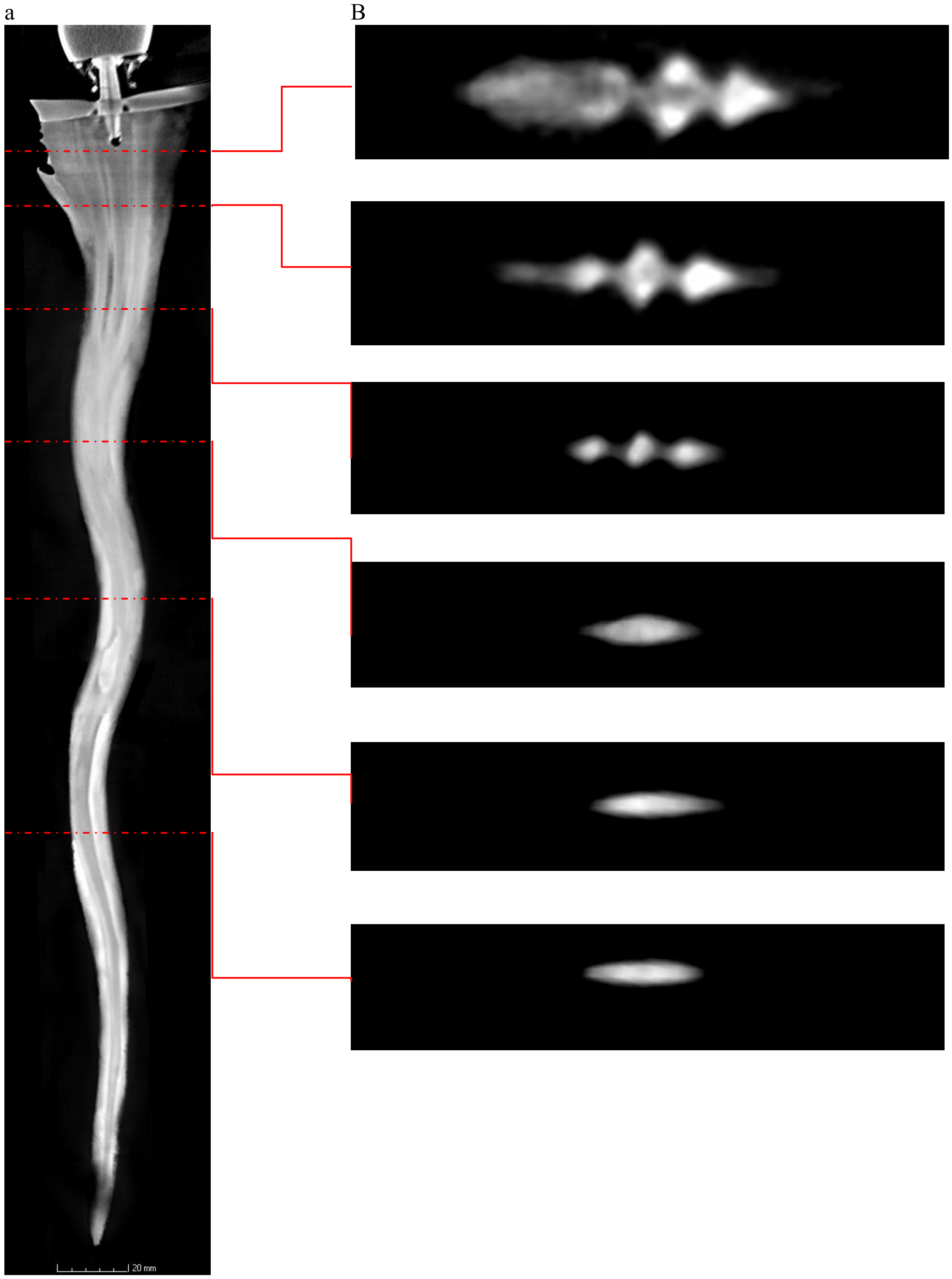

Figure C2: The white beam tomographic reconstruction is reported as reference in *a*. The cross sections obtained from the energy selective tomography *b* are taken at different heights of the sample at the position indicated by the red line. Bright areas indicate the presence of ferrite, kamacite or taenite, dark regions stand for cementite rich areas.

- K3: Inv. 5144 - *kris* of early *majapahit* shape, made in Semarang

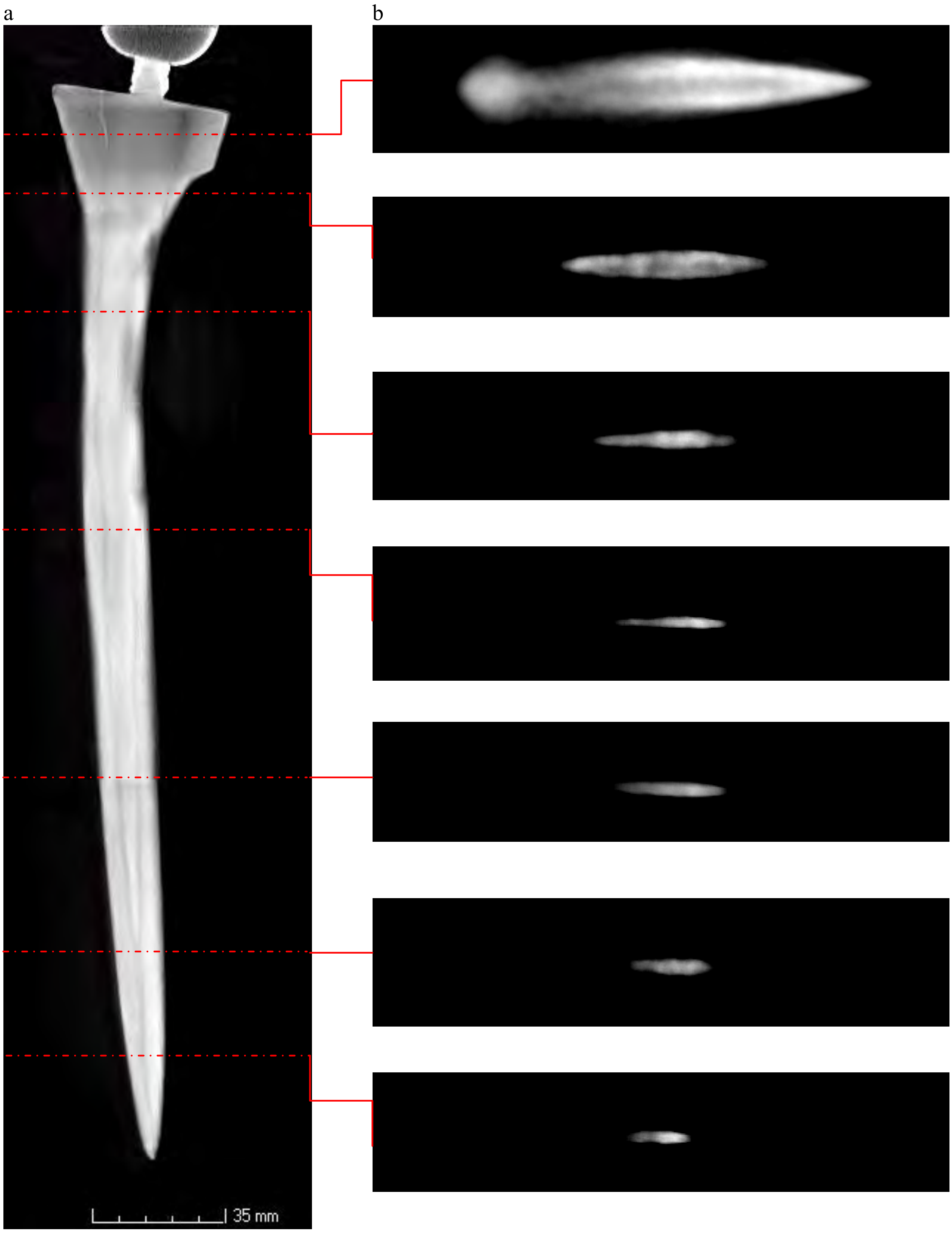

Figure C3: The energy-selective tomography revealed a similar structure for all the *kris*; a soft steel was used for shaping the edge and the tip (bright area), while a hard-core was inserted inside (dark areas), as visible from the reported cross section in *b*.

- K4: Inv 5145 - *kris* of *majapahit picit* shape, made in Ambon Island

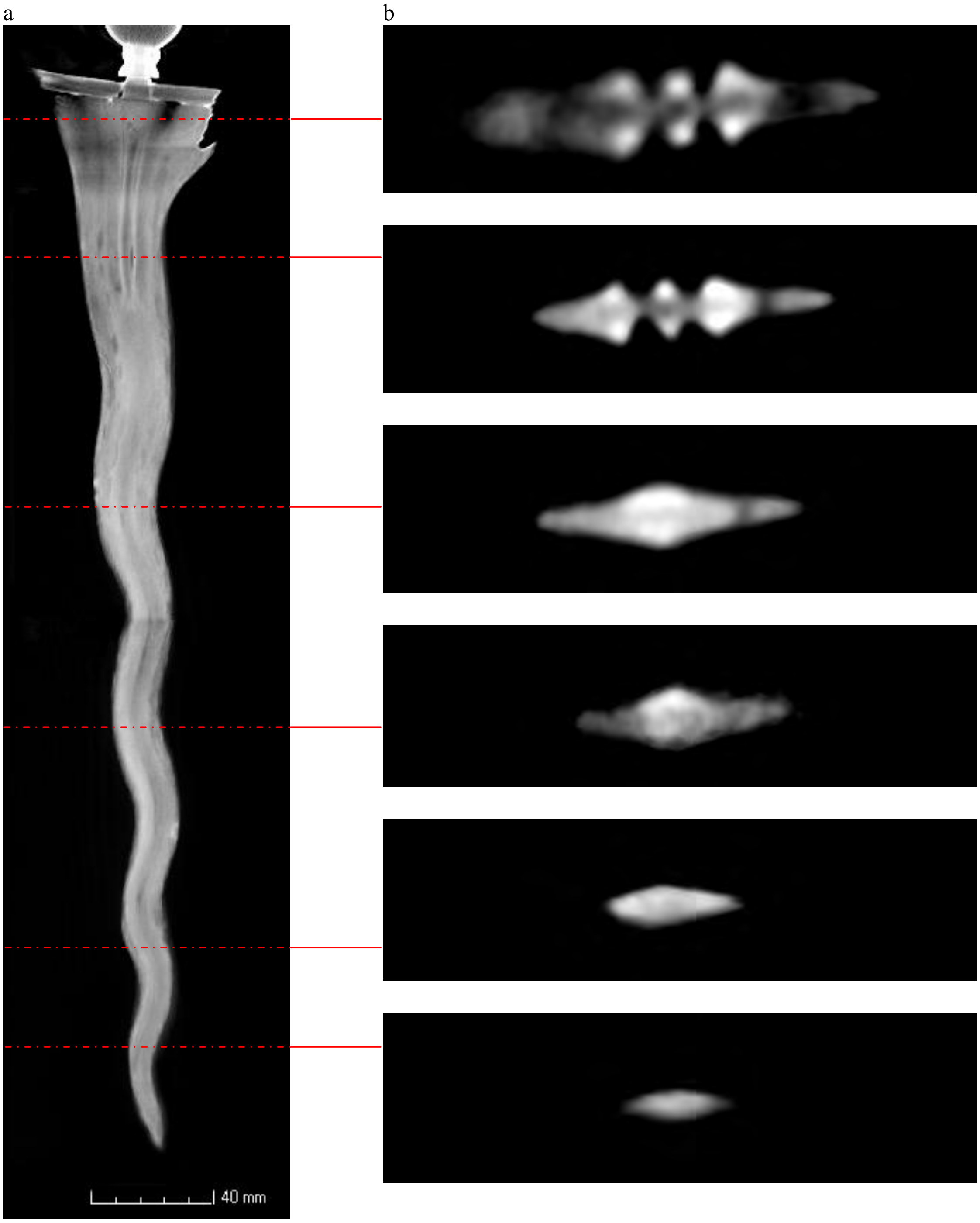

Figure C4: Also *Kris* K4 was manufactured by assembling a “jacket” of low-carbon steel around a very hard steel composing the “core” of the sword as shown in the cross sections *b*.

Appendix D

Morphological characterization of Roman *styli*

The second group of *styli* consists of samples all showing the presence of large-size inner cracks located in the body. Subcategories are defined basing on the extension of sectional cracks in the tip and/or in the *spatula*.
Analyzing tomographic reconstructions of this second group, it includes a first subcategory of 25 samples exhibiting the presence of cracks crossing the *stylus* body only (Tab. 5.11, white colour). A large amount of these samples shows the presence of non-homogeneous parts in the body (Fig. 5.70-1903). Moreover the samples 1910, 1959, 1940, 1932, 1887 (Fig. 5.70), 1872 and 1935 also reveal rust along cracks, suggesting bad burial conditions.
Styli 1960 (Fig. 5.70) and 1907 appear to have a homogeneous body, instead, similar to samples 1874, 1886 and 1929 where, however, some inside diffused rust is present .
Sample 1886 appears quite unique (Fig. 5.70): the tomography allowed to detect the presence of an empty area in correspondence tothe tip insertion: it should be correlated to the possible use of a different assembling procedure, described at the end of this section or, simply, to the loss of the easiest alterable portion of the *stylus*: the tip.

Inside the second group, the second (and last) subcategory of *stylus* is the most represented one. It is characterized by the extension of the crack not only in the body but also in the tip and/or the *spatula*. This group can be further divided into three morphological sets.
The first one, including 28 samples (Tab. 5.11, red colour), shows inner cracks starting from the tip insertion area , crossing the iron body of the *stylus* and stopping before the *spatula*. The samples are usually characterized by abundant rust and non-homogeneous areas. On the contrary, sample 1877 appears as a homogeneous bar in good state of conservation. No evidence of rust and slag inclusions are visible in samples 1962, 1901, 1961, 1916, 1878, and 1884 (Fig. D1).
In the second set, central inner cracks reach the bottom of the *spatula* for 11 samples (Tab. 5.11, violet colour) but they don't cross the tip. Only the *stylus* 1928 doesn't evidence inclusions, already detected in association with spots of rust in all the other samples (Fig. D2).
The bad conservation condition did not allow to clearly define the inner structure of *styli* 1951 and Sac-a-L.
Inner cracks, crossing the whole *stylus* volume, are typical of the last set, constituted by 18 samples (Tab. 5.11, green colour): samples 1944, 1893, 1946, and Sac-a-c there do not show inclusions, while no rust is evidenced in sample 1864 only (Fig. D3).

Use of neutron tomography also permitted to identify the presence of decorations applied on the surface. As a matter of fact, the trace of a decoration was detected in the form of bright rings in the tomography slices, surrounding the chiselled portion under the tip of sample 1944. The high attenuation coefficient of that volume suggests that it might be made of gold. Moreover the absence of slag inclusions inside the sample allowed to hypothesize this sample was one of the finest artefacts. Even sample 1891 presents a ring shaped decoration mixed within a rusty surface. The difference in attenuation of the two areas is small but, in the tomography, it is possible to distinguish the presence of a sharp border between the two volumes and the continuous shape typical of a ring-like decoration with respect to the appearance of rust in fragmented spots (Fig. D4).
Also *styli* 1871, 1965 and 1902 show the presence of a similar material apposition for decorative purposes, while the sample 1886 appears integrally coated (Fig. 5.70).

Finally, samples 1872 and 1905 have a cup-shaped decoration coated by a material characterized with less neutron attenuation coefficient: probably a copper alloy based on Sn, Zn and/or Pb (Fig. 5.70).

The following image-stacks are cross sections taken from the computed tomographic reconstruction of a selection of the analyzed *styli*. Each sample is virtually cut along three orthogonal directions: the upper image is always referred to the axial section, whose position is defined by the horizontal red line crossing the normal and transversal views, placed side by side on the bottom. Red dotted lines are linked to extra axial section, showed on the side of the image. The normal and transversal slices are acquired at the centre of the axial one. At the top of each slice-group, the sample reference number is reported. Moreover, the tomographic reconstruction are shown in false colour enhancing the contrast in order to help in detecting structural features: the green colour stands for iron, the dark-blue for slag inclusion rich areas, the yellow-orange for rust and decoration, finally black stands for empty areas. As a matter of facts, a gradient bar is placed at the bottom of each figure: from blue to red, colours are associated to a rising macroscopic total attenuation cross section. The enlarged areas, framed in red, are filter-treated to point out specific structural characteristics inside the volume of the sample.

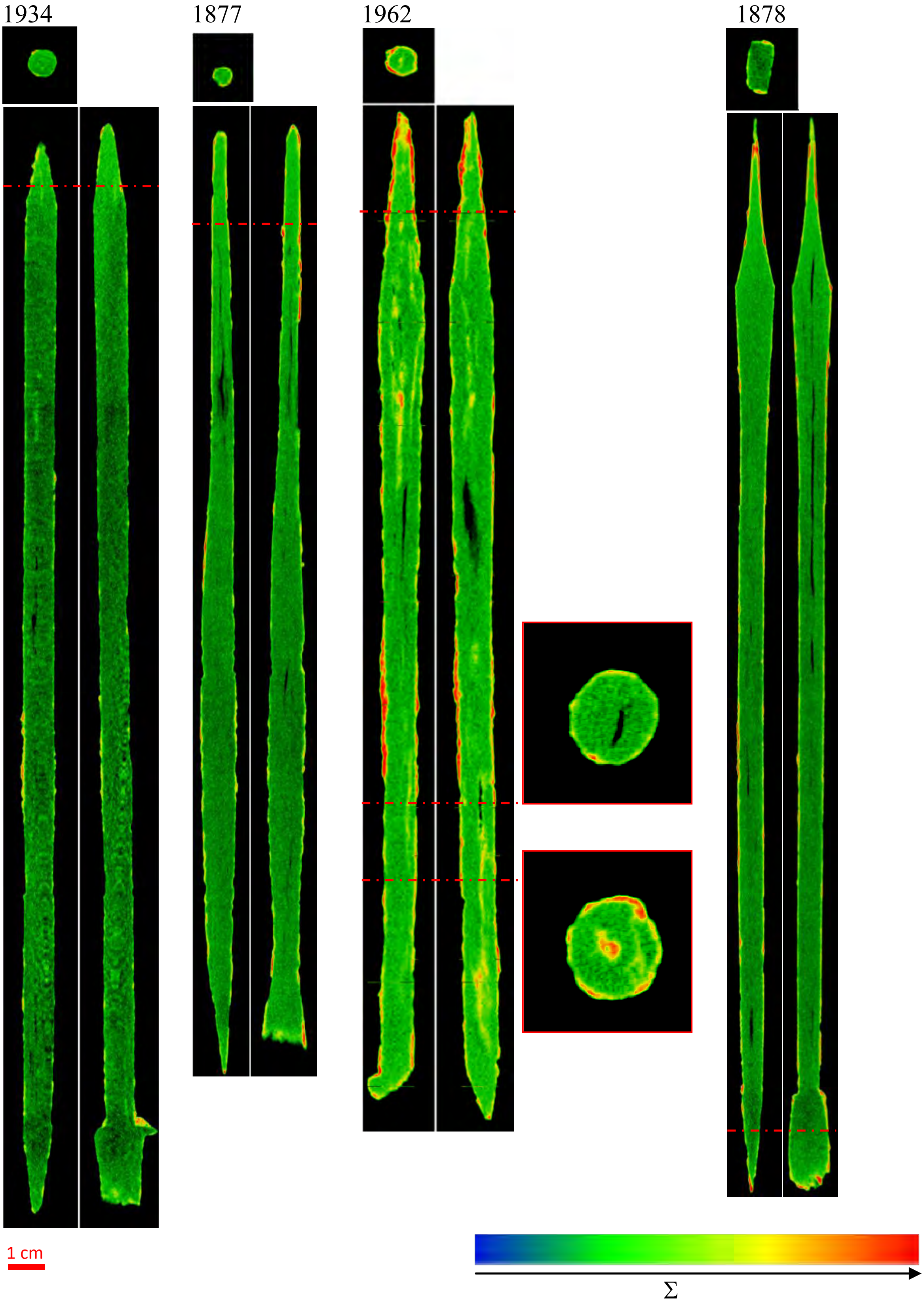

Figure D1: Here, samples of artifacts with crack crossing the tip and the body are shown. Rust and non-homogenous areas are detected in *stylus* 1934, while they are absent in 1877. As evidenced by the two enlarged axial cross sections, the rust diffused along the inner crack of sample 1962. In the *spatula* of the sample 1878, a dark area is present.

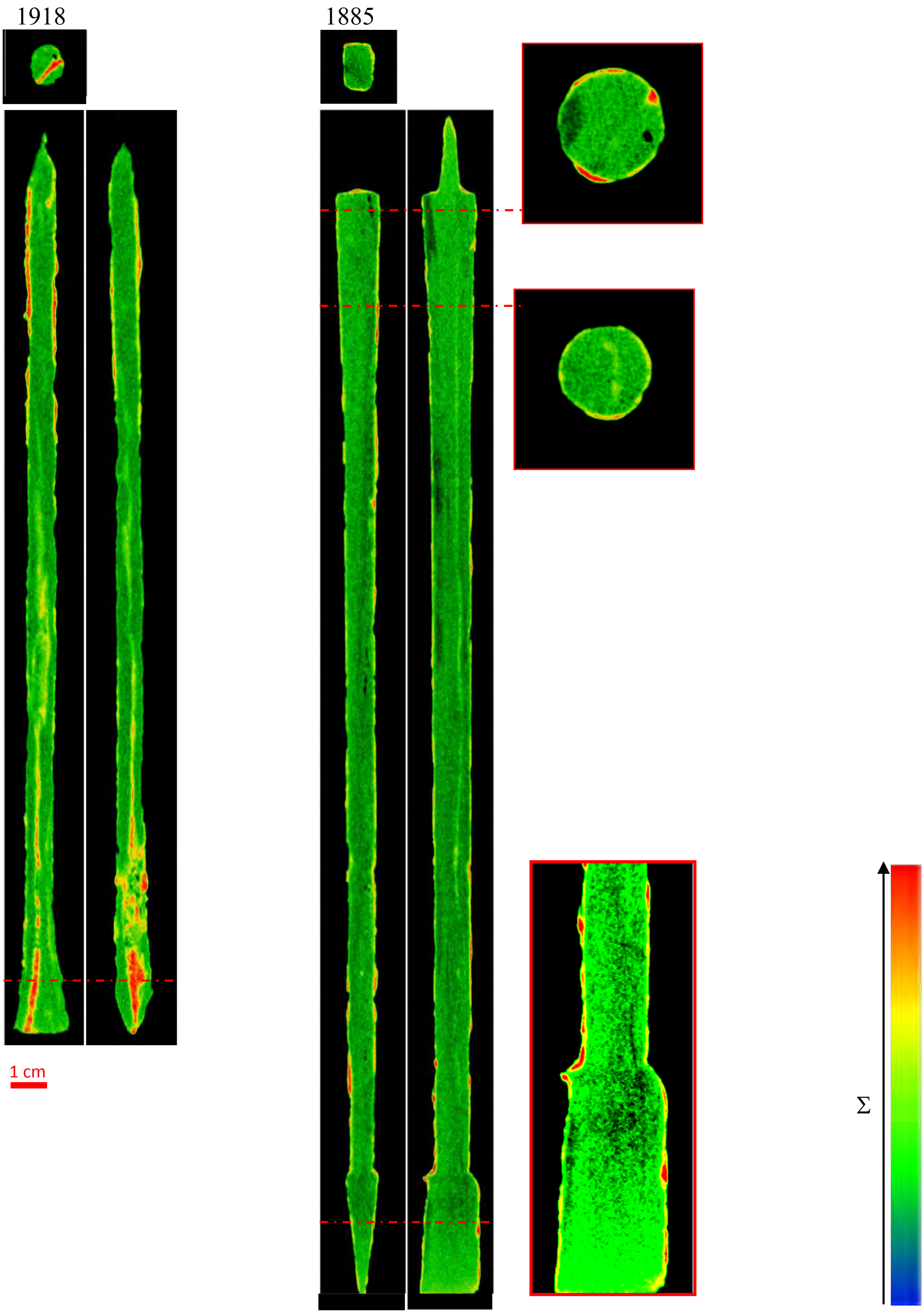

Figure D2: Cracks penetrated the body and the *spatula* of these two samples: the first (1918) shows diffuse rust and slag inclusions; the second (1928) display only rust and a non-homogeneous area in the *spatula*. Immediately under the surface, dark areas are detected and pointed out in the enlarged images: they can be probably related to the alteration process.

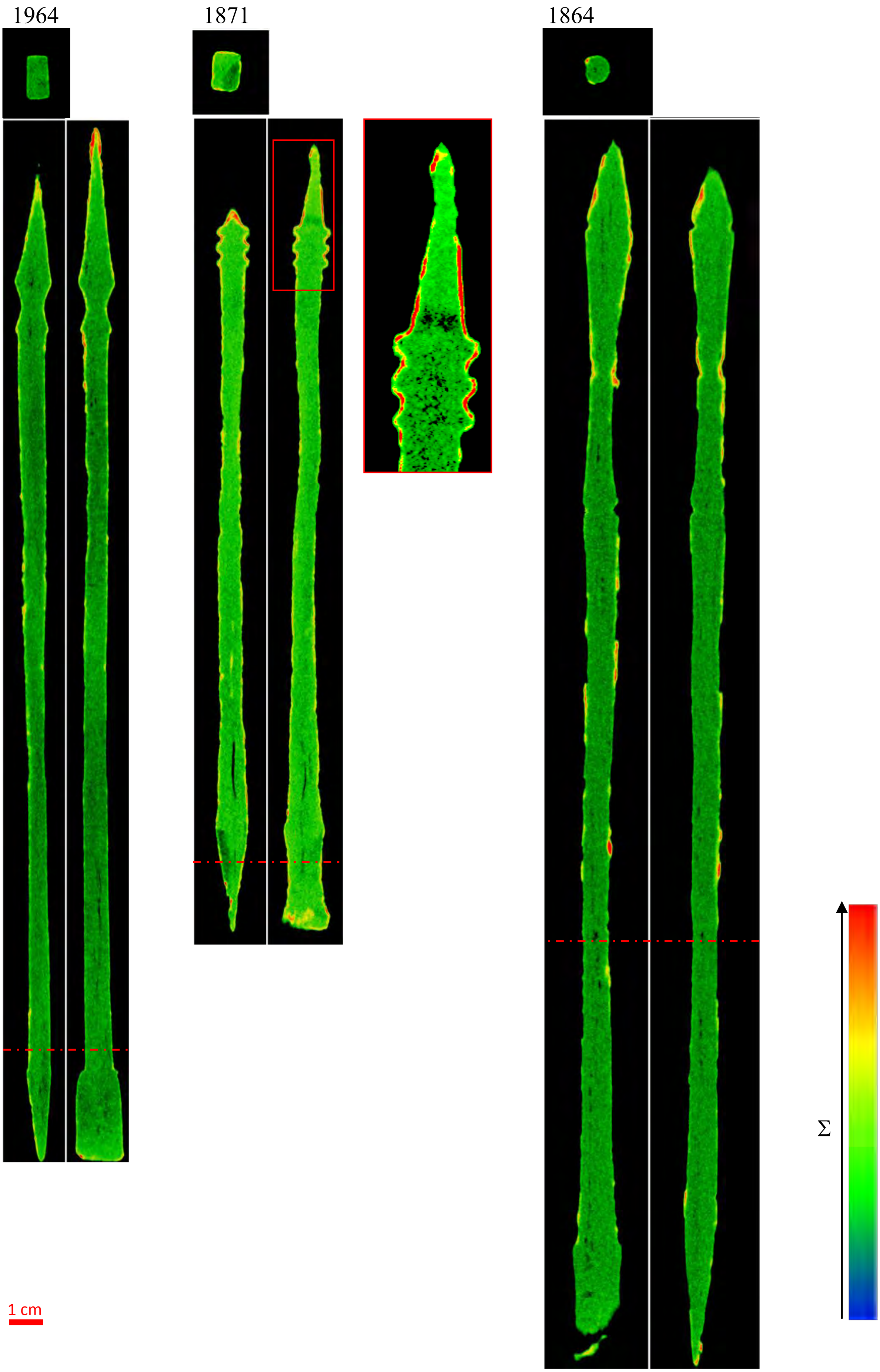

Figure E 3: Samples from *styli* with a whole fractured body: 1964 contains non-homogeneous areas, slag inclusions and rust. The same features are in 1864. An anomalous dark region is visible in 1871.

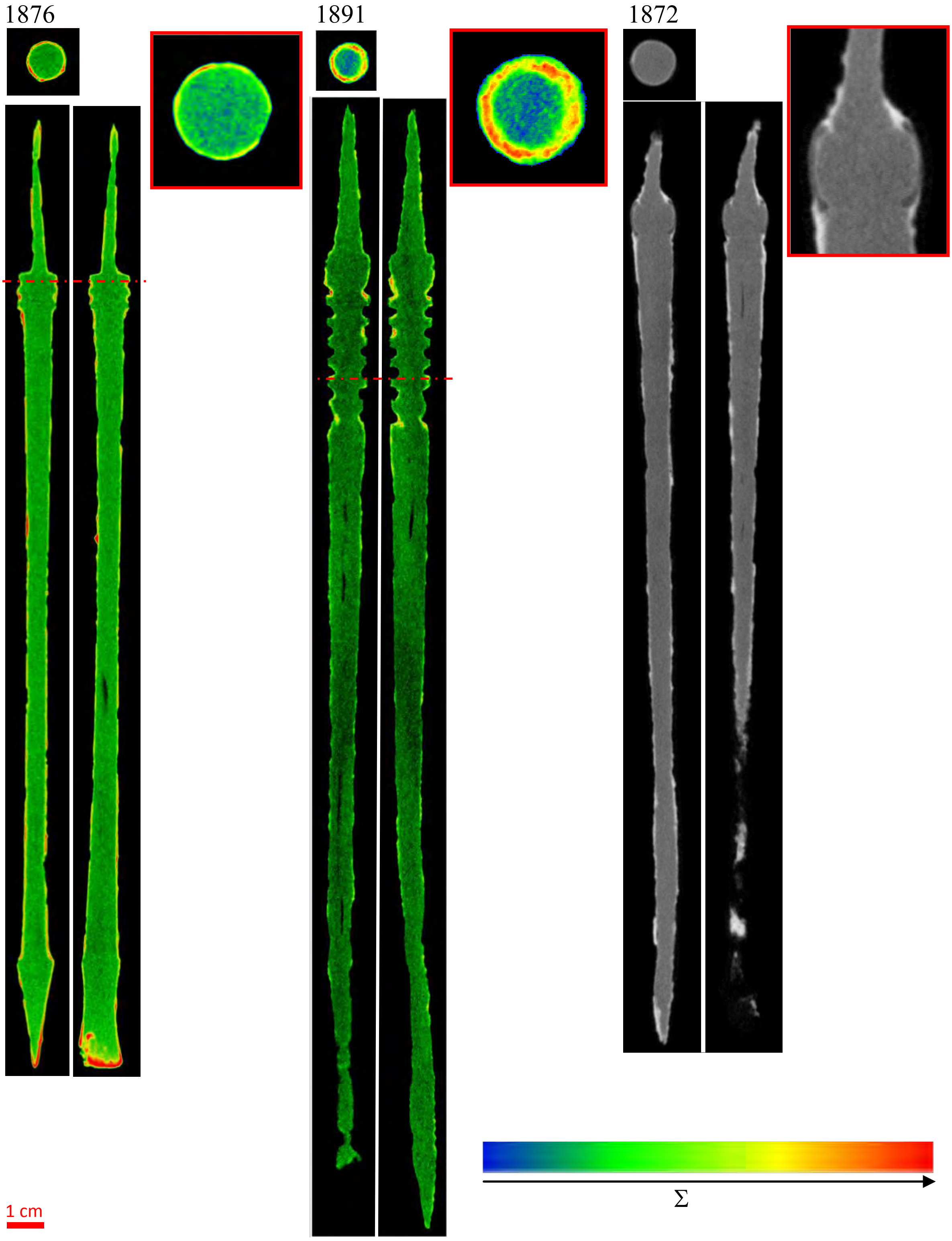

Figure D4: On the left the magnification of the axial cross section points out the presence of rust on the outer surface of sample 1876, while on *stylus* 1891, the evidence of a material decoration is detected. This sample shows non-homogeneous areas. The *stylus* 1872 is reported in gray tone in order to enhance the cup-shaped layer evidenced in the enlarged image.

References

Z. B. Alfassi, *Activation Analysis, Volumes I and II*, CRC Press (1990).

H. G. Backmann, *The identification of slags from archaeological site*, Institution of Archaeology-Occasional Pubblication 6 (1968).

S. Baechler, N. Kardjilov, M. Dierick, J. Jolie, G. K.uhne, E. Lehmann, T. Materna, *Nuclear Instruments and Methods in Physics Research A* 491 (2002) 481–491.

J. F. Barrett and N. Keat, *RadioGraphics* 24 (2004) 1679–1691.

E. Barzagli *et al.* (2013) (submitted to PNAS).

K.H. Beckurts, K. Wirtz, *Neutron physics*, Springer (1964).

A. Beer, *Annual Review of Physical Chemistry* 86:78 (1852).

M. Benvenuti, *Studio e conservazione di Manufatti Archeologici*, Nardini Editore, Firenze (2004).

M.C. Bishop and J.C.N. Coulston, *Roman Military Equipment*, II edition, Oxbow Books (2006).

E. Blakelock, M. Martinón-Torres, H. Veldhuijzen, T. Young, *Journal of Archaeological Science* 36 (2009) 1745-1757.

W.L. Bragg, *Proceedings of the Cambridge Philosophical Society* 17 (1913) 43-57.

B. L. Bramfitt*, Metallographer's Guide: Practice and Procedures for Irons and Steels*, ASM International (2002).

N. S. Brommelle and P. Smith editors, *Urushi: Proceedings of the Urushi Study Group (June 10-27, 1985 Tokyo),* The Getty Conservation Institute (1988).

B. Bronson, *Journal of the Historical Metallurgy Society* 21:1 (1987).

R.A. Brooks, G. Di Chiro, *Theory of image reconstruction in computed tomography Radiology* 117 (1975) 561-572.

G. Brusin, P.L. Zovatto, *Monumenti romani e cristiani di Iulia Concordia*, Pordenone (1960).

T. Bücherl, E. Steichele, *Computerized tomography with thermal neutrons*, International Symposium on Computerized Tomography for Industrial Applications, June 8-10, 1994 Berlin (1995) 49-56.

V.F. Buchwald, *Iron and Steel in Ancient Times*, Kgl. Danske Videnskabernes Selskab (2005).

H.J. Bunge, *Experimental techniques of texture analysis*, Oberursel, Germany, DMG Informationsgemeinschaft (1986) 442.

H.J. Bunge, *Texture and structure of polycrystals* in: R.L. Snyder, J. Fiala, H.J. Bunge (eds), *Defects and microstructure analysis by diffraction*, International Union of Crystallography, Oxford University Press (1999) 405-519.

W. D. jr. Callister, *Materials Science and Engineering: An introduction*, VIII edition, John Wiley & Sons Incorporated (2009).

H. Cleere and B. Scott, *The craft of the blacksmith*, Symposium Beéfast, Belfast (1984).

M. D. Coe, P. Connolly, A. Harding, V. Harris, D.J. LaRocca, A. North, T. Richardson, C. Spring, F. Wilkinson, *Swords and Hilt Weapons*, Prion Book Limited (2012).

H.H. Coghlan, *Notes on the prehistoric metallurgy of copper and bronze in the Old World,* Pitt Rivers Mueum, Oxford University Press (1975).

J.C.N. Coulston, *Roman Archery E Equipment*, in *The Production and Distribution of Roman Military Equipment: Proceedings of the Second Roman Military Equipment*, Oxford (1985) 220-337.

A.M. Cormack, *Journal* of *Applied* Physics 34:9 (1963) 2722-2727.

P.T. Craddock, *Early metal mining and production*, Edinburgh University Press (1995) 363.

M. Dierick, B. Masschaele & L. Van Hoorebeke, *Measurement Science & Technology* 15:7 (2004) 1366-1370.

E. Di Filippo Balestrazzi, and A. Vigoni, *Punte di freccia dall'area del teatro Romano di Iulia Concordia, Aquileia Nostra* LXXX (2009) 143-160.

P. Dillmann, M. L'He' ritier, *Journal of Archaeological Science* 34 (2007) 1810–1823.

J.C. Domanus, *Commission of the European Communities, Euratom, Neutron Radiography Working Group, in Practical Neutron Radiography*, Springer (1992).

D.F. Draeger, *The Weapons and Fighting Arts of Indonesia*, Tuttle Publishing (2001).

W. Durant, *The Story of Civilization I: Our Oriental Heritage*, New York (1963).

Eitoku Sugimori, *Japanese Patinas*, Brynmorgen Press (2004).

A. Evans, S. Van Petegem, H. Van Swygenhoven, *Neutron News* 20 (2009) 17.

A. Fedrigo, F. Grazzi, A. Williams, A. Scherillo, F. Civita & M. Zoppi, *Journal of Analytical Atomic Spectrometry* 286 (2013) 908-915.

P.T. Flawn, *Mineral resources. Geology, engineering, economics, politics, law*, John Wiley & Sons, New York (1966) 406.

R.J. Forbes, *Studies in ancient technology*, II revisited edition, volume IX, Leiden (1964).

E. Frey, *The Kris Mystic Weapon of The Malay World*, III edition, Oxford University Press (2010).

H. Friedrich, V. Wagner, and P. Wille, *Physica B* 156&157 (1989) 547–549.

G.B. Gardner, *Keris and other Malay weapons*, B. Lumsden Milne, II edition (1936).

G. Gassmann, *New Discoveries and excavation of Early Celtic Iron Smelting Furnace (6^{th} to 2^{nd} Century B.C.) in Germany*, proceedings BUMA IV, Kunibiki Messe, Matsue, Shimane, Japan (1998).

M. Gener, *Metallographic study of some 17th and 18th C, European sword (rapier) blades*, in *2nd International Conference Archaeometallurgy in Europe 2007. Selected papers*, Associazione Italiana di Metallurgia (2009) 282-293.

R.J. Gettens and G.L. Stout, *Painting materials: a short encyclopaedia*, II edition, Dover Publications (1966).

L. Giller, U. Filges, G. Kühne, M. Wohlmuther, L. Zanini, *Nuclear Instruments and Methods in Physics Research A* 586 (2008) 59–63.

I.H Goodall, *Society for Medieval Archaeology Monographs* 31 (2012).

D.G. Grant, *IEEE Transactions on Biomedical Engineering* 19 (1972) 20.

F. Grazzi, L. Bartoli, S. Siano, M. Zoppi, *Analytical and Bioanalytical Chemistry* 397 (2010) 2501-2511.

F. Grazzi, F. Civita, A. Williams, A. Scherillo, E. Barzagli, L. Bartoli, D. Edge, M. Zoppi, *Analytical and Bioanalytical Chemistry* (2011) 1494-1500.

F. Grazzi, L. Bartoli, F. Civita, R. Franci, A. Paradowska, A. Scherillo and M. Zoppi, *Journal of Analytical Atomic Spectrometry* 26 (2011) 1030.

F. Grazzi, P. Pallecchi, P. Petitti, A. Scherillo, and M. Zoppi; Non-invasive quantitative phase analysis and microstructural properties of an iron fragment retrieved in the copper-age Selvicciola Necropolis in southern Tuscia, *Journal of Analytical Atomic Spectrometry* 27 (2012) 293

B. Hammouda, *Probing Nanoscale Structures – The Sans Toolbox*, National Institute of Standards and Technology Center for Neutron Research Gaithersburg (2009) MD 20899-6102.

H. Hatherly, *Introduction to Textures in Metals*, Paperback Publisher, Inst of Materials (1979).

Hai-Yen Nguyen, *Computed Tomography for the non-destructive imaging of cultural heritage: x-ray, gamma and neutron sources*, thesis submitted to the Department of Art in conformity with the requirements for the degree of Master of Art Conservation, Queen's University Kingston, Ontario, Canada (2011).

A. Hauptmann, *5000 Jahre Kupfer in Oman*, Der Anschnitt, Beiheft 4 (1985) 147.

A. Hauptmann *et al.*, *Archaeomaterials* 6:1 (1992) 1-33.

L. Helfen, T. Baumbach, P. Mikulı´k, D. Kiel, P. Pernot, P. Cloetens, J. Baruchel, *Applied Physics Letters* 86 (2005) 071915.

L. Helfen, A. Myagotin, A. Rack, P. Pernot, P. Mikulík, M. Di Michiel, T. Baumbach, *Physica Status Solidi (a)* 204:8 (2007) 2760–2765.

L. Helfen, T. F. Morgeneyer, F. Xu, M. N. Mavrogordato, I. Sinclair, B. Schillinger, T. Baumbach, *Nuclear Instruments and Methods in Physics Research A* 651:1 (2011) 135-139.

L. Helfen, T. F. Morgeneyer, F. Xu, M. N. Mavrogordato, I. Sinclair, B. Schillinger, T. Baumbach, *International Journal of Materials Research* (2012) 170-173.

Herodotus, *Histories*, John M. Marincola (Editor, Introduction), Aubery de Selincourt (Translator), Revised (Penguin Classics) (2003).

H. Hoshi and M. Sasaki, *Tetsu-to-hagane* 91 (2005) 103-107.

G.N. Hounsfield, *British Journal of Radiology* 46 (1973) 1016.

G.N. Hounsfield, *Science* 210, 4465 (1980) 22-28.

M.T. Hutchings, P.J. Withers, T.M. Holden, T. Lorentzen, *Introduction to the Characterization of Residual Stress by Neutron Diffraction*, I edition, CRC Press (2005).

T. Inoue, *Acta Mechanica* 214, N1-2 (2009) 17-30.

J.H. Lambert, *Photometria sive de mensura et gradibus luminis, colorum et umbrae* ("Photometry or on the measure and gradations of light, colors, and shade") (Augsburg "Augusta Vindelicorum", Germany: Eberhardt Klett (1760).

E. H. Lehmann, P. Vontobel & L. Wiezel, *Nondestructive Testing and Evaluation* 16:2-6 (2001) 191-202.

E. Lehmann, L. Josic, and G. Frei, *Neutron News* 20:20 (2009).

E. Lehmann And S. Hartmann, *Archaeometry* 52:3 (2010) 416–428.

E. Lehmann, E. Deschler-Erb, A. Ford, *Archaeometry* 52:272 (2010).

E.H. Lehmann, A. Kaestner, L. Josic, S. Hartmann, D. Mannes, *Nuclear Instruments and Methods in Physics Research Section A: Accelerators, Spectrometers, Detectors and Associated Equipment* 651:1 (2011) 161–165.

K. Janssens and R. van Grieken, *Non-destructive Micro Analysis of Cultural Heritage Materials*, Elsevier Science (2004).

C. Johnson, *Some Aspects of the Metallurgy and Production of European Armor*, Armored Proceedings Symposium Notes (1999).

L. Josic, A. Steuwer, E. Lehmann, *Applied Physics A* 99:515 (2010).

L. Josic, E. Lehmann, A. Kaestner, *Nuclear Instruments and Methods in Physics Research Section A: Accelerators, Spectrometers, Detectors and Associated Equipment* 651:1 (2011) 166–170.

G. Juleff, *World Archeology* 41:4 (2009) 553-577.

A. P. Kaestner, S. Hartmann, G. Kuhne, G. Frei, C. Grunzweig, L. Josic, F. Schmid, E. H. Lehmann, *Nuclear Instruments and Methods in Physics research section A-accelerators spectrometers detectors and associated equipment* 659:387 (2011).

A.C. Kak and M. Slaney, *Principles of Computerized Tomographic Imaging*, IEEE Press, New York (1988).

Kanzan Soto, *The Japanese Sword: A Comprehensive Guide*, Kodansha (1983).

L. and H. Kapp, Y. Yoshihara, *The Craft of the Japanese sword*, Kodansha International (1987).

N. Kardjilov, B. Schillinger, E. Steichele, *Applied Radiation and Isotopes* 61:4 (2004) 455-460.

N. Kardjilov, A. Hilger, I. Manke, M. Strobl, S. Williams, M. Dawson, J. Banhart, *Nuclear Instruments and Methods in Physics Research A*, 651:1 (2011) 47-52.

N. Kardjilov, M. Dawson, A. Hilger, I. Manke, M. Strobl, D. Penumadu, F.H. Kim, F. Garcia-Moreno and J. Banhart, *Nuclear Instruments and Methods in Physics Research A* 651:1 (2011) 95-99.

N. Kardjilov, I. Manke, A. Hilger, M. Strobl, J. Banhart, *Materials Today* 14:6 (2011) 248-2565.

N. Kardjilov, I. Manke, A. Hilger, S. Williams, M. Strobl, R. Woracek, M. Boin, E. Lehmann, D. Penumadu, J. Banhart, *International Journal of Materials Research* 103:151 (2012).

B. Kaufman, *Metallurgy and ecological change in the ancient near east*, in *Backdirt Annual Review of the Cotsen Institute of Archaeology* (2011).

C. Kittel, *Introduction to Solid State Physics*, VII edition, John Wiley & Sons Inc. (1996).

W. Kockelmann, S. Siano, M. Schreiner, *Time-of-flight neutron diffraction for characterising archaeological artefacts*, in *Studio e conservazione di manufatti archeologici*, Nardini Editore, Firenze (2004).

U.F. Kocks, C.N.Tom, R.H.Wenk, *Texture and Anisotropy*, Cambridge University Press, Cambridge (1998).

A.M. Kossevich, *The Crystal Lattice-Phonons, Solitons, Dislocations*, Wiley-vch, I edition (1999).

Kozan Sakakibara, *The manufacture of armour and helmets in 16th century Japan:(chūkokatchū seisakuben)*; translated by T. Wakameda, revised by Koop, A. J., and Hogitarō Inada, 1912; revised and edited by Robinson, Russel H., The Holland Press, London (1963).

K. Krug, L. Porra, P. Coan, G. Tauber, A. Wallert, J. Dik, A. Coerdt, A. Bravin, M. Elyyan, L. Helfen, T. Baumbach, *Journal of Synchrotron Radiation* 15 (2008) 55.

R. Maddin, J.D. Muhly and T. Stech, *Early metalworking at Çayönü,* in: A. Hauptmann, E. Pernicka, T. Rehren & Yalçin Ü. (eds), *The beginnings of metallurgy*, Der Anschnitt, Beiheft 9, Bochum (1999) 37- 44.

S. Magotti, *Nipponto - L'Anima del Samurai-Evoluzione, arte, tecnica dell'arma più efficiente della storia*, Ponchiroli editore (2011).

D.C. Mannes, *Non-Destructive Testing of Wood by means of Neutron Imaging in comparison with similar methods*, A dissertation submitted to Eth Zurich for the Degree of Doctor of Sciences, Dipl. Forstwirt, Albert-Ludwigs-Universit¨at Freiburg I. Br. (D) (2009).

J.W.F. Markgraf, R. Matfield, *Neutron beam,* in: *Practical neutron radiography,* Ed. J.C. Domanus, Kluwer, Dordrecht. (1992) 26-50.

T.E. McDonald Jr., T.O. Brun, T.N. Claytor, E.H. Farnum, G.L. Greene, C. Morris, *Nuclear Instruments and Methods in Physics Research A* 424 (1999) 235.

P.R.S. Moorey, *Ancient Mesopotamian Materials and Industries: The Archaeological Evidence*, Oxford/New York: Clarendon Press (1994).

K. Nagayama, *The Connoisseurs Book of Japanese Swords*, Kodansha International (1997).

W. Nicodemi, *Siderurgia. Processi e impianti*, AIM, Milano (1994).

M.R. Notis, *Materials Characterization* 45 (2000) 253-258, and references within.

M. Pallottino, *Gli Etruschi*, Bompiani, Milano, 1998.

C. Panseri, *GLADIU* S1: 9 (1965) 5.

A. M. Paradowska, A. Tremsin, J. F. Kelleher, S. Y. Zhang, S. Paddea, G. Burca, J. James, R. Ahmed, N. H. Faisal, F. Grazzi, G. Festa, C. Andreani, F. Civita, P. J. Bouchard, W. Kockelman and M. E. Fitzpatrick, *Journal of Solid Mechanics and Materials Engineering* 6:6 (2012) 408–418.

W. Pearson, *Handbook of Lattice Spacings & Structures of Metals & Alloys (International Series of Monographs on Metals Physics & Physical Metallurgy*, Franklin Book Co (1964).

W. B. Pearson and George H. Vineyard, Reviewer, *A Handbook of Lattice Spacings and Structures of Metals and Alloys,* Brookhaven National Laboratory, American Institute of Physics (1958).

S. Peetermans, L. Josic, H.V. Swygenhoven and E.H. Lehmann, *A new monochromator for energy-selective imaging,* Neuwave-4 Conference (2011).

S. Peetermans, F. Grazzi, F. Salvemini and E.H. Lehmann, *Physics Procedia* 43 (2013) 121-127.

J. Piaskowski, Journal of the Iron and Steel Institute 202 (1964).

V.C. Pigott, *The Archaeometallurgy of the Asian Old World*. Philadelphia: University of Pennsylvania Museum of Archaeology and Anthropology (1999) 8.

R. Pleiner, *The Celtic Sword*, Clarendon Press, Oxford (1993).

R. Pleiner, *Das fruhe Eisen: Von der Kleinwaagemengen zu der altesten Industrie Ethnographisch-Archaologische Zeitschrift* (1996) 283-289.

T.M. Porter, *The Cambridge History of Science,* Cambridge University Press (2003) 684.

B. Prakash and V. Tripathi, *Iron technology in ancient India, Historical Metallurgy* (1986) 578.

C. Qui and S van der Zwaag, *Dilatation measurement of plain carbon steel and their therodynamic analysis*, Laboratory of Materials Science, Delft University of Technology, Delft, 68:1 (1997) 32-38.

J. Radon, *Über die Bestimmung von Funktionen durch ihre Integralwerte längs gewisser Mannigfaltigkeiten. Ber. Ver. Sächs. Akad. Wiss. Leipzig*, Math-Phys. Kl:69 (1917) 262–277.

V. Randle and O. Engler, *Introduction to Texture Analysis: Macrotexture, Microtexture, and Orientation Mapping*, II edition, Crc Pr I Llc (2009).

P. Rinard, *Neutron interactions with matter*, in: *Passive Nondestructive Assay of Nuclear Materials*, Eds. D. Reilly, N. Ensslin, H. Smith Jr., Nuclear Regulatory Commission, NUREG/CR-5550 (1991) 357–377.

B.W. Robinson, *The Arts of the Japanese Sword*, R. MacLehose and Company (1970).

F. Salvemini, F. Grazzi, S. Peetermans, F. Civita, R. Franci, S. Hartmann, E. Lehmann, M. Zoppi, *Journal of Analytical Atomic Spectrometry* 27:1494 (2012).

F. Salvemini, F. Grazzi, A. Agostino, R. Iannaccone, F. Civita, S. Hartmann, E. Lehmann, M. Zoppi, *Archaeological and Anthropological Sciences* 5:3 (2013) 197-204.

F. Salvemini, F. Grazzi, A. Fedrigo, A. Williams, F. Civita, A. Scherillo, P. Vontobel, S. Hartmann, E. Lehmann and M Zoppi, *The European Physical Journal Plus* 128:87 (2013).

J.R. Santisteban, L. Edwards, A. Steuwer, P.J. Withers, *Journal of Applied Crystallography* 34 (2001) 289–297.

K. Sato, *The Japanese Sword: A Comprehensive Guide*, Kodansha International (1997).

P. Scherrer, *Nachr. G¨ott.* 2 (1918) 98-100.

B. Schillinger, W Blümlhuber, A. Fent, M. Wegner, *Nuclear Instruments and Methods in Physics Research Section A: Accelerators, Spectrometers, Detectors and Associated Equipment* 424:1 (1999) 58-65.

B. Schillinger, E. Lehmann, P. Vontobel, *Physica B* 276-278 (2000) 59-62.

D.A. Scott, *Metallography and microstructure of ancient and historic metals*, The J. Paul Getty Institute (1991).

V. F. Sears, *Neutron News* 3, 29 (1992).

E. Shurmann, *Die Reduktion des Eisens im Rennfeuer*, Stahl und Eisen, 78 (1958) 1297-1307.

S. Siano, W. Kockelmann, U. Bafile, M. Celli, M. Iozzo, M. Miccio, O. Moze, R. Pini, R. Salimbeni, M. Zoppi, *Applied Physics A* 74:S1139–S1142 (2002).

S. Siano, L. Bartoli, M. Zoppi, W. Kockelmann, M. Daymond, J.A. Dann, G. Garagnani, *Archaeometallurgy in Europe* 2 (Associazione Italiana di Metallurgia, Milano) (2003) 319-329.

C. Sinclaire, *Samurai: The Weapons and Spirit of the Japanese Warrior*, The Lyons Press, Guilford (2004).

G. L. Squires, *Introduction to the theory of Thermal Neutron Scattering*, Dover Publication Inc. New York (1996).

A.M. Stevens, *A comprehensive Indonesian-English Dictionary*, PT Mizan Publika (2004)

U. Stuhr, *Nuclear Instruments and Methods in Physics Research A* 545 (2005) 319-329.

U. Stuhr, H. Spitzer, J. Egger, A. Hofer, P. Rasmussen, D. Graf, A. Bollhalder, M. Schild, G. Bauer, W. Wagner, *Nuclear Instruments and Methods in Physics Research* A 545 (2005) 330–338.

U. Stuhr, M. Grosse, W. Wagner, *Materials Science and Engineering A* 437 (2006) 134

M. Tamaki, *Nuclear instruments and methods in physics research A* 542 (2005) 32-37

K. Tawara, *Nippon-to no Kogataki Kenkyu (Scientific Study of Japanese Swords),* Tokyo (1953).

Toshikatsu Nakasato, *Science for conservation* 37 (1998) 46-58.

W. Treimer, M. Strobl, N. Kardjilov, A. Hilger, I. Manke, *Applied Physics Letters* 89: 20 (2006).

A. Tuffanelli, M. Sánchez del Río, G. Pareschi, M. Gambaccini, A. Taibi, A. Fantini and M. Ohler, A comparative characterization of Highly Oriented Pyrolytic Graphite by means of diraction topography, *Proceedings of the SPIE - The International Society for Optical Engineering,* 3773 (1999) 192-198

R.F. Tylecote, *The early history of metallurgy in Europe,* Longman Archeological Series, London (1987).

R. F. Tylecote and B. J. Gilmour, *The metallurgy of early ferrous edge tools and edged weapons*, *BAR, British Series*, 155, Oxford (1956).

A. G. Van Zonneveld, *Traditional Weapons of the Indonesian Archipelago*, Koninklyk Instituut Voor Taal Land (2002).

A. Vigoni, *Il canale interno di Iulia Concordia. Dati storici, archeologici e topografici*, in D. Morandi Bonacossi, E. Rova, F. Veronese, P. Zanovello (edited by), *Tra Oriente e Occidente*, Padova (2006) 451-468.

M.L. Wayman, *All the glisters. Readings from Metallurgical History*, Canadian Institute of Mining and Metallurgy, Montreal (1989).

S. C. Welch, *India: Art and Culture*, Metropolitan Museum of Art New York (1985)

T.S. Wheeler And R. Maddin, *Metallurgy and ancient man,* in*:* T.A. Wertime and J.D. Muhly eds., *The coming of the age of iron*, Yale Univ. Press, New Haven-London (1980) 99-126.

A. Williams, *Gladius XIII* (1977) 75-101.

A. Williams, *The Knight and the Blast Furnace: A History of the Metallurgy of Armour in the Middle Ages & the Early Modern Period*, Brill Academic Pub (2003).

A. Williams, *The Sword and the Crucible: a History of the Metallurgy of European Swords up to the 16th Century*, Brill Academic Pub (2012).

C. Windsor, *Pulsed Neutron Scattering*, Taylor and Francis, London (1981).

D. Wittner, *Technology and the culture of progress in meiji Japan*, New York, NY: Routledge (2007) 24-26.

Ü. Yalçin and E. Pernicka, *Frühneolithische Metallurgie von A_ikli Höyük.* in: A. Hauptmann, E. Pernicka, T. Rehren & Yalçin Ü. (eds), *The beginnings of metallurgy*, Der Anschnitt, Beiheft 9, Bochum (1999) 45-54.

B.G. Ziedses des Plantes, *Acta Radiologica* 13 (1932) 182.

P.L. Zovatto, *Portogruaro, Museo Nazionale Concordiese. Concordia: scavi, battistero. Summaga: abbazia. Sesto al Reghena: abbazia. Caorle*, in *Musei d'Italia, meraviglie d'Italia*, III edition, Bologna (1971).

Sitography

http://www.thejapanesesword.com/tatara

http://www.psi.ch/niag/neutron-physics

http://www.psi.ch/niag/neutron-interaction-with-matter#

http://www.psi.ch/niag/neutron-imaging-setup

http://www.psi.ch/niag/neutron-tomography#

http://www.nippon-kako.co.jp/patent.html

http://nekotani.lix.jp/diary/index.php?e=345

http://www.rufinoturranio.it/ita_concordia_sagittaria_romana_associazione_culturale_onlus_rufino_turranio_provincia_venezia_veneto_italia.asp

Acknowledgments

I would not have been able to complete this journey without the aid and support of countless people over the past three years. I must first express my gratitude towards my supervisors, Dr. Marco Zoppi and Dr. Francesco Grazzi.

Dr. Marco Zoppi's leadership, support, attention to detail, and scholarship have set an example for me. Dr. Francesco Grazzi has supported me throughout my thesis with his patience and knowledge, while allowing me to work in my own way. I attribute the level of my research to his encouragement and effort: without him this thesis could not have been completed. One simply could not wish for a better or friendlier supervisor.

Of course, this project would not have been possible without the collaboration of many experts and institutions.

I need to express my gratitude to Dr. Alan Williams from the Wallace Collection in London for illuminating discussions.

I would gratefully thank Dr. Francesco Civita and Dr. Riccardo Franci from Museo Stibbert in Florence, Dr. Marc Gener from Instituto de Historia (IH-CSIC) in Madrid, Dr. Gloria Roselli and Dr. Giovanni Pratesi from Museo di Storia Naturale in Florence, Dr. Ivana Angelini and Prof. Gilberto Artioli from University of Padova, Dr. Alberto Vigoni from Dedalo s.n.c. in Padova, Dr. Romano Marchi and Dr. Jonathan Barrett, for their invaluable contribution and for making samples available for investigation.

I would like to take this opportunity to record my sincere gratitude especially to Prof. Eberard Lehemann, whose insightful comments and suggestions were an enormous help to me, and Dr. Peter Vontobel, Dr. Anders Kaestner, Steven Peetermans, Dr. Vadim Davydov from Paul Scherrer Institut in Villigen (CH) for the assistance and facilities they provided.

I'm also indebted to Florian Schmid for his hard work on the VG Studio animation attached to this thesis.

I owe a very important debt to Dr. Nikolay Kadjilov, who shared his memories and experiences, and Frank Wieder, Dr. André Hilger, Dr. Ingo Manke, who patiently guided and supported me professionally during my three-month internship at the Helmholtz-Zentrum Berlin in Wannsee (DE).

My thanks also go to Dr. Marco Benvenuti from University of Florence, Dr. Antonella Scherillo from Science and Technology Facility Council in Didcot (UK), Dr. Alessandro Lo Giudice and his research group from University of Torino, for all their useful suggestions and help.

My training in the complex word of neutrons has greatly benefited, too, from the enormous contribution of the Italian Neutron Spectroscopy Society (SISN).

Deepest gratitude is also due to Prof. John Banhart from Institute of Materials Science and Technology-Berlin Institute of Technology (TU Berlin), and Dr. Heloisa N. Bordallo from Niels Bohr Institute-University of Copenhagen (DK) for acting as external referees of my thesis.

It would not have been possible to write this doctoral thesis without the help and support of the kind people around me, to only some of whom it is possible to give particular mention here.I would like to thank my life partner, Alessandro. He was always there cheering me up and stood by me through the good times and bad.

My gratitude goes to my parents, Dora and Michele, for instilling in me the confidence and drive needed to pursue my PhD. Thank you to my sister, Simona, and my brother, Cosimo, for their continual love.

I must thank Lucia and Giuseppe for always considering me a part of their wonderful family. They have consistently helped me keep perspective on what is important in life.

Many thanks also to Luca and Fabrizia for their encouragement throughout this year as part of my “extended” family.
I must acknowledge as well the many friends and colleagues who assisted, advised, and supported my research and writing efforts.
I wish to thank Anna for introducing me to the pleasures of Carcassonne and for experiencing with me the beauty of watching a film at the Cinema Odeon in Florence. Also, my compatriot Roberta, who has spoiled me by preparing delicious dishes and sharing memories about how wonderful our home region is in every aspect. Elisa, my first office mate in Florence, who has made synchronized swimming exciting and whose strength in dealing with the difficulties of life is a model for me. It would have been a lonely office without you. Your friendship has supported, enlightened, and entertained me during these years.
Many thanks to Francesco the *Strullino*. Your radiant personality and, above all, chocolate gifts have sustained me during hard days. Filippo, I know displays of affection drag you out of your comfort zone, however your free cruelty and unique sarcasm will always be a reference. My special thanks are extended to Veronica, who was great company throughout this journey.
I would like to thank Marcello and Sirpa, who were always willing to help and give their best suggestions. There will always be a guest room for you wherever I go.
Special thanks go to Elisa’s parent for adopting me, despite the unfavorable opinion their son developed of me due to my vegetarian diet.
Thanks also to three special people who have welcomed me with open arms and made me feel at home in Florence, my flat mates, Ada, Debora and Tiziana.
Although we were so far away, Cristina and Grazia, your encouragement and friendship are, have been and always will be a constant for me. Thank you!